Nano-Optics and Nanophotonics

Yong Sheng Zhao *Editor*

Organic Nanophotonics

Fundamentals and Applications

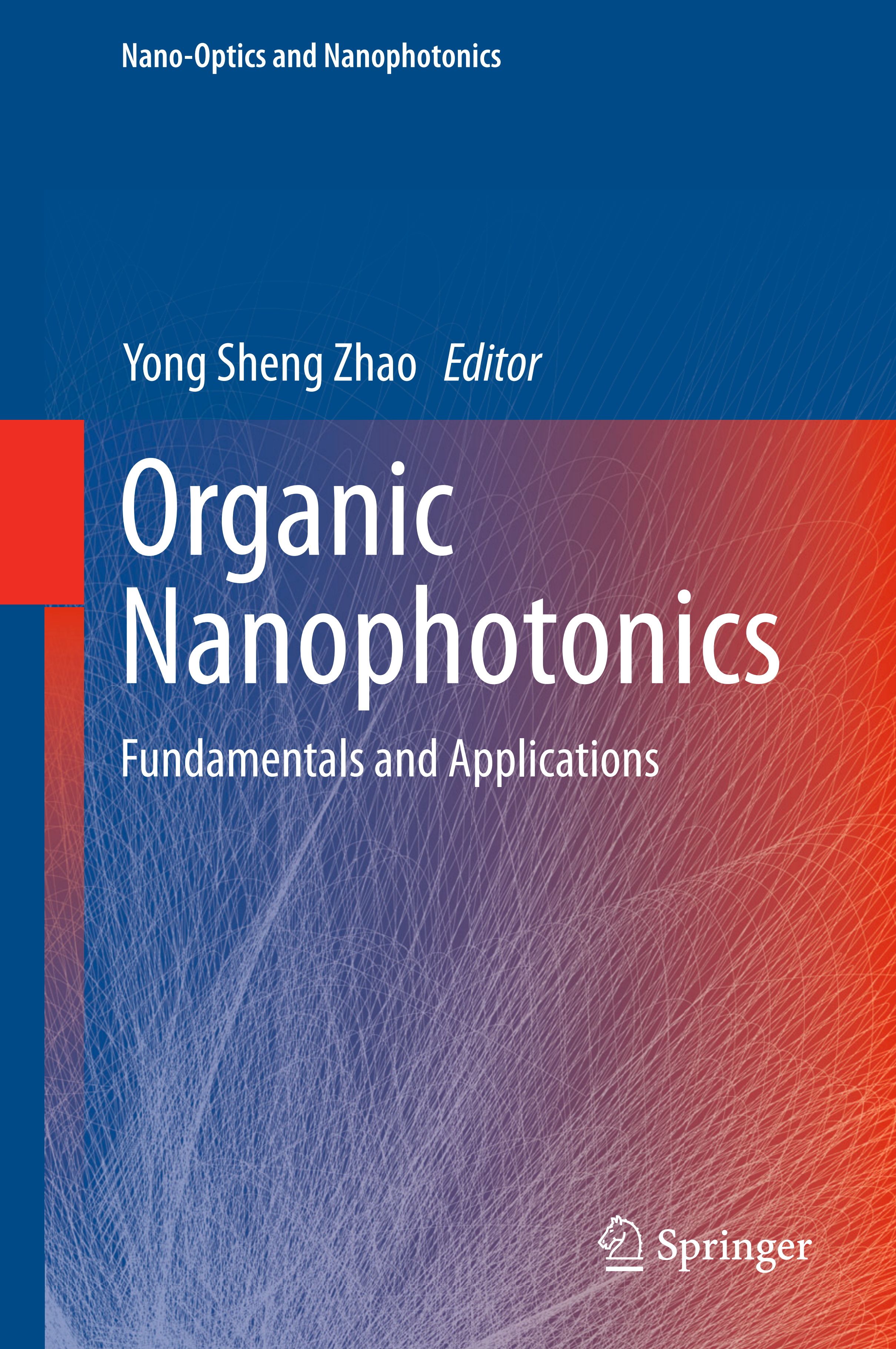

Springer

Nano-Optics and Nanophotonics

The Springer Series in Nano-Optics and Nanophotonics provides an expanding selection of research monographs in the area of nano-optics and nanophotonics, science- and technology-based on optical interactions of matter in the nanoscale and related topics of contemporary interest. With this broad coverage of topics, the series is of use to all research scientists, engineers and graduate students who need up-to-date reference books. The editors encourage prospective authors to correspond with them in advance of submitting a manuscript. Submission of manuscripts should be made to the editor-in-chief, one of the editors or to Springer.

More information about this series at http://www.springer.com/series/8765

Yong Sheng Zhao
Editor

Organic Nanophotonics

Fundamentals and Applications

Springer

Editor
Yong Sheng Zhao
Institute of Chemistry
Chinese Academy of Sciences
Beijing
China

ISSN 2192-1970 ISSN 2192-1989 (electronic)
ISBN 978-3-662-45081-9 ISBN 978-3-662-45082-6 (eBook)
DOI 10.1007/978-3-662-45082-6

Library of Congress Control Number: 2014954237

Springer Heidelberg New York Dordrecht London

© Springer-Verlag Berlin Heidelberg 2015
This work is subject to copyright. All rights are reserved by the Publisher, whether the whole or part of the material is concerned, specifically the rights of translation, reprinting, reuse of illustrations, recitation, broadcasting, reproduction on microfilms or in any other physical way, and transmission or information storage and retrieval, electronic adaptation, computer software, or by similar or dissimilar methodology now known or hereafter developed. Exempted from this legal reservation are brief excerpts in connection with reviews or scholarly analysis or material supplied specifically for the purpose of being entered and executed on a computer system, for exclusive use by the purchaser of the work. Duplication of this publication or parts thereof is permitted only under the provisions of the Copyright Law of the Publisher's location, in its current version, and permission for use must always be obtained from Springer. Permissions for use may be obtained through RightsLink at the Copyright Clearance Center. Violations are liable to prosecution under the respective Copyright Law.
The use of general descriptive names, registered names, trademarks, service marks, etc. in this publication does not imply, even in the absence of a specific statement, that such names are exempt from the relevant protective laws and regulations and therefore free for general use.
While the advice and information in this book are believed to be true and accurate at the date of publication, neither the authors nor the editors nor the publisher can accept any legal responsibility for any errors or omissions that may be made. The publisher makes no warranty, express or implied, with respect to the material contained herein.

Printed on acid-free paper

Springer is part of Springer Science+Business Media (www.springer.com)

Preface

This book contains eight chapters on the progress made in recent years in the fabrication, processing, and performance of organic nanophotonic materials and devices. To the best of my knowledge, it is the first monograph in this field.

Nanophotonics deals with the generation, transfer, modulation, and detection of photons in a confined system, which provides an effective solution to the current obstacles that seriously limit the further improvement of modern electronics. Chemists and material scientists have contributed enormously to the achievement of novel optical properties with inorganic materials, such as ZnO, CdSe as well as noble metal nanostructures.

While their inorganic counterparts have flourished, organic materials and devices are gradually becoming a good alternative choice due to their numerous advantages. Organic compounds possess high photoluminescence quantum yields, tunable optical properties, and rapid photoresponses. The excellent flexibility and processability are also big pluses in the construction and assembling of functional photonic devices. Overall, there is no doubt that organic molecular materials would bring great innovation in the design and fabrication of functional elements toward photonic integrated circuits.

Nowadays, research on *Organic Nanophotonics* is growing rapidly. The editor and authors attempted to give a fairly comprehensive introduction to the fabrication, properties, and functionalities of organic nanophotonic materials and devices. The book is useful for scientists and engineers who want to get deeper insights into the novel applications of nanophotonics that will be of key importance in our lives and for wider society, both today and in the future.

Chapter 1 (Duan et al.) discusses photonic nanofabrications and microscopy imaging based on multiphoton processes. Chapters 2 (La Rocca et al.), 3 (Ma et al.), and 4 (Pei et al.) present nanoscale light sources for integrated nanophotonic circuits, including organic nano/microcavities, organic laser materials, and polymer light-emitting electrochemical cells (LECs). All these chapters are related to light emission, but it should be remarked that they present distinct nanoscale light sources and microscopic processes. Chapters 5 (Takazawa et al.), 6 (Inoue et al.), and 7 (Barillé et al.) are based on the interactions between light and matter, including the propagation of light in organic nanostructures, photoswitches based on nonlinear optical polymer photonic crystals, and photoresponsive molecules, respectively. Chapter 8 (Zhao et al.) discusses the integration of miniaturized photonic devices and circuits with various organic nanophotonic elements.

The editor hopes that this book will be a valuable reference source for scientists, graduate students, engineers, industrial researchers, and other professionals working at the interfaces of chemistry, physics, materials, optics, information, etc. This book is a must-have reference for university libraries, research establishments, government libraries, and high-tech companies engaged in research and development of photonics and nanotechnology.

Finally, I would like to express my gratitude to all the authors for contributing comprehensive chapters. I also thank colleagues who offered invaluable advice to ensure the quality of this book, and the editorial staff of Springer, especially June Tang, for their guidance and suggestions throughout the preparation of this book. I expect that this book will attract students' attention and stimulate their interests and innovative ideas in this promising and fascinating field.

Beijing, China Yong Sheng Zhao

Contents

Contributors

R. Barillé Moltech Anjou, CNRS UMR 6200, PRES UNAM, University of Angers, Angers, France

Xuan-Ming Duan Laboratory of Organic NanoPhotonics and Key Laboratory of Functional Crystals and Laser Technology, Technical Institute of Physics and Chemistry, Chinese Academy of Sciences, Beijing, People's Republic of China; Chongqing Institutes of Green and Intelligent Technology, Chinese Academy of Sciences, Beibei District, Chongqing, People's Republic of China

Huier Gao Soft Materials Research Laboratory, Department of Materials Science and Engineering, Henry Samueli School of Engineering and Applied Science, University of California, Los Angeles, CA, USA

J. Inoue National Institute for Materials Science (NIMS), Tsukuba, Japan

Shin-ichiro Inoue Advanced ICT Research Institute, National Institute of Information and Communications Technology (NICT), Kobe, Japan

Giuseppe C. La Rocca Scuola Normale Superiore and CNISM, Pisa, Italy

Lu Li Soft Materials Research Laboratory, Department of Materials Science and Engineering, Henry Samueli School of Engineering and Applied Science, University of California, Los Angeles, CA, USA

Jiajie Liang Soft Materials Research Laboratory, Department of Materials Science and Engineering, Henry Samueli School of Engineering and Applied Science, University of California, Los Angeles, CA, USA

Linlin Liu State Key Laboratory of Luminescent Materials and Devices, Institute of Polymer Optoelectronic Materials and Devices, South China University of Technology, Guangzhou, People's Republic of China

Yuguang Ma State Key Laboratory of Luminescent Materials and Devices, Institute of Polymer Optoelectronic Materials and Devices, South China University of Technology, Guangzhou, People's Republic of China

Leonardo Mazza NEST, Scuola Normale Superiore and Instituto Nanoscienze—CNR, Pisa, Italy

Paolo Michetti Institut für Theoretische Physik, Technische Universität Dresden, Dresden, Germany

K. Mitsuishi National Institute for Materials Science (NIMS), Tsukuba, Japan

J.M. Nunzi Department of Chemistry, Queen's University, Kingston, ON, Canada

E. Ortyl Department of Polymer Engineering and Technology, Wrocław University of Technology, Wrocław, Poland

Qibing Pei Soft Materials Research Laboratory, Department of Materials Science and Engineering, Henry Samueli School of Engineering and Applied Science, University of California, Los Angeles, CA, USA

K. Takazawa National Institute for Materials Science (NIMS), Tsukuba, Japan

Zengqi Xie State Key Laboratory of Luminescent Materials and Devices, Institute of Polymer Optoelectronic Materials and Devices, South China University of Technology, Guangzhou, People's Republic of China

Yongli Yan Beijing National Laboratory for Molecular Science (BNLMS), CAS Key Laboratory of Photochemistry, Institute of Chemistry, Chinese Academy of Sciences, Beijing, China

Zhibin Yu Soft Materials Research Laboratory, Department of Materials Science and Engineering, Henry Samueli School of Engineering and Applied Science, University of California, Los Angeles, CA, USA

Yong Sheng Zhao Beijing National Laboratory for Molecular Science (BNLMS), CAS Key Laboratory of Photochemistry, Institute of Chemistry, Chinese Academy of Sciences, Beijing, China

Mei-Ling Zheng Laboratory of Organic NanoPhotonics and Key Laboratory of Functional Crystals and Laser Technology, Technical Institute of Physics and Chemistry, Chinese Academy of Sciences, Beijing, People's Republic of China

S. Zielinska Department of Polymer Engineering and Technology, Wrocław University of Technology, Wrocław, Poland

Chapter 1
Multiphoton Process in Nanofabrication and Microscopy Imaging

Mei-Ling Zheng and Xuan-Ming Duan

Abstract Under the intense intensity of femtosecond laser pulse, various nonlinear optical effects between laser and matter can occur. Among them, one nonlinear optical effect, multiphoton absorption (MPA), is easily induced by femtosecond laser pulse, which provides an opportunity to achieve the spatial resolution smaller than optical diffraction limit. Multiphoton process using femtosecond laser has provided a powerful technique for fabricating three-dimensional (3D) micro/nanostructures and microscopy imaging due to its intrinsic 3D penetration depth and high spatial resolution at nanometric scale. As an emerging micro/nanofabrication technique, multiphoton polymerization (MPP) based on multiphoton process has been used in fabricating various micromachines and microdevices with conventional photoresists and polymer nanocomposites, such as microneedles, micropumps, microgear sets, and 3D photonic crystals. Aside from MPP based on multiphoton process, microscopy imaging is another research field employing multiphoton process. Two-photon-excited fluorescence (TPEF) microscopy, an established nonlinear microscopy technique, is more practically useful for noninvasive live cell imaging because of the deeper penetration, less photobleaching, and higher spatial resolution. Second-harmonic generation (SHG) is a nonlinear optical process, in which photons with the same frequency interacting with a nonlinear material are effectively "combined" to generate new photons with twice the energy, and therefore twice the frequency and half the wavelength of the initial photons. SHG, as an even-order nonlinear optical effect, is only allowed in

---

M.-L. Zheng · X.-M. Duan (✉)
Laboratory of Organic NanoPhotonics and Key Laboratory of Functional Crystals and Laser Technology, Technical Institute of Physics and Chemistry, Chinese Academy of Sciences,
No. 29, Zhongguancun East Road, Beijing 100190, People's Republic of China
e-mail: xmduan@mail.ipc.ac.cn

X.-M. Duan
Chongqing Institutes of Green and Intelligent Technology, Chinese Academy of Sciences,
No. 266, Fangzheng Ave, Shuitu Technology Development Zone, Beibei District,
Chongqing 400714, People's Republic of China

Y.S. Zhao (ed.), *Organic Nanophotonics*, Nano-Optics and Nanophotonics,
DOI 10.1007/978-3-662-45082-6_1

mediums without inversion symmetry. In recent years, SHG microscopy has been used for extensive studies. Stimulated Raman scattering (SRS) is another phenomenon based on multiphoton process. The investigation on multiphoton process in nanofabrication and microscopy imaging would open up new avenues for developing new laser techniques in nanophotonics, plasmonics, and biosciences.

1.1 Introduction

Laser has gained much attention due to its application in both science and industry since its development in 1960. Owing to the advantage of higher power, better monochromaticity and less divergence angle compared to other light sources, laser has been widely used in human science, medicine, manufacturing industry, and so on. Femtosecond laser has played an important role during the development of lasers. Under the intense intensity of femtosecond laser pulse, various nonlinear optical effects between laser and matter can occur. Among them, one of the nonlinear optical effects, multiphoton absorption (MPA), is easily induced by femtosecond laser pulse, which provides an opportunity to achieve the spatial resolution smaller than the optical diffraction limit. Multiphoton process using femtosecond laser has provided a powerful technique for fabricating three-dimensional (3D) micro/nanostructures and microscopy imaging due to its intrinsic 3D penetration depth and high spatial resolution at nanometric scale. This chapter focuses on the recently developed and emerging laser nanofabrication and microscopy techniques.

As an emerging micro/nanofabrication technique, multiphoton polymerization (MPP) based on multiphoton process has been considered as an economical and powerful maskless means for high-resolution and intrinsic 3D microstructure fabrication. In MPP process, the femtosecond laser is tightly focused into the photoresist and thus the desired pattern can be created. By using this technique, various complicated structures, such as microneedles, micropumps, microgear sets, and 3D photonic crystals, are able to be fabricated with conventional photoresist, polymer nanocomposite and even metal aqueous solution, which would provide high potential for the application in electronics and nanophotonics.

Aside from MPP based on multiphoton process, microscopy imaging is another research field employing multiphoton process. Two-photon-excited fluorescence (TPEF) microscopy, an established nonlinear microscopy technique, is more practically useful for noninvasive live cell imaging because of the deeper penetration, less photobleaching and higher spatial resolution. Second-harmonic generation (SHG) is a nonlinear optical process, in which photons with the same frequency interacting with a nonlinear material are effectively “combined” to generate new photons with twice the energy, and therefore twice the frequency and half the wavelength of the initial photons. SHG, as an even-order nonlinear optical effect, is only allowed in mediums without inversion symmetry. SHG microscopy has been used for extensive studies. Stimulated Raman scattering (SRS) is another phenomenon based on multiphoton process. The investigation on multiphoton process in nanofabrication and microscopy imaging would open up new avenues for developing new laser techniques in nanophotonics, plasmonics, and biosciences.

1.2 Femtosecond Laser and Multiphoton Absorption

1.2.1 History of Femtosecond Laser

The field of ultrafast optics emerged from pioneering mode-locking studies of solid-state and organic dye lasers in the 1960s and early 1970s [1, 2]. Meanwhile, seminal contributions were also carried out accompanying the practical investigations. Organic dye solutions provided adequate gain bandwidths in colliding-pulse, which would facilitate the mode-locked dye lasers to generate sub-100 fs optical pulses [3, 4]. However, the poor practicality and low efficiency features of such lasers made them mainly suitable to laboratory applications. In spite of their limitations, many impressive research-based applications using femtosecond dye lasers in either oscillator or oscillator–amplifier configurations [5] have been carried out. In 1980s, a significant effort was devoted to femtosecond lasers that operated in the near-infrared spectral region using color-center crystals as the gain media [6]. At that time, some research emphasis was transferred to the study of nonlinear effects. The fast development of the high average power femtosecond amplified near-infrared lasers [7] has opened up new avenues in the field of non-equilibrium materials processing.

In general, the ultrafast pulse laser can be classified into solid-state laser, fiber laser, and semiconductor laser according to diversity of ultrafast pulse laser oscillator [3]. Figure 1.1 demonstrates the diversity of ultrashort-pulse laser oscillators, which shows the dependence of peak power on the average power. Indicative positions are given for the key source technologies, though it must be acknowledged that the performance from each type of source may vary outside these limits particularly when extra-cavity amplification/pulse compression is undertaken. Three application sectors with desirable source parameters are also placed in Fig. 1.1. It is interesting to note that oscillators continue to develop rapidly enabling broad coverage of the peak power/average power space to be achieved and initiating new application possibilities.

1.2.2 Multiphoton Absorption and Nonlinear Optics

The wavelength of femtosecond laser ranges from extreme ultraviolet to mid-infrared. The advantages of the femtosecond laser can be summarized as follows. Firstly, the high spatial, temporal electronic, and vibrational excitation densities created by the absorption of ultrashort light pulses. Secondly, since the pulse durations of these lasers are shorter than material’s relaxation time, the laser–material

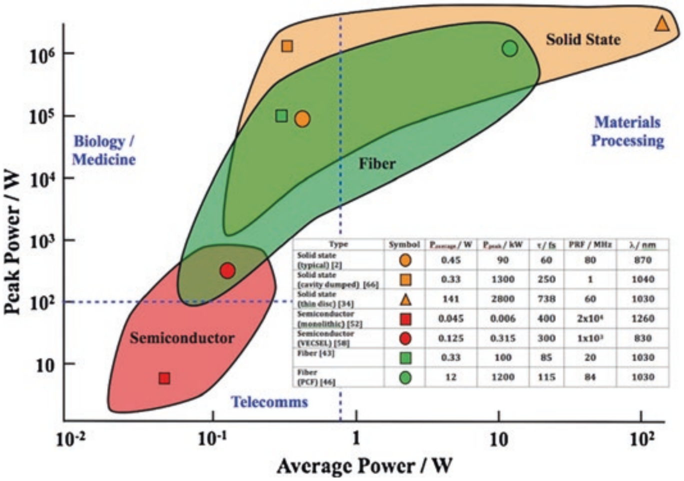

Type	Symbol	$P_{average}$ / W	P_{peak} / kW	τ / fs	PRF / MHz	λ / nm
Solid state (typical) [2]	🟠	0.45	90	60	80	870
Solid state (cavity dumped) [66]	🟧	0.33	1300	250	1	1040
Solid state (thin disc) [34]	△	141	2800	738	60	1030
Semiconductor (monolithic) [52]	🟥	0.045	0.006	400	$2\text{x}10^4$	1260
Semiconductor (VECSEL) [58]	🔴	0.125	0.315	300	$1\text{x}10^3$	830
Fiber [43]	🟩	0.33	100	85	20	1030
Fiber (PCF) [46]	🟢	12	1200	115	84	1030

Fig. 1.1 A plot of peak power versus average power for a range of ultrashort-pulse laser oscillator technologies. Also included are indicative application areas placed in appropriate regions of laser performance. The inset in the figure shows the performance of the sources indicated. Reproduced from [3] by permission of the Optical Society

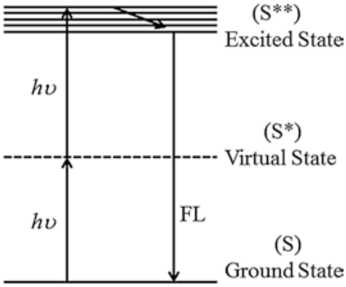

Fig. 1.2 Schematic illustration of MPA. *S* stands for the ground state, S^* stands for the virtual state, and S^{**} is the excited state. *h* and υ are Planck's constant and the frequency of the incident light, respectively. *FL* is the up-converted fluorescence emission

interaction, rather than material thermal properties, generally determines the outcome of the laser process. Thirdly, the high probability of the laser-induced nonlinear processes, such as MPA, opens new pathways to the new phenomenon, rather than the pathway through thermal equilibrium. The induced polarization at high intensity ceases to be a simple linear function of the electric field, and thus, the nonlinear effect will appear.

MPA is the simultaneous absorption of two or more photons of identical or different frequencies in order to excite a molecule from one state (usually the ground state) to a higher energy electronic state (Fig. 1.2). The energy difference between the involved lower and upper states of the molecule is equal to the sum of the energies of the multiple photons. Two-photon absorption (TPA), typical MPA, is a third-order process several orders of magnitude weaker than linear absorption. It is different from the linear absorption that the strength of absorption depends on the square of the light intensity, and thus leading to a nonlinear optical process. The phenomenon was originally predicted by Maria Goeppert-Mayer in 1931 in her doctoral dissertation [8]. In honor of her work, the molecular TPA cross section is usually quoted in the units of Goeppert-Mayer (GM), where 1 GM is equal to 10^{-50} cm^4 s photon^{-1} molecule^{-1}.

To meet the demand for high intensity, the experimental demonstration of TPA relied on the invention of the laser. In 1960s, the invention of the laser permitted the first experimental verification of the TPA when TPEF was detected in a europium-doped crystal and subsequently observed in a cesium vapor [3]. However, the broad utilization of TPA has not been carried out since its demonstration due to the lackness of laser with high power for achieving the nonlinear optical effect. This situation changed with the development of relatively simple, solid-state femtosecond lasers in the late 1980s and early 1990s.

TPA is a nonlinear optical process, in particular, the imaginary part of the third-order nonlinear susceptibility is related to the extent of TPA in a given molecule. The selection rules for TPA are therefore different from that for one-photon absorption, which is dependent on the first-order susceptibility. For example, in a centrosymmetric molecule, one- and two-photon-allowed transitions are mutually exclusive. In quantum mechanical terms, this difference results from the need to conserve angular momentum. The third order can be rationalized by considering that a second-order process creates a polarization with the doubled frequency. In the third order, the original frequency can be generated again by different frequency generation. The phase between the generated polarization and the original electric field leads to the Kerr effect or to the TPA. In SHG, the difference in frequency generation is a separated process, and thus, the energy of the fundamental frequency can be also absorbed. In harmonic generation, multiple photons interact simultaneously with a molecule without absorption events. Because n-photon harmonic generation is essentially a scattering process, the emitted wavelength is exactly $1/n$ times the incoming fundamental wavelength [5]. Compared to one-photon case, the absorption in TPA alone is a first-order process and any fluorescence from the final state of the second transition will be of second order, which means it will rise as the square of the incoming intensity. The virtual-state argument is quite orthogonal to the anharmonic oscillator argument. It states for example that in a semiconductor, absorption at high energies is impossible if two photons cannot bridge the band gap. Thus, many materials can be used for the Kerr effect that do not show any absorption and thus have a high damage threshold.

Generally, TPA can be measured by TPEF and nonlinear transmission (NLT) techniques. Pulsed lasers are of the most frequently used laser excitation source, this is because TPA is a third-order nonlinear optical process requiring very high intensities. The advantages of using ultrafast pulses to drive TPA are illustrated by the titanium–sapphire laser. A typical titanium–sapphire laser puts out pulses with duration of 100 fs or less at a repetition rate of approximately 80 MHz.

The time between pulses is therefore on the order of 12 ns. Thus, a sufficient peak intensity to drive efficient TPA can be realized at a low average laser power. While the output of a titanium–sapphire laser is in the range of hundreds of milliwatts, two-photon excitation can generally be accomplished at average powers of a few milliwatts or less, depending on the focusing conditions and the species being excited. Most titanium–sapphire lasers operate at a center wavelength of about 800 nm, although with appropriate optics they can operate in the range of 700–1,100 nm. Phenomenologically, TPA is regarded as the third term in a conventional anharmonic oscillator model for depicting vibrational behavior of molecules [9].

The nonlinear intensity dependence of the absorption process allows the excitation to be localized within the focal volume of a laser beam. To see how this process works, assume a sample in which the absorbing molecules are distributed homogeneously. The rate of absorption in a transverse cross section of a laser beam depends upon the product of the intensity (number of photons per time per area) and the number of molecules in the cross section (which is proportional to the area). Thus, the absorption rate does not depend upon area. The number of molecules excited by single-photon absorption is constant in any transverse plane of a focused laser beam, and so there is no localization of excitation in the focal region (Fig. 1.3, left). In the case of TPA, the rate of absorption in a transverse cross section of a laser beam is proportional to the intensity squared the number of molecules in the cross section. The absorption rate therefore scales inversely with area. The greatest density of excited molecules will therefore be in the region in which the laser beam is focused most tightly (Fig. 1.3, right). This localization was first utilized in 1990 by Denk, Strickler, and Webb in TPEF microscopy [10].

The "nonlinear" in the description of multiphoton process means that the strength of the interaction increases faster than that of linearly in the electric field of the light. In fact, the rate of TPA is proportional to the square of the field intensity under ideal conditions. This dependence is intuitively obvious when one

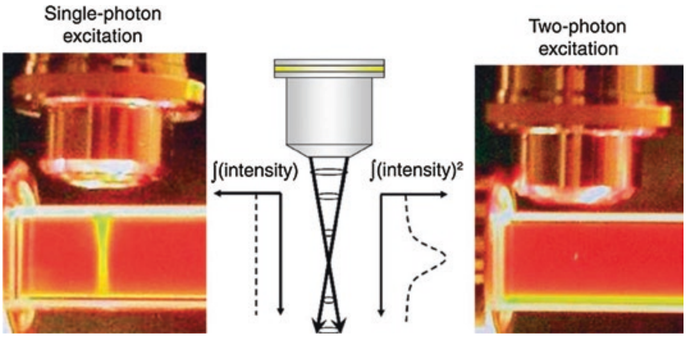

Fig. 1.3 Fluorescence in a rhodamine B solution excited by single-photon excitation from a UV lamp (*left*) and by TPA of a mode-locked titanium–sapphire laser tuned to 800 nm (*right*). In the former case, the integrated intensity is equal in all transverse planes, while in the latter case the integrated intensity squared is peaked in the focal region. Reprinted from [9], Copyright 2007, with permission from Elsevier

considers that it requires two photons to coincide in time and space, though it can be derived quantum mechanically. This requirement for high light intensity means that lasers are needed for studying the TPA phenomena. Furthermore, in order to understand the TPA spectrum, monochromatic light is also desired to measure the TPA cross section at different wavelengths. Hence, tunable pulsed lasers [such as frequency-doubled Nd:YAG-pumped optical parametric oscillators (OPOs) and optical parametric amplifier (OPAs)] are the choice of excitation.

1.3 Multiphoton Nanofabrication

1.3.1 Protocol of Multiphoton Nanofabrication

The laser multiphoton nanofabrication has become a popular application of femtosecond laser by employing the TPA property and nonlinear optical effect. Among multiphoton nanofabrication technique, MPP and multiphoton photoreduction (MPR) are two typical techniques based on multiphoton process [11–15]. In MPP technique, the femtosecond laser is tightly focused into the photoresist and scanned according to the preprogrammed pattern. Then, the photoresist is developed and the desired 3D micro/nanostructures after the photopolymerization can be fabricated [16, 17]. In MPR process, the femtosecond laser is focused into metal-ion aqueous solutions or metal/polymer nanocomposites. After the laser scanning, the metal ions will be photoreduced and the predesigned structures such as metal dots, metal lines, and metal coils are able to be achieved [14, 18, 19]. Figure 1.4 shows some 3D micro/nanostructures, such as microhorse, photonic

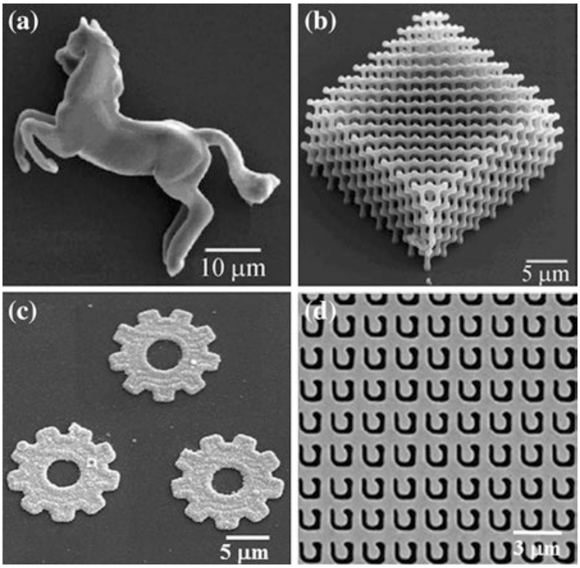

Fig. 1.4 Examples of micro/nanostructures created by MPP and MPR techniques, respectively. Reproduced from [14] by permission of the Optical Society

crystal, microgear, and split-ring resonators, created by MPP and MPR techniques. The photonic crystal, luminescent animals, pyramid, and any other arbitrary micro/nanostructures can be achieved by multiphoton fabrication.

1.3.2 Optics for Multiphoton Nanofabrication

The experimental optical setup of a typical micro/nanofabrication system is schematically shown in Fig. 1.5. Experimentally, multiphoton micro/nanofabrication is carried out through an optical setup with a mode-locked femtosecond laser, which produces pulses with a center wavelength of 780 nm, a pulse width of 80 fs, and a repetition rate of 80 MHz, respectively. A neutral density filter and a mechanical shutter are used for controlling the laser power and exposure time. The average output power can be tuned from several milliwatts to more than 1 W. The beam is generally expanded in order to overfill the back aperture of the objective lens. A microscope is usually adopted to hold, position, and view the sample. In the experimental setup shown here, the laser beam passes through the dichroic mirror of the inverted microscope and is tightly focused into the sample by a high numerical aperture (N. A.) objective lens. A computer is used to control the scanning operation of the high-precision nanopositioning piezostage according to the preprogrammed pattern. Transmitted light and reflected illuminated light are used to view the sample with a CCD camera and a video screen by tracing the positioning of the sample and making it possible to monitor the micro/nanofabrication in real time. The sample rests on a piezostage that can be moved in three dimensions relative to

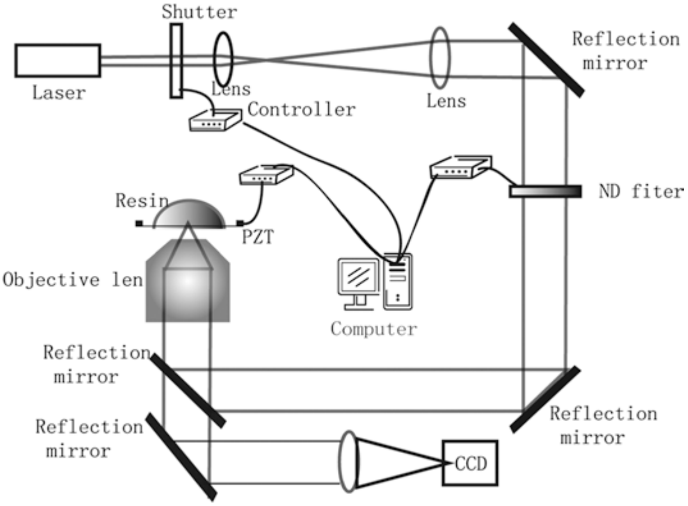

Fig. 1.5 Optical setup for multiphoton nanofabrication. *PZT* is high-precision nanopositioning piezostage, and *CCD* represents charge-coupled device camera

the focus of the laser beam. After the preprogrammed pattern is completely fabricated, the corresponding post-treatment will be employed. As an alternation, a pair of galvano-mirrors can be employed to move the focus spot relative to the sample.

1.3.3 Multiphoton Polymerization

The commercially available photopolymers such as urethane acrylates and epoxies were widely used in the multiphoton microfabrication. In order to achieve certain mechanical and chemical properties of the micro/nanostructures or devices, many kinds of materials such as photoresists, the hydrogel and biocompatible materials, inorganic-organic polymers, and hybrid polymers containing metal ions have been investigated in the micro/nanofabrication.

Generally, the MPP process includes the initiation, propagation, and termination reactions, which is briefly illustrated in Fig. 1.6 [9]. In the initiation step of the multiphoton micro/nanofabrication process, the photosensitizer (S) in the photopolymerizable resin is excited by absorbing two or more photons simultaneously and then emits fluorescence in the UV-Vis region. Consequently, the fluorescence will be absorbed by photoinitiators (I) with good chemical reactivity and give rise to radicals ($R^{\cdot}$). Then, the radicals react with monomers (M) or oligomers during the propagation, resulting in the production of the monomer radicals, which would expand in a chain reaction until two radicals meet. Finally, the low molecular weight monomers are polymerized into cross-linked, high molecular weight materials, leading to the termination of the MPP.

MPP is usually employed in the fabrication of the photoresists. Negative photoresist is the more widely used one, in which the portion of the photoresist that is exposed to light becomes insoluble to the photoresist developer. The unexposed portion of the photoresist is dissolved by the photoresist developer. In contrast, the positive resist behaviors in the opposite way, in which the portion of the photoresist that is exposed to light becomes soluble to the photoresist developer. The portion of the photoresist that is unexposed remains insoluble to the photoresist developer. Various micro/nanostructures can be created by using the MPP. During the multiphoton fabrication process, the femtosecond laser is tightly focused into the photoresist by a high N. A. objective lens. The photoresist will be polymerized to achieve the predesigned pattern by using a computer-controlled program. After

$$\text{Initiation: } \mathrm{S} \xrightarrow{h\nu,h\nu} \mathrm{S}^* \cdots \xrightarrow{\mathrm{I}} \mathrm{I}^* \rightarrow \mathrm{R}^{\cdot}$$

$$\text{Propagation: } \mathrm{R}^{\cdot} + \mathrm{M} \rightarrow \mathrm{RM}^{\cdot} \rightarrow \mathrm{RMM} \cdots \rightarrow \mathrm{RM}_{\mathrm{n}}^{\cdot}$$

$$\text{Termination: } \mathrm{RM}_{\mathrm{n}}^{\cdot} + \mathrm{RM}_{\mathrm{m}}^{\cdot} \rightarrow \mathrm{RM}_{\mathrm{n+m}}\mathrm{R}$$

Fig. 1.6 Schematic illustration of the MPP process. S stands for the photosensitizer, I denotes the photoinitiator, $R^{\cdot}$ is the radical, and M is the monomer. S^* and I^* are the excited states of the photosensitizer and photoinitiator after absorbing the photon energy, respectively fabrication, the sample will be developed with a certain organic solvent by removing the unpolymerized low molecular weight resist, and thus, the cross-linked, high molecular weight material will be remained.

There are several groups' research directions focused on the multiphoton fabrication techniques. Kawata et al. [20] in Osaka University fabricated the microbull in 2001, which has become the symbol of multiphoton nanofabrication. The commercially available resin (SCR500; JSR, Japan) was used in this study. It consists of urethane acrylate monomers, oligomers as well as photoinitiators, and is transparent to an infrared laser allowing it to penetrate deeply. The resin can be photopolymerized to create 3D structures based on TPA effect. In the multiphoton process, a titanium–sapphire laser operating in mode-lock at 76 MHz and 780 nm with a 150 fs pulse width was usually used as the exposure source. The laser was focused by an objective lens of high N. A. (~1.4). Figure 1.7 shows scanning electron micrographs of "microbull" sculptures. Bull sculptures produced by raster scanning

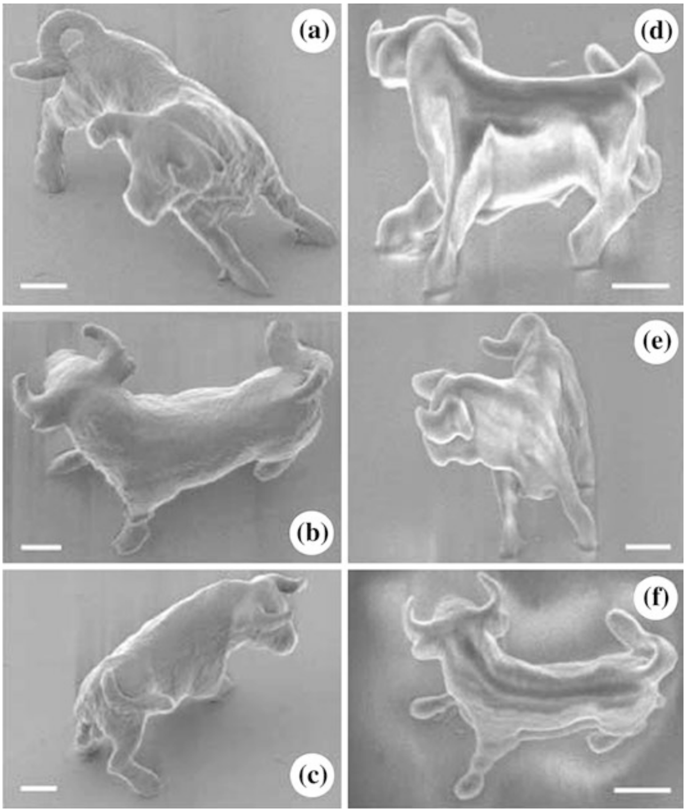

Fig. 1.7 **a**–**c** Bull sculpture produced by raster scanning, the process took 180 min. **d**–**f** The surface of the bull was defined by TPA (surface-profile scanning) and was then solidified internally by illumination under a mercury lamp. Reprinted by permission from Macmillan Publishers Ltd: [20], copyright 2001

are shown in Fig. 1.7a–c, the process took 180 min. In Fig. 1.7d–f, the surface of the bull was created by the surface-profile scanning and then solidified internally by illumination under a mercury lamp. Compared to the raster scanning, the surface-profile scanning reduces the TPA-scanning time to 13 min. These microbulls are about 10 μm long, 7 μm high, which are about the size of a red blood cell. The tiny volume of these micromachines enables them to be transported to locations inside the human body through the smallest blood vessels, for instance, to deliver clinical treatments.

Conventional photolithography has the limitation in creating 3D, complex microstructures [21]. Thus, it is difficult to fabricate the high-aspect-ratio microstructures with uniform cross sections and the microstructures with differing heights on the same substrate by using conventional photolithography. Microfluidic devices are generally created using conventional photolithography consisting of rectangular channels of uniform height with an aspect ratio of 3 or less. Even with more complex fabrication techniques, only a limited range of cross-sectional shapes can be created. It would be beneficial to have channels with different heights and cross sections in a single device. MPP is a microfabrication technique that overcomes many of the limitations of conventional photolithography. In MPP, photoexcitation is confined to the focal region of an incident laser beam. 3D structures are created by translating the laser focal point within a resist [22]. MPP provides true 3D fabrication capability and thus play a unique role in the fabrication of microfluidic master structures, particularly when conventional photolithography is unattractively complex or even infeasible.

SU8 is a commercial photoresist that is often employed to create microfluidic masters. It is a negative-tone resist consisting of epoxy oligomers and a low concentration of a photoacid generator (PAG). J. T. Fourkas et al. have developed the fabrication of microfluidic channels with arbitrary cross sections and high aspect ratios [23]. The authors demonstrate that by employing a novel PAG in an SU8 resist for MPP, high-aspect-ratio masters with uniform, rectangular cross sections can be produced. The masters with arbitrary, nonrectangular cross sections, combining channels with different aspect ratios and cross sections in a single device, are created. In addition, this resist enables real-time monitoring of MPP. The author performed high-speed fabrication over centimeter-scale, by employing writing speeds that are much faster than those typically used, enabling the fabrication of large-scale microfluidic masters on a practical timescale. The high-aspect-ratio FLUOR-SU8 walls demonstrate the viability of using FLUOR-SU8 microstructures as masters for microfluidic devices (Fig. 1.8). These walls have uniform cross sections and vertical side-wall profiles. Such master structures can assist diffusive mixing and allow for high packing densities in microfluidic devices. Channels of the molds that were 20 mm wide with aspect ratios ranging from 5 to 10 were undamaged by the bonding process (Fig. 1.8).

H.B. Sun's group has developed microelectromechanical systems (MEMS) by using MPP and enables its various functions [24]. Since the miniaturized smart machines with micro/nanometer-sized moving parts have now been utilized for on-site, in vivo sensing, monitoring, analysis and treatment in narrow

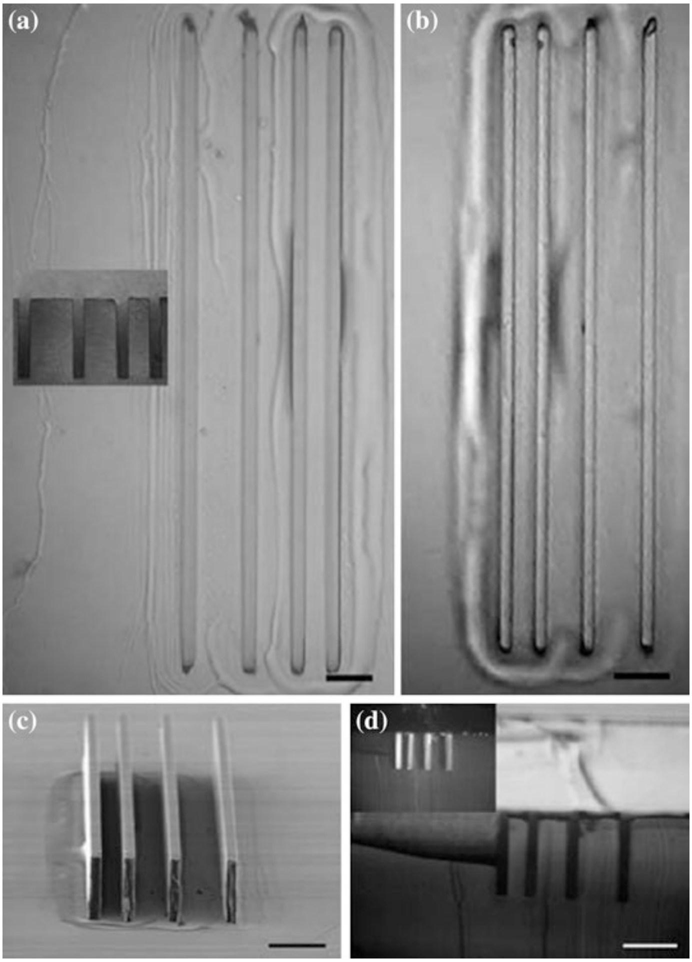

Fig. 1.8 **a** An optical image of a mold of high-aspect-ratio FLUOR-SU8 walls (1,000 × 160 × 20 µm). A slice from this mold is shown in the inset. The spaces between adjacent channels, from *left* to *right*, are 100, 75, and 50 µm. Optical (**b**) and SEM (**c**) images of the master for this mold. **d** An optical image of a slice from a mold bonded to glass shows that the bonding process does not deform the high-aspect-ratio channels. The inset displays a different optical image of the same structure. *Scale bars* are 100 µm. Reproduced from [23] by permission of the Royal Society of Chemistry

enclosure, harsh environment, and even inside human body, the investigation on smart machines has been paid much attention. MPP, as a designable 3D micro/nanoprocessing method, provides a novel route for fabricating micro/nanomechines with higher spatial resolution and smaller size. However, introduction of driven force to these tiny devices for precise micro/manipulation constitutes the main problem for the advanced applications of these micro/nanomachines, for example, remote control is indispensable for intelligent

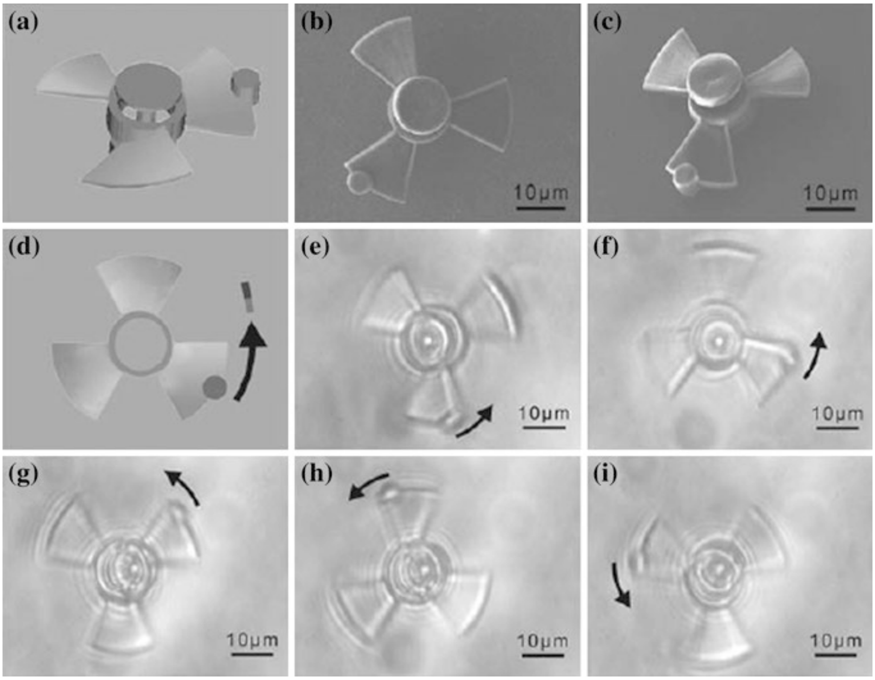

Fig. 1.9 Remote control of the microturbine in acetone. **a** Model of the microturbine, **b**, **c** SEM images of the microturbine, **d** *top view* scheme model for circumgyration, **e–i** optical microscopy images of the microturbine in a circumgyration cycle. Reproduced from [24] by permission of Wiley

micromachine that may be placed in blood vessels for health care. Therefore, it is of great importance to find novel fabricative and driven techniques for making functional micro/nanomachines with precise motion control.

To meet this demand, the authors have demonstrated the fabrication of remote-controllable micromachines by femtosecond laser-induced MPP of a stable, homogeneous, and transparent ferrofluids resin that composed of methacrylate groups modified Fe_3O_4 nanoparticles (NPs) and photoresists. Microspring and a microturbine have been successfully fabricated for remote control under additional magnetic force. A collar joint microturbine (Fig. 1.9) which is of the same size compared to the predesigned model (Fig. 1.9a) was successfully created. The microturbine obtained was about 35 μm in diameter with a central axletree and three blades. The development of remotely controllable MEMS would shorten the distance between actionless micro/nanostructures and smart micro/nanorobots.

It is found that femtosecond lasers are suitable for maskless photolithography with submicron resolution, which is attractive for saving the high photomask cost. Direct femtosecond laser writing of lithographic patterns is reported with submicron feature width on thin positive photoresist film. A lot of microstructures, such as 3D photonic crystals [25] and MEMS [16] have been fabricated with negative photoresists by the MPP. The functional negative photoresists, such as nanocomposite-doped and metal-ion-doped photoresist, have been used for fabricating various micro/nanodevices [11]. The spatial resolution of negative photoresist achieved by MPP has been improved to 50 nm on the surface of a glass substrate and 15 nm as suspended lines, respectively [26]. Compared with negative photoresists, positive photoresists are used more widely for fabricating integrated circuit (IC) and MEMS, owing to the nonshrinkage, developing process with less pollution solvent and easy to be stripped off after the pattern transfer. A few 3D microstructures have been obtained by MPP of positive photoresists [27]. However, the widths of trenches have been only achieved at sub-micrometer scale [28, 29].

Duan et al. in Technical Institute of Physics and Chemistry, Chinese Academy of Sciences, have fabricated a T-gate with a gate length of about 200 nm on the AlGaN/GaN substrate by combining MPP of positive photoresist with semiconductor devices processing techniques [30, 31]. A scanning electron microscope is used to investigate the feature sizes of femtosecond laser lithography, which are determined by the incident laser power, the number of scan times and the substrate materials. Submicron T-shaped gates have been fabricated using a two-step process of femtosecond laser lithography where the gate foot and head can be separately defined on positive AZ4620 photoresist film. The photoresist AZ P4620 (AZ Electronic Materials) is a commercial G-line positive photoresist and has been widely used in MEMS and semiconductor devices fabrication. It does not have linear absorption around the wavelength of 780 nm, which is the most frequently used wavelength of femtosecond laser in MPP. Figure 1.10a shows the dependence of the feature size on the incident laser power on 500-nm-thick AZ4620 photoresist which is used to define the gate head. The feature size is expanded much by either increasing the incident laser power or by separately scanning twice with a space of 100 nm. Figure 1.10b shows the best T-gate structure on the sample of AlGaN/GaN on Si substrate with 50-nm-thick Si_3N_4-assisted layer, in which the gate head has a length of 803 nm and the gate foot has a length of 271 nm. The best T-gate for the sample of GaN on sapphire substrate coated with 50-nm-thick Si_3N_4 is shown in Fig. 1.10c. The gate head fabricated on the 260-nm-long gate foot has a length of 923 nm. It should be noted in Fig. 1.10d that the best T-gate on the sample of GaN on sapphire substrate coated with 100-nm-thick SiO_2, in which a length of 1.42 μm, was fabricated on the 248-nm-long gate foot. This work has provided a protocol for the fabrication of sub-300-nm T-gates on the samples of GaN on sapphire substrate and AlGaN/GaN on Si substrate.

The smallest trench width has been achieved by using MPP of a commercial positive photoresist (AZ4620) thin film, and the mechanism of the cross-sectional shape formation and spatial resolution have been further studied theoretically and experimentally [26]. The trench with a width of 95 nm was fabricated by scanning once at 1.07 mW. Theoretical analysis based on the exposure kinetics was carried out and showed good agreement with the dependence of trench width on the incident laser power. The inverted trapezoidal cross-sectional shape of trench which impeded further improving spatial resolution was ascribed to the standing wave interference. Furthermore, a spatial resolution of 85 nm, about one-ninth of the

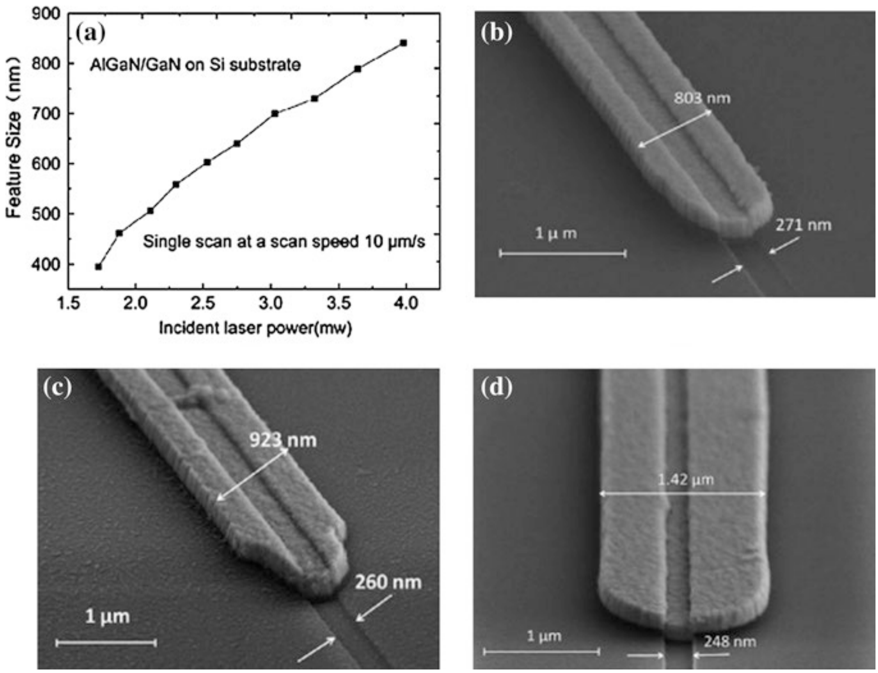

Fig. 1.10 **a** Feature sizes of T-gate head on 500-nm-thick AZ4620 versus incident laser power. **b** SEM image of T-shaped gate on AlGaN/GaN on Si substrate coated with 50-nm-thick Si_3N_4 on the *top*. **c** SEM image of T-shaped gate on GaN on sapphire substrate coated with 50-nm-thick Si_3N_4 on the *top*. **d** SEM image of T-shaped gate on GaN on sapphire substrate coated with 100-nm-thick SiO_2 on the top. Reproduced from [31] by permission of SPIE

laser wavelength at 780 nm, has been achieved by using multiscanning protocol at 0.330 mW (Fig. 1.11). The laser focus was lowered 100 nm in the z direction from the center of the 145-nm-thick photoresist thin film. The trench was scanned with a speed of 10 μm/s. The scanning process was continued 10 times while the laser focus elevated 20 nm after every scan. Combining with controlled laser power close to the threshold of photoresist, this multiscanning method could improve the resolution of MPP and realize nanoscale lithography with laser direct writing technique. This result exhibits the potential of MPP of positive photoresist thin film for fabricating IC structures and other micro/nanodevices.

1.3.4 Multiphoton Photoreduction

Metal nanostructures are one of the most important components in many micro/nanodevices, such as nanoelectronic integrated circuits, metamaterials, micro/nanofluidics and MEMS/NEMS. In the MPR process, the metal ions absorb

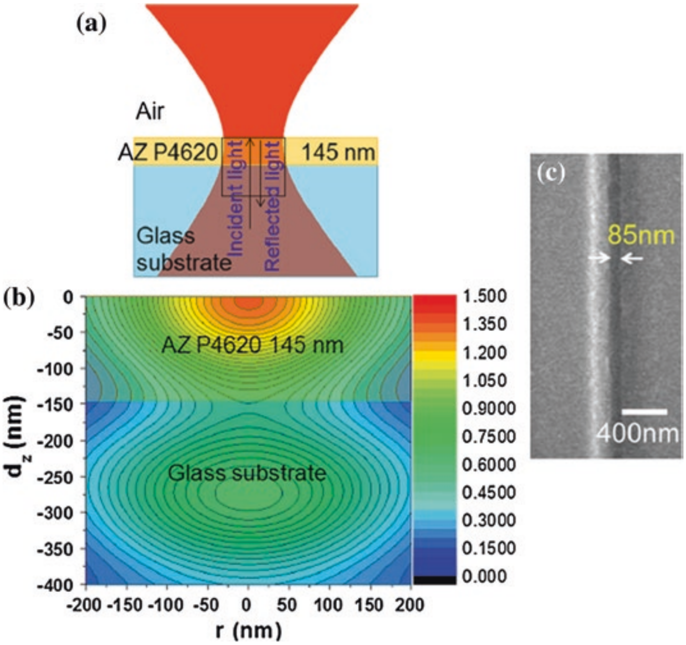

Fig. 1.11 **a** Schematic diagram of light distribution in glass substrate and AZ P4620 photoresist film. **b** Intensity distribution (in the *black square* frame of Fig. 1.11a under the condition of standing wave interference. d_z is the distance from the interface between air and photoresist film. **c** SEM of trench fabricated with incident laser power of 0.330 mW at 10 μm/s. It was scanned 10 times. The laser focus was lowered 100 nm from the center of the photoresist film before lithography. The height of the laser focus was elevated 20 nm after every scan. Reprinted with permission from [26]. Copyright 2013, American Institute of Physics

two or more photons simultaneously and being reduced into metal NPs. In the MPR of metal ions by a dye sensitizer, transfer of an electron from the excited dye to the metal ion leads to the formation of a silver atom which can either: (a) react with other silver atoms to nucleate, (b) add onto an existing particle, or (c) undergo charge recombination. Thus, the formation and growth of metal particles is limited by the competition between the rate of growth or nucleation and charge recombination, as well as local depletion of metal ions. Since growth rates are generally much greater than nucleation rates and depend on the number of nucleation centers, it is reasonable that introduction of NP seeds into the composite could significantly enhance the efficiency of formation of a continuous metal phase. S. R. Marder and J. W. Perry et al. have explored the incorporation of ligand-coated metal NPs into a photoactive material system to provide controllable nucleation centers [32].

To achieve ideal metallic microstructures, various novel routes have been developed. For example, 3D metallic microstructures were successfully created in the polymers matrix containing homogeneously doped metal ion [33]. Due to the effective support of polymer matrix, continuous microstructures could be retained after developing. Tanaka et al. achieved 3D metallic microstructure through MPR of the metal ions aqueous solution. In this process, ions in a metal-ion aqueous solution were directly reduced by a tightly focused femtosecond pulsed laser to fabricate arbitrary 3D structures. The self-standing 3D silver microstructures with arbitrary shapes were fabricated on a glass substrate [34, 35]. A freestanding silver-tilted rod, silver cup, and microsized 3D silver gate structure have been reported. The length of the rod and the angle relative to the substrate are 34.64 μm and 60°, respectively. The height and the top and bottom diameters of the cup are 26, 20, and 5 μm, respectively. The width, height, and linewidth of the microsized 3D silver gate structure are 12, 16, and 2 μm, respectively. Moreover, the conductivity of the silver gate was only 3.3 times lower than that of bulk silver, while the resolution was at micrometric scale.

X.-M. Duan et al. have reported the femtosecond direct laser writing of gold-nanostructures by amino-terminated ionic liquid-assisted MPR (IL-MPR) [14], which is developed for the direct writing of subwavelength gold nanostructures in $AuCl_4^-$ ions aqueous solution by femtosecond laser. It was revealed that the carbon chain length was crucial for morphology and size control of gold nanostructures.

A 228 nm width of gold nanostructure, which was beyond the optical diffraction limit, was fabricated by the matching between IL and the power and scanning speed of the laser beam. The measured conductivity is of the same order as that of bulk gold. Furthermore, a U-shaped terahertz planar metamaterial whose spectral response is consistent with the theoretical expectation has been successfully fabricated. As shown in Fig. 1.12a, the 2D arrays of U-shaped gold split-ring resonators (SRRs) have been fabricated at the laser power of 1.57 mW and scanning speed of 3 μm/s. The magnified images (top and bottom) showed the uniformity of the gold SRRs in different areas. The periodicity of a unit cell is 2 μm, the width is 633 nm, the height is 150 nm, and the arm length of the SRR is 1.9 μm. The optical transmission and reflection spectra for linear polarized incident light (Fig. 1.12b) were characterized by FTIR, which clearly shows an electric resonance around 63 THz for x-polarized wave, but no resonances are observed for y-polarization. Theoretically, we have further numerically calculated the transmission and reflection spectra using finite element method. There is a good qualitative agreement between numerical simulations and measurements (Fig. 1.12c). The electric field and current distributions at the resonant frequency shown in Fig. 1.12d indicate that the observed resonance is excited by the electric field and strong coupling effect occurs between two closed arms in the adjacent unit cell. The IL-MPR nanofabrication protocol is expected to play an important role in the fabrication of fine metallic micro/nanostructures for applications in MEMS, nanoelectronics, and nanophotonics.

In addition, X.-M. Duan et al. have proposed the mechanism of multiphoton photoreduction of metal ions with the assistance of surfactant [13, 15]. The photoreduction of the metal nanostructures can be divided into three stages: nucleation, growth, and aggregation of metal NPs. It was found that the surfactant plays an important role in the growth and aggregation processes. The surfactant

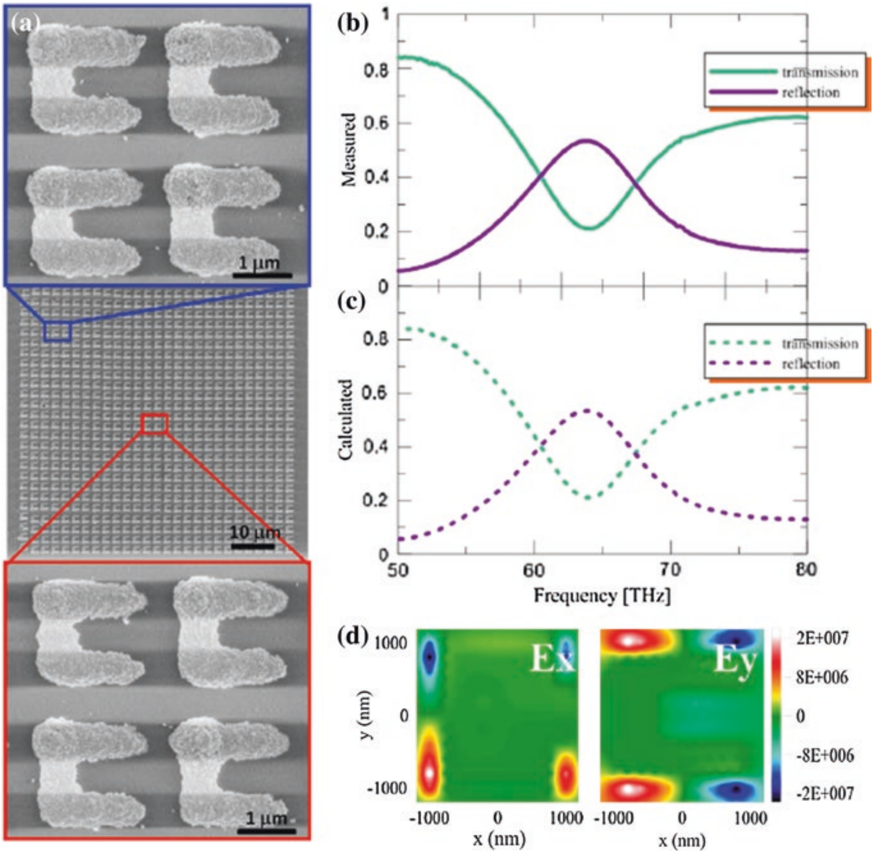

Fig. 1.12 **a** SEM images of the U-shape gold resonance rings on glass substrate, which was fabricated under the laser power of 1.57 mW and the scanning speed of 2 µm/s using the sample solution with C5, $L = 1.9$ µm, $H = 150$ nm, $W = 640$ nm, $P = 3$ µm. Magnified images in the edge (*top*, *blue*) and *center* (*bottom*, *red*) of the resonance rings. Measured (**b**) and numerical calculated (**c**) transmission and reflection spectra for the metamaterials with *x*-polarized illumination. **d** Simulated electric field and current density at the resonant frequency for *x*-polarized illumination. Reproduced from [14] by permission of the Optical Society

molecules made a significant contribution to the control of the diameters of NPs down to tens of nanometers and resulting in the silver stripe with narrow linewidth. In the absence of surfactant n-decanoylsarcosine sodium (NDSS) which has the alkyl carboxylate, a silver pattern with a lateral resolution of 1 µm consisting of large silver particles has been fabricated [34, 36]. The nucleation process was initiated by laser irradiation, and afterward the silver nuclei grew up to 1 µm. This ungoverned metal growth leads to large metal particles. The existence of the large particles leads to thick silver lines and prevents the spatial resolution reaching hundred-nanometer scale after the aggregation of the particles. On the other hand, the probability of the nucleation is assumed to be the same as that with NDSS. However, the NDSS molecules cover the surface of the silver particles immediately after the nucleation process and its covered layer eliminates the further metal growth and decreases the particle size down to around 20 nm. In this case, the degree of particle growth suppression increases with the increasing of the surfactant concentration. These growth-suppressed particles aggregate to form silver patterns. In this stage, the concentration of particles is higher at the center of the focused laser spot, since there is a higher nucleation probability associated with the higher laser power. Meanwhile, the higher laser power also helps to break the surfactant layer surrounding the particles [37], which in turn enhances the particle aggregation. These two possibilities lead to the aggregation of silver particles directed to the center of the laser beam.

Figure 1.13a shows a free-standing silver pillar on the cover slip, which was obtained by scanning the focused laser spot along the direction normal to the plane of the cover slip. The silver pillar was created with a laser power of 1.14 mW and scanning speed of 3 μm s^{-1}. SEM images reveal that this pillar has a minimum linewidth of 180 nm. Scanning the focused spot under the control of a computer enabled creation of 3D structures of arbitrary geometry. Figure 1.13b demonstrates the truly free-standing 3D silver pyramids fabricated with a scanning speed of 2.5 μm s^{-1} and laser power of 1.3 mW. These silver pyramid structures were strong enough to resist the surface tension in the washing process, which demonstrated that the silver particles were closely combined. The detail of the silver pyramid shown in Fig. 1.13b reveals that the height is 5 μm and the angle for each edge relative to the substrate is 60°. Consequently, the direct photoreduction of the metal ions with surfactants could also lead to 3D metal structures with resolution exceeding the diffraction limit of light.

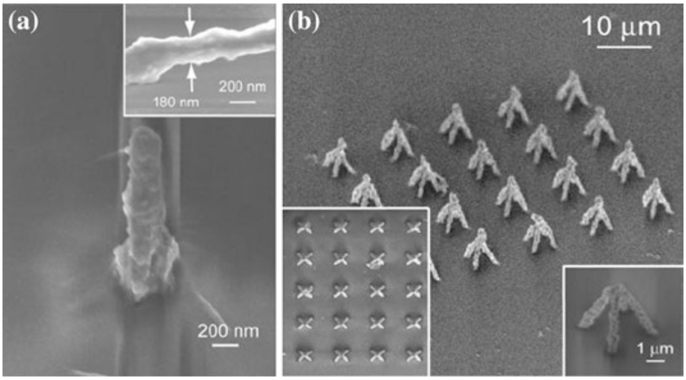

Fig. 1.13 **a** SEM image of the free-standing silver pillar on the cover slip, made by using a laser power of 1.14 mW and a linear scanning speed of 3 μm s^{-1}, taken at an observation angle of 45°. The inset is a close-up view of the silver pillar parallel to the substrate, which demonstrates the linewidth of the smallest portion of the silver pillar as 180 nm. **b** SEM image of silver pyramids, fabricated with a laser power of 1.3 mW and scanning speed of 2.5 μm s^{-1}, taken at an observation angle of 45°. The inset on the *left* is a *top view* of the silver pyramid array. The inset on the *right* is a close-up view of the silver pyramid. Reproduced from [15] by permission of Wiley

1.3.5 Applications of Multiphoton Nanofabrication in Nanophotonics

Based on the development of multiphoton nanofabrication, the further application in nanophotonics and biophotonics has been employed. As reported, X.-M. Duan et al. have presented the fabrication of color tunable 3D microstructures by using multiphoton fabrication technique in conjunction with the in situ synthesis of photoluminescent semiconductor NPs in 3D microstructured polymer matrices [11]. In this study, cadmium methacrylates ($Cd(MA)_2$) was used as precursors for CdS NPs, as well as monomers for photopolymerization. A commercially available oligomer, dipentaerythritol hexaacrylate (DEP-6A), has been selected as the cross-linker. Methacrylic acid (MA) and MMA (Beijing Chemicals) have been used as monomers with 1 wt% of benzyl (Aldrich) as the photoinitiator and 1 wt% 2-benyl-2-(dimethylamino)-4′-morpholinobutyrophenone (Aldrich) as the photosensitizer. First, 3D microstructures of polymers containing CdS precursors have been fabricated by the multiphoton fabrication technique. Subsequently, the in situ synthesis of CdS NPs has been performed in the fabricated 3D polymeric microstructures.

For the fabrication of 3D microstructures, a mode-locked titanium–sapphire laser was used, whose center wavelength, pulse width, and repetition rate were 780 nm, 80 fs, and 82 MHz, respectively. The lasing source was tightly focused by a 100 oil-immersion objective lens with a high N. A. (1.4, Olympus). The focal spot was focused onto the liquid photopolymerizable sample, which was placed on a xyz-step piezostage controlled by a computer. After laser fabrication, the unpolymerized resins were washed away using ethanol. The obtained microstructures were used for characterization or further treatment. The emission wavelength of the micro/nanostructures can be tuned by changing the size of CdS NPs (Fig. 1.14). A fluorescent 3D microbull and a 3D microlizard have been successfully fabricated from resins containing different components.

Furthermore, multiphoton nanofabrication can be also applied in tissue engineering. Tissue engineering applies the principles of engineering and life sciences toward the development of biological substitutes that restore, maintain, or improve tissue function. The scaffold for cell cultivation can greatly influence the attachment, migration, and proliferation of cells. Scaffold materials that are not rejected by the human body upon implantation can be selected from metals, ceramics, synthetic polymers, and biopolymers. Among them, biomaterials that are bioresorbable and biodegradable on a similar time scale as tissue formation are preferred. MPP was explored for constructing permanent scaffolds. M. Farsari et al. reported the 3D biodegradable structures that fabricated by MPP [38]. The 3D structures were fabricated using the biodegradable triblock copolymer poly(ε-caprolactone-*co*-trimethylenecarbonate)-*b*-poly(ethylene glycol)-*b*-poly(ε-caprolactone-*co*-trimethylenecarbonate) with 4,4′-bis(diethylamino) benzophenone as the photoinitiator. This triblock copolymer is not only biocompatible and biodegradable, but also degrades on a similar time scale as tissue formation.

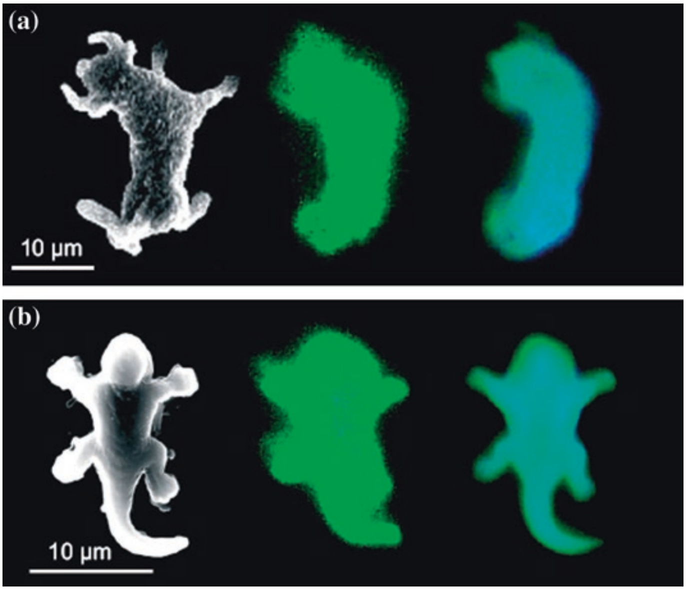

Fig. 1.14 Images of SEM (*left*) and fluorescence microscopy of a 3D microbull (**a**) and a 3D microlizard (**b**) fabricated from resins contained different components. Reproduced from [11] by permission of Wiley

A 2D scaffold structure with a length and width of 400 μm was fabricated by MPP. The fabricated structures were of good quality and had four micron resolution. Initial cytotoxicity tests show that the material does not affect cell proliferation. In Fig. 1.15, a cell-permeable green fluorescent dye is utilized to stain live cells. Dead cells can be easily stained by a cell nonpermeable red fluorescent dye (propidium iodide, PI). Stained live and dead cells were visualized by fluorescence microscopy using a band-pass filter. After 2–7 days of cultivation, a confluent monolayer (10 × magnifications) of well-defined 3T3 mouse fibroblast cells was observed exhibiting cell-to-cell contact (Fig. 1.15). This figure strongly indicates that fibroblast cells can attach and divide on the surface of the polymer as effectively as on the glass coverslips. These preliminary experiments show that the copolymer does not affect cell proliferation. These studies demonstrate the potential of MPP as a technology for the fabrication of biodegradable scaffolds for tissue engineering.

1.4 Multiphoton Microscopy Imaging

Multiphoton microscopy, or commonly called two-photon microscopy, is a fluorescent technique that is used to image deep into tissues. Besides, the second/third-harmonic-generation microscopy and SRS microscopy are also the multiphoton

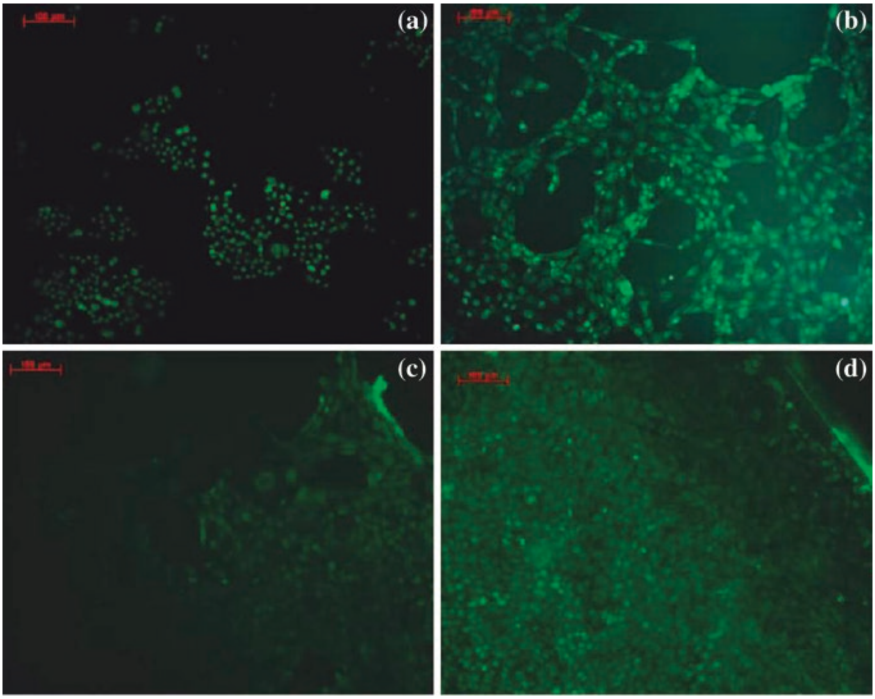

Fig. 1.15 Cells spreading on glass surface after 2 days (**a**) and 7 days (**c**), and on polymer films after 2 days (**b**) and 7 days (**d**). Reprinted with the permission from [38]. Copyright 2009 American Chemical Society

microscopy techniques based on the multiphoton process. A two-photon excitation results in the subsequent emission of a fluorescence photon, typically at a higher energy than either of the two excitation photons. The probability of the near-simultaneous absorption of two photons is extremely low. Therefore, a high flux of excitation photons from a femtosecond laser is typically required. The purpose of employing the two-photon effect is that the axial spread of the point-spread function (PSF) is substantially lower than that for single-photon excitation. As a result, the resolution along z dimension is improved, allowing for the observation of thin optical sections. Moreover, two-photon microscopes are less damaging to the sample than a single-photon confocal microscope. The shape of the spot and its size can be designed to realize specific desired goals in many interesting cases [39].

1.4.1 Two-Photon-Excited Fluorescence Microscopy

A very well-known and trailblazing use of ultrafast lasers is related to two-photon microscopy [10]. TPEF microscopy, which is also referred to as nonlinear, multiphoton, or two-photon laser scanning microscopy, is an alternative to confocal microscopy that provides distinct advantages for 3D imaging. In particular, TPEF microscopy allows the imaging of living tissue up to a very high depth, that is up to about 1 mm. Two-photon excitation benefits for imaging of living cells, especially within intact tissues such as embryos, brain slices, whole organs, and even entire animals. The effective sensitivity of fluorescence microscopy, especially with thick specimens, is generally limited by out-of-focus flare. This limitation is greatly reduced in the confocal microscopy technique by employing a confocal pinhole to reject out-of-focus background fluorescence and produce thin (less than 1 micrometer), unblurred optical sections.

Being a special variant of the multiphoton fluorescence microscope, TPEF microscopy employs TPA effect, a concept first described by Maria Goeppert-Mayer (1906–1972) in her doctoral dissertation in 1931 [8] and first observed in 1961 in a $CaF_2:Eu^{2+}$ crystal using laser excitation by Kaiser and Garrett [40]. For each excitation, two photons of the infrared light are absorbed by the fluorescent dyes. Using infrared light can minimize scattering in the tissue, and the background signal can be strongly suppressed due to MPA, leading to an increased penetration depth. TPEF microscopy can be a superior alternative to confocal microscopy due to its deeper tissue penetration, reduced phototoxicity and efficient light detection [10]. Longer wavelengths are scattered less than shorter ones, which is a benefit to high-resolution imaging in light-scattering tissue [41]. In addition, these lower-energy photons are less likely to cause damage outside the focal volume. Compared to a confocal microscope, photon detection is much more effective since even scattered photons contribute to the usable signal. These benefits for imaging in scattering tissues were only recognized several years after the invention of TPEF microscopy. The femtosecond pulse lasers are needed for TPEF microscopy rather than the continuous wave (CW) lasers used in confocal microscopy.

The TPA spectrum of a molecule may vary significantly from its one-photon counterpart. For very thin objects such as isolated cells, single-photon (confocal) microscopy can produce images with higher optical resolution due to their shorter excitation wavelengths. In scattering tissue, the superior optical sectioning and light detection capabilities of the TPEF microscopy result in better performance. TPEF microscopy was pioneered by Winfried Denk and Watt W. Webb at Cornell University in 1990 [10]. He combined the idea of TPA with the use of a laser scanner. A typical nonlinear microscopy based on TPA is shown in Fig. 1.16 [42]. In TPEF microscopy, an infrared laser beam is focused through an objective lens. The normally used titanium–sapphire laser has a pulse width of approximately 100 fs and a repetition rate of about 80 MHz, allowing the high photon density and flux required for TPA and is tunable across a wide range of wavelengths. The microscope consisting of galvanometer-mounted mirrors was used for beam scanning, realizing the x–y plane scan. Polarizers (P) P1 and P2 were used to tune the polarization direction of excitation laser source. P3 was used to change the polarization direction of detection. A high N. A. objective lens was used to excite the sample and another high N. A. objective lens will be used to collect the signal. Subsequently, the TPEF fluorescence and/or the SHG signal were then collected by a high-sensitivity detector, such as a photomultiplier tube in the forward

Fig. 1.16 A typical nonlinear microscopy based on TPA. Reprinted with the permission from [42]. Copyright 2011 American Chemical Society

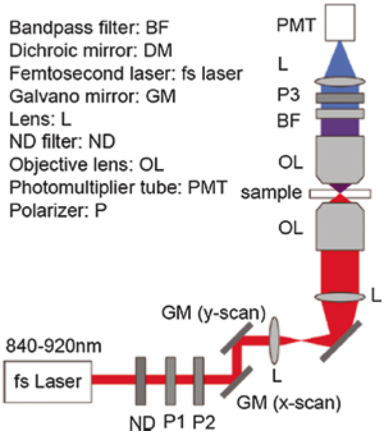

direction. A band-pass filter was used to remove the excitation laser light. The observed light intensity becomes one pixel in the eventual image, and the focal point is scanned throughout a desired region of the sample to form all the pixels of the image. The high penetration depth and high contrast have been achieved in multiphoton microscopy [43, 44]. Figure 1.17 shows the 3D functional imaging in brain slices, which demonstrates the good contrast and high penetration depth [44].

A potentially important development is the design of fluorescent chromophores with significantly improved TPA cross sections [45]. The most commonly used TPEF fluorophores exhibit excitation spectra in the 400–500 nm range, whereas the laser used to excite the TPEF lies in the wavelength range of 700–1,000 nm (near infrared). If the fluorophore absorbs two infrared photons simultaneously, it will absorb enough energy to be raised into the excited state. The fluorophore will then emit an up-converted emission typically in the visible spectrum. The probability for fluorescent emission from the fluorophores increases quadratically with the excitation intensity since two photons are absorbed during the excitation of the fluorophore. Therefore, much more TPEF fluorescence is generated where the laser beam is tightly focused compared to that of diffuse case. In Fig. 1.18, the TPEF fluorescence was collected at 532–554 nm upon excitation at 870 nm. The excitation is effectively restricted to the tiny focal volume, resulting in a high degree of rejection of out-of-focus objects. This localization of excitation is the key advantage compared to single-photon excitation microscopes, in which the additional elements such as pinholes are required to reject the out-of-focus fluorescence.

1.4.2 Second/Third-Harmonic-Generation Microscopy

The effect of second/third-harmonic generation has been promising for high-resolution optical microscopy in biological and medical sciences. Only noncentrosymmetric structures are capable of emitting SHG light because of the nonzero

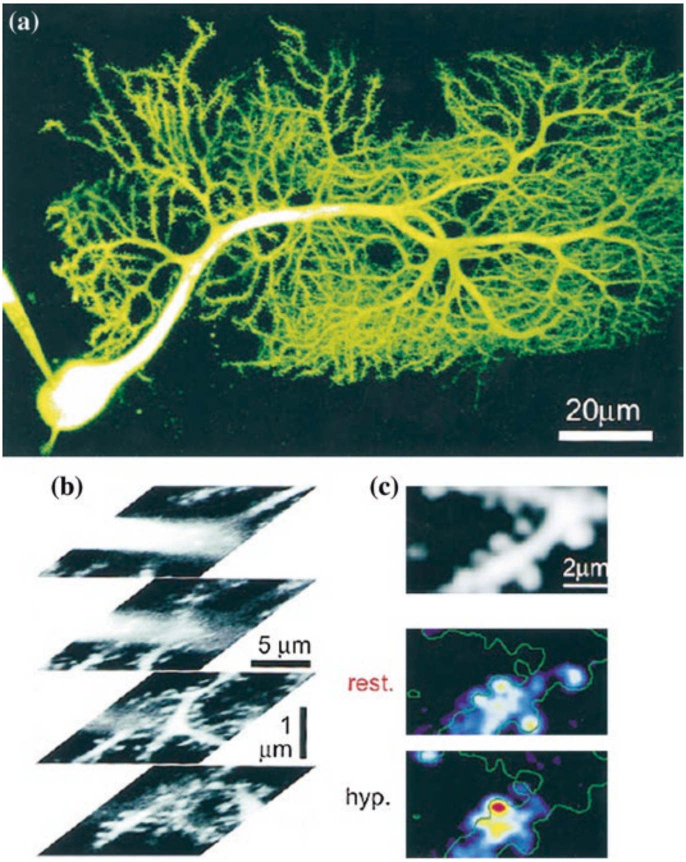

Fig. 1.17 3D functional imaging in brain slices. **a** TPEF image of a stack of optical sections through a living Purkinje cell filled with fluorescein dextran (400 mm). **b** At higher resolution, a sequence of sections taken at 1.8-mm focus intervals (objective lens: 633, 0.9 N. A., water immersion, Zeiss) of a piece of dendrite belonging to the same cell. **c** The anatomy of a spiny branchlet and its response to focal stimulation of parallel fibers while the cell is held at its resting potential (rest.) and at strongly hyperpolarized levels. Reprinted from [44], Copyright 1997, with permission from Elsevier

second-harmonic coefficient. SHG polarization anisotropy can be used to determine the orientation and degree of organization of proteins in tissues since SHG signals have well-defined polarizations. The first demonstration of SHG was performed in 1961 by Franken et al. [46] by using a quartz sample. Typically, an inorganic crystal is used to produce SHG signal such as lithium niobate ($LiNbO_3$), potassium titanyl phosphate ($KTP = KTiOPO_4$), and lithium triborate ($LBO = LiB_3O_5$). Some biological materials can be highly polarizable, and assemble into fairly ordered, large noncentrosymmetric structures though SHG requires a material to have specific molecular orientation in order for the incident light to be frequency-doubled. Biological materials such as collagen, microtubules, and muscle myosin

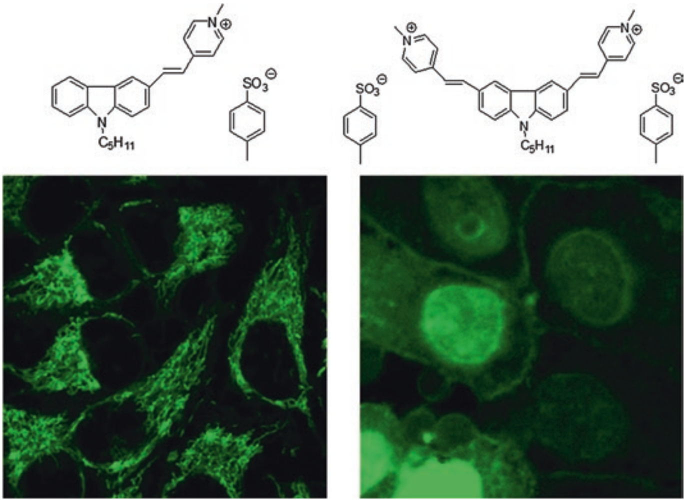

Fig. 1.18 TPEF probes and the corresponding TPEF image. The fluorescence was collected at 532–554 nm upon excitation at 870 nm with a femtosecond laser pulse. The excitation intensity at the focus was 4.5 mW

can produce SHG signals. The SHG pattern is mainly determined by the phase matching condition. The excitation light can be easily separated from the emitted, frequency-doubled SHG signal by using a short-pulse laser such as a femtosecond laser and a set of appropriate filters. This allows for very high axial and lateral resolution without using pinholes compared to that of confocal micros copy.

Second/third-harmonic imaging microscopy is based on a nonlinear optical effect known as SHG/THG. SHG signal emerging from an SHG material is exactly half of the excitation wavelength (frequency-doubled). TPEF is also a two-photon process. TPEF loses some energy during the relaxation of the excited state, and SHG is energy conserving. A typical setup for an SHG imaging system will have a laser scanning microscope with a titanium–sapphire mode-locked laser as the excitation source (Fig. 1.16). Second/third-harmonic imaging microscopy has been established as a viable microscope imaging contrast mechanism for the visualization of cell and tissue structure and function. Second/third-harmonic imaging microscopy offers several advantages for live cell and tissue imaging. SHG does not involve the excitation of molecules like other techniques such as fluorescence microscopy; therefore, the molecules should not suffer the effects of phototoxicity or photobleaching. Since 2010, SHG has been extended to styryl dyes and whole-animal in vivo imaging [42, 47, 48]. Figure 1.19 shows the SHG image of a single styryl dye (DAST) crystal and the corresponding polarization dependence. By using near-infrared wavelengths for the incident light, second/third-harmonic imaging microscopy has the ability to construct 3D images of specimens by imaging deeper into thick tissues [49]. Also, since many biological structures produce strong SHG signals, the labeling of molecules with exogenous probes is not

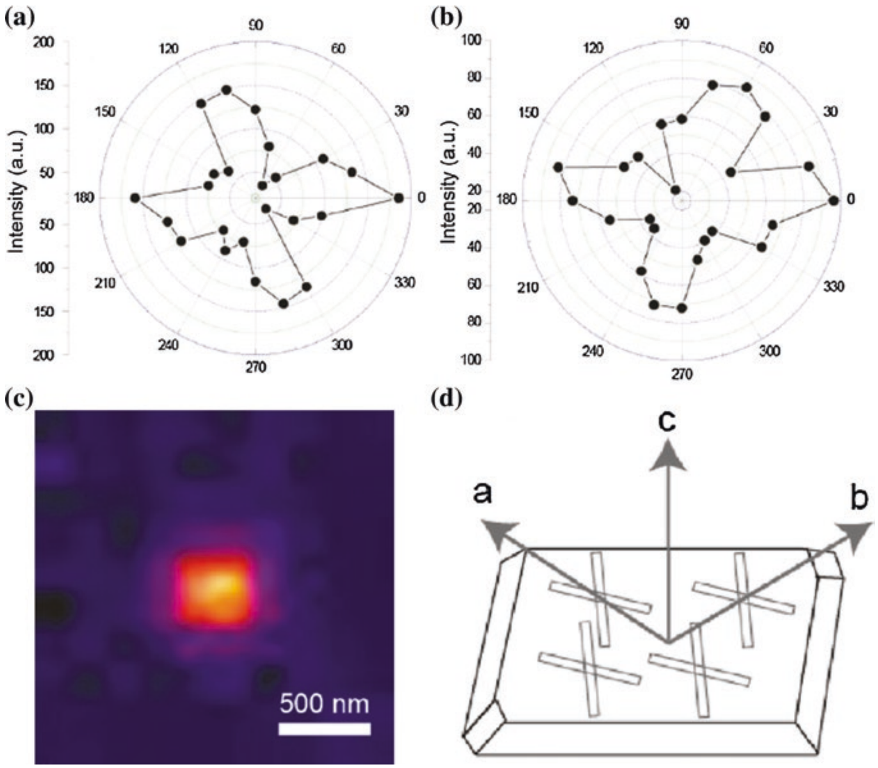

Fig. 1.19 **a**, **b** Polar graphs of DAST ONCs. The excitation wavelength is 870 nm. **c** Scanning image of SHG emitted from a single DAST ONC, which was bigger than that showed in SEM image due to the diffraction limit of light. **d** Schematic illustration of DAST crystal habit showing the orientation of crystal axes relative to habit geometry. Reprinted with the permission from [42]. Copyright 2011 American Chemical Society

required which can also alter the way a biological system functions. SHG microscopy has been used for the extensive studies of cornea [50] and lamina cribrosa [51], both of which consist of collagen primarily. Collagen is the most commonly studied SHG materials, which is found in most load-bearing tissues.

A SHG microscope obtains contrasts from variations in a specimen's ability to generate second-harmonic signal from the incident light, while a conventional optical microscope obtains its contrast by detecting variations in optical density, path length, or refractive index of the specimen. SHG requires intense laser light passing through a material with a noncentrosymmetric molecular structure. The SHG signal is propagated in the forward direction. However, some experiments have shown that objects on the order of about a tenth of the wavelength of the SHG produced nearly equal forward and backward signals [50, 52]. The striking fact demonstrated in Fig. 1.20 is that the intensity of the backward SHG from sclera is even comparable to the forward SHG.

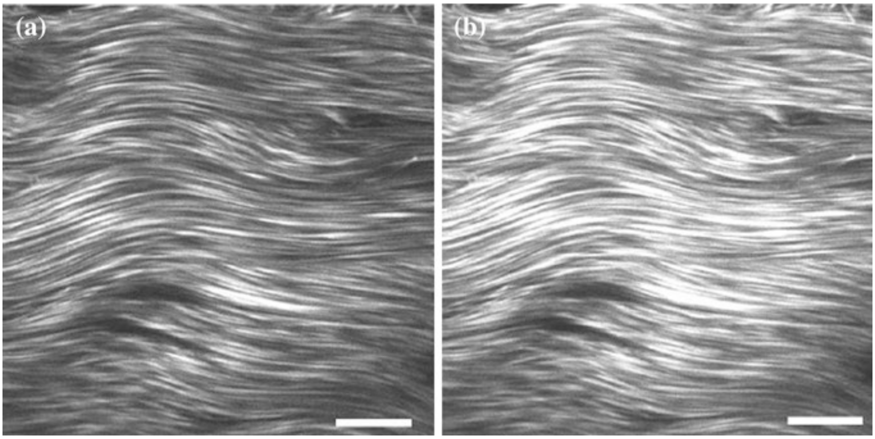

Fig. 1.20 SHG imaging of scleral collagen fibrils in **a** forward and **b** backward directions. In contrast to cornea, the backward SHG signals from sclera are significant. Identical structures are revealed by forward and backward SHG imaging. Reproduced from [50] by permission of the Optical Society

1.4.3 Stimulated Raman Scattering Microscopy

The ability to track specific biological molecules following their spatial distribution and temporal dynamics in vivo is essential for understanding their physiological impacts and regulatory mechanisms. Up to date, fluorescence microscopy is currently the most popular imaging contrast used in biological studies. Various fluorescence-based techniques such as confocal laser scanning, TPEF, single-molecule microscopy and super-resolution imaging have emerged [10, 53]. However, owing to the physical size and chemical invasiveness of fluorescent tags, fluorescence microscopy is not well suited for visualizing small molecules and some important molecules which play essential roles in the biochemistry of living cells in vivo, such as lipids, carbohydrates, metabolites, and drugs. In order to have a better understand of the biology behavior of the cell function, new imaging methods are highly desirable to directly and specifically visualize those molecules and analyze their regulation.

Due to characteristic frequencies of various chemical bonds, the vibrational microscopy based on Raman scattering, which is fundamentally different from fluorescence microscopy, is considered as a suitable lable-free biomedical imaging technology for visualizing protein, DNA, lipids, and small metabolites in vivo [54–56]. Spontaneous Raman scattering microscopy adopts a single frequency laser with short wavelength at a frequency ω_p as an excitation source, and the signal is generated at the Stokes and anti-Stokes frequencies, ω_s and ω_{as}, respectively, due to inelastic scattering. However, Spontaneous Raman scattering is insensitive and exciting laser energy is always kept at low power to protect the sample and avoid the thermal effect, which has limited the imaging speed [57]. Coherent anti-Stokes Raman scattering (CARS) microscopy as a coherent nonlinear optical microscopy technique has provided a way to visualize unstained biological samples with high imaging speed [58]. Unfortunately, owing to significant nonresonant background and auto-fluorescence, a CARS spectrum is different from its corresponding spontaneous Raman spectrum, which complicates spectral assignment, causes difficulties in image interpretation, and is not suited for straight forward quantification. SRS is another nonlinear Raman phenomenon. The SRS microscopy has a significantly greater sensitivity than Spontaneous Raman microscopy and is able to overcome the limitations of CARS microscopy. Therefore, SRS microscopy has attracted lots of interesting and has emerged as a new label-free imaging technique for biomedical researches (Fig. 1.21).

No matter CARS or SRS, both of them are based on Raman scattering, so what is Raman scattering? When light, (for example, a laser beam) illuminates a sample and interacts with individual molecules, most photons will elastically scatter (Rayleigh scatter), maintaining the energy of the incident light. However, a much smaller fraction of photons undergoes inelastic scattering by interacting with the vibrational state of molecules. Different vibrational states are dictated by the composition of the molecules and the chemical bonds that are present. When the scattering photons have less energy than the incoming photons while the chemical bonds get excited to a higher energy vibrational level, they are normally called Stokes Raman photons. On the contrary, by interacting with the chemical bonds in an excited vibrational state, the scattering photons will have higher energy than the incident ones, which are called as anti-Stokes Raman photons. The frequency difference, as known as Raman shifts, between the incoming and scattering light is only determined by the vibrational energy levels of the chemical bonds. A complex molecule will generate a complicated Raman spectrum consisting of the combined Raman shift peaks from all the consisting chemical bonds. Therefore, the Raman spectra can provide a characteristic fingerprint of specific molecules in the sample, which allows their identification without labeling. However, as mentioned above, the signal from Spontaneous Raman scattering is weak. It will take a long time to achieve a clear Raman spectrum, which is not suitable for the imaging of biomedical samples.

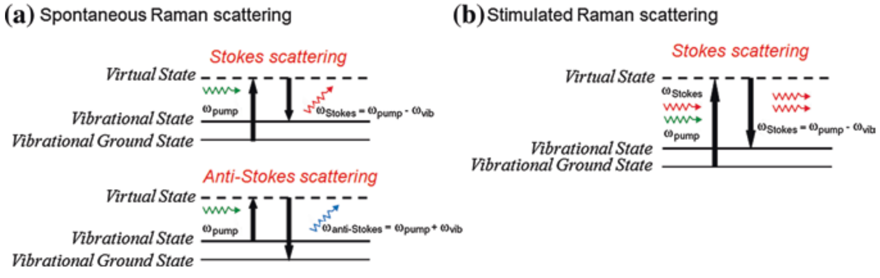

Fig. 1.21 Principle of **a** spontaneous Raman scattering and **b** stimulated Raman scattering

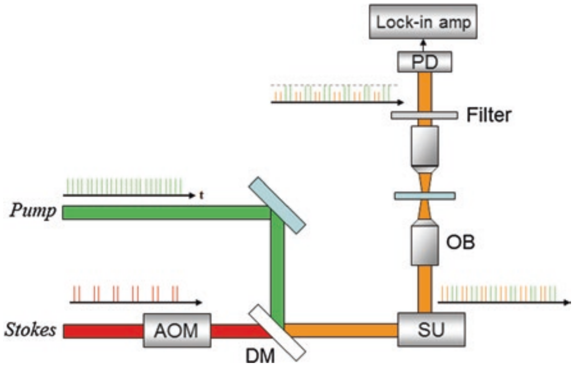

Fig. 1.22 Diagram of SRS microscopy. The pump laser beam is modulated at a high frequency (~10 MHz). The filter is used to block the Stoke beam completely. The transmitted pump beam containing SRL signals is detected by a photodiode (*PD*). An electronic device, lock-in amplifier, is used to demodulate the SRL signals carried on the pump beam

Similar to CARS, SRS relies on two laser beams at ω_p and ω_s coincided on the sample. When their energy difference, $\Delta\omega = \omega_p - \omega_s$, also known as the Raman shift, matches a particular molecular vibrational frequency, the molecular vibrational excitation is stimulated after nonlinear interaction. This is accompanied by the energy transfer from the pump beam to the Stokes beam and results in the intensity loss of the pump beam called stimulated Raman loss (SRL) and the intensity gain of the Stokes beam called stimulated Raman gain (SRG). In contrast, when $\Delta\omega$ does not match with the target molecule vibrational frequency or any vibrational resonance, there is no energy transfer between the pump and Stokes beams, and no SRG or SRL signals. Thus, SRS microscopy is free from the nonresonant background. The schematic illustration of SRS microscopy is shown in Fig. 1.22.

In an SRS microscope, the intensity of the incoming Stokes laser beam is temporarily modulated at a high frequency, whereas the incident pump beam (before interacting with the sample) remains unmodulated. After interacting with the samples, the pump beam intensity change is detected and amplified via a lock-in amplifier. The extracted signals will be utilized for image construction. Owing to the nonlinear dependence, SRS has inherent 3D sectioning capability. The SRL signal intensity is linearly associated with the concentration of the targeted molecules in the sample, which is crucial for quantification. SRS microscopy was first demonstrated in biological imaging in 2008 [54], which was followed immediately by works from two other groups in 2009 [59, 60]. This new label-free microscopy technique allows imaging biological molecules in living cells with high resolution, sensitivity, and speed. It has been broadly applied to lipid measurement, drug delivery monitoring, and tumor cell detection [54, 61–63].

The advanced SRS microscope would allow for fingerprint Raman band mapping of metabolites such as cholesterol ester, glycogen, lactate, and essential amino acids such as L-glutamine. Such SRS imaging of single cells could potentially unveil the unknown metabolic pathways and identify new genes that regulate cell metabolism. It should be mentioned, the expensive instruments and complexity of system are limited the application of SRS. So new technology development and commercialization will lower the cost and ease the use, which will allow the SRS technology being used by more groups.

1.4.4 Applications of Multiphoton Microscopy Imaging in Biophotonics

In two-photon microscopy process, the focused near-infrared laser radiation is used to excite fluorescence from a region of interest. By contrast with a single-photon excitation at a shorter wavelength, in this case the excited region is defined by the 3D positioning of the focal zone due to the intensity dependence of the nonlinear process, thereby allowing z-sectioning to be performed by adjusting the focal position without the need for a more complex confocal arrangement. Such techniques by using excitation in the near infrared where biological transmission is maximized provide scope for in-depth tissue imaging. When the average power is kept low, subject the sample to reduced heating compared to other approaches. While in its early days this technique was confined within a laboratory, more recent developments in endoscopy are beginning to show clinical promise in deep tissue imaging [64] and in in vivo brain imaging [65].

Time-lapse imaging of glioma angiogenesis in mouse CA1 reveals progressive distortions to vascular geometry and reduced microcirculatory speeds (Fig. 1.23). Dual-color microendoscopy allows us to visualize both tumor cells and blood vessels by using GFP-transfected GL261 cells and intra-vascular injection of rhodamine dye (Fig. 1.23a). Quantitative studies of angiogenic dynamics relied on un-transfected GL261 cells and one fluorescence channel dedicated to vascular imaging. Over the weeks of glioma growth, we saw progressive deformations and size increases of tumor vessels (Fig. 1.23b, c). Tumor vessels showed distortions from normal shapes (Fig. 1.23c).

Figure 1.24 shows the high-contrast autofluorescence of the in vivo samples excited at 760 nm and SHG image excited at 840 nm, which demonstrates the autofluorescent elastin network as well as the arrangement of the SHG-active collegeneous fibrils within the dermis. This result demonstrates that multiphoton microscopy technique is a powerful tool for visualizing deep tissues.

With the development of multiphoton process, many microscopy techniques have also been developed. In 2000, K. Fujita in Osaka University has developed the confocal multipoint multiphoton excitation microscope, where a confocal pinhole-array is used to enhance the 3D spatial resolution and the depth-penetration property [66]. The images obtained with pinhole-array show the contrast enhancement of fluorescence images and the sharper depth-discrimination property in the confocal system compared to that without the pinhole-array. Furthermore, the longer penetration depth was obtained with the confocal system, in contrast to results with a typical multiphoton excitation microscope by single-focus scanning.

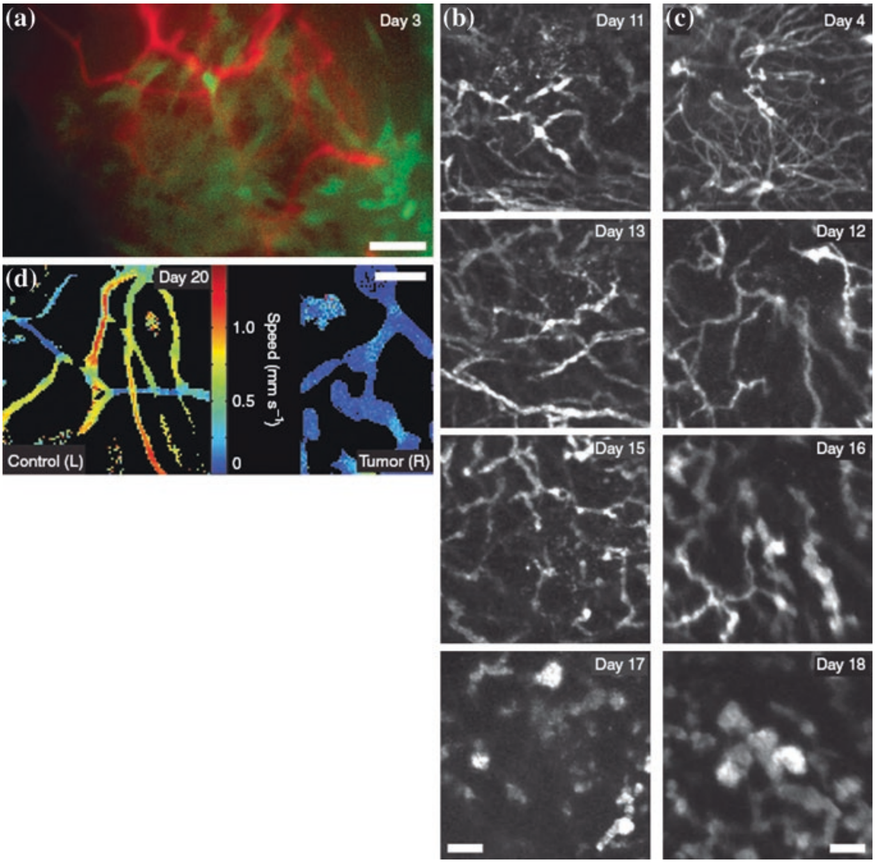

Fig. 1.23 Time-lapse imaging of glioma angiogenesis in mouse CA1 reveals progressive distortions to vascular geometry and reduced microcirculatory speeds. **a** Dual-color image of GFP-expressing mouse glioma cells (*green*) and rhodamine-dextran-labeled microvasculature (*red*), acquired in a live mouse by one-photon fluorescence microendoscopy on 3 days after glioma cell inoculation. **b**, **c** Time-lapse sequences of two-photon microendoscopy image stacks, projected to 2D, showing the progressive distortion of the microvasculature due to glioma angiogenesis. Each stack contained 40–50 images acquired 3.7 μm apart in depth. **d** Maps of average erythrocyte speed, determined from 10-s videos acquired at 100 Hz by one-photon microendoscopy, in *left* (control) and *right* (experimental) hemispheres of a live mouse on 20 days after glioma inoculation. *Scale bars*, 100 μm. Reprinted by permission from Macmillan Publishers Ltd: [65], copyright 2011

Figure 1.25 shows the propagation of Ca ion concentration in a living cultured rat cardiac myocyte. By using the confocal system, the imaging property for observation of moving objects can be achieved. Ca ion wave propagating in the cells upward and downward was imaged. In the experiments, Ca ion dynamics within 25.4 s was recorded with 839 frames.

Based on the understanding of multipoint multiphoton excitation microscopy, a multifocus scanning technique in SHG microscopy has also been developed [67].

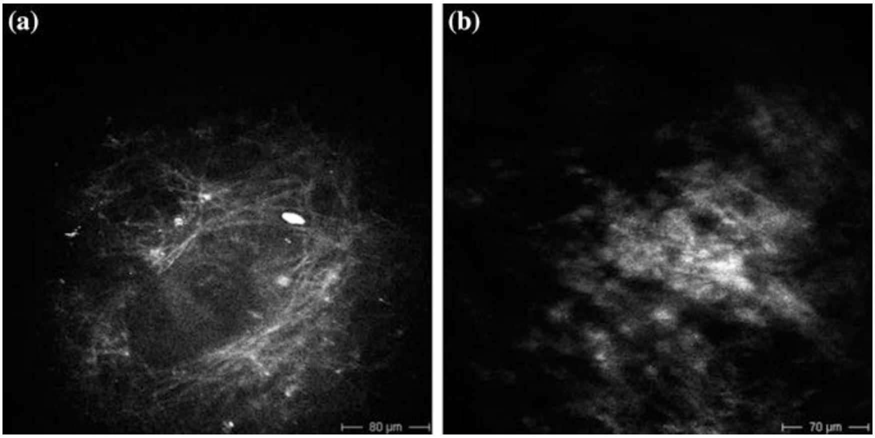

Fig. 1.24 Clinical microendoscopic investigation of the extracellular matrix of patients. **a** Autofluorescence image of the two-photon, 760-nm excited elastin network. **b** SHG image of intradermal 840-nm excited collagen structures. Reproduced from [64] by permission of Wiley

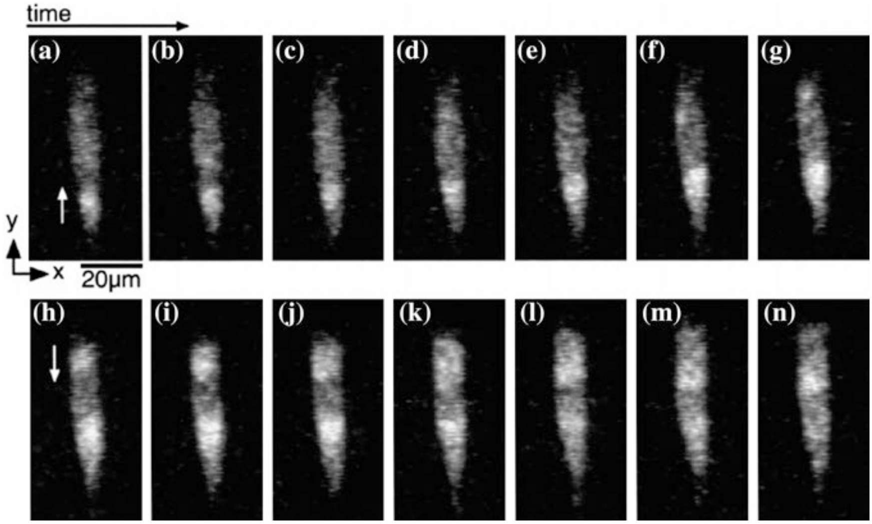

Fig. 1.25 Multiphoton excitation images of Ca ion concentration propagating in a living rat cardiac myocyte. Fluo-3rAM was used as a Ca ion indicator. N. A. of a used objective lens was 0.8 water and the excitation wavelength was 780 nm. Arrows in the images indicate the direction of Ca ion wave propagation. Reprinted from [66], Copyright 2000, with permission from Elsevier

The SHG detection efficiency and the image acquisition rate are improved by several tens of times compared with typical single-focus scanning techniques. By employing a microlens array scanner, the laser beam of a mode-locked titanium–sapphire laser is split into 100 beamlets, and the same number of foci is formed in the specimen.

Parallel scanning of the foci enables the observation of real-time images of the specimen. The imaging properties and the usefulness of the microscope are demonstrated by SHG images of living HeLa cells and rat cardiac myocytes. How the electric potential propagates spatially and temporally and how the propagation affects the contraction of the cells can be induced from the SHG images.

More fat in general is bad, but not all fat is the same. Protective effects of unsaturated fat, especially, polyunsaturated fat are well documented. However, specific analysis of unsaturated fat in vivo at both cellular and organismal levels is challenging, since lipids are intrinsically nonfluorescent and difficult to be tagged with fluorophores, which limits the use of fluorescence microscopy. Fortunately, lipids contain large amounts of fatty acid side chains that have abundant C–H bonds and specific CH_2 stretching frequency, which can be obviously detected in the Raman spectra. Therefore, SRS microscopy can specifically detect the CH_2 stretching vibration or the $C = C$ double bonds, well suited to analyze lipid molecules directly in vivo. C. W. Freudiger et al. have done the first study to demonstrate SRS microcopy in 2008, as a new label-free biochemical imaging technology [54]. The SRS imaging was performed on a stimulated Raman loss SRL microscope equipped with a synchronously pumped fs optical parametric oscillator (OPO)

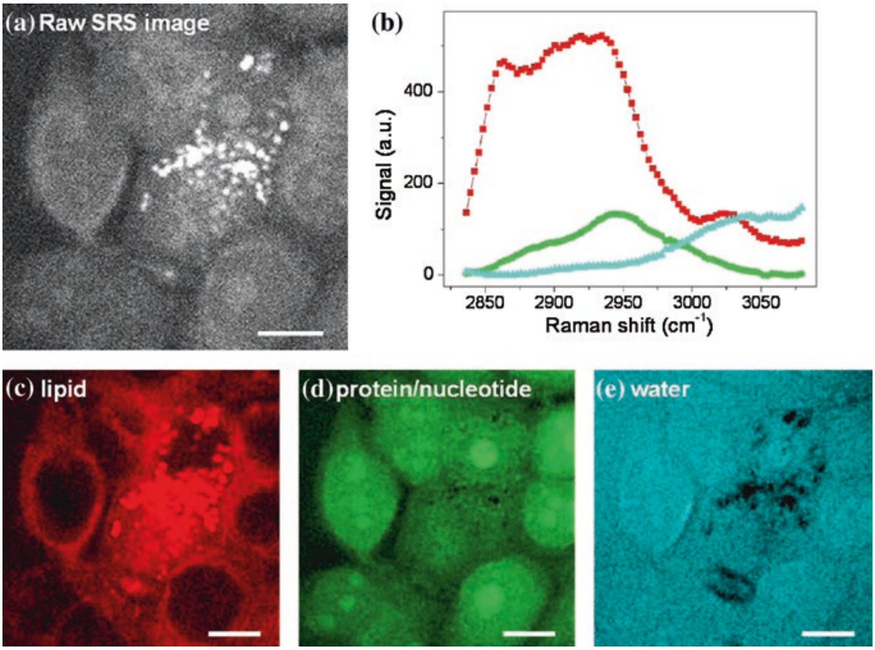

Fig. 1.26 Hyperspectral SRL imaging and MCR analysis of breast cancer MCF7 cells. **a** Single frame of hyperspectral SRL image of cells recorded at 2,920 cm^{-1}. **b** Retrieved spectra of the lipid (*red*), protein/nucleotide (*green*), and water (*blue*) by MCR analysis. **c–e** Reconstructed images corresponding to lipid, protein/nucleotide, and water, respectively. *Scale bars* are 10 μm. Reprinted with the permission from [55]. Copyright 2013 American Chemical Society

system. In 2013, Zhang et al. [55] utilized a SRL microscope to achieve the hyperspectral SRL image of breast cancer MCF7 cells. From the result of the principal component analysis (PCA) method, the major chemical components of sample are assumed as lipid, DNA/protein, and water, respectively. In the spectral range from 2,830 to 3,010 cm^{-1}, the Raman peak at 2,860 cm^{-1} indicates the symmetric vibration of CH_2 which mainly reflect lipid contents, whereas the Raman peak at 2,940 cm^{-1} showed CH_3 symmetric stretching vibration from methyl group, abundant in proteins. Based on the analysis by a multivariate curve resolution (MCR) method, the image has been reconstruct to quantitative concentration images for each individual component and retrieve the corresponding vibrational Raman spectra, as shown in Fig. 1.26. Both lipid and protein can be clearly imaged without any stains.

1.5 Outlook

Multiphoton process has played an important role in the development of multiphoton nanofabrication and multiphoton microscopy techniques. The ultrafast laser processing enables the interactions between light and matter. The better understanding of the optical nonlinear effect in the multiphoton process would be of high potential for prompting the further application in nanophotonics. For near-infrared laser, the high density of electronic excitation, short pulse duration, and high peak intensity, make it possible to realize the multiphoton nanofabrication on polymers, semiconductors, as well as metals. Meanwhile, the femtosecond laser also facilitates the development of multiphoton microscopy techniques, which have attracted much attention recently due to its prospective application in organic nanophotonics and biophotonics. In this chapter, the multiphoton nanofabrication and multiphoton microscopy techniques, such as two-photon excitation fluorescence microscopy, second/third-harmonic generation microscopy, and the SRS microscopy, have been introduced, and the current studies in nanophotonics and biophotonics have been reviewed.

Multiphoton process-based technique is currently a fast-growing research area in which new ideas and improvements continue to emerge. In the future, aside from the application of multiphoton process in the nanofabrication and multiphoton microscopy, the multiphoton process is also expected to be applied into the multiphoton dynamic therapy practically and will be further extended to the fields of photodynamic therapy, photochemistry, and photonics.

References

1. W. Schmidt, F.P. Schaefer, Self-mode-locking of dye-lasers with saturable absorbers. Phys. Lett. **26A**, 558–559 (1968)
2. C.V. Shank, E.P. Ippen, Subpicosecond kilowatt pulses from a modelocked cw dye laser. Appl. Phys. Lett. **24**, 373–376 (1974)

3. W. Sibbett, A.A. Lagatsky, C.T.A. Brown, The development and application of femtosecond laser systems. Opt. Express **20**, 6989–7001 (2012)
4. P.M.W. French, The generation of ultrashort laser pulses. Rep. Prog. Phys. **58**, 169–267 (1995)
5. A.M. Weiner, E.P. Ippen, Novel transient scattering technique for femtosecond dephasing measurements. Opt. Lett. **9**, 53–55 (1984)
6. L.F. Mollenauer, R.H. Stolen, The soliton laser. Opt. Lett. **9**, 13–15 (1984)
7. M.D. Perry, G. Mourou, Terawatt to petawatt subpicosecond lasers. Science **264**, 917–924 (1994)
8. M. Göppert-Mayer, Über Elementarakte mit zwei Quantensprüngen. Ann. Phys. (Leipzig) **9**, 273–294 (1931)
9. L.J. Li, J.T. Fourkas, Multiphoton polymerization. Mater. Today **10**, 30–37 (2007)
10. W. Denk, J.H. Strickler, W.W. Webb, Two-photon laser scanning fluorescence microscopy. Science **248**, 73–76 (1967)
11. Z.B. Sun, X.Z. Dong, W.Q. Chen, S. Nakanishi, X.M. Duan, S. Kawata, Multicolor polymer nanocomposites: in situ synthesis and fabrication of 3D microstructures. Adv. Mater. **20**, 914–919 (2008)
12. X.Z. Dong, Z.S. Zhao, X.M. Duan, Improving spatial resolution and reducing aspect ratio in multiphoton polymerization nanofabrication. Appl. Phys. Lett. **92**, 091113 (2008)
13. W. Jin, M.L. Zheng, Y.Y. Cao, X.Z. Dong, Z.S. Zhao, X.M. Duan, Morphology modification of silver microstructures fabricated by multiphoton photoreduction. J. Nanosci. Nanotechnol. **11**, 8556–8560 (2011)
14. W.E. Lu, Y.L. Zhang, M.L. Zheng, Y.P. Jia, J. Liu, X.Z. Dong, Z.S. Zhao, C.B. Li, Y. Xia, T.C. Ye, X.M. Duan, Femtosecond direct laser writing of gold nanostructures by ionic liquid assisted multiphoton photoreduction. Opt. Mater. Express **3**, 1660–1673 (2013)
15. Y.Y. Cao, N. Takeyasu, T. Tanaka, X.M. Duan, S. Kawata, 3D metallic nanostructure fabrication by surfactant-assisted multiphoton-induced reduction. Small **5**, 1144–1148 (2009)
16. W.K. Wang, Z.B. Sun, M.L. Zheng, X.Z. Dong, Z.S. Zhao, X.M. Duan, Magnetic nickel-phosphorus/polymer composite and remotely driven three-dimensional micromachine fabricated by nanoplating and two-photon polymerization. J. Phys. Chem. C **115**, 11275–11281 (2011)
17. W.E. Lu, X.Z. Dong, W.Q. Chen, Z.S. Zhao, X.M. Duan, Novel photoinitiator with a radical quenching moiety for confining radical diffusion in two-photon induced photopolymerization. J. Mater. Chem. **21**, 5650–5659 (2011)
18. X.Z. Dong, W.Q. Chen, Z.S. Zhao, X.M. Duan, Femtosecond laser two-photon micro/nanofabrication and the application. Sci. China Press **53**, 2–13 (2008)
19. Y.P. Jia, Y.L. Zhang, X.Z. Dong, M.L. Zheng, J. Li, J. Liu, Z.S. Zhao, X.M. Duan, Complementary chiral metasurface with strong broadband optical activity and enhanced transmission. Appl. Phys. Lett. **14**, 011108 (2014)
20. S. Kawata, H.B. Sun, T. Tanaka, K. Takada, Finer features for functional microdevices. Nature **412**, 697–698 (2001)
21. A. del Campo, C. Greiner, SU-8: a photoresist for high-aspect-ratio and 3D submicron lithography. J. Micromech. Microeng. **17**, R81–R95 (2007)
22. J. Wang, Y. He, H. Xia, L.G. Niu, R. Zhang, Q.D. Chen, Y.L. Zhang, Y.F. Li, S.J. Zeng, J.H. Qin, B.C. Lin, H.B. Sun, Embellishment of microfluidic devices via femtosecond laser micronanofabrication for chip functionalization. Lab Chip **10**, 1993–1996 (2010)
23. G. Kumi, C.O. Yanez, K.D. Belfield, J.T. Fourkas, High-speed multiphoton absorption polymerization: fabrication of microfluidic channels with arbitrary cross-sections and high aspect ratios. Lab Chip **10**, 1057–1060 (2010)
24. H. Xia, J. Wang, Y. Tian, Q.D. Chen, X.B. Du, Y.L. Zhang, Y. He, H.B. Sun, Ferrofluids for fabrication of remotely controllable micro-nanomachines by two-photon polymerization. Adv. Mater. **22**, 3204–3207 (2010)
25. X.Z. Dong, Q. Ya, X.Z. Sheng, Z.Y. Li, Z.S. Zhao, X.M. Duan, Photonic bandgap of gradient quasidiamond lattice photonic crystal. Appl. Phys. Lett. **92**, 231103 (2008)

26. H.Z. Cao, M.L. Zheng, X.Z. Dong, F. Jin, Z.S. Zhao, X.M. Duan, Two-photon nanolithography of positive photoresist thin film with ultrafast laser direct writing. Appl. Phys. Lett. **102**, 201108 (2013)
27. W. Zhou, S.M. Kuebler, K.L. Braun, T. Yu, J.K. Cammack, C.K. Ober, J.W. Perry, S.R. Marder, Two-photon-generated photoacid applied to positive-tone 3D microfabrication. Science **296**, 1106–1109 (2002)
28. J.K. Gansel, M. Thiel, M.S. Rill, M. Decker, K. Bade, V. Saile, G. von Freymann, S. Linden, M. Wegener, Gold helix photonic metamaterial as broadband circular polarizer. Science **325**, 1513–1515 (2009)
29. I.B. Sohn, M.J. Ko, Y.S. Kim, Y.C. Noh, Direct femtosecond laser lithography for photoresist patterning. Opt. Eng. **48**, 024301 (2009)
30. Y.D. Du, H.Z. Cao, W. Yan, W.H. Han, Y. Liu, X.Z. Dong, Y.B. Zhang, F. Jin, Z.S. Zhao, F.H. Yang, X.M. Duan, T-shaped gate AlGaN/GaN HEMTs fabricated by femtosecond laser lithography without ablation. Appl. Phys. A **106**, 575–579 (2012)
31. Y.D. Du, W.H. Han, W. Yan, X.N. Xu, Y.B. Zhang, X.D. Wang, F.H. Yang, H.Z. Cao, F. Jin, X.Z. Dong, Z.S. Zhao, X.M. Duan, Y. Liu, Femtosecond laser lithography technique for submicron T-gate fabrication on positive photoresist. Opt. Eng. **51**, 054303 (2012)
32. F. Stellacci, C.A. Bauer, T. Meyer-Friedrichsen, W. Wenseleers, V. Alain, S.M. Kuebler, S.J.K. Pond, Y. Zhang, S.R. Marder, J.W. Perry, Laser and electron-beam induced growth of nanoparticles for 2D and 3D metal patterning. Adv Mater **14**, 194–198 (2002)
33. K. Kaneko, H.B. Sun, X.M. Duan, S. Kawata, Two-photon photoreduction of metallic nanoparticle gratings in a polymer matrix matrix. Appl. Phys. Lett. **83**, 1426–1428 (2003)
34. T. Tanaka, A. Ishikawa, S. Kawata, Two-photon-induced reduction of metal ions for fabricating three-dimensional electrically conductive metallic microstructure. Appl. Phys. Lett. **88**, 081107 (2006)
35. A. Ishikawa, T. Tanaka, S. Kawata, Improvement in the reduction of silver ions in aqueous solution using two-photon sensitive dye. Appl. Phys. Lett. **89**, 113102 (2006)
36. S. Maruo, T. Saeki, Femtosecond laser direct writing of metallic microstructures by photoreduction of silver nitrate in a polymer matrix. Opt. Express **16**, 1174–1179 (2008)
37. K. Abe, T. Hanada, Y. Yoshida, N. Tanigaki, H. Takiguchi, H. Nagasawa, M. Nakamoto, T. Yamaguchi, K. Yase, Two-dimensional array of silver nanoparticles. Thin Solid Films **327–329**, 524–527 (1998)
38. F. Claeyssens, E.A. Hasan, A. Gaidukeviciute, D.S. Achilleos, A. Ranella, C. Reinhardt, A. Ovsianikov, X. Shizhou, C. Fotakis, M. Vamvakaki, B.N. Chichkov, M. Farsari, Three-dimensional biodegradable structures fabricated by two-photon polymerization. Langmuir **25**, 3219–3223 (2009)
39. I. Kaminer, J. Nemirovsky, M. Segev, Optimizing 3D multiphoton fluorescence microscopy. Opt. Lett. **38**, 3945–3948 (2013)
40. W. Kaiser, C. Garrett, Two-photon excitation in CaF_2:Eu^{2+}. Phys. Rev. Lett. **7**, 229–231 (1961)
41. F. Helmchen, W. Denk, Deep tissue two-photon microscopy. Nat. Methods **2**, 932–940 (2005)
42. M.L. Zheng, K. Fujita, W.Q. Chen, X.M. Duan, S. Kawata, Two-photon excited fluorescence and second-harmonic generation of the DAST organic nanocrystals. J. Phys. Chem. C **115**, 8988–8993 (2011)
43. W. Denk, K.R. Delaney, A. Gelperin, D. Kleinfeld, B.W. Strowbridge, D.W. Tank, R. Yuste, Anatomical and functional imaging of neurons using 2-photon laser scanning microscopy. J Neurosci. Methods **54**, 151–162 (1994)
44. W. Denk, K. Svoboda, Photon upmanship: why multiphoton imaging is more than a gimmick. Neuron **18**, 351–357 (1997)
45. M.L. Zheng, K. Fujita, W.Q. Chen, N.I. Simith, X.M. Duan, S. Kawata, Comparison of staining selectivity for subcellular structures by carbazole-based cyanine probes in nonlinear optical microscopy. ChemBioChem **12**, 52–55 (2011)
46. P.A. Franken, A.E. Hill, C.W. Peters, G. Weinreich, Generation of optical harmonics. Phys. Rev. Lett. **7**, 118–120 (1961)

47. B.E. Cohen, Biological imaging: beyond fluorescence. Nature **467**, 407–408 (2010)
48. P. Pantazis, J. Maloney, D. Wu, S.E. Fraser, Second harmonic generating (SHG) nanoprobes for in vivo imaging. Periklis Pantazis **107**, 14535–14540 (2010)
49. P.J. Campagnola, L.M. Loew, Second-harmonic imaging microscopy for visualizing biomolecular arrays in cells, tissues and organisms. Nat. Biotechnol. **21**, 1356–1360 (2003)
50. M. Han, G. Giese, J.F. Bille, Second harmonic generation imaging of collagen fibrils in cornea and sclera. Opt. Express **13**, 5791–5797 (2005)
51. D.J. Brown, N. Morishige, A. Neekhra, D.S. Minckler, J.V. Jester, Application of second harmonic imaging microscopy to assess structural changes in optic nerve head structure ex vivo. J. Biomed. Opt. **12**, 024029 (2007)
52. P. Stoller, K.M. Reiser, P.M. Celliers, A.M. Rubenchik, Polarization-modulated second harmonic generation in collagen. Biophys. J. **82**, 3330–3342 (2002)
53. E. Betzig, G.H. Patterson, R. Sougrat, O.W. Lindwasser, S. Olenych, J.S. Bonifacino, M.W. Davidson, J. Lippincott-Schwartz, H.F. Hess, Imaging intracellular fluorescent proteins at nanometer resolution. Science **313**, 1642–1645 (2006)
54. C.W. Freudiger, W. Min, B.G. Saar, S. Lu, G.R. Holtom, C. He, J.C. Tsai, J.X. Kang, X.S. Xie, Label-free biomedical imaging with high sensitivity by stimulated Raman scattering microscopy. Science **322**, 1857–1861 (2008)
55. D. Zhang, P. Wang, M.N. Slipchenko, D. Ben-Amotz, A.M. Weiner, J.X. Cheng, Quantitative vibrational imaging by hyperspectral stimulated raman scattering microscopy and multivariate curve resolution analysis. Anal. Chem. **85**, 98–106 (2013)
56. M. Okada, N.I. Smith, A.F. Palonpon, H. Endo, S. Kawata, M. Sodeoka, K. Fujita, Label-free Raman observation of cytochrome c dynamics during apoptosis. PNAS **109**, 28–32 (2013)
57. J.X. Cheng, X.S. Xie, Coherent anti-stokes Raman scattering microscopy: instrumentation, theory, and applications. J. Phys. Chem. B **108**, 827–840 (2004)
58. C.L. Evans, X.S. Xie, Coherent anti-stokes Raman scattering microscopy: chemical imaging for biology and medicine. Annu. Rev. Anal. Chem. **1**, 883–909 (2008)
59. Y. Ozeki, F. Dake, S. Kajiyama, K. Fukui, K. Itoh, Analysis and experimental assessment of the sensitivity of stimulated Raman scattering microscopy. Opt. Express **17**, 3651–3658 (2009)
60. P. Nandakumar, A. Kovalev, A. Volkmer, Vibrational imaging based on stimulated Raman scattering microscopy. New J. Phys. **11**, 033026 (2009)
61. A. Folick, W. Min, M.C. Wang, Label-free imaging of lipid dynamics using coherent anti-stokes Raman Scattering (CARS) and stimulated Raman scattering (SRS) microscopy. Curr. Opin. Genet. Dev. **21**, 585–590 (2011)
62. M.C. Wang, W. Min, C.W. Freudiger, G. Ruvkun, X.S. Xie, RNAi screening for fat regulatory genes with SRS microscopy. Nat. Methods **8**, 135–138 (2011)
63. C.W. Freudiger, W. Min, G.R. Holtom, B. Xu, M. Dantus, X.S. Xie, Highly specific label-free molecular imaging with spectrally tailored excitation-stimulated Raman scattering (STE-SRS) microscopy. Nat. Photonics **5**, 103–109 (2011)
64. K. Koenig, A. Ehlers, I. Riemann, S. Schenkl, R. Bueckle, M. Kaatz, Clinical two-photon microendoscopy. Microsc. Res. Tech. **70**, 398–402 (2007)
65. R.P.J. Barretto, T.H. Ko, J.C. Jung, T.J. Wang, G. Capps, A.C. Waters, Y. Ziv, A. Attardo, L. Recht, M.J. Schnitzer, Time-lapse imaging of disease progression in deep brain areas using fluorescence microendoscopy. Nat. Med. **17**, 223–229 (2011)
66. K. Fujita, O. Nakamura, T. Kaneko, M. Oyamada, T. Takamatsu, S. Kawata, Confocal multipoint multiphoton excitation microscope with microlens and pinhole arrays. Opt. Commun. **174**, 7–12 (2000)
67. M. Kobayashi, K. Fujita, T. Kaneko, T. Takamatsu, O. Nakamura, S. Kawata, Second-harmonic-generation microscope with a microlens array scanner. Opt. Lett. **27**, 1324–1326 (2002)

Chapter 2
Strongly Coupled Organic Microcavities

Paolo Michetti, Leonardo Mazza and Giuseppe C. La Rocca

Abstract The photophysics of planar microcavities which employ organic materials as the optically resonant medium to achieve the strong-coupling regime is discussed. While as a result of the light–matter coupling, cavity polariton branches appear which are analogous to those observed in inorganic microcavities, many properties of organic-based microcavities are qualitatively and quantitatively different. The electronic excitations involved are molecular Frenkel excitons, rather than large radius Wannier excitons, which lead to large Rabi splitting values. The effects of disorder are typically much more pronounced as well as the exciton-phonon coupling, possibly leading to vibronic replicas. As a consequence, polariton relaxation and polariton-polariton scattering mechanisms also show features specific to the organic material employed. The field of organic-based microcavities is attracting an increasing interest as high excitation density phenomena such as polariton lasing have recently been reported. In view of their experimental relevance, two different kinds of organic microcavities, disordered J-aggregate-based microcavities and crystalline anthracene microcavities, are considered.

2.1 Introduction

The effort to improve the performance of optoelectronic devices drives the ongoing research of novel materials and architectures. In order to tame the light–matter interaction, while, on the one hand, compounds with improved linear and

---

P. Michetti (✉)
Institut für Theoretische Physik, Technische Universität Dresden, 01062 Dresden, Germany
e-mail: paolo.michetti@tu-dresden.de

L. Mazza
NEST, Scuola Normale Superiore and Instituto Nanoscienze—CNR, 56126 Pisa, Italy
e-mail: leonardo.mazza@sns.it

G.C. La Rocca
Scuola Normale Superiore and CNISM, Piazza dei Cavalieri 7, 56126 Pisa, Italy
e-mail: larocca@sns.it

Y.S. Zhao (ed.), *Organic Nanophotonics*, Nano-Optics and Nanophotonics,
DOI 10.1007/978-3-662-45082-6_2

nonlinear optical properties have been synthesized, on the other hand, dielectric microstructures have been developed engineering the photonic dispersion law and density of states (DOS), a paramount instance being photonic crystals. Rather than tailoring each of the two players—matter and light—individually to stretch the rules that govern their interaction, an alternative approach is to blend them together into hybrid entities—the polaritons—exhibiting novel potentialities.

This is precisely what happens in a high finesse microcavity (MC) in which the cavity mode is resonant with a narrow electronic excitation such that their coupling overcomes the damping mechanisms. In this strong-coupling regime, the relevant eigenmodes are no longer photons and the excitons individually, but rather their coherent superpositions, i.e., the lower polariton (LP) and the upper polariton (UP) modes, which become the key players.

2.1.1 Inorganic Microcavities

Strongly coupled MCs based on inorganic semiconductors have been investigated since the early 1990s culminating with the recent observation of macroscopic quantum coherent effects such as Bose-Einstein Condensation (BEC) of cavity polaritons (see, e.g., the reviews in [1–3]). The polariton notion in bulk crystals is a traditional one [4], and in inorganic semiconductors, it comprises both the case of exciton-polaritons, wherein the matter excitation is a large radius optically allowed Wannier exciton [5], and of phonon-polaritons, wherein the matter excitation is an optical phonon in a polar lattice [6]. Bulk polaritons are characterized by a conserved three-dimensional (3D) wave vector and are not easily accessible experimentally. In typical planar microcavities, instead, a quantum well exciton is coupled to a cavity photon, and cavity polaritons are characterized by a two-dimensional (2D) in-plane wave vector. In particular, if the cavity mode cutoff energy at vanishing in-plane wave vector is lower than the exciton energy (i.e., for a negatively detuned cavity), for increasing in-plane wavevectors, the cavity photon steep dispersion and the flat exciton dispersion would cross each other, but in the strong-coupling regime, the UP and LP branches do anticross: Their separation is the Rabi splitting, proportional to the square root of the exciton oscillator strength (OS).

The MC mirrors which are usually distributed Bragg reflectors are not totally reflecting and the cavity polaritons are very weakly coupled to the 3D free-space photons having a matching in-plane wave vector and a vertical wave vector (which is not conserved) dictated by energy conservation. Injection and detection of cavity polaritons can thus be directly accomplished via angle-dependent spectroscopy, and angle-resolved reflectivity spectra are routinely employed to map the cavity polariton dispersion. The typical signature of the strong-coupling regime is a doublet of reflectivity dips, as first observed by Weisbuch et al. [7] (see Fig. 2.1).

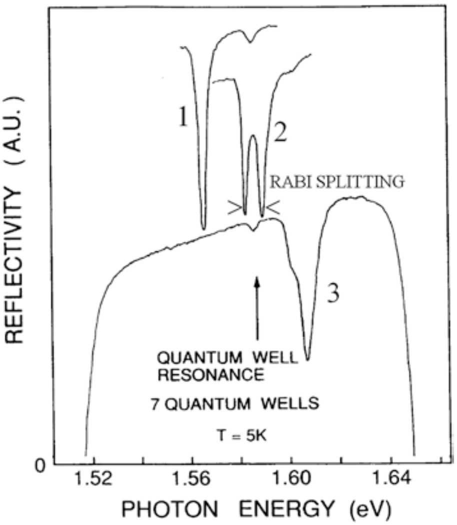

Fig. 2.1 Low-temperature reflectivity of a strongly coupled MC containing 7 GaAs quantum wells. The three spectra correspond to different cavity detunings: Spectrum 2 is on resonance and directly shows the Rabi splitting (Adapted from [7], Copyright 1992, with the permission of The American Physical Society)

While bulk polaritons have a lower branch with an energy linearly vanishing at small wave vectors, cavity polaritons have a lower branch with a minimum energy (which for a resonant cavity is the cavity mode cutoff energy minus half the Rabi splitting) and in its vicinity, a parabolic dispersion with a very small mass, determined by the steep cavity mode dispersion, which flattens out as soon as the in-plane wave vector increases. Cavity polaritons behave as bosonic particles and, differently from free photons in vacuum, have a finite lifetime (due to leakage through the mirrors and exciton non-radiative recombination) and mutual interactions (due to the exciton-exciton scattering). Under resonant or non-resonant pumping, a bosonic-stimulated buildup of cavity polaritons at the bottom of the LP branch may occur leading eventually to a Bose-Einstein condensate—as first observed by Kasprzak et al. in 2006, see Fig. 2.2—and to superfluidity. From the technological viewpoint, interest in such phenomena has also been triggered by polariton lasing whereby the light emitted through the cavity mirrors inherits the coherence properties of the polariton ensemble. The field of inorganic-based MCs has flourished in recent years, and important new results keep being reported.

2.1.2 *Organic and Hybrid Microcavities*

An intrinsic limitation of inorganic-based MCs is the weak binding energy of Wannier excitons and their small OS leading to Rabi splitting values typically of the order of 10 meV. Much larger Rabi splitting values have been anticipated for MCs based on molecular Frenkel excitons [9] and already in the pioneering experiment by Lidzey et al. [10] , a Rabi splitting as large as 160 meV has

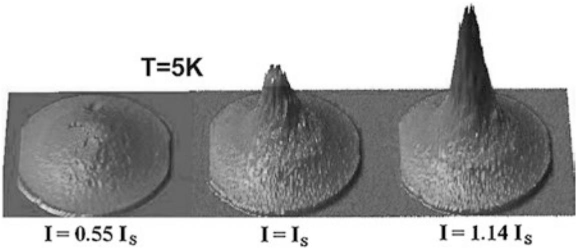

Fig. 2.2 Low-temperature angular distribution of light emitted by the LPs in a CdTe-based MC within a 23° cone around the normal direction following non-resonant excitation. The three spectra from *left* to *right* correspond to an excitation power below, at and above the threshold intensity I_S for BEC, the latter case being dominated by the emission from polaritons with a vanishing in-plane wavevector. (Adapted from [8], Copyright 2006, with permission of Macmillan Publishers Ltd: Nature)

been observed [10] employing a porphirine molecule (4TBPPZn) blended in a polysterene film as optically resonant material at room temperature. Since then, strongly coupled MCs have been demonstrated using a variety of organic materials (see, e.g., the reviews in [11–13]) which can be either classified as non-crystalline, e.g., J-aggregate blends, or (poly)crystalline, e.g., naphtalene and anthracene [14]. The knowledge accumulated for inorganic MCs can only partially be useful to understand organic MCs because, in particular, disorder effects and the electron–phonon interaction are much stronger [4, 14]. While the field of organic-based microcavities has not yet reached a maturity comparable to that of inorganic ones, very recently manifestations of nonlinearities and bosonic stimulation of organic cavity polaritons have been reported and attracted much attention [15–17].

The strategy of combining in the same MC organic and inorganic optically resonant media has also been fruitfully pursed to realize hybrid cavity polaritons [18, 19] as earlier theoretically suggested [9]. Organic–inorganic systems may capitalize on the best properties of either constituent, such as the large OS and quantum yield of organics on the one hand and the good electrical injection and transport properties of inorganic semiconductors on the other one. In strongly coupled hybrid MC, the cavity mode and both the Frenkel and Wannier excitons coherently mix so that the hybrid cavity polaritons share the properties of both of them.

Hybrid systems and MCs have been reviewed in [13]. Here, our current understanding of organic microcavities is discussed considering as illustrative examples of non-crystalline and crystalline systems disordered J-aggregate MCs and crystalline anthracene MCs, respectively, because of their experimental relevance. The field indeed appears ripe for further theoretical and experimental developments which promise to rival those of inorganic MCs.

2.2 Amorphous J-Aggregate Microcavities

J-aggregates thin films represent the most commonly employed class of amorphous organic optically active materials for the realization of strongly coupled systems [20–22]. J-aggregates are obtained as a result of the aggregation of specific organic dyes (i.e., cyanine dyes) in polar solvents, under appropriate conditions. Upon aggregation, the optical features of the system spectacularly change into narrow and intense absorption and emission lines characterized by a very weak Frank-Condon shift, due to the rigidity of the molecular chain. These optical features are well understood as a manifestation of superradiance phenomena typical of one-dimensional Frenkel exciton systems [23]. At sufficiently low concentration, in order to avoid strong inter-aggregate interaction (and therefore the broadening of the resonance line), J-aggregates are randomly arranged in an inert host matrix. Because of their optical features, such organic materials are ideal for the observation of strong light–matter coupling. A concrete example for a J-aggregate MC structure is presented in Fig. 2.3.

The following discussion is meant to provide an introduction to the physics of J-aggregate MCs. In Sect. 2.2.1, we more broadly discuss the effect of disorder in amorphous MCs, analyzed with a minimal model [24], where an inhomogeneously broadened ensemble of two-level chromophores undergos strong light–matter coupling. In Sect. 2.2.2, we present a theoretical model [25] of the photo-excitation dynamics of J-aggregate MCs under non-resonant pumping. This model is particularly instructive, because it allows the simulation of the photoluminescence (PL) of an organic MC, starting from a microscopical description of the bare optically active material.

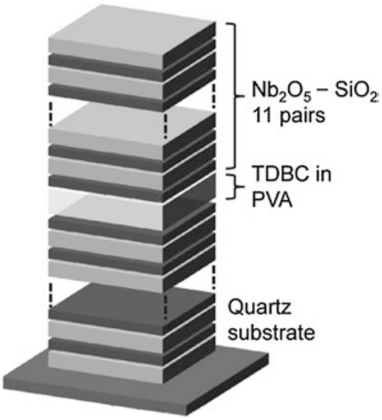

Fig. 2.3 Example of an experimental structure of a J-aggregate MC consisting of a 220-nm-thick layer of TDBC J-aggregate dispersed in a polyvinyl alcohol matrix between two niobia–silica distributed Bragg reflectors (DBRs) of 11λ/4 pairs. (Adapted from [26], Copyright 2011, with permission of WILEY-VCH Verlag, Advanced Functional Materials)

2.2.1 Disorder Effects

In organic-based MCs, the optically active electronic resonances are quite different with respect to the inorganic ones, being molecular excitations rather than large radius excitons. In particular, due to electron–phonon interaction or disorder scattering the molecular Frenkel excitons may behave as incoherent (diffusive) excitations rather than Bloch plane waves having a well-defined wave vector and group velocity [27]. Moreover, excitons in molecular amorphous materials, such as J-aggregate dispersed in an host matrix, are by their nature localized within a molecular aggregate with typical extensions around tens of nm. It is only the light–matter interaction that, in strong-coupling, polarizes the medium giving birth to delocalized polaritons with a well-defined wave vector. Therefore, amorphous organic films intrinsically introduce excitonic disorder of orientational, positional, and diagonal kind in the strongly coupled system. The molecules are in fact randomly arranged in the host matrix, at least at low concentration, where ordering phenomena do not arise (such as liquid crystal arrangements). Each molecule feels a different environment, thus their molecular resonance energies are shifted with respect to their average transition energy, resulting in a static inhomogeneously broadened excitonic resonance, also at low temperature. At finite temperature, dynamical disorder, due the presence of vibrations, can also contribute to the inhomogeneous linewidth. Structural disorder scattering breaks the translational invariance and the *coherence* (in this context, a coherent state is a delocalized plane-wave-like state of definite momentum) imposed by the medium polarization due to light–matter interaction, bringing about localized states quite different from plane-wave-like polaritons [24, 28]. On the other hand, orientational disorder restores a macroscopic rotational symmetry in the plane of the film, which is generally absent in an organic crystalline environment, characterized, instead, by a strong anisotropy of the optical features.

A macroscopic approach to disorder consists in solving Maxwell equations for a transverse electromagnetic wave in presence of a broad and dispersionless excitonic resonance [4, 28]. This provides a first insight on the effect of disorder in a strongly coupled system. The equation for a wave of in-plane momentum q and frequency $\omega = E/\hbar$ assumes the form

$$\left[E - E_{\mathrm{ph}}(q)\right](E - E_{\mathrm{ex}} + i\gamma_{\mathrm{ex}}) = \Delta^2/4, \tag{2.1}$$

with the Rabi splitting $\Delta^2 = \frac{f_{\mathrm{ex}}}{4\varepsilon_b}$, being f_{ex} the OS of the excitonic resonance line at energy E_{ex} and ε_b the background dielectric constant, where $E_{\mathrm{ph}}(q)$ is the dispersion of the cavity mode and γ_{ex} the total broadening of the excitonic resonance. Equation (2.1) is solved for the real energies, giving the UP (sign $+$) and LP polariton (sign $-$) dispersion curves $E_\pm(q)$ [see (2.9)], and for their imaginary part $\delta E_\pm(q)$, accounting for the energy uncertainty. One obtains that the energy uncertainty $\delta E_\pm(q) = \gamma_{\mathrm{ex}} C_\pm^{(\mathrm{ex})}(q)$ is simply proportional to the exciton content of the polaritonic state [see (2.8)]. For a given wave vector, the momentum uncertainty can be quantified through the group velocity

$$\delta q_{\pm}(q) \approx \delta E_{\pm}(q)/\hbar v_{\pm}(q) \tag{2.2}$$

$$v_{\pm}(q) = \frac{1}{\hbar}\frac{\mathrm{d}E_{\pm}(q)}{\mathrm{d}q}, \tag{2.3}$$

and regions where polaritons possess quality of ‘good’ quasi-particles must satisfy $\delta q < q$. This procedure allows to determine a minimum and a maximum endpoint on the LP branch. Inside this range, polaritons have a coherent (delocalized) nature, while polariton localization occurs outside this region. Similarly, a minimum endpoint is defined for the UP branch, above which polaritons have a coherent nature.

Numerical and analytical results [24, 29–32] have confirmed the validity of the macroscopic model (see the following discussion in this section) and analyzed the effect of different kinds of structural disorder. Special attention has been given to the case of the disorder scattering at the bottom of the LP branch that, possessing small group velocity, is especially susceptible to suffer localization. Evidences of localized polaritons in J-aggregates have been found analyzing the reflectivity and luminescence spectra, in which a third peak between the UP and the LP branches appears [33]. This third emission peak at energy near the bare exciton resonance is found at all external angles and, being the angle related to the in-plane wave vector, we can associate it to states of high wave vector uncertainty, therefore localized for the uncertainty principle.

Now, following [24], we set up a minimal quantum mechanical model for a one-dimensional MC of length L. The MC contains two kinds of one-excitation states: N localized excitons (two-level chromophores) placed at sites r_i and delocalized photon modes, coupled by the light–matter interaction. The system is described by the model Hamiltonian (neglecting all damping processes)

$$H = \sum_q E_{\mathrm{ph}}(q) c_q^+ c_q + \sum_j E_j b_j^+ b_j + \sum_{q,j} \left(V_{j,q} c_q^+ b_j + \text{h.c.} \right) \tag{2.4}$$

$$V_{j,q} = \frac{\Delta}{2\sqrt{N}} e^{-iqr_j}, \tag{2.5}$$

where c_q is the annihilation operator for a photon of in-plane momentum q and b_j the annihilation operator acting on the molecular exciton at the j-th site. The excitonic energies E_j have a random Gaussian distribution around their average value E_{ex}, with standard deviation σ. We apply cyclic boundary conditions for the photons so that allowed wavevectors are $q = 2\pi n/L$ with $n \in \mathbb{N}$. A direct diagonalization gives us access to the polariton eigenmodes of the system (which we arbitrarily define as the modes having a photon content larger then 5 %), which we can then completely analyze.

In an ideal situation $E_j = E_{\mathrm{ex}}$ and $r_j = j\,L/N$ for $j = 0, 1, \ldots, N-1$, after introducing the momentum basis for the exciton operators

$$b_q = \sum_j \frac{e^{-iqr_j}}{\sqrt{N}} b_j, \tag{2.6}$$

the system eigenstates are described by ideal cavity polaritons (ICPs)

$$p_{q,\pm} = C_{\pm}^{(\mathrm{ex})}(q) b_q + C_{\pm}^{(\mathrm{ph})}(q) c_q, \tag{2.7}$$

where the exciton and photon content is given by the Hopfield coefficients

$$\begin{aligned} C_{\pm}^{(\mathrm{ex})}(q) &= \frac{\Delta/2}{\sqrt{\Delta^2/4 + [E_{\pm}(q) - E_{\mathrm{ex}}]^2}} \\ C_{\pm}^{(\mathrm{ph})}(q) &= \sqrt{1 - [C_{\pm}^{(\mathrm{ex})}(q)]^2} \end{aligned} \tag{2.8}$$

and the corresponding eigenenergies are

$$E_{\pm}(q) = \frac{E_{\mathrm{ex}} + E_{\mathrm{ph}}(q)}{2} \pm \frac{1}{2}\sqrt{[E_{\mathrm{ex}} - E_{\mathrm{ph}}(q)]^2 + \Delta^2}. \tag{2.9}$$

In Fig. 2.4a, b, we present the analysis of the eigenstates for a single realization of the model in (2.5) with on-site energetic disorder. Plotting the eigenenergies against the average wave vector (calculated on the photonic component of the eigenstates) of eigenstates with photon component larger than 5 %, we easily identify the upper and LP branches. Between the two branches, we note the presence of a large number of eigenstates, corresponding to energies similar to the bare excitation energy of the chromophores. Plotting the excitonic content of the eigenstates (in Fig. 2.4a), we note that such states are mostly exciton-like. The analysis of the standard deviation of the wave vector calculated on the photonic component [in Fig. 2.4b] reveals that these states have an incoherent nature (they do not have a well-defined momentum). Experimentally, this is consistent with the measurement of a PL peak for frequencies between the polariton branches, persisting at all observation angles [33]. In Fig. 2.4c, we plot the mean extension of the polaritonic states averaged on 5,000 disorder configurations. This analysis confirms the existence of localized states with finite exciton–photon mixing between the two polariton branches (at energies near the bare exciton resonance) and at the bottom of the LP branch, and hence the validity of the previously discussed macroscopic approach.

Now, we analyze in more detail the polariton localization at the LP bottom induced by excitonic disorder, in view of its importance for polariton condensation experiments. In Fig. 2.5, we show the mean eigenstate extension versus their energy of the four lowest lying polariton states, for an ensemble of 1,000 disorder configurations with $\sigma = 5$, 10, 15, and 20 meV. In the $\sigma = 5$ meV panel, we can indeed distinguish that the eigenstates are separated in four groups of increasing energy. For larger σ, it is instead no more possible to clearly distinguish the four eigenstates, because they form a dispersed cloud, which extends toward lower energies and increased localization values for increasing σ.

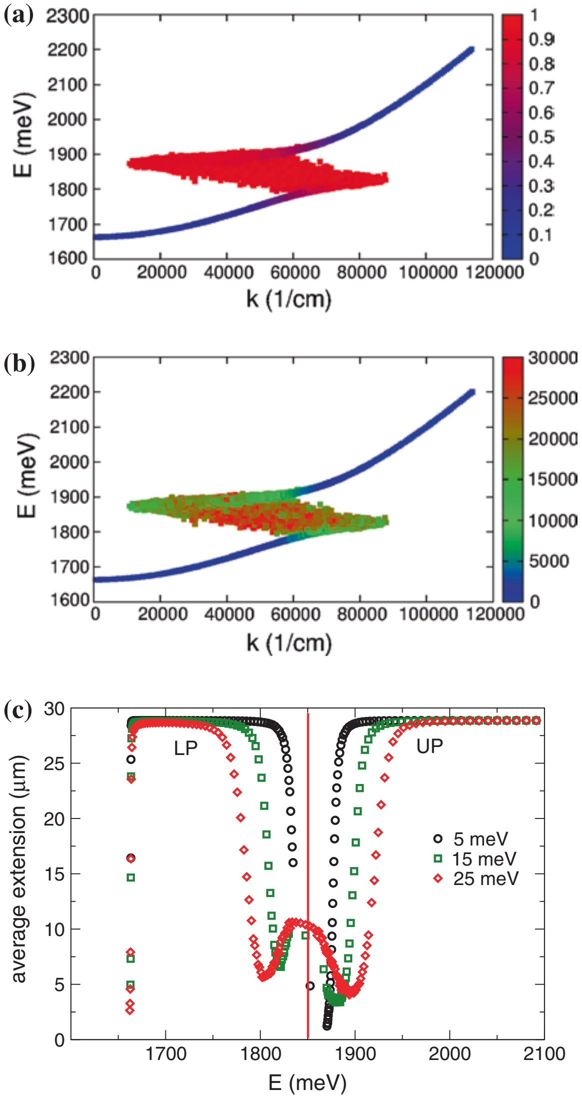

Fig. 2.4 Analysis of the eigenstates of a system of $N = 1{,}000$ chromophores of average on-site energy $E_{\mathrm{ex}} = 1,850\,\mathrm{meV}$ and standard deviation $\sigma = 20\,\mathrm{meV}$ in a 1D MC of length $L = 10^{-6}\,\mathrm{m}$ realizing a Rabi splitting $\Delta = 120\,\mathrm{meV}$.**a** Color plot of the excitonic fraction of each eigenstates plotted against the average wave vector calculated on its the photonic part. **b** Standard deviation on the average wave vector calculated on the photonic part of the eigenstates. **c** Mean extension of the (polariton-like) eigenstates having photonic fraction >5 %, averaged on the spectral intervals and on an ensemble of 5,000 disorder configurations, for systems with σ = 5, 10 and 20 meV

In order to better understand the mechanism that rules the localization of the lowest energy state, we now build a simplified analytical model for the LP bottom state in presence of a single exciton defect. Let us consider a model Hamiltonian (2.5), where all chromophores have the same excitation energy E_{ex} with the exception of a single defect in the origin of the real space, with the excitonic potential energy is given by $E_{\mathrm{ex}} - \sigma R \delta(x)$, with R the nearest neighbor distance being. We work on the reciprocal ICP space [span by (2.7)] near the bottom of the LP branch, for which the dispersion curve can be well captured by an effective mass

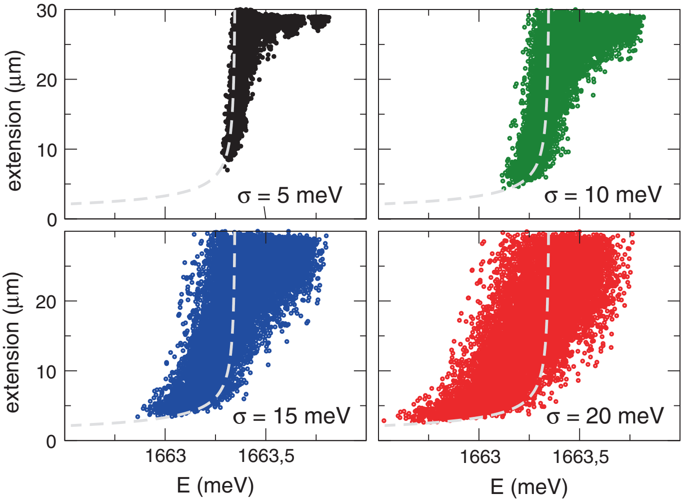

Fig. 2.5 Analysis of real space extension of the lowest four eigenstates of a system similar to that in Fig. 2.4, for 1,000 disorder configurations. Different panels represent results obtained with different value of energetic on-site disorder $\sigma = 5$, 10, 15 and 20 meV. A dashed line, shown in each panels, represents the mean extension of the bound state eigenenergy obtained with the analytical model in (2.10) of a MC with a single excitonic defect, for a LP effective mass $m = 0.5 \times 10^{-5}$meV, $R = 100$ nm and varying V_0 from 0 to 50 meV

approximation. We also consider for simplicity a constant excitonic coefficient $\mathrm{C}_-^{(\mathrm{ex})}(k) \approx \mathrm{C}_-^{(\mathrm{ex})}(0)$ in the restricted k-space near the bottom of the LP branch. In the ICP basis, the Hamiltonian (2.5) is diagonal and, in effective mass approximation, the model Hamiltonian in real space becomes

$$H_{\mathrm{model}} = E_-(0) + \frac{\hbar^2}{2m}\frac{\mathrm{d}^2}{\mathrm{d}x^2} - V_0 R\delta(x), \tag{2.10}$$

with the effective defect energy $V_0 = \sigma|C_-^{(\mathrm{ex})}(0)|^2$ and effective LP branch mass m. Equation (2.10) allows for a bound level of eigenenergy

$$E_b = E_-(0) - \frac{mV_0^2R^2}{2\hbar^2}, \tag{2.11}$$

corresponding to an eigenfunction of the form $\psi(x) = \sqrt{\chi}e^{-\chi|x|}$ of mean extension

$$\lambda_b = \frac{1}{\sqrt{2}\chi} = \frac{\hbar}{2\sqrt{mE_b}}, \tag{2.12}$$

In each panel of Fig. 2.5, we plot λ_b against E_b, while V_0 is varying from 0 to 50 meV. We see that, although taking in account only one excitonic energy defect, the analytical model captures the qualitative behavior of the mean extension with increasing disorder obtained from the numerical analysis. With diminishing energy, we can see an initial rapid decrease of the localization length (because the LP bottom has relatively flat dispersion curve), after a certain degree of localization, the Fourier components needed in order to further localize the wave function become higher in energy, therefore a further decrease of the localization length requires larger excitonic defects.

As a conclusion of this section, disorder in organic MCs leads to the coexistence of delocalized polariton states with localized ones, distributed in different spectral regions. Localization of strongly coupled states is expected at the LP bottom and near the bare exciton energy. From these two kind of polaritons, completely different behaviors also from the point of view of their time evolutions properties have been predicted [31, 32], with delocalized polaritons featuring a ballistic motion and localized polaritons being instead diffusive.

2.2.2 Relaxation Dynamics

A complete microscopical analysis of the excitation dynamics of a strongly coupled MC should ideally start from a model describing the bare optically active material, and as a second step, this model should be refined for the strong-coupling limit. However, this procedure is difficult in organic MCs where, often, models describing the excitation dynamics in the bare materials are not known or very complex, or do not have a broad range of validity, even in the same class of materials. For this reason, the model developed for describing the full excitation dynamics of J-aggregate MCs in linear regimes [25, 34], which is directly derived as an extension of the Frenkel exciton model of the uncoupled material, assumes also a conceptual importance. This is made possible by the simple description of the bare J-aggregate film as an ensemble of one-dimensional Frenkel exciton systems [23, 35–37] and recurring to a phenomenological ansatz for the polariton wave function [25].

A linear J-aggregate can be considered as a chain composed of N_d monomers (dye molecules) described by the following Frenkel exciton Hamiltonian [23, 35]

$$H = \sum_{i}^{N_d} E_i b_i^\dagger b_i + \sum_{i \neq j}^{N_d} V_{i,j} (b_i^\dagger b_j + b_j^\dagger b_i) \tag{2.13}$$

The b_i is the monomer exciton operator, and $E_i = \varepsilon_i + D_i^{agg}$ is the sum of the bare energy of the monomer excited state and energy shift due to the interaction of the ith excited molecule with the other molecules and the host medium in their ground states. The exciton transfer term is given by $V_{i,j} = -J/|i-j|^3$, where $J > 0$ is the nearest neighbor coupling strength. When the molecules are put together, the interactions among them give rise to excitation transfer with the formation of delocalized Frenkel excitons (having a 1D energy dispersion curve called J-band) and thus to the superradiance phenomena. On the other hand, the presence of diagonal disorder is introduced as a Gaussian stochastic fluctuation of the monomer energies; it brings about the fragmentation of the excitons in localized structures on the aggregate chain, especially in the spectral region at the bottom of J-band, with the consequence of inhomogeneous broadening. The diagonal disorder standard deviation is $\sigma = \tilde{\sigma} J$, where $\tilde{\sigma}$ is used as a parameter of the disorder strength. The eigenstates are found by direct diagonalization of the Frenkel exciton Hamiltonian and are described by the following operators:

$$B_\alpha^\dagger = \sum_i c_i^{(\alpha)} b_i^\dagger \tag{2.14}$$

where c_i^α is the coefficient of the αth exciton on the ith molecule. The OS of each state is proportional to:

$$F_\alpha = \left| \sum_i c_i^{(\alpha)} \right|^2 \tag{2.15}$$

with $\sum_\alpha F_\alpha = N_d$, with the molecules of equal dipole transition, and with wavelength much greater than the aggregate dimension. In Fig. 2.6, we show the DOS and the OS for state for an ensemble of aggregates with disorder parameter $\tilde{\sigma} = 0.54$ and $J = 75$ meV, averaged over specific spectral intervals. Almost the whole OS of the film is concentrated among the superradiant excitons in a spectral region at the bottom of the J-band.

The Frenkel exciton model for the J-aggregates is then put into contact with a thermal bath that provides a mean for the thermalization of excitations [35–37]. The linear exciton–vibration coupling, treated with the Fermi golden rule, leads to the definition of scattering rates between initial and final excitonic states mediated by the emission/absorption of a vibrational quantum. For a continuous spectrum of vibrations, scattering rates have the following form [35–37]

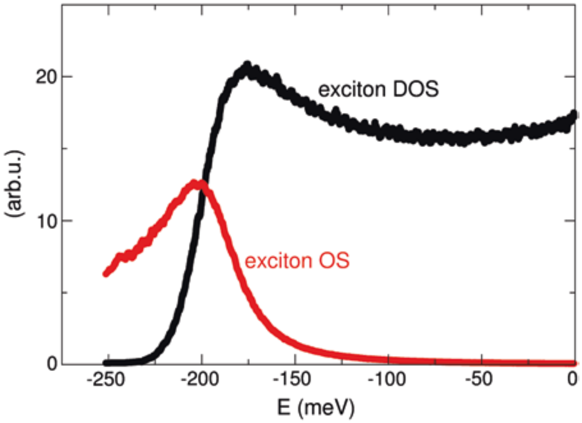

Fig. 2.6 The DOS of the J-band dispersion (*black*) for an ensemble of J-aggregate with $\tilde{\sigma} = 0.54$ and the corresponding oscillator strength (*red*). The oscillator strength (OS) is accumulated in the states at the bottom of the J-band and inhomogeneously broadened by static disorder

$$W_{i',i} = W_0 \Xi_{i,i'} \times (N_{|\Delta E|} + \Theta_{(\Delta E)}) \left(\frac{|\Delta E|}{J} \right)^p, \tag{2.16}$$

while for discrete optical vibrations we obtain

$$W_{i',i} = \frac{2\pi E_{vib}^2}{\hbar} \Xi_{i,i'} \times (N_{|\Delta E|} + \Theta_{(\Delta E)}) \delta(|\Delta E| - E_{vib}), \tag{2.17}$$

where $i = (I, \alpha)$, with I running on different aggregates in the film and α on different Frenkel excitons of the same aggregate, $\Delta E = E_{\alpha'} - E_\alpha$, Θ is the step function, N_E is the Bose-Einstein occupation factor of the states of the vibrational bath, $W_0 = 2\pi\xi J/\hbar$, with ξ and p are parameters that describe the strength and spectral shape of the exciton scattering with vibrations [36, 37]. The overlap factor $\Xi_{i,i'}$ is defined as

$$\Xi_{i,i'} = \delta_{I,I'} \sum_{n=1}^{N_d} \left| c_i^{(\alpha)} c_i^{(\alpha')} \right|^2. \tag{2.18}$$

The homogeneous linewidth of the states is due to the radiative lifetime and to the temperature-dependent dephasing processes that are dominated by the exciton-phonon scattering [37]. Each exciton state is broadened as a Lorentzian lineshape around the bare energy E_α:

$$g_\alpha(E) = \frac{\Delta E_\alpha / \pi}{(E_\alpha - E)^2 + (\Delta E_\alpha)^2} \tag{2.19}$$

with the energy uncertainty given by

$$\Delta E_\alpha = \hbar \Big(\sum_{\alpha'} W_{\alpha',\alpha} + \gamma_\alpha \Big) \tag{2.20}$$

We can now describe the excitation dynamics of a J-aggregate film, through the definition of rate equations for the Frenkel excitons in the low excitation density approximation

$$\dot{n}_\alpha = \sum_{\alpha'} (W_{\alpha,\alpha'} n_{\alpha'} - W_{\alpha',\alpha} n_\alpha) - \gamma_\alpha n_\alpha + P_\alpha \tag{2.21}$$

where we have added the radiative decay rate γ_α which, for excitons, is given by $\gamma_\alpha = F_\alpha \gamma_0$, where γ_0 is the spontaneous emission of the dye monomer, typically 0.3 ns^{-1}. We also add a pump term P_α on the upper energy tail of the exciton DOS.

This model can be extended to a strongly coupled J-aggregate MC through the introduction of a model polariton wave function, for which we formulate the following ansatz

$$p_{k,\pm}^+ = C_\pm^{(ph)}(k) c_k^+ + \frac{C_\pm^{(ex)}(k)}{\sqrt{N_{agg}}} \sum_I^{N_{agg}} \sum_\alpha^{N_d} \phi_{\alpha,I}^{(k)} B_{\alpha,I}^+ \tag{2.22}$$

where $C_k^{(ex)}, C_k^{(ph)}$ are given by (2.8) and $|\phi_{\alpha,I}^{(k)}| = \sqrt{F_\alpha/N_d}$. This allows us to calculate the coupling of polariton states with the thermal bath acting on the molecular Frenkel excitons of the aggregates and to derive the form of the scattering rates between all states of the system [25, 34, 38]. The scattering rates have the same form as (2.16) and (2.17), where now i, i' runs on the excitonic states of the film $n' = (\alpha, I)$, i.e., the αth exciton of the Ith aggregate, and on the delocalized polaritons $k = (\pm, q)$, ± polariton branch and momentum q. However, different overlap factors $\Xi_{i,i'}$ have to be employed for different processes (we refer to the original literature for the full details [25]). We only mention that overlap factors involving polaritons ($\Xi_{k,n'}$, $\Xi_{n',k}$, and $\Xi_{k',k}$), are suppressed by a factor N_{agg}, being the number of sites on which the polariton state is delocalized. This is due to the contrast between extended polariton states and the localized nature of vibrations.

In addition to the phonon-mediated scattering, we have also considered a radiative pumping rate from exciton to polariton [25, 38] in the following form:

$$W_{\mathbf{k},\alpha}^{\text{rad}} = \beta^{\text{rad}} \gamma_\alpha \frac{|C_k^{(ph)}|^2 g_\alpha(E_k)}{\sum_{\mathbf{k}'} |C_{k'}^{(ph)}|^2 g_\alpha(E_{k'})}. \tag{2.23}$$

Such radiative scattering is proportional to the exciton OS and the transfer matches energy conservation, while the normalization is chosen to obtain a net exciton radiative decay toward polaritons of β^{rad} times the spontaneous emission (γ_α). The broadening g_α is given by (2.19), calculated for the cavity system. This process usually accounts for the presence of a residual weakly coupled excitons in the system, but can also more generally describe the presence of emitting weakly coupled excitons of different nature as it happens in [39], where the authors have engineered a MC with an exciton reservoir (ER) of weakly coupled molecules (chemically different from the molecules giving the strong coupling) resonant with the LP branch bottom. The radiative process described by (2.23) is exploited to efficiently populate of the LP bottom from this ER (which is non-resonantly pumped).

To deal with the 2D MC, we assume isotropic conditions in which the polariton population depends only on the modulus of the wave vector. We describe the dynamics of excitation relaxation by means of a rate equation for the population of state $f_i(t)$:

$$\dot{f}_i(t) = -\Gamma_i f_i(t) + \sum_{i'} (W_{i,i'} f_{i'}(t) - W_{i',i} f_i(t)) + P_i \tag{2.24}$$

where the indices i, i' run over all the spectrum of excitations and can refers to both polariton (k, upper or lower) or localized excitons (n). The damping rate due to the escape through the cavity mirrors is given by $\Gamma_k = |C_\pm^{(ph)}(q)|^2/\tau_p$. The typical photon lifetime is about $\tau_p = 35$ fs, corresponding to a photon linewidth of the order of 30 meV. P is the pumping rate that we apply as for the aggregate film to the high energy tail of the J-band. For the details of numerical implementation and solution of (2.24) for a J-aggregate MC with a sensible ensemble average over the J-aggregate disorder configurations, see [25].

A comprehensive study of the behavior of this model as a function of its parameters can be found in the original literature [25, 38, 40], including the analysis of the time-dependent solution of (2.24) [40]. We discuss here the overall physical picture that emerges from this model of J-aggregate MCs under non-resonant pumping, which is schematized in Fig. 2.7. The pumping of high energy Frenkel exciton states of the J-aggregates is followed from a rapid relaxation toward the bottom of the excitonic DOS, on timescales shorter then 1 ps. And here, the excitations are accumulated, due to a bottleneck in the relaxation, so that the bottom of the excitonic DOS can be seen as an ER, from which further relaxation on the polaritonic states takes place. The scattering from the ER toward the polariton branches has typical scattering times on the order of 100 ps and therefore cannot lead to an efficient polariton population, due to the short polariton lifetime. The fate of polariton states is twofold. They can be efficiently scattered back into the ER on timescales of the order of 10–50 fs or they can be radiatively emitted on time scales of 30–100 fs. The first process is mainly effective in depleting higher polariton branches, preventing their radiative emission, while generally does not affect the LP branch bottom. This process is the key feature leading to the efficient ultra-fast transfer mechanism between two different excitonic species, mediated by strong coupling, recently observed in hybrid J-aggregate MCs [41]. The relaxation along the polariton branches is frozen due to its long timescales (≈100 ps) with respect to the polariton depletion times. The picture of the photophysics of J-aggregate MCs evinced by the model here presented has been validated through the accurate comparison with experimental PL data [26, 42]. As an example, we present in Fig. 2.8 the comparison between the experimentally measured PL data and the corresponding results of a simulation where the scattering with discrete vibrations, observed in Raman spectroscopy have been accounted for. The model is also compatible with the interpretation of ultra-fast spectroscopy measurements [43] and PL excitation spectroscopy data [44].

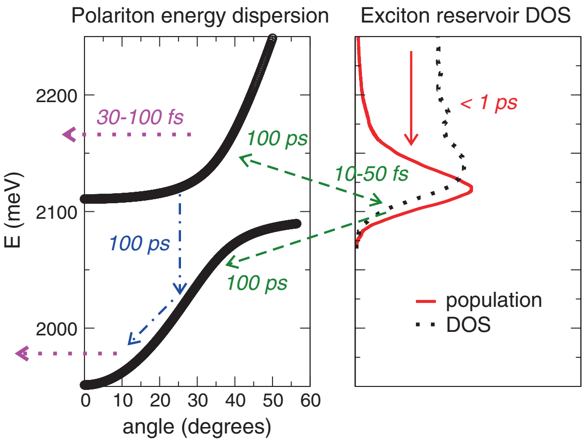

Fig. 2.7 Scheme of the relaxation mechanism in J-aggregate MC, accounting for molecular exciton DOS and the delocalized polaritons

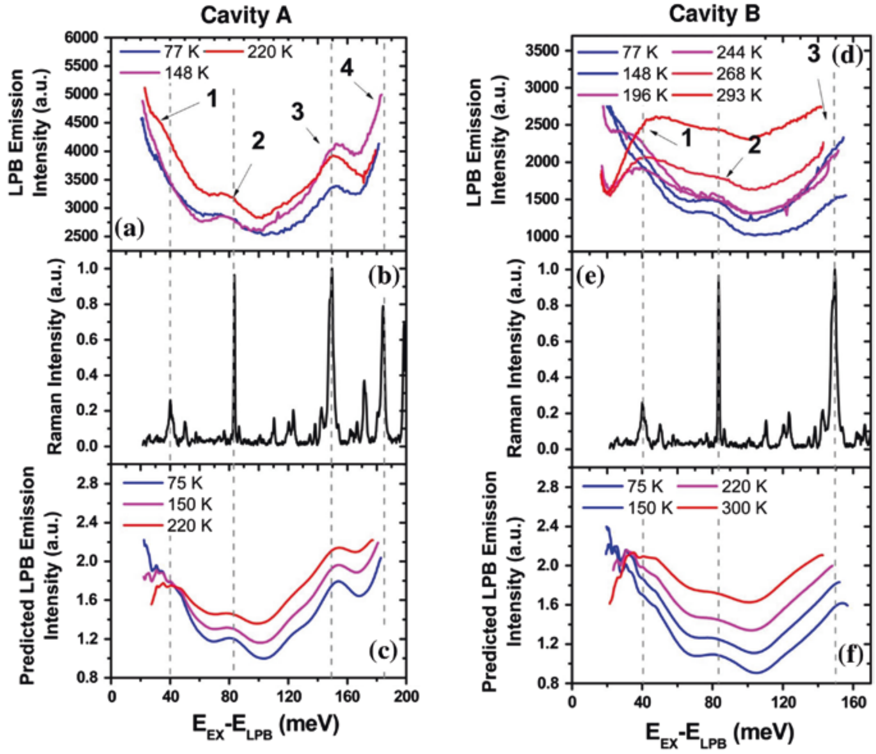

Fig. 2.8 Comparison between the experimental Lambertian-corrected LPB emission intensity as a function of energy separation between the exciton reservoir and the LPB shown in for the cavity A in **a** and for the cavity B in **d**, and the simulated PL emission in **c** and **f** with parameters corresponding to the A and B MCs, respectively. **b** and **e** Raman spectrum of TDBC for the A and B MCs, respectively. Full details on this comparison can be found in [26]. (Reprinted from [26], Copyright 2011, with permission of WILEY-VCH Verlag, Advanced Functional Materials)

2.3 Polariton Lasing in Organic Crystalline Microcavities

Polariton lasing has recently been observed in strongly coupled crystalline anthracene MCs [15], thus providing the first unequivocal experimental proof of nonlinear optics in organic-based MCs. In this section, we focus on some aspects concerning nonlinear physics in such heterostructures.

At high excitation densities, the buildup of a large population at the bottom of the LP branch is favored by bosonic final-state stimulation as soon as the occupation per mode of the LP states exceeds unity. Coherent light-emission, called polariton lasing, results from this macroscopic population due to the finite lifetime of the polaritons which leak out of the cavity via their photonic component. In contrast to the case of inorganic MCs, manifestations of bosonic stimulation using organic cavity polaritons have been quite elusive. Recently, however, several nonlinear phenomena were reported: Room temperature polariton lasing in an anthracene single crystal MC [15], indirect pumping of J-aggregate lasing MCs [39] (discussed also in Sect. 2.2.2) and even evidence of a polariton condensate featuring a blueshift of the low-energy polariton states [16, 17] (see Fig. 2.9).

In anthracene, the observation of a threshold for nonlinear emission was accompanied by a significant line narrowing and by a collapse of the emission lifetime. In that case, a comparison with the best-case estimate of the threshold for conventional lasing inferred from amplified stimulated emission measurements shows that the lasing threshold observed in the strongly coupled MC is slightly lower than that anticipated for a conventional laser [15]. The temperature dependence of the polariton lasing threshold has also been investigated and shows an order of magnitude decrease from room temperature to low temperatures [45].

Employing two different amorphous organic semiconductors, which also lower the technical intricacies of the fabrication of these samples, two competing groups have been recently able to observe the distinctive features of a polariton condensate once a pumping threshold was overcome [16, 17] (see Fig. 2.9). Measurements recorded with a Michelson interferometer between the emitted light and its retroreflected copy display the appearance of fringes which indicate the phase coherence between different points of the condensate. These important features are accompanied by a blueshift of the emitting polariton, which can be interpreted as the result of the interacting nature of the excitonic part of the polariton. The investigation of the different behaviors of these setups for different temperatures provides distinctive clues of the relaxation mechanisms which characterize these systems.

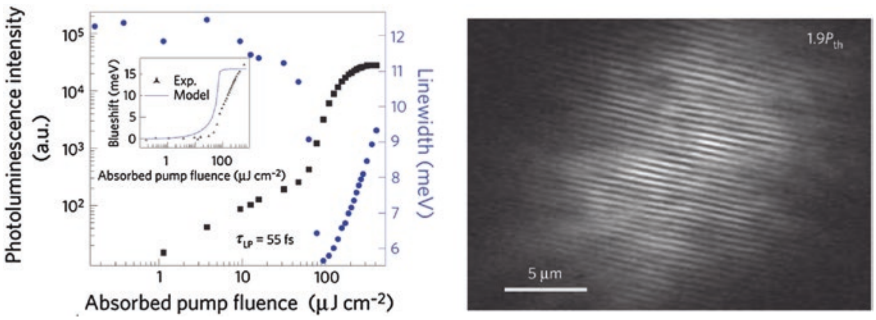

Fig. 2.9 Experimental evidences of polariton condensation in MCs filled with a thin film of 2,7-bis[9,9-di(4-methylphenyl)-fluoren-2-yl]-9,9- di(4-methylphenyl)fluorene. (*Left*) The dependence of the peak PL intensity (*black squares*) and linewidth (*blue circles*) on the absorbed pump fluence is shown for the 120-nm-thick low-Q MC. Note the clear lasing threshold. The *inset* shows the blueshift of the luminescence peak. (*Right*) Interferograms recorded in a Michelson interferometer in the retroreflector configuration for above-threshold pump; the fringes are observed over the entire area signal macroscopic phase coherence throughout the condensate. (Reprinted from [17]. Copyright 2014, with permission from Macmillan Publishers Ltd: Nature Materials. Similar measurements are reported in [16])

These remarkable experiments are triggering new theoretical work. In [46], the authors investigate the condensation physics of polaritons where the matter excitations are vibrationally dressed, a typical situation in organic materials. Using mean-field methods, the authors argue on the appearance of sequences of normal-superradiant-normal phases as temperature is decreased. Moreover, for sufficiently strong vibrational couplings, the phase transition can become first order.

The possibility of observing nonlinear phenomena in MCs embedding organic amorphous solids, whose fabrication is easier with respect to inorganic and organic crystals, will surely trigger a boost in the field of polaritonics. Among the several fields where we expect important developments in the next future, we mention here the long-standing goal of realizing an electrically pumped organic laser: The possibility of overcoming the encountered difficulties via the strong-coupling physics is currently renewing the race [47].

In this section, we focus on the lasing measurements in anthracene MCs and present a simple model which describes the onset of the lasing threshold based on a master equation. The mechanism governing the buildup of the polariton population—namely bosonic-stimulated scattering from the ER via a vibronically assisted process—is characterized and its efficiency calculated on the basis of a microscopic theory [48–50].

2.3.1 Two-level Model for Polariton Lasing

In this section, we model the dynamics of the lasing process using a minimal rate–equation approach; we obtain an estimate for the typical timescale of the mechanism which selectively transfers excitations from the reservoir to the bottom of the polariton branch, without any assumptions on its microscopic nature.

2.3.1.1 The Master Equation

The anthracene crystal has two molecules per unit cell and strongly anisotropic optical properties [14, 51]. Excitations in this material are well described within the Frenkel exciton framework, which is based on the intramolecular promotion of an electron from the highest occupied molecular orbital to the lowest unoccupied one. Because of molecular dipole–dipole interaction, the excitation can propagate, resulting in two orthogonal transition dipole moments, $\boldsymbol{\mu}_{a,b}$, directed along the in-plane **a** and **b** axes. When a thin anthracene crystal is placed between two mirrors, light couples to both *a*- and *b*-polarized excitons and creates two orthogonally polarized LP branches. Measurements are usually reported for light polarized along **a** and **b** [15, 51]: In these cases, the *p* and *s* in-cavity light polarizations separately couple to the dipole moments $\boldsymbol{\mu}_{a,b}$ and no mixing effect is present.

We focus only on b-polarized excitons [14], i.e., those with largest OS, for which lasing has been reported [15] and neglect other polaritonic and excitonic states. The initial relaxation of the pump excitations is also neglected, and the presence of an effective excitonic reservoir at a fixed energy independent on the cavity properties is considered [25]. We note that the experimental PL from anthracene MCs shows always a clear maximum at energy ~2.94 eV regardless of the cavity thickness [15, 52], and indeed lasing has been achieved in a cavity where the minimum of the LP is exactly at 2.95 eV. This is a signature that the microscopic dynamics resulting in the lasing phenomenon is that of a two-level process rather than that of the well-known polariton bottleneck. We thus develop a two-level master equation for $\nu_e(t)$ and $\nu_p(t)$, the surface density of reservoir excitons and of lasing polaritons located near $\mathbf{k} = 0$, respectively.

We denote with $\mathscr{A}_0$ the subregion of the Brillouin zone located around $\mathbf{k} = 0$ which is occupied by the lasing polaritons. Because states at the bottom of the LP branch do not have a well-defined wave vector k, we consider all of the localized wave packets with energy $\sim E_{\mathrm{LP}}(\mathbf{k} = 0)$ as equally contributing to the lasing process. N_{pol} is the number of such polaritonic states, while N_{exc} is the number of excitonic states. The polariton and exciton decay rates are $\varGamma_p = |C^{(ex)}|^2/\tau_e + |C^{(ph)}|^2/\tau_p$ and $\varGamma_e = 1/\tau_e$, respectively, where $\tau_p(\tau_e)$ is the bare photon (exciton) lifetime and $C^{(\mathrm{ph})}\left(C^{(\mathrm{ex})}\right)$ is the photonic (excitonic) Hopfield coefficient for the lasing polaritons.

The parameter Z^e is the decay rate via other channels, such as phonons, LPs outside the $\mathscr{A}_0$ region and leaky modes, whereas bimolecular quenching processes are treated separately, with a rate γ'. A standard pump term proportional to $P'(t)$ is included; in order to take into account possible saturation effects the term $(1 - \nu_e/\bar{\nu}_e)$ has been considered ($\bar{\nu}_e = N_{\mathrm{exc}}/A$ is the surface density of excitonic states and A is the area of the sample).

The rate of resonant excitation transfer from the reservoir to the lasing polaritons is W^{ep}. We retain the bosonic enhancement term $(1 + \nu_p/\bar{\nu}_p)$ responsible for lasing effects, where $\bar{\nu}_p = N_{\mathrm{pol}}/A$ is the surface density of polaritonic states.

The master equation for $\nu_e(t)$ and $\nu_p(t)$, whose physics is sketched in Fig. 2.10, reads (see [50] for the full derivation and more comprehensive discussion):

$$\begin{aligned}\dot{\nu}_e = &- \Gamma_e \nu_e - W^{ep}\nu_e\left(1 + \frac{\nu_p}{\bar{\nu}_p}\right) - Z^e\nu_e - \gamma'\nu_e\left(\nu_e + |C^{(ex)}|^2\nu_p\right)\\ &+ \left(1 - \frac{\nu_e}{\bar{\nu}_e}\right)P'(t)\end{aligned} \tag{2.25a}$$

$$\dot{\nu}_p = -\varGamma_p\nu_p + W^{\mathrm{ep}}\nu_e\left(1 + \frac{\nu_p}{\bar{\nu}_p}\right) - \gamma'\left(\nu_e + |C^{(\mathrm{ex})}|^2\nu_p\right)|C^{(\mathrm{ex})}|^2\nu_p \tag{2.25b}$$

Note that the resulting equations are completely analogous to those describing conventional lasing [53], with the important difference that the lasing state is a polariton and thus retains an excitonic component.

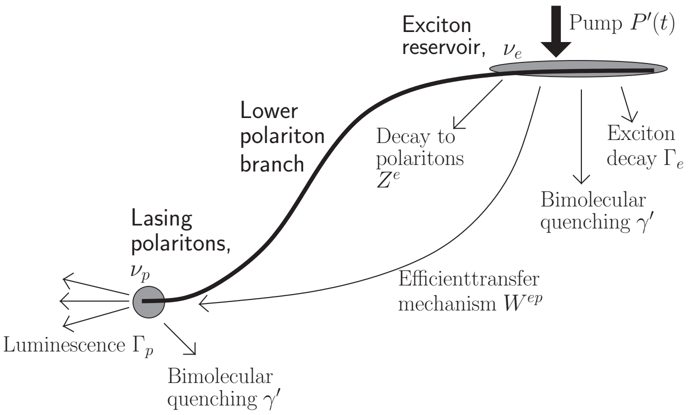

Fig. 2.10 Sketch of the LP branch and of the physical processes and scattering mechanisms included in the master equation (2.1). (Reprinted from [50], Copyright 2013, with permission from American Physical Society)

2.3.1.2 Parameters

We relate (2.25a) and (2.25b) to the experimental system in [15] using the following parameters.

Anthracene Crystal. The experimental MC embeds a crystal of anthracene with thickness $L_z = 120$ nm; the molecular density is $\rho_0 = 4.2 \times 10^{21}\mathrm{cm}^{-3}$: We ignore the monoclinic structure of the unit cell and instead estimate its linear size as $a = (\rho_0/2)^{-1/3} = 7.8 \times 10^{-8}$cm, including the presence of two molecules per unit cell. The number of layers is estimated as $N = L_z/a \approx 153$. The absorption maximum of the anthracene crystal is at energy $E_0 = 3.17$ eV. The exciton measured lifetime is of the order of $\tau_e \sim 1 - 3$ ns and in the next simulations, we take the intermediate value $\tau_e = 2$ ns. The contribution of Z^e is neglected because it can be included into τ_e without any substantial difference as long as $\tau_e < 1/Z^e$, which can be safely assumed.

MC and Polaritons. If we assume homogeneous broadening, the cavity lifetime can be estimated from the polariton linewidth at $\mathbf{k} = 0$, where it is mostly photon-like. Using this approach, we obtain a lower bound $\tau_p = 85$ fs. An exact calculation assuming perfect interfaces for the mirrors results in an upper bound $\tau_p = 1$ ps. We will estimate W^{ep} corresponding to both extrema. The Hopfield coefficients of the LP branch are [51]: $C^{(\mathrm{ph})} = 0.92$ and $C^{(\mathrm{ex})} = 0.39$.

For small $|\mathbf{k}|$, the $\mathscr{A}_0$ region has cylindrical symmetry [54–56]. Its radius, q_0, can be estimated using $E_{\mathrm{LP}}(q_0) - E_{\mathrm{LP}}(k = 0) = \Gamma_0/2$, where $\Gamma_0 = 15$ meV is the linewidth of polaritons at $\mathbf{k} = 0$ below threshold [15]; we obtain $q_0 = 2.2 \times 10^4\ \mathrm{cm}^{-1}$.

Pump. The pump density is: $P'(t) = P'_0 \exp\left[-t^2/(2\sigma_t^2)\right]$ ($\sigma_t \sim 64$ fs), with $P'_0 = P_0/(\pi r_0^2 \hbar\omega_{\mathrm{pump}})$ where $r_0 = 110$ μm is the radius of the pump spot and $\hbar\omega_{\mathrm{pump}} = 3.45$ eV is the energy of the pump photons. P_0 can be derived from the relation $E_{\text{tot}} = \int P(t)\text{d}t = \sqrt{2\pi} P_0 \sigma_t$, where E_{tot} is the experimentally measured total absorbed energy.

Bimolecular Quenching Rate. To the best of our knowledge, there are no measurements of the bimolecular quenching rate, γ', for 2D anthracene crystals. According to the standard theory for bimolecular quenching [14], $\gamma_{3\text{D}} = 8\pi RD$, where R is the Förster radius of the exciton and sets the volume around the exciton in which annihilation happens, while D is the diffusion coefficient of excitons. Measurements for 3D anthracene crystals have yielded values of [14] $\gamma_{3\text{D}} = 10^{-8}\text{cm}^3\text{s}^{-1}$ and [14, 57] $D \sim 1 - 10 \times 10^{-3}\text{cm}^2\text{s}^{-1}$. The corresponding diffusion length $\ell = (\tau_e D)^{1/2} \sim 1 - 3 \times 10^{-6}$ cm is smaller than $L_z = 1.2 \times 10^{-5}$ and suggests that excitons can be treated as diffusing in a 3D environment. As a result, we initially fix $\gamma' = \gamma_{3D}/L_z = 7 \times 10^{-4}\ \text{cm}^2\text{s}^{-1}$.

2.3.1.3 Results

Since all other parameters are known, we leave only W^{ep} as a fit parameter. We numerically integrate (2.25a) and (2.25b) and once the complete time-dependent functions $\nu_{e,p}(t)$ are known we compute the integral $\int \nu_p(\tau)\,\text{d}\tau$ and compare it with the experimental values.

In Fig. 2.11, the fits obtained for the extreme values of $\tau_p = 85$ fs and 1 ps are shown. The value of W^{ep} has been fit to the experimentally observed threshold

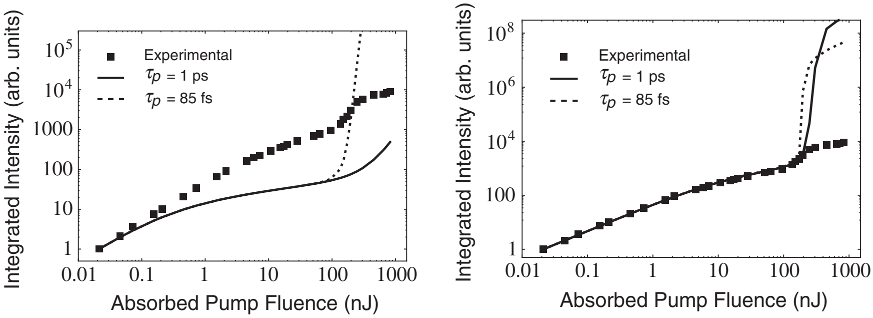

Fig. 2.11 Time-integrated surface density of polaritons $\int \nu_p(\tau)d\tau$ calculated from solution of (2.25a) and (2.25b) (*lines*) and from experimental data (*squares*). The input calculation parameters are: (i) $\tau_p = 85$ fs (*dashed line*) and (ii) $\tau_p = 1$ ps (*solid line*). (*Left*) The bimolecular quenching rate is taken from the measured 3D bulk value: $\gamma' = \gamma_{3D}/L_z$. (*Right*) The bimolecular quenching parameter γ' is used to fit the below-threshold behavior of the experimental data. The fit yields the following values for W^{ep} : $7 \times 10^5\ \text{s}^{-1}$ and $7 \times 10^5\ \text{s}^{-1}$, respectively. The fit yields the following values for γ' : $1.5 \times 10^{-5}\ \text{cm}^2\ \text{s}^{-1}$ and γ' : $1.6 \times 10^{-5}\ \text{cm}^2\ \text{s}^{-1}$, respectively. Regarding W^{ep}, the results are: $4 \times 10^5\ \text{s}^{-1}$ and $3.5 \times 10^4\ \text{s}^{-1}$, respectively. Because the experimental data is in arbitrary units, here and in the following fits the experimental data is normalized so that the first experimental and theoretical points coincide. (Reprinted from [50], Copyright 2013, with permission from American Physical Society)

value. In both cases, W^{ep} is of the order 10^5 s^{-1}. The agreement with the experiment is poor and it is apparent that the chosen value of γ' does not properly describe the transition between linear and sublinear region below threshold. Note that the exciton lifetime $\tau_e \sim 2$ ns is shorter than the reported bulk value [14] $\tau_{e,\mathrm{bulk}} \sim 10$ ns; surface interactions or defects within the layers could explain this discrepancy. In this situation, the excitonic diffusion coefficient can be smaller, resulting in a reduced possibility for excitons to pairwise annihilate.

Because a fit of γ' which determines the onset of bimolecular quenching can be readily decoupled from that of W^{ep}, both parameters are allowed to vary and the resulting fits are shown in Fig. 2.11. We obtain $\gamma' \approx 1.5 \times 10^{-5}\mathrm{cm}^2\mathrm{s}^{-1}$ independently of τ_p, as expected. Note that this value is two orders of magnitude smaller than $\gamma_{3\mathrm{D}}/L_z$. The resulting values for W^{ep} are $4 \times 10^5\,\mathrm{s}^{-1}$ and $3.5 \times 10^4\,\mathrm{s}^{-1}$ for $\tau_p = 85$ fs and 1 ps, respectively. Even if the scattering process acts on a sensibly longer timescale compared to the exciton and polariton lifetimes, it can lead to observable effects in presence of high excitonic densities. We can roughly estimate the surface density of excitons at threshold via $\Gamma_p \nu_p = W^{\mathrm{ep}} \nu_e (1 + \nu_p/\bar{\nu}_p)$. Assuming that at threshold $\nu_p = \bar{\nu}_p$, we obtain:

$$\frac{\nu_{e,\mathrm{th}}}{\bar{\nu}_e} = \frac{\bar{\nu}_p}{\bar{\nu}_e} \frac{\Gamma_p}{2\,W^{ep}} \sim 0.01 \tag{2.26}$$

The density of excitations is thus extremely high, though not unrealistic. Moreover, this is consistent with what shown in Fig. 2.12, where at threshold, the peak exciton value is of few percents. Note that $\nu_{e,\mathrm{th}}/\bar{\nu}_e$ does not depend on the value of q_0, because both W^{ep} and $\bar{\nu}_p$ depend linearly on the size of the $\mathscr{A}_0$ region.

Note that even if the two fits yield very different values for W^{ep}, the fit is not ill-conditioned. The fit of the below-threshold region depends only on two parameters, $\tau_p W^{\mathrm{ep}}$ and γ' . It is our ignorance of τ_p, whose value can vary by more than one order of magnitude and still be compatible with the measurements, which propagates an uncertainty of one order of magnitude on W^{ep}. In Sect. 2.3.2, we show a simple analytical model which corroborates this picture.

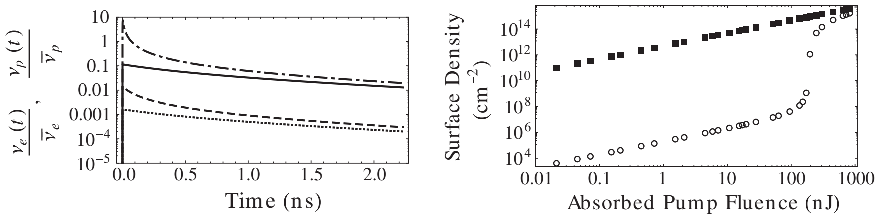

Fig. 2.12 (*Left*) Time dependence of the normalized surface density of excitons $\nu_e(t)/\bar{\nu}_e$ and of polaritons $\nu_p(t)/\bar{\nu}_p$ below threshold (≈ 0.047, *dotted line* and *solid line,* respectively) and at threshold ($E_{\mathrm{tot}} = 150\,\mathrm{nJ}$, *dashed line* and *dashed-dotted line*) plotted for $^{-1}$ fs. Note that this time dependence is in good agreement with that reported in [15]. (*Right*) Maximal population density of excitons $\max_t \nu_e(t)$ (*squares*) and of lasing photons $\max_t \nu_p(t)$ (*circles*). See Fig. 2.11 for the parameters; $\tau_p = 85$ fs (Reprinted from [50], Copyright 2013, with permission from American Physical Society)

Although the fit below threshold is excellent, the region above threshold is poorly described. It can be seen in Fig. 2.12, which shows the time dependence and peak of the normalized surface exciton and polariton densities, that at threshold, the exciton density reaches a few percent of the total molecular density. Such high excitation densities may require a more refined description of the annihilation process. Indeed, our calculation above threshold seems to be in better agreement with recent low-temperature data, where the threshold occurs at lower excitation density [45]. Moreover, above threshold, when the polariton density becomes important, the details of the theoretical model used for the polariton–polariton bimolecular quenching become important [58–60]. Note that the mean-field polariton–polariton interaction [61] has not been included.

2.3.2 Analytical Model Below Threshold

We present an analytical solution of (2.25a) and (2.25b) for the pump regime below threshold. For simplicity, we assume that the pumping process happens at a timescale faster than the polariton dynamics, so that at time $t = 0$, there is an exciton density:

$$\nu_e(t=0) = \int_0^\infty P'(\tau)\,\mathrm{d}\tau \doteq \nu_{e0}. \tag{2.27}$$

We thus consider the following master equation:

$$\dot{\nu}_e = -\Gamma_e \nu_e - W^{ep}\nu_e - Z^e\nu_e - \gamma'\nu_e\nu_e;\;\; \nu_e(t=0) = \nu_{e0}; \tag{2.28a}$$

$$\dot{\nu}_p = -\Gamma_p \nu_p + W^{ep}\nu_e;\;\; \nu_p(t=0) = 0. \tag{2.28b}$$

Because the density of polaritons is much smaller than the density of excitons we can exclude the polariton contribution to bimolecular quenching. Moreover, the whole bimolecular quenching in (2.28b) has been neglected because $\Gamma_p \gg \gamma'|C^{(\mathrm{ex})}|^2\nu_e(t)\,\forall t$. Indeed, for it to be relevant, the 2D density of reservoir excitons should be larger than $\Gamma_p/(\gamma'|C^{(\mathrm{ex})}|^2) \sim 4\times 10^{17}\mathrm{cm}^{-2}$, which is unrealistic (see for example Fig. 2.12).

The solution of (2.28a) is:

$$\nu_e(t) = \nu_{e0} e^{-(\Gamma_e + W^{ep} + Z^e)t}\left[1 + \gamma'\nu_{e0}\frac{1 - e^{-(\Gamma_e + W^{ep} + Z^e)t}}{\Gamma_e + W^{ep} + Z^e}\right]^{-1}. \tag{2.29}$$

The integrated polariton PL, which is fitted in Fig. 2.11, is:

$$\int_0^\infty \nu_p(\tau)\mathrm{d}\tau = -\frac{\nu_p(\tau)}{\Gamma_p}\bigg|_0^\infty + \frac{W^{ep}}{\Gamma_p}\int_0^\infty \nu_e(\tau)\mathrm{d}\tau = \frac{W^{ep}}{\Gamma_p\gamma'}\log\left[1 + \frac{\gamma'\nu_{e0}}{\Gamma_e + W^{\mathrm{ep}} + Z^e}\right]$$

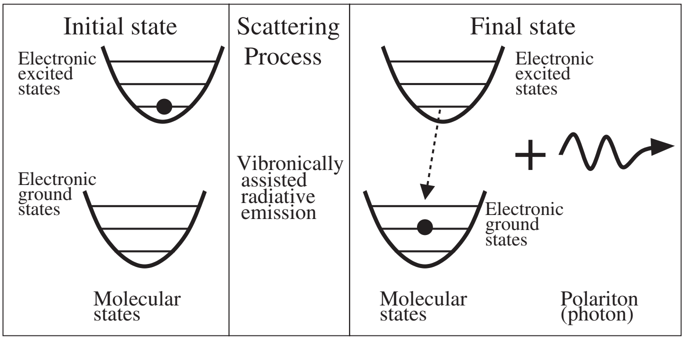

Fig. 2.13 Sketch of the radiative microscopic mechanism responsible for the efficient excitation transfer in the Franck–Condon approximation. (Reprinted from [50], Copyright 2013, with permission from American Physical Society)

Let us now observe that in our system $\Gamma_e \gg W^{\mathrm{ep}}, Z^e$ and that the experimental data are proportional to $\int \nu_p \mathrm{d}\tau$ via an unknown constant, which in the fits in Sect. 2.3.1 is chosen so that the experimental and theoretical points for the lowest pump fluence coincide. This makes the fit of the below-threshold region dependent only on γ' and independent on W^{ep} and τ_p.

2.3.3 *The Scattering Mechanism*

In this section, we focus on the microscopic origin of the excitation transfer of Sect. 2.3.1 and propose as the relevant scattering mechanism the radiative recombination of a molecular exciton assisted by the emission of a vibrational quantum of the electronic ground state. We show that the resulting scattering rate is in good agreement with that obtained in the previous section; we also consider an alternative and possibly coexisting model based on the non-radiative emission of an optical phonon [62].

2.3.3.1 Radiative Transition

The absorption and PL spectra of anthracene show several vibronic resonances [63]. The resonances observed in absorption correspond to the molecular vibrations of the first electronically excited state, and those in PL to the vibrations of the electronic ground state [14]. Strong light-matter coupling has only been demonstrated for the former [64], since the fraction of vibrationally excited ground-state molecules is negligible at room temperature. However, as shown schematically in Fig. 2.13, the transitions responsible for the vibronic structure in PL result in the scattering of excitons to lower energy polaritons, where the missing energy exactly corresponds to that of the vibrational quantum, $E_{01} \sim 173\,\text{meV}$ [49]. In [50] we discuss the approximations needed to apply the known microscopic theory [49, 55] to the present system [51] and refer to such reference for a more comprehensive analysis, whose main ideas are here only sketched.

We develop a microscopic expression for the scattering rate W^{jk} from one molecular exciton (labeled by j) to a lasing polariton (labeled by k) which involves the parameters of an anthracene MC [50]:

$$W^{jk} \approx \frac{V_1^2}{\hbar} \frac{\pi^2 S |C^{(\text{ph})}|^2}{2} \frac{1}{MN} \delta(E_0 - E_{\text{LP}}(\mathbf{k}) - E_{01}) \tag{2.30}$$

V_1 is the strength of the light–matter coupling as extracted from a simple coupled-harmonic-oscillators model [51]; S is the Huang-Rhys parameter, which is approximately ~1 [65]. M is the number of unit cells in the 2D quantization surface and N is the number of anthracene monolayers. E_0 is the energy of the ER, E_{01} the energy of the vibronic quantum, and $E_{\text{LP}}(\mathbf{k})$ the dispersion relation of the LP branch.

Working in the energy space and defining the spectral region of lasing polaritons $E \in [E_{\text{inf}}^{\mathscr{A}_0}, E_{\text{sup}}^{\mathscr{A}_0}]$ and the polariton DOS $D(E)$, we get:

$$W^{ep} = \int_{E_{\text{inf}}^{\mathscr{A}_0}}^{E_{\text{sup}}^{\mathscr{A}_0}} \frac{V_{1\pm}^2}{\hbar} \frac{\pi^2 S |C^{(\text{ph})}|^2}{2MN} f(E_0 - E - E_{01}) D(E) \mathrm{d}E; \tag{2.31}$$

where the delta function $\delta(E)$ has been substituted by the normalized lineshape of the (0–1) PL, dubbed here $f(E)$. The 2D density of state is

$$D(E) = \frac{mMa^2}{2\pi\hbar^2} \theta[E - E_{\text{LP}}(\mathbf{k} = 0)],$$

where the effective mass m can be obtained from the fits of the dispersion relations: $m \sim 1.7 \times 10^{-5} m_e$; moreover $\bar{\nu}_e = 2N/a^2$. The normalized linewidth of (0–1) PL $f(E)$ is a Lorentzian centered in zero with FWHM $\Gamma = 100\,\text{meV}$; we also assume $E_{\text{inf}}^{\mathscr{A}_0} = E_0 - E_{01} = E_{\text{LP}}(\mathbf{k} = 0)$, whereas $E_{\text{sup}}^{\mathscr{A}_0} = E_{\text{inf}}^{\mathscr{A}_0} + 7.5\,\text{meV}$ (see Sect. 2.3.1). We obtain:

$$W^{\text{ep}} = \frac{\pi S |C^{(\text{ph})}|^2}{2} \frac{m V_1^2}{\bar{\nu}_e \hbar^3} \int_{E_{\text{inf}}^{\mathscr{A}_0}}^{E_{\text{sup}}^{\mathscr{A}_0}} f(E_{\text{inf}}^{\mathscr{A}_0} - E) \mathrm{d}E. \tag{2.32}$$

The rate before the integral is equal to $\approx 1.0 \times 10^7 \text{s}^{-1}$, while the contribution from the integral, which comes from the lineshape, is ≈ 0.047. Thus, the theoretical microscopic mechanism is $W^{ep} \approx 5 \times 10^5 \text{s}^{-1}$.

Because the theoretical model neglects effects which can possibly lower the efficiency of the resonant scattering, we consider our estimate to be in good agreement with the values estimated from data in Sect. 2.3.1.

2.3.3.2 Non-radiative Transition

We now consider an alternative and possibly coexisting relaxation channel, which is non-radiative [62]. An exciton is scattered from the reservoir to one polariton state by the emission of a molecular vibration of the electronic excited state. This is due to the intramolecular exciton–phonon coupling [4, 66] which has been demonstrated to play a key role in the modeling of the PL of J-aggregates MCs [26, 38] (see also Sect. 2.2.2).

Note that in this case, the considered phonon belongs to the electronic excited state, whereas in the radiative case, it was related to the electronic ground state. Moreover, the resulting scattering element W^{ek} includes the excitonic content of the out coming polariton, whereas (2.32) is weighted by the photonic Hopfield coefficient. The scattering rate from one molecular exciton (labeled by j) to one lasing polariton (labeled by k) is given by [62]:

$$W^{jk} = \frac{2\pi}{\hbar} S E_{11}^2 \frac{|C^{(e)}|^2}{2NM} \delta(E_0 - E_{\mathrm{LP}}(\mathbf{k}) - E_{11}) \tag{2.33}$$

where $\sqrt{S} \sim 1$ is the strength of the exciton–phonon coupling [65] and E_{11} is the energy quantum of a vibration of the excited state. Even if the Franck–Condon model which we are using prescribes $E_{11} = E_{01}$, this is not necessarily true in general. The factor $|C^{(\mathrm{ex})}|^2/(2NM)$ is the Hopfield coefficient for the exciton of the molecule j relative to the polariton k [62].

The comparison of (2.33) with (2.30) for the radiative case shows that the ratio of the two processes is:

$$\frac{W^{jk}_{\mathrm{RAD}}}{W^{jk}_{\mathrm{NON-RAD}}} = \frac{\pi V_1^2}{2E_{11}^2} \cdot \frac{|C^{(\mathrm{ph})}|^2}{|C^{(\mathrm{ex})}|^2}. \tag{2.34}$$

Since both V_1 and E_{11} are of the same order of magnitude, 100 meV, the efficiency ratio mainly depends on the Hopfield coefficients of the bottom polaritons. Thus, as in our case $|C^{(\mathrm{ph})}|^2/|C^{(\mathrm{ex})}|^2 \approx 5$, we expect the radiative mechanism to be the main origin of the excitation transfer which results in lasing, even if to understand the importance of the non-radiative transfer a more detailed analysis is necessary. An experimental analysis exploring several organic crystals would thus be of the greatest interest.

2.3.4 The Effect of Temperature

Reported data for anthracene MCs show a reduction of the lasing threshold of slightly less than an order of magnitude once temperature is lowered from 300 to

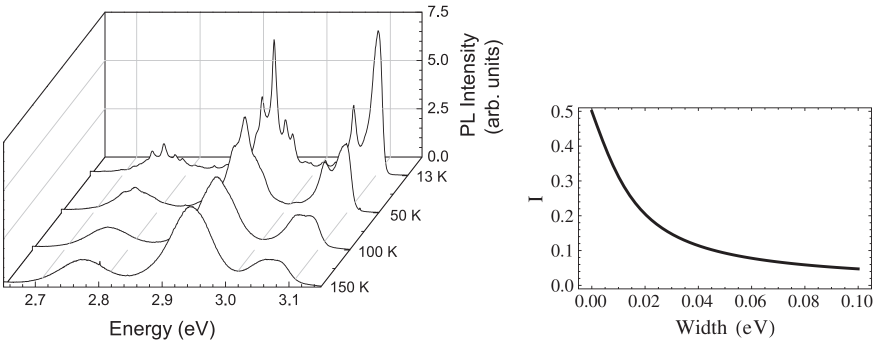

Fig. 2.14 (*Left*) PL spectra of anthracene layers for temperatures between 13 and 150 K (courtesy of S. Kéna-Cohen). (*Right*) Dependence of the integral (35) appearing in (32) on the width of *f*(*E*), which is a Lorentzian function

12 K [45]. In this section, we discuss temperature effects within the framework of the developed model and the related consequences on the lasing properties.

Experimental studies on the PL from bulk anthracene crystals have shown a strong temperature dependence characterized by considerable spectral narrowing [67]. The temperature dependence obtained using thin crystals grown from solution is shown in Fig. 2.14. Here, the crystals were grown on silicon substrates to ensure good thermal contact to the cryostat cold finger and were excited using 1 ns-long pulses at $\lambda = 337$ nm. A composite vibronic structure emerges, which can be understood in terms of a high-energy phonon (considered in this work) and of a low-energy phonon, which is not resolved at room temperature because of thermal broadening. Such a system requires the use of two-phonon states in order to exactly reproduce the spectra [68]; however, we ignore this complication because we are only interested in the phenomenological properties of the line which is responsible for lasing.

The scattering rate W^{ep} in (2.32) depends on temperature via $f(E)$. On the one hand, at low temperature, the Lorentzian is narrower, and thus a smaller fraction of the OS is dispersed into non-lasing modes. On the other hand, only a fraction of the OS of the (0–1) transition contributes to lasing, because the other lines are far detuned. Additionally, both the quantum yield, estimated at room temperature to be 0.5, and the exciton lifetime τ_e are expected to increase at low temperature.

In Fig. 2.14, we compute the dependence of the integral appearing in (2.32):

$$I \doteq \int_{E_{\mathrm{inf}}^{\mathscr{A}_0}}^{E_{\mathrm{sup}}^{\mathscr{A}_0}} f(E_{\mathrm{inf}}^{\mathscr{A}_0} - E)\,\mathrm{d}E \tag{2.35}$$

on the width of the Lorentzian function *f*(*E*) which represents the normalized spectrum of the (0–1) PL emission. Whereas at room temperature, the FWHM is ≈0.1 eV, at 12 K, it is $\sim 0.01 - 0.02$ eV, and thus W^{ep} increases of at least a factor of 5.

Roughly speaking, the observed thermal reduction of the threshold is of less than one order of magnitude [45], and thus similar to the numbers of our estimates. This points out a possible connection between the temperature dependence of the laser threshold and of the PL of anthracene crystals. A more systematic analysis, both theoretical and experimental, goes beyond the scope of this work and will be the focus of future investigations. As long as the thermal linewidth narrowing is considered, we observe that when the radiative transition is not perfectly resonant with the lasing , it could even result in the opposite effect.

For the sake of completeness, in [50], we also include the thermal population of the vibrations of the molecular ground state in the master (2.25a) and demonstrate that it can be safely neglected.

Concluding, we have presented a minimal model to describe the polariton lasing physics observed in crystalline anthracene MCs. Only the essential features of the physical processes involved have been included: The incoherently pumped ER, the vibronically assisted radiative scattering from the reservoir to the bottom of the LP branch, the onset of bosonic stimulation and the buildup of the polariton population with increasing pump intensity, the polariton losses through the mirrors, and bimolecular quenching processes. All the relevant material parameters, except from the bimolecular quenching rate, have been determined independently from the experimental data on the pump dependence of the polariton emission. In particular, the efficiency of the scattering mechanism here considered—which takes into account the prominent role of vibronic replicas in the photophysics of anthracene MCs—has been calculated microscopically. The numerical simulations obtained are in good agreement with the data and describe well the onset of the nonlinear threshold for polariton lasing.

Acknowledgements We would like to thank for many insightful discussions V.M. Agranovich, S. Kéna-Cohen, D. Lidzey, R. Mahrt, L. Silvestri. We acknowledge financial support from the European FP7 ICARUS program (Grant Agreement No. 237900), the Regione Toscana POR FSE 2007-2013, and the Deutsche Forschungsgemeinschaft.

References

1. M.S. Skolnick, T.A. Fisher, D.M. Whittaker, Semicond. Sci. Technol. **13**, 645 (1998)
2. A. Kavokin, J.J. Baumberg, G. Malpuech, F.P. Laussy, *Microcavities* (Oxford University Press, Oxford, 2007)
3. I. Carusotto, C. Ciuti, Rev. Mod. Phys. **85**, 299 (2013)
4. V.M. Agranovich, *Excitations in Organic Solids* (Oxford University Press, Oxford, 2009)
5. F. Bassani, G.P. Parravicini, *Electronic States and Optical Transitions in Solids* (Pergamon Press, Oxford, 1975)
6. M. Born, K. Huang, *Dynamical Theory of Crystal Lattices* (Oxford University Press, Oxford, 1954)
7. C. Weisbuch, M. Nishioka, A. Ishikawa, Y. Arakawa, Phys. Rev. Lett. **69**, 3314 (1992)
8. J. Kasprzak, M. Richard, S. Kundermann, A. Baas, P. Jeambrun, J.M.J. Keeling, F.M. Marchetti, M.H. Szymańska, R. André, J.L. Staehli, V. Savona, P.B. Littlewood, B. Deveaud, L.S. Dang, Nature **443**, 409 (2006)

9. V.M. Agranovich, H. Benisty, C. Weisbuch, Solid State Commun. **102**, 631 (1997)
10. D.G. Lidzey, D.D.C. Bradley, M.S. Skolnick, T. Virgili, S. Walker, D.M. Whittaker, Nature (London) **395**, 53 (1998)
11. R.F. Oulton, N. Takada, J. Koe, P.N. Stavrinou, D.C.C. Bradley, Semicond. Sci. Technol. **18**, S419 (2003)
12. D.G. Lidzey, in *Electronic Excitations in Organic Based Nanostructures*, ed. by V.M. Agranovich, F. Bassani (Elsevier, Amsterdam, 2003), p. 355
13. V.M. Agranovich, Y.N. Gartstein, M. Litinskaya, Chem. Rev. **111**, 5179 (2011)
14. M. Pope, C.E. Swenberg, *Electronic Processes in Organic Crystals and Polymers* (Oxford University Press, Oxford, 1999)
15. S. Kéna-Cohen, S. Forrest, Nat. Photonics **4**, 371 (2010)
16. J.D. Plumhof, T. Stoferle, L. Mai, U. Scherf, R.F. Mahrt, Nat. Mater. **13**, 247 (2014)
17. K.S. Daskalakis, S.A. Maier, R. Murray, S. Kéna-Cohen, Nat. Mater. **13**, 272 (2014)
18. R.J. Holmes, S. Kéna-Cohen, V.M. Menon, S.R. Forrest, Phys. Rev. B **74**, 235211 (2006)
19. J. Wenus, R. Parashkov, S. Ceccarelli, A. Brehier, J.S. Lauret, M.S. Skolnick, E. Deleporte, D.G. Lidzey, Phys. Rev. B **74**, 235212 (2006)
20. D.G. Lidzey, D.D.C. Bradley, A. Armitage, M.S. Skolnick, Science **288**, 1620 (2000)
21. P. Schouwink, H.V. Berlepsch, L. Dähne, R.F. Mahrt, Chem. Phys. Lett. **344**, 352 (2001)
22. S. Ceccarelli, J. Wenus, M.S. Skolnick, D.G. Lidzey, Superlattices Microstruct. **41**, 289 (2007)
23. T. Kobayashi (ed.), *J-Aggregates*, (World Scientific, Singapore, 1996)
24. P. Michetti, G.C. La Rocca, Phys. Rev. B **71**, 115320 (2005)
25. P. Michetti, G.C. La Rocca, Phys. Rev. B **77**, 195301 (2008)
26. D.M. Coles, P. Michetti, C. Clark, W.C. Tsoi, A.M. Adawi, J.-S. Kim, D.G. Lidzey, Adv. Func. Mat. **21**, 3691 (2011)
27. M.D. Fayer, in *Spectroscopy and Excitation Dynamics of Condensed Molecular Systems*, ed. by V.M. Agranovich, R.M. Hochstrasser, (North-Holland, NY, 1983) p. 185
28. V.M. Agranovich, M. Litinskaia, D.G. Lidzey, Phys. Rev. B **67**, 85311 (2003)
29. V.M. Agranovich, G.C. La Rocca, Solid State Commun. **135**, 544 (2005)
30. M. Litinskaya, P. Reineker, Phys. Rev. B **74**, 165320 (2006)
31. V.M. Agranovich, Y.N. Gartstein, Phys. Rev. B **75**, 75302 (2007)
32. P. Michetti, G.C. La Rocca, Physica E **40**, 1926 (2008)
33. D.G. Lidzey, D.D.C. Bradley, T. Virgili, A. Armitage, M.S. Skolnick, S. Walker, Phys. Rev. Lett. **82**, 3316 (1999)
34. P. Michetti, G.C. La Rocca, Phys. Status Solidi B **245**, 1055 (2008)
35. M. Bednarz, V.A. Malyshev, J. Knoester, J. Chem. Phys. **117**, 6200 (2002)
36. M. Bednarz, V.A. Malyshev, J. Knoester, Phys. Rev. Lett. **91**, 217401 (2003)
37. D.J. Heijs, V.A. Malyshev, J. Knoester, Phys. Rev. Lett. **95**, 177402 (2005)
38. P. Michetti, G.C. La Rocca, Phys. Rev. B **79**, 035325 (2009)
39. G.M. Akselrod, E.R. Young, M.S. Bradley, V. Bulovic, Opt. Expr. **21**, 12122 (2013)
40. P. Michetti, G.C. La Rocca, Phys. Status Solidi C **6**, 403 (2009)
41. D.M. Coles, N. Somaschi, P. Michetti, C. Clark, P.G. Lagoudakis, P.G. Savvidis, D.G. Lidzey, Nat. Mater. (2014). doi:10.1038/nmat3950
42. D.M. Coles, P. Michetti, C. Clark, A.M. Adawi, D.G. Lidzey, Phys. Rev. B **84**, 205214 (2011)
43. T. Virgili, D. Coles, A.M. Adawi, C. Clark, P. Michetti, S.K. Rajendran, D. Brida, D. Polli, G. Cerullo, D.G. Lidzey, Phys. Rev. B **24**, 245309 (2011)
44. D.M. Coles, R.T. Grant, D.G. Lidzey, C. Clark, P.G. Lagoudakis, Phys. Rev. B **88**, 121303 (2013)
45. M. Slootsky, Y. Zhang, S.R. Forrest, Phys. Rev. B **86**, 045312 (2012)
46. J.A. Ćwik, S. Reja, P.B. Littlewood, J. Keeling, Europhys. Lett. **105**, 47009 (2014)
47. P. Lagoudakis, Nature Mat. **13**, 227 (2014)
48. L. Fontanesi, L. Mazza, G.C. La Rocca, Phys. Rev. B **80**, 235313 (2009)
49. L. Mazza, L. Fontanesi, G.C. La Rocca, Phys. Rev. B **80**, 235314 (2009)

50. L. Mazza, S. Kéna-Cohen, P. Michetti, G.C. La Rocca, Phys. Rev. B **88**, 075321 (2013)
51. S. Kéna-Cohen, M. Davanço, S.R. Forrest, Phys. Rev. Lett. **101**, 116401 (2008)
52. S. Kéna-Cohen, Ph.D. thesis, Princeton University, 2010
53. A.E. Siegman, *Lasers* (University Science Books, Mill Valley, 1986)
54. M. Litinskaya, P. Reineker, V.M. Agranovich, Phys. Stat. Solidi A **201**, 646 (2004)
55. H. Zoubi, G.C. La Rocca, Phys. Rev. B **71**, 235316 (2005)
56. S. Kéna-Cohen, M. Davanço, S.R. Forrest, Phys. Rev. B **78**, 153102 (2008)
57. R.C. Powell, Z.G. Soos, J. Lumin. **11**, 1 (1975)
58. G.M. Akselrod, Y.R. Tischler, E.R. Young, D.G. Nocera, V. Bulovic, Phys. Rev. B **82**, 113106 (2010)
59. V.M. Agranovich, M. Litinskaya, G.C. La Rocca, D.G. Lidzey, in: *Organic Nanophotonics Nato Science Series II*, vol. 100, ed. by F. Charra, V.M. Agranovich, F. Kajzar (2003), p. 291
60. M. Litinskaya, P. Reineker, V.M. Agranovich, J. Lumin. **119**, 277 (2006)
61. H. Zoubi, G.C. La Rocca, Phys. Rev. B **72**, 125306 (2005)
62. M. Litinskaya, P. Reineker, V.M. Agranovich, J. Lumin. **110**, 364 (2004)
63. G.C. Morris, M.G. Sceats, Chem. Phys. **3**, 164 (1973)
64. R.J. Holmes, S.R. Forrest, Phys. Rev. Lett. **93**, 186404 (2004)
65. T.-S. Ahn, A.M. Müller, R.O. Al-Kaysi, F.C. Spano, J.E. Norton, D. Beljonne, J.-L. Brédas, C.J. Bardeen, J. Chem. Phys. **128**, 054505 (2008)
66. M. Hoffmann, Z.G. Soos, Phys. Rev. B **66**, 024305 (2002)
67. L.E. Lyons, L.J. Warren, Aust. J. Chem. **25**, 1411 (1972)
68. L. Silvestri, S. Tavazzi, P. Spearman, L. Raimondo, F.C. Spano, J. Chem. Phys. **160**, 234701 (2009)

Chapter 3
Crystalline Organic Materials Toward Laser Application

Zengqi Xie, Linlin Liu and Yuguang Ma

Abstract Although optically pumped organic laser has been observed and investigated intensively in the past few decades, realization of electrically pumped organic laser is still a great challenge. Toward this challenge, efforts from both material science and device engineering research fields have been and will be made by scientists. In this chapter, the relationship between molecular stacking and optoelectronic properties in crystalline organic materials is discussed in detail first. Based on the deep understanding of the structure-property relationship, the recent progresses on highly efficient electroluminescent (EL) materials and light-emitting field-effect transistors are reviewed respectively. At last, a perspective is given on further development of organic materials and devices for laser application.

3.1 Introduction

The history of organic lasers is almost as long as that of lasers since the discovery of liquid dye lasers based on highly luminescent π-conjugated molecules (dyes) as early as in the mid-sixties [1]. The liquid dye lasers are still popular sources of tunable visible radiation nowadays, but suffered from the cumbersome designs and the inconvenience of toxic solvents [2]. With the quick development of organic light-emitting diodes (OLEDs) based on organic semiconductors, the development of organic solid-state lasers was accelerated [3–5]. Conjugated organic molecules are intrinsically four-level systems; that is, the excited state S_1 and the ground state S_0 are both coupled to a multitude of vibronic states. This four-level system guarantees low-threshold lasing since no minimum pump power is required to

---

Z. Xie · L. Liu · Y. Ma (✉)
Institute of Polymer Optoelectronic Materials and Devices, State Key Laboratory of Luminescent Materials and Devices, South China University of Technology,
510640 Guangzhou, People's Republic of China
e-mail: ygma@scut.edu.cn

Y.S. Zhao (ed.), *Organic Nanophotonics*, Nano-Optics and Nanophotonics,
DOI 10.1007/978-3-662-45082-6_3

achieve population inversion. Very low thresholds could be demonstrated in thin-film based on organic semiconductors; furthermore, the devices turned out to be easy to handle and compact, while keeping all the advantages of organic materials.

Although people already observed optically pumped lasers in various organic systems including small molecular crystals and polymeric films [6–10], there is still no demonstration of electrically pumped organic laser, or "organic laser diode (OLD)." This becomes an important breakthrough worth to be targeted, potentially opening the way to a new class of extremely compact, tunable, cheap, and flexible laser. The challenges to realize direct electrical pumping of a laser device are numerous and complex. Lasing behavior requires net gain, i.e., light amplification surpassing all kinds of losses due to both the material itself and the environment. Because π-conjugated systems have short excited-state lifetime (a few ns), then a high exciton recombination rate will be required to run a laser. Thus, firstly, a material with high photoluminescence efficiency can reduce the "inner" exciton energy loss through non-radiation processes; secondly, an ambipolar transporting material with high mobility can increase the exciton formation.

Compared with optically pumped lasers, it makes clear that electrical driving brings extra-losses, due to the presence of metallic electrodes, and also because of absorption and quenching attributed to charge carriers and triplet excitons [7]. The presence of triplet excitons toward OLDs is the most difficult to overcome. Triplets are more abundant than singlet excitons under electrical excitation: firstly because of the 3:1 unfavorable creation probability ratio, and secondly because their much longer lifetime (~ms) makes them pile up. Triplets cause issues because they will absorb laser photons (meaning increased cavity loss) and because they will quench singlets through a Förster-type non-radiative dipole–dipole interaction referred to as singlet–triplet annihilation. In addition, the electrodes used for electrical injection are problematic. The lowest thresholds in optically pumped devices have been obtained with waveguide lasers, because they enable a long interaction with the gain medium, are consequently a natural design choice for a future OLD. However, the guided mode leaks outside the high-index active part and overlaps with the absorbing metallic electrodes, a feature which is amplified by the fact that all organic films tend to have similar indices of refraction, not helping optical confinement. As a result, the threshold is greatly increased.

The mobilities of amorphous organic semiconductors are in the range of 10^{-5}–10^{-2} cm^2 V^{-1} s^{-1}, which means that achieving a high current flow will mobilize a high number of polarons that may absorb lasing photons. A low mobility also means a high resistivity, so that electrodes must be set close to each other to provide a high electric field. So both the polaron and electrode issues are in fact directly related to the low mobility of organic semiconductors. To overcome the mobility problem, organic single crystals indeed become one of the most promising materials since the highly ordered molecular stacking makes the charge transport much easier; also from the device view, organic light-emitting field-effect transistor (OLEFET) is a promising laser architecture, which shows potential for solving the electrode and the polaron problems simultaneously. The field-effect mobility is higher than the bulk mobility, so that higher current densities can be obtained. This device configuration also makes it possible to position the emission zone far away from the metallic contacts. Thus, OLEFET based on high-luminescent single crystals might be one of the most possible approaches for the realization of electrically pumped lasers.

This chapter is structured as follows. In Sect. 3.2, we briefly introduce the approach to achieve high-luminescent crystalline materials. Section 3.3 will be devoted to summarize the high-mobility crystalline materials. The most recent progress on the next-generation materials about controlling the singlet/triplet formation in EL devices will be reviewed in Sect. 3.4. The device progress on OLEFET will be given in Sect. 3.5. At last, we will show a prospect on further design of high-performance crystalline organic material for laser application in the end of this chapter as Sect. 3.6.

3.2 High-Luminescent Crystalline Materials

3.2.1 The Relationship Between Organic Crystal Luminescence Efficiency and Molecular Stacking Modes

As is well known, there is a phenomenon called the aggregation-induced fluorescence quenching: Generally speaking, the luminescence efficiency of molecules in solution is higher than that in aggregate solid or in the film. However, aggregation-induced emission (AIE) [11] is an exception due to their special molecular structure. The luminescence efficiency of molecules in aggregation state largely depends on the molecular stacking modes in aggregation state. Usually, there are three kinds of molecular stacking modes in aggregation state, namely H-aggregate, J-aggregate, and X-aggregate. H-aggregate widely exists in most π-conjugated materials, in which molecular long axes are mutually parallel, and the molecular dipole is commonly along with the direction of molecular long axes. So the molecular dipole stacking mode in H-aggregation is mutually parallel, which is always responsible for serious fluorescence quenching in aggregation state. This is because the lowest splitting energy level is optically forbidden in mutually parallel molecular dipole stacking mode. Therefore, one method to increase luminescence efficiency of organic crystals is to modulate the molecular dipole stacking mode, such as enlarging the inter-dipole distance, forming crossed dipole stacking mode (X-aggregation), and realizing parallel dipole stacking with offset along the dipole direction, namely J-aggregation [12–14].

According to the theoretical results given by Cornil et al. [15, 16], when the distance between two parallel π-conjugated molecules in H-aggregation is small, the inter-dipole inactions will be bad for solid-state luminescence, arousing luminescence quenching. However, when the distance between two parallel π-conjugated molecules is large enough, the inter-dipole interactions will be effectively weakened. So an effective method to increase the luminescence efficiency

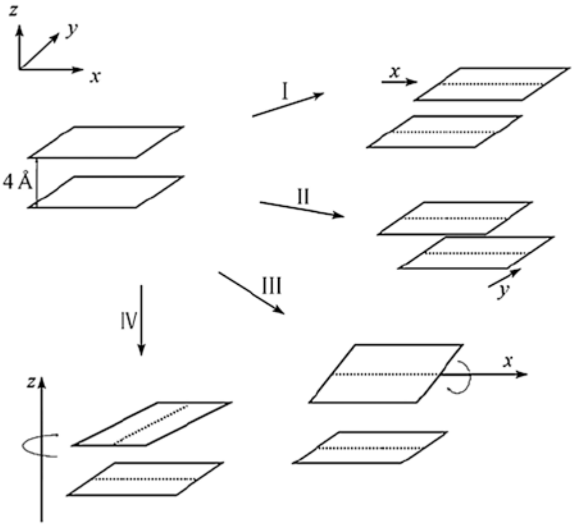

Fig. 3.1 Sketch of the operations applied to a coplanar dimer formed by two stilbene molecules separated by 4 Å when investigating the role of positional disorder. The modifications are induced by the translation of one molecule along the chain-axis direction (*I*), the translation of one molecule along the in-plane transverse axis (*II*), the rotation of one stilbene unit around its long axis (*III*), and the rotation of one stilbene molecule around the stacking axis while keeping the parallelism between the molecular planes (*IV*)

of organic crystals is to enlarge the inter-dipole distance by using bulky substituents on the chromophore or dispersing molecules in host materials. However, although the solid-state luminescence efficiency could be effectively increased by this method, the charge transportation ability of organic crystals will be decreased dramatically, which will severely limit the application of organic materials in laser. Therefore, the best way to realize high solid-state luminescence efficiency is to modulate the molecular dipole stacking mode, which will not influence the charge carrier transportation ability markedly in organic crystals.

Cornil et al. had calculated the energy splitting degree of molecular orbits in four different molecular stacking modes of stilbene, respectively. Figure 3.1 shows the molecular dimers in different moving orientation. The translation of one molecule along the chain-axis direction or in-plane transverse axis (I and II) and the rotation of one stilbene unit around its long axis (III) could not effectively decrease the inter-dipole interactions. The most effective method to weaken the inter-dipole interactions is the rotation of one stilbene molecule around the stacking axis (IV). With the increase in rotary angle, the energy splitting of the lowest excited state of the dimer decreased gradually, which makes the second excited state transit to the first excited state easily and benefit to increase luminescence efficiency. When the inter-dipole angle is increased up to 90°, the inter-dipole coupling is negligible, which means that, in such configuration, the absence of inter-dipole interaction will lead to an intense absorption with weak red shifted

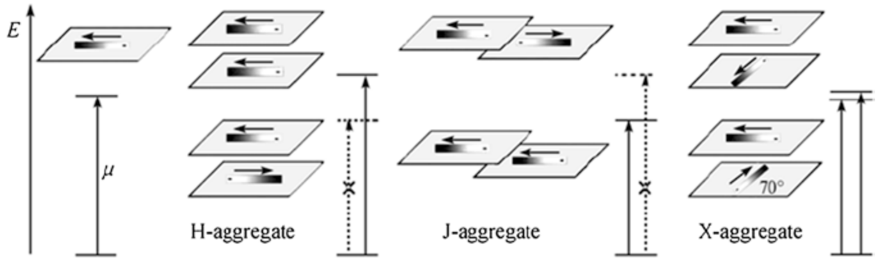

Fig. 3.2 Three basal dipole stacking modes in aggregate state

compared with the single molecule. In other words, crystal with cross-dipole stacking has similar luminescence properties to the isolated molecules in solutions, maintaining high solid-state efficiency.

In Fig. 3.1, if the distance of the translation of one molecule along its long axis direction is large enough, it is also beneficial for luminescence for the molecular dipole stacking mode turns from H-aggregate to J-aggregate. In J-aggregate, the transition dipoles are added in the same direction, and the lowest excited state induced by the inter-dipole interactions is optically allowed, which make the aggregates have very high luminescence efficiency [17, 18].

Figure 3.2 illustrates the energy splitting of the optically allowed transition of a single chain (sketched in the left) in a coplanar configuration (H-aggregate), staggered configuration (J-aggregate), and crossed configuration (cross-stacking). In the coplanar dimer (H-aggregate), the lowest excited state corresponds to the destructive combination of the transition dipole moment of the individual chains and is optically forbidden; in a staggered geometry (J-aggregate), the oscillator strength can be concentrated in the lowest excited state when one chain is translated by an adequate amount with respect to the other; in a crossed image (X-aggregate), the energy splitting can be neglected with emission properties similar to the dilute solution.

3.2.2 The Methods for High Crystalline Luminescence Efficiency

Based on the information above, it is reasonable to design high-solid-state luminescent materials through the following possible approaches. The first approach is enlarging the inter-molecular distance to make a solid solution of the chromophore for high crystal luminescence efficiency. Enlarging the inter-molecular distance could effectively weaken the interactions between adjacent excitons. There are two methods: (1) introducing bulky substituents into the chromophore [19, 20] and (2) adopting twisted molecular configurations. Actually, the method of enlarging the inter-molecular distance to realize high luminescence efficiency is similar to dispersing luminescent molecules into host materials. When the interactions of adjacent excitons are weakened, the carrier transition probability between adjacent molecules is also weakened at the same time. The contradiction in the above-mentioned system could be resolved by introducing the substituents with carrier transport functions, if that could not influence luminescence. A special class of luminescent materials with aggregation-induced emission (AIE) [11] property is ideal for high solid-state luminescence. The molecules with twisted configurations usually have very low luminescence efficiency in dilute solutions. However, the inter-molecular interactions in the solid state could restrict the luminescence quenching, and the non-planar configurations could effectively restrict the face-to-face parallel stacking (where the distance between molecules is enlarged), so the solid state will have high luminescence efficiency. In recent years, materials with AIE properties have attracted more and more attention. It is also difficult to form tight stacking between molecules due to their twisted configurations.

The second approach is constructing crossed dipole stacking (X-stacking) for high crystal luminescence efficiency. Crossed dipole stacking could effectively weaken the interactions between excitons, and it is beneficial for high solid-state luminescence efficiency. The methods to realize crossed dipole stacking include two categories: (1) forming intramolecule crossed configuration by chemical bond and (2) forming crossed stacking between adjacent molecules by inter-molecular interactions [21]. Up to now, the representative intramolecular crossed dipole systems include entirely rigid spiro molecules and partly flexible molecules [22, 23]. These crossed molecules are more suitable to fabricate amorphous thin films for the changeable molecular configures. Although intramolecular crossed dipole stacking is realized in these systems, the arrangement modes of adjacent molecules are stochastic in amorphous thin films.

The third approach is constructing staggered parallel dipole stacking (J-stacking) [24] for high crystal luminescence efficiency. In staggered parallel molecular stacking (J-stacking), especially under the instance of existing strong π–π interactions, excitons are delocalized to several molecules and the aggregate is highly emissive. The strong π–π interactions mean strong coupling between molecular π-orbits, which is beneficial for carrier transfer between molecules. Therefore, in this system, it is possible to combine high luminescence efficiency and high carrier mobility in one crystal, which is significant to fabricate high-performance electroluminescence device, especially for realizing electrically pumped laser.

3.3 High-Mobility Materials

3.3.1 The Essential Factors Influencing Mobility Properties in Organic Single Crystals

The charge transport properties of materials depend critically on the microscopic arrangement of the fundamental units within a meso- or macroscopic structure [25].

A semi-classical theory was formulated by Marcus to describe the rate of electron transfer k_{ET} [26]:

$$k_{\mathrm{ET}} = \frac{4\pi^2}{h}\frac{1}{\sqrt{4\pi k_B T\lambda}}t^2 \exp\left(-\frac{\lambda}{4k_B T}\right)$$

where T is the temperature, λ is the reorganization energy, t is the transfer integral, and h and k_{B} are the Planck and Boltzmann constants, respectively. Electron transfer is a temperature-activated process, dependent on two key material parameters: the reorganization energy (λ) and the transfer integral (t). The reorganization energy represents the degree to which a molecule relaxes upon accepting or donating an electron and is therefore explicitly a single-molecule property. The transfer integral, on the other hand, represents the degree of overlap of adjacent molecular units within the structure and is therefore a more complex function of both molecular identity and arrangement. This theoretical framework has been employed rather extensively to explore the performance of a variety of materials, with mixed success, such as polyacenes system and silole system [27, 28].

An interesting case study is that of the rubrene single crystal, which shows field-effect mobility as high as 15.4 cm^2 V^{-1} s^{-1} [29] in a novel device architecture. Compared to pentacene (Fig. 3.3a), a benchmark high-performance organic semiconductor, rubrene (Fig. 3.3b), has bulky side groups resulting in a larger offset and greater separation of the molecular units. While this implies a negative impact on performance, the calculated electronic coupling (transfer integral) of the highest occupied molecular orbital (HOMO) evolves to a maximum at the offset observed in the rubrene crystal structure. This trend is shown in Fig. 3.3c, along with that for the lowest unoccupied molecular orbital (LUMO).

3.3.2 The Modulation of Molecular Stacking Structure for High Charge Mobility

For a special molecule, single-crystal mobility performance is strongly dependent on the molecular stacking modes. Siegrist et al. [30] found that pentacene single crystals from PVT had tighter molecular stacking than those from solution, and this tight molecular stacking structure effectively improved the physical performance; that is, the field-effect mobility could be up to 3 cm^2 V^{-1} s^{-1} at room temperature. The typical "herringbone" molecular stacking modes like pentacene could not form the most effective π-orbital overlap (electronic coupling). Many synthesis chemists hope to modulate molecular stacking modes by the change of molecular structures to form face-to-face molecular stacking for example, when large substituents were introduced into the side of pentacene, which could restrain the formation of herringbone structures, and parallel molecular stacking modes beneficial for inter-molecular electronic coupling could be obtained [31–33].

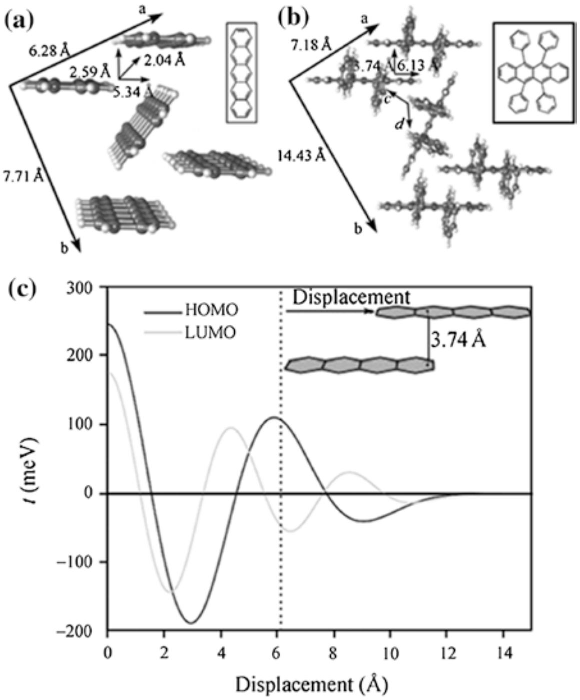

Fig. 3.3 **a** Crystal structures of pentacene; **b** crystal structures of rubrene; **c** evolution of electronic coupling of the core tetracene units of rubrene as a function of displacement at the intermolecular spacing seen in the crystal arrangement

3.3.3 *Anisotropy of Charge Mobility in Organic Single Crystal*

Compared with the amorphous thin films, the crystals have the anisotropic characteristic of the charge carrier mobility, which is determined by the highly structural order of molecular arrangement in crystals. The signatures of this intrinsic transport are the anisotropy of the carrier mobility, μ [34]. Most of organic crystals grown from physical vapor transport are shaped as elongated “needles” or thin platelets, which may be determined by the anisotropy of inter-molecular interaction in crystals. The direction of the most π-orbital overlap between molecules is the same with that of the biggest crystal dimension, also the direction with the highest mobility. In the experiment of rubrene single-crystal field-effect mobility by two-probe measurements, the mobility along *b*-axis direction was higher than that along *a*-axis direction in rubrene crystal structure. The reason is that the extent to which π–π overlaps along *b*-axis direction was stronger than that along *a*-axis direction which was more beneficial for the carrier transport [35].

3.4 Electroluminescent (EL) Materials Beyond Exciton Statistics

Exciton statistics is a physical principle based on the statistics of spin multiplicity [36]. In electroluminescence, injected electrons and holes have randomized spin states; the formation of the ratio of singlet or triplet excitons is usually 1:3 according to the four spin-dependent states. Exciton statistics determines that the upper limit of internal quantum efficiency is 25 % in fluorescent devices, since only singlet exciton can decay radiatively. However, both experimental and theoretical evidence indicate that the actual efficiency can exceed the exciton statistics limit of 25 % by utilizing materials with special electronic structure and optimized device structures. These results bring light to break through the exciton statistics limit and develop new fluorescent materials for the OLEDs.

Organic EL contains several complex physical processes, including the carrier injection and recombination, the formation of weakly bound polaron, the transformation from weakly bound polaron to strongly bound Frenkel excitons, and radiative decay of Frenkel excitons. All the above processes are likely to change the prediction of the exciton statistics. As a result, many researchers concentrated on developing new materials and device structures, for the purpose of breakthrough in the exciton statistics. Up to now, important progress has been made in this field, for instance, the fluorescent materials breaking the exciton statistics limit (25 %), the delayed fluorescent materials via the reverse inter-system crossing (RISC) from triplet to singlet, and the "hot exciton" materials based on the hybridized local and charge-transfer (HLCT) state developed by Chinese scientists.

In 1999, Cao and Heeger found that the formation ratio of singlet state (χ_S) excitons can reach up to 50 % in some fluorescent conjugated polymers. It was the first report for $\chi_S > 25$ % in fluorescent OLEDs, having important scientific significance and the practical value [37]. In the next few years, the exciton statistics became a research hotspot in the field of organic electronics. In 2000, Friend et al. also observed that the χ_S of conjugated polymers reached 35–45 % [38]. On the basis of the experimental results by Cao and Friend, Shuai and Brédas proposed that the inter-chain charge-transfer (CT) state in polymer solid film may be the transition state for the exciton formation process [39]. Their theoretical analysis showed that CT state was spin selective and could change the ratio of S/T. In fact, the determination of χ_S is a complicate process, since many factors have significant influence on that, including the qualities of the materials and the optimization for the device efficiency. Indeed, the mechanism is not clear yet, and the structure property relationship is still ambiguous up to now.

Conversion of T excitons to S excitons through RISC was another approach to enhancing the χ_S. Initially, RISC was based on the traditional exciton statistics, and as a follow-up process, a large proportion of T_1 excitons could be converted

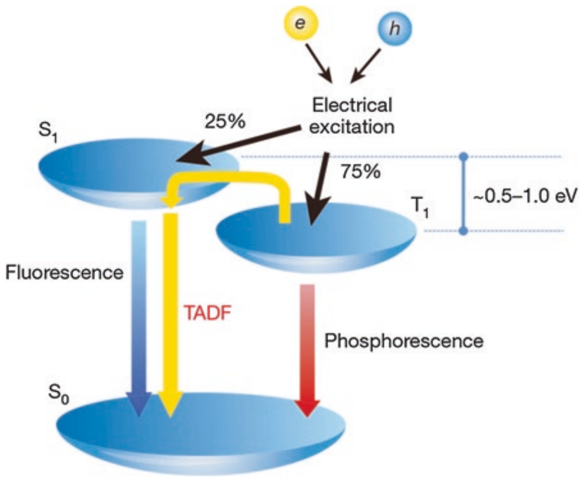

Fig. 3.4 Energy diagram of the TADF mechanism. Reprinted with permission from [40]. Copyright 2012, rights managed by Nature Publishing Group

into the radiative S_1 excitons through RISC, leading to an enhanced S. Triplet–triplet annihilation (TTA) and thermally activated delayed fluorescence (TADF) are the two major methods that were used to achieve the efficient RISC. Because the materials based on above mechanisms typically exhibit long fluorescent lifetime, they are also called delayed fluorescence materials. Generally, TADF molecules possess a much smaller energy gap between S_1 and T_1, which allows the conversion of T_1 excitons into the radiative S_1 excitons through the thermally activated RISC, leading to the increased χ_S. Different from the traditional fluorescent materials, TADF materials typically show a positive correlation between the fluorescent efficiency and the temperature. Since the RISC rate (~10^6 s^{-1}) is usually lower than the radiative rate (~10^9 s^{-1}), the thermally activated RISC is a long lifetime process, resulting in an inefficient conversion from T_1 to S_1.

The concepts in designing TADF materials can be summarized as follows: (i) achieving small S_1 and T_1 energy gaps through well-separated electron and hole wave functions of CT materials, which is favorable in realizing TADF under thermal activation; (ii) employing crowded D-A units to increase the overlap of electron and hole wave functions and structural rigidity (suppressing the non-radiative transitions), which can accordingly enhance the radiation efficiency (Fig. 3.4). According to this rule, Adachi et al. designed a strong intramolecular CT system, which greatly reduced the energy gap between T_1 and S_1. As a result, the intramolecular CT promoted the RISC process and further increased the χ_S (>90 %) [40–42].

TTA (Fig. 3.5), as a photochemical phenomenon, was first observed in the solutions of polycyclic aromatic hydrocarbons (such as phenanthrene and pyrene) by Dikun et al. [43]. Both TTA and TADF belong to delayed fluorescence, but TTA molecules do not require the small energy gap between S_1 and T_1. Monkman et al. have focused on improving χ_S through TTA process for several years [44, 45]. Recently, they developed a series of TTA molecules with special electronic

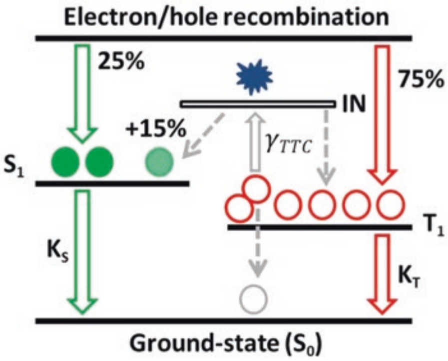

Fig. 3.5 Singlet and triplet exciton relaxation decay pathway in the TTF

structures, in which T_2–T_1 energy gap was increased and inefficient TTA routines were suppressed. Their TTA device achieved high EQE of 6 % and χ_S of 59 %.

In the past years, Ma's groups have been devoted to resolving the contradiction between exciton delocalization (weak binding energy benefits the increase in S) and exciton localization (strong binding energy is in favor of highly efficient luminescence). They proposed a new concept on material design considering the moderate exciton binding energy; that is, CT and locally excited (LE) states are combined into a new state, named here as HLCT excited state [46–48]. Such a new strategy is expected to realize the fluorescence OLED with the high efficiency. The basic principle for molecular design is that the molecular structure should consist of several donors (D) and acceptors (A). On the one hand, not too strong interaction is designed between D and A fragments to prevent CT state becoming the lowest excited state; on the other hand, not too weak interaction is desired to form CT state effectively. Their further experiments demonstrate that CT excitons with lower binding energy are in favor of raising the exciton utilization efficiency. Later, they innovate a novel strategy of "hot exciton" process (compared to the process involved the low-lying excited state (S_1, T_1) called "cold exciton" process) to enhance exciton utilization efficiency on the basis of HLCT molecular design principle (Fig. 3.6) [49, 50]. HLCT should be an ideal excited state because it possesses two combined and compatible characteristics: large transition moment from LE state and weakly bound exciton from CT state. The former contributes to a high-efficiency fluorescence radiative decay, while the latter guarantees the generation of a high fraction of singlet exciton (S). Moreover, high-lying CT and low-lying LE are found to be the optimal energy level structure responsible for high χ_S and high fluorescent radiation, which corresponds to the so-called hot exciton and cold exciton, respectively. For a series of D-A material systems they designed, their devices exhibited favorable EQEs and low roll-off, and especially χ_S exceeded the limit of 25 %. The highly efficient EL can be ascribed to the high radiation from "cold-LE exciton" and the high T → S conversion along with "hot-CT exciton" in the HLCT characteristic excited states. Their strategy provides a new approach to design next-generation organic EL materials with low cost and high performance beyond TADF.

Fig. 3.6 Model for exciton relaxation in the EL process

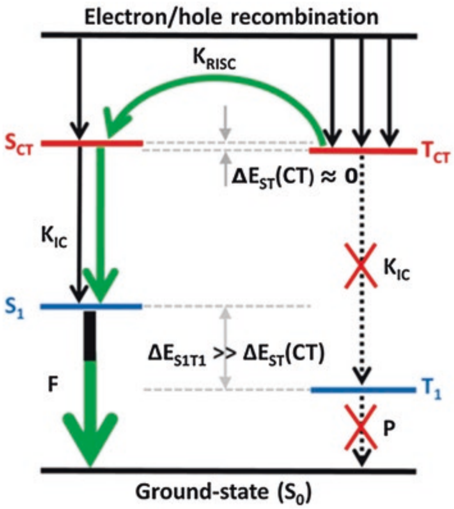

3.5 Light-Emitting Field-Effect Transistors

OLEFET are a new class of electro-optical devices that could provide a novel architecture to address open questions concerning charge carrier recombination and light emission in organic materials. These devices have potential applications in optical communication systems, advanced display technology, solid-state lighting, and electrically pumped organic lasers. The device structure and the main optoelectronic processes occurring in an OLEFET are shown in Fig. 3.7 [51].

LEFET is a three-terminal device that couples the electrical characteristics of a FET to the controlled radiative recombination of the electrons and holes injected in the channel via the drain and source contacts (Fig. 3.7). Excitons are thus created by the recombination of in-plane moving electron and hole currents, which are controlled by the gate electrode. Electroluminescence intensity is tuned by both the drain and gate voltage. The gate electrode allows higher control on charge

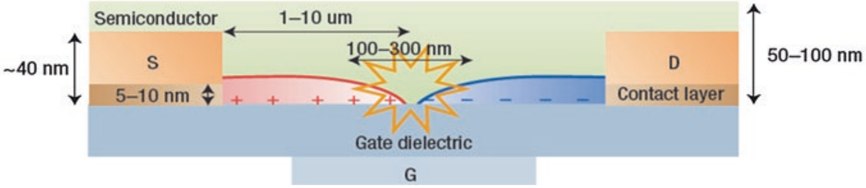

Fig. 3.7 Schematic representation of the device structures and of the main optoelectronic processes occurring in an OLEFET. Reprinted with permission from [51]. Copyright 2006, rights managed by Nature Publishing Group

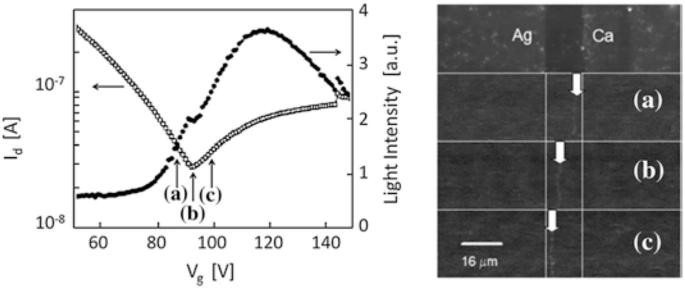

Fig. 3.8 (*Left*) Transfer scan (I_d vs. V_g) for the LEFET along with the corresponding emitted light intensity versus V_g. The emission zone is located in the channel: (*a*) Near the Ca source electrode, (*b*) near the center of the channel, and (*c*) near the Ag drain electrode. (*Right*) The *top photograph* shows the Ag and Ca electrodes and the channel of the two-color LEFET. Photographs (*a*), (*b*), and (*c*) are taken in the *dark* while the device is operating. The emission zone moves from near the Ca electrode, (a) $V_g = 88$ V, to mid-channel, (b) $V_g = 93$ V, and then approaches the Ag electrode, and (c) $V_g = 98$ V. Reprinted with permission from [53]. Copyright 2005, rights managed by AIP Publishing LLC

injection, electron, and hole currents balance and light generation processes with respect to the standard sandwich configuration of an LED.

Crucial aspects of the device's characteristics concern (i) metal electrodes that should guarantee efficient electron and hole injection; (ii) active materials that should sustain ambipolar field-effect transport and efficient electroluminescence emission; and (iii) dielectric surfaces that should be trap free to favor effective mobility of both electrons and holes at the dielectric/active material interface. The different injection and transport ability of electron/hole would determine the emission zone in the channel [52].

Figure 3.8 (left) shows the detail transfer data (I_d vs. V_g scan) for the LEFET based on super yellow material, together with the gate dependence of the light emission [53]. The transfer scan was run with a constant drain voltage V_d of 200 V. The low-work-function source electrode Ca was grounded, and the gate voltage V_g was swept from 0 to 200 V. When $V_g = 0$, there is no voltage drop between the source and gate. There is, however, a 200 V drop between the drain and gate which polarizes the gate dielectric and induces a hole channel in the vicinity of the high-work function drain electrode Ag. The current in this region at lower V_g values of the transfer scan is hole dominated. As V_g increases, the voltage drop between the drain and gate decreases, causing the magnitude of the hole current to decrease. Simultaneously, the voltage drop between the source and the gate increases, but is oppositely charged, causing the gradual buildup of an electron channel near the low-work-function source electrode Ca. At about $V_g = 90$ V, I_d reaches a minimum and then begins to increase again. This is the crossover point from hole-dominated current to electron-dominated current. Crossover is expected to occur at $V_g = 1/2\ V_d$, in good agreement with the data in Fig. 3.8 (left).

The light intensity data corresponding to the transfer scan are also shown in Fig. 3.8 (left). The light intensity data begin increasing around 80 V, while hole current still dominates, reaching a maximum around 120 V, well into the electron-dominated current regime. By employing the two-color electrode geometry, light emission should be observed when both electron and hole currents are simultaneously present during device operation, consistent with the light intensity versus V_g data in Fig. 3.8 (left). At the crossover point, the hole and electron currents are nearly equal to each other, and the quantum efficiency for light emission is maximum. Note, however, that the light intensity peaks at $V_g = 120$ V, i.e., when the electron current is greater than the hole current. A higher electron current might be necessary to achieve maximum brightness because the higher density of electron traps would reduce the number of electrons available for recombination.

The images taken of the channel region during operation show the location and width of the emission zone. The emission was found to be in a very narrow region (<2 μm) within the channel. The emission zone is not stationary within the channel, but in fact moves from the source to the drain as the gate voltage is swept from (a) 88 to (b) 93 to (c) 98 V in Fig. 3.8 (left). Shown in Fig. 3.8 (right) are photographs which image the position of the emission zone corresponding to points (a), (b), and (c) in Fig. 3.8 (left). In Fig. 3.8 (right)-(a), the emission zone is close to the calcium source electrode. As V_g increases, the emission moves across the channel Fig. 3.8 (right)-(b), finally approaching the silver drain electrode Fig. 3.8 (right)-(c). This gate-induced shift in the emission zone from the source to the drain takes place over a small voltage range near the current crossover point. The emission line is near the center of the channel at the point where current crossover occurs.

The actual application of LEFET is limited for its low external quantum efficiency and brightness. The materials can be used in LEFET and often need good electroluminescence efficiency and charge carrier mobility. However, most of the emissive material used in OLEDs cannot be applied to LEFET for its low mobility, but FET material with high mobility cannot be applied to LEFET for its concentration quenching effect.

Here, recent advances of light-emitting field-effect transistors are explored, with particular emphasis on organic semiconductors and the role played by the material properties, device features, and the active layer structure in determining the device performances. There are two main methods to improve the performance of LEFET.

One of the methods is to adjust the charge carrier injection ability by regulating the device structure [54]. The optoelectronic gate dielectric (OEG) consists of three pairs of alternating high and low refractive index layers of quarter-wave thickness and gives an LEFET with excellent electrical characteristics, very high brightness of 4,500 cd/m^2, and an efficiency at this brightness of 0.9 cd/A. The efficiency was improved by a factor of 4.5 compared to the control device on a SiN_x gate dielectric. The light emission zone of the device was close to the edge of the Ca electrode, and its width was 5.0 ± 0.5 μm. The location of the emission zone was independent of the gate bias. In recent years, many literatures have been reported to adjust the charge carrier injection ability to improve the performance of OLEFET, like modify ordered polymer nanofibers [55], using the split gate

[56], designing non-planar electrode device [57], doping carbon nanotubes [58], and so on.

Another method is to dope the phosphorescent materials in a suitable charge transport host. Phosphorescent materials have been successfully used to improve the efficiency of OLEDs. The incorporation of heavy atoms into organometallic complexes induces spin–orbit coupling which enables efficient inter-system crossing from the singlet to the triplet states and therefore leads to efficient OLED devices that are able to harvest the emission from both singlet and triplet excitations. The development of materials for LEFETs is, however, more demanding because the channel length is three orders of magnitude larger than the film thickness in OLEDs, meaning that the mobility of phosphorescent OLED materials is insufficient for their direct application in LEFETs. In order to overcome this challenge, the phosphorescent materials could be doped in a suitable charge transport host [59].

3.6 Perspective

The first optically pumped organic semiconductor laser was realized in 1996. Since then, the electrically pumped organic laser was claimed as the main goal but remained unrealized till now, and the task seems more complicated than previously thought, because of many additional losses brought by the injected current that have been identified during the past few decades. The three major issues being quantified properly include electrode losses, polaron absorption/qunenching, and triplet absorption/quenching. The last issue is the most problematic one, which may be partially addressed by using the most recently developed EL materials, i.e., "hot exciton" materials based on the HLCT state. The mechanism of evolution of hot exciton shows a brilliant approach to solve the triplet absorption/quenching problem, which may pave the way to develop novel laser materials. Relatively low charge mobility of organic materials causes the polaron absorption/quenching issue, which needs to be solved through designing the laser materials with enhanced optoelectronic properties. Besides developing novel materials, the design of device structure is another key point to realize electrically pumped organic laser.

Acknowledgments We thank the doctoral students from our research group especially T.C. Yu, H.C. Gao, and X.Y. Wu for their help in collecting the reference materials, and financial support from Natural Science Foundation of China (91233113), National Basic Research Program of China (973 Program) (2013CB834705).

References

1. T.H. Maiman, Stimulated optical radiation in ruby. Nature **187**, 493–494 (1960)
2. F.P. Schäfer, W. Schmidt, J. Volze, Organic dye solution laser. Appl. Phys. Lett. **9**, 306–309 (1966)
3. C.W. Tang, S.A. Vanslyke, Organic electroluminescent diodes. Appl. Phys. Lett. **51**, 913–915 (1987)

4. N. Tessler, G.J. Denton, R.H. Friend, Lasing from conjugated-polymer microcavities. Nature **382**, 695–697 (1996)
5. F. Hide, M.A. DiazGarcia, B.J. Schwartz, M.R. Andersson, Q.B. Pei, A.J. Heeger, Semiconducting polymers: a new class of solid-state laser materials. Science **273**, 1833–1836 (1996)
6. F. Hide, M.A. DiazGarcia, B.J. Schwartz, M.R. Andersson, Q.B. Pei, A.J. Heeger, Semiconducting polymers: a new class of solid-state laser materials. Science **273**, 1833–1836 (1996)
7. S. Chénais, S. Forget, Recent advances in solid-state organic lasers. Poly. Int. **61**, 390–406 (2012)
8. J.H. Andrews, M. Crescimanno, K.D. Singer, E. Baer, Melt-processed polymer multilayer distributed feedback lasers: progress and prospects. J. Poly. Sci. B-Poly. Phys. **52**, 251–271 (2014)
9. E.M. Calzado, P.G. Boj, M.A. Díaz-García, Amplified spontaneous emission properties of semiconducting organic materials. Int. J. Mol. Sci. **11**, 2546–2565 (2010)
10. Y. Qian, Q. Wei, G. Del Pozo, M.M. Mróz, L. Lüer, S. Casado, J. Cabanillas-Gonzalez, Q. Zhang, L.H. Xie, R.D. Xia, W. Huang, H-shaped oligofl uorenes for highly air-stable and low-threshold non-doped deep blue lasing. Adv. Mater. **26**, 2937–2942 (2014)
11. Y. Hong, J.W.Y. Lam, B.Z. Tang, Aggregation-induced emission. Chem. Soc. Rev. **40**, 5361–5388 (2011)
12. M. Kasha, H.R. Rawls, M.A. Bayoumi, The exciton model in molecular spectroscopy. Pure Appl. Chem. **11**, 371–392 (1965)
13. T. Förster, Transfer mechanisms of electronic excitation. Dis. Faraday Soc. **27**, 7–17 (1959)
14. Z.Q. Xie, B. Yang, Y.G. Ma, J.C. Shen, π-Conjugated oligomers in supramolecular crystals and their optoelectronic functions. Chin. J. Poly. Sci. **25**, 9–23 (2007)
15. J. Cornil, D.A. Dos Santos, X. Crispin, R. Silbey, J.L. Brédas, Influence of interchain interactions on the absorption and luminescence of conjugated oligomers and polymers: a quantum-chemical characterization. J. Am. Chem. Soc. **120**, 1289–1299 (1998)
16. J. Cornil, D. Beljonne, J.P. Calbert, J.L. Brédas, Interchain interactions in organic π-conjugated materials: impact on electronic structure, optical response, and charge transport. Adv. Mater. **13**, 1053–1067 (2001)
17. M.A. Baldo, R.J. Holmes, S.R. Forrest, Prospects for electrically pumped organic lasers. Phys. Rev. B **66**, 035321 (2002)
18. I. Sokolik, R. Priestley, A.D. Walser, R. Dorsinville, Bimolecular reactions of singlet excitons in tris(8-hydroxyquinoline) aluminum. Appl. Phys. Lett. **69**, 4168–4170 (1996)
19. C.-H. Zhao, A. Wakamiya, Y. Inukai, S. Yamaguchi, Highly emissive organic solids containing 2,5-diboryl-1,4-phenylene unit. J. Am. Chem. Soc. **128**, 15934–15935 (2006)
20. Y.P. Li, F. Li, H.Y. Zhang, Z.Q. Xie, W.J. Xie, H. Xu, B. Li, F.Z. Shen, L. Ye, M. Hanif, D. Ma, Y.G. Ma, Tight intermolecular packing through supramolecular interactions in crystals of cyano substituted oligo(*para*phenylene vinylene): a key factor for aggregation-induced emission. Chem. Commun. **3**, 231–233 (2007)
21. Z.Q. Xie, B. Yang, F. Li, G. Cheng, L.L. Liu, G.D. Yang, H. Xu, L. Ye, M. Hanif, S.Y. Liu, D.G. Ma, Y.G. Ma, Cross dipole stacking in the crystal of distyrylbenzene derivative: the approach toward high solid-state luminescence efficiency. J. Am. Chem. Soc. **127**, 14152–14153 (2005)
22. F. He, H. Xu, B. Yang, Y. Duan, L.L. Tian, K.K. Huang, Y.G. Ma, S.Y. Liu, S.H. Feng, J.C. Shen, Oligomeric phenylenevinylene with cross dipole arrangement and amorphous morphology: enhanced solid-state luminescence efficiency and electroluminescence performance. Adv. Mater. **17**, 2710–2714 (2005)
23. A. Bilge, A. Zen, M. Forster, H.B. Li, F. Galbrecht, B.S. Nehls, T. Farrell, D. Neher, U. Scherf, Swivel-cruciform oligothiophene dimmers. J. Mater. Chem. **16**, 3177–3182 (2006)
24. W.J. Feast, P.W. Lövenich, H. Puschmann, C. Taliani, Synthesis and structure of 4,4′-bis(2,3,4,5,6-pentafluorostyryl)stilbene, a self-assembling J aggregate based on aryl–fluoroaryl interactions. Chem. Commun. **1**, 505–506 (2001)

25. C.L. Wang, H.L. Dong, W.P. Hu, Y.Q. Liu, D.B. Zhu, Semiconducting π-conjugated systems in field-effect transistors: a material odyssey of organic electronics. Chem. Rev. **112**, 2208–2267 (2012)
26. R. Marcus, On the theory of oxidation-reduction reactions involving electron transfer. J. Chem. Phys. **24**, 966–978 (1956)
27. J.L. Brédas, D. Beljonne, V. Coropceanu, J. Cornil, Charge-transfer and energy-transfer processes in π-conjugated oligomers and polymers: a molecular picture. Chem. Rev. **104**, 4971–5004 (2004)
28. S.W. Yin, Y.P. Yi, Q.X. Li, G. Yu, Y.Q. Liu, Z.G. Shuai, Balanced carrier transports of electrons and holes in silole-based compounds—a theoretical study. J. Phys. Chem. A **110**, 7138–7143 (2006)
29. V.C. Sundar, J. Zaumseil, V. Podzorov, E. Menard, R.L. Willett, T. Someya, M.E. Gershenson, J.A. Rogers, Elastomeric transistor stamps: reversible probing of charge transport in organic crystals. Science **303**, 1644–1646 (2004)
30. T. Siegrist, C. Kloc, B. Batlogg, R.C. Haddon, S. Berg, G.A. Thomas, Enhanced physical properties in a pentacene polymorph. Angew. Chem. Int. Ed. Engl. **40**, 1732–1736 (2001)
31. J.E. Anthony, D.L. Eaton, S.R. Parkin, A road map to stable, soluble, easily crystallized pentacene derivatives. Org. Lett. **4**, 15–18 (2002)
32. J.E. Anthony, J.S. Brooks, D.L. Eaton, S.R. Parkin, Functionalized pentacene: improved electronic properties from control of solid-state order. J. Am. Chem. Soc. **123**, 9482–9483 (2001)
33. K. Kobayashi, R. Shimaoka, M. Kawahata, M. Yamanaka, K. Yamaguchi, Synthesis and cofacial π-stacked packing arrangement of 6,13-bis(alkylthio)pentacene. Org. Lett. **8**, 2385–2388 (2006)
34. V. Podzorov, E. Menard, A. Borissov, V. Kiryukhin, J.A. Rogers, M.E. Gershenson, Intrinsic charge transport on the surface of organic semiconductors. Phys. Rev. Lett. **93**, 086602 (2004)
35. V.C. Sundar, J. Zaumseil, V. Podzorov, E. Menard, R.L. Willett, T. Someya, M.E. Gershenson, J.A. Rogers, Elastomeric transistor stamps: reversible probing of charge transport in organic crystals. Science **303**, 1644–1646 (2004)
36. P.F.R. Atkins, *Molecular Quantum Mechanics*, 4th edn. (Oxford University Press, Oxford, 2005)
37. Y. Cao, I.D. Parker, G. Yu, C. Zhang, A.J. Heeger, Improved quantum efficiency for electroluminescence in semiconducting polymers. Nature **397**(6718), 414–417 (1999)
38. J.S. Wilson, A.S. Dhoot, A.J.A.B. Seeley, M.S. Khan, A. Köhler, R.H. Friend, Spin-dependent exciton formation in π-conjugated compounds. Nature **413**(6858), 828–831 (2001)
39. Z. Shuai, D. Beljonne, R.J. Silbey, J.L. Brédas, Singlet and triplet exciton formation rates in conjugated polymer light-emitting diodes. Phys. Rev. Lett. **84**(1), 131–134 (2000)
40. H. Uoyama, K. Goushi, K. Shizu, H. Nomura, C. Adachi, Highly efficient organic light-emitting diodes from delayed fluorescence. Nature **492**(7428), 234–238 (2012)
41. Q. Zhang, J. Li, K. Shizu, S. Huang, S. Hirata, H. Miyazaki, C. Adachi, Design of efficient thermally activated delayed fluorescence materials for pure blue organic light emitting diodes. J. Am. Chem. Soc. **134**, 14706–14709 (2012)
42. Q. Zhang, B. Li, S. Huang, H. Nomura, H. Tanaka, C. Adachi, Efficient blue organic light-emitting diodes employing thermally activated delayed fluorescence. Nat. Photonics **8**, 326–332 (2014)
43. P.P. Dikun, A.A. Petrov, B.Y. Sveshnikov, Phosphorescence lifetimes of benzene and its derivatives. Zh. Eksp. Teor. Fiz. **21**, 150–163 (1951)
44. C.J. Chiang, A. Kimyonok, M.K. Etherington, G.C. Griffiths, V. Jankus, F. Turksoy, A.P. Monkman, Ultrahigh efficiency fluorescent single and bi-layer organic light emitting diodes: the key role of triplet fusion. Adv. Funct. Mater. **23**, 739–746 (2013)
45. S. Sinha, C. Rothe, R. Guntner, U. Scherf, A.P. Monkman, Electrophophorescence and delayed electroluminescence from pristine polyfluorene thin-film devices at low temperature. Phys. Rev. Lett. **90**(12), 127402 (2003)
46. S.K. Kim, B. Yang, Y. Ma, J.H. Lee, J.W. Park, Exceedingly efficient deep-blue electroluminescence from new anthracenes obtained using rational molecular design. J. Mater. Chem. **18**(28), 3376–3384 (2008)

47. B. Yang, S.K. Kim, H. Xu, Y.I. Park, H. Zhang, C. Gu, Y.G. Ma, The origin of the improved efficiency and stability of triphenylamine- substituted anthracene derivatives for OLEDs: A theoretical investigation. Chem. Phys. Chem. **9**(17), 2601–2609 (2008)
48. W.J. Li, D.D. Liu, F.Z. Shen, D.G. Ma, Z.M. Wang, T. Feng, Y.G. Ma, A twisting donor-acceptor molecule with an intercrossed excited state for highly efficient, deep-blue electroluminescence. Adv. Funct. Mater. **22**(13), 2797–2803 (2012)
49. W.J. Li, Y.Y. Pan, R. Xiao, Q.M. Peng, S.T. Zhang, D.G. Ma, F. Li, F.Z. Shen, Y.H. Wang, B. Yang, Y.G. Ma, Employing ~100 % excitons in OLEDs by utilizing a fluorescent molecule with hybridized local and charge- transfer excited state. Adv. Funct. Mater. **24**, 1609–1614 (2013)
50. L. Yao, S.T. Zhang, R. Wang, W.J. Li, F.Z. Shen, B. Yang, Y.G. Ma, Highly efficient near-infrared organic light-emitting diode based on a butterfly-shaped donor-acceptor chromophore with strong solid-state fluorescence and a large proportion of radiative excitons. Angew. Chem. Int. Ed. **53**, 2119–2123 (2014)
51. M. Muccini, A bright future for organic field-effect transistors. Nat. Mater. **5**, 605–613 (2006)
52. J. Zaumseil, R.H. Friend, H. Sirringhaus, Spatial control of the recombination zone in an ambipolar light-emitting organic transistor. Nat. Mater. **5**, 69–74 (2006)
53. J.S. Swensen, C. Soci, A.J. Heeger, Light emission from an ambipolar semiconducting polymer field-effect transistor. Appl. Phys. Lett. **87**, 253511–253513 (2005)
54. E.B. Namdas, B.B.Y. Hsu, J.D. Yuen, I.D.W. Samuel, A.J. Heeger, Optoelectronic gate dielectrics for high brightness and high-efficiency light-emitting transistors. Adv. Mater. **23**, 2353–2356 (2011)
55. B.B.Y. Hsu, J. Seifter, C.J. Takacs, C. Zhong, H.R. Tseng, I.D.W. Samuel, E.B. Namdas, G.C. Bazan, F. Huang, Y. Cao, A.J. Heeger, Ordered polymer nanofibers enhance output brightness in bilayer light-emitting field-effect transistors. ACS Nano **7**, 2344–2351 (2013)
56. B.B.Y. Hsu, C. Duan, E.B. Namdas, A. Gutacker, J.D. Yuen, F. Huang, Y. Cao, G.C. Bazan, I.D.W. Samuel, A.J. Heeger, Control of efficiency, brightness, and recombination zone in light-emitting field effect transistors. Adv. Mater. **24**, 1171–1175 (2012)
57. M. Ullah, K. Tandy, S.D. Yambem, M. Aljada, P.L. Burn, P. Meredith, E.B. Namdas, Simultaneous enhancement of brightness, efficiency, and switching in rgb organic light emitting transistors. Adv. Mater. **25**, 6213–6218 (2013)
58. M.C. Gwinner, F. Jakubka, F. Gannott, H. Sirringhaus, J. Zaumseil, Enhanced ambipolar charge injection with semiconducting polymer/carbon nanotube thin films for light-emitting transistors. ACS Nano **6**, 539–548 (2012)
59. E.B. Namdas, B.B.Y. Hsu, Z. Liu, S.C. Lo, P.L. Burn, I.D.W. Samuel, Phosphorescent light-emitting transistors: harvesting triplet excitons. Adv. Mater. **21**, 4957–4961 (2009)

Chapter 4
Stable Junction Polymer Light-Emitting Electrochemical Cells

Jiajie Liang, Zhibin Yu, Lu Li, Huier Gao and Qibing Pei

Abstract Polymer light-emitting electrochemical cells (PLECs) employ a thin layer of a luminescent conjugated polymer admixed with an ionic source and an ionic conductor for the in situ formation of a p-i-n junction to facilitate the injections of both electrons and holes. The junction formation enables the use of an air-stable conductor as the cathode and a relatively thick emissive polymer layer which is more compatible with low-cost, scalable coating processes. This chapter overviews the operation mechanism, as well as the recent progress in employing crosslinkable ionic conductors to stabilize the p-i-n junction in PLECs. The static junction results in electroluminescence at high brightness, high efficiency, and prolonged lifetime. Solution-processable and printable electrode materials, such as silver nanowire, carbon nanotube, graphene, and conducting polymer, can be used in PLECs, thus opening a way to fully printable and stretchable displays.

4.1 Introduction

Electroluminescent devices have been widely used in modern society for lighting and information displays. In either category, the main challenge in device development has been to achieve higher electricity to light conversion efficiency and longer lifetime at lower fabrication cost. Light-emitting diodes (LEDs) based on inorganic and organic semiconductors have shown superior performance over incandescent light bulbs and in certain cases even over fluorescent light tubes, indicating a great potential for energy saving if a replacement could be fostered. Nonetheless, the current cost of LEDs has limited the wide range adoption of such technologies.

J. Liang · Z. Yu · L. Li · H. Gao · Q. Pei (✉)
Soft Materials Research Laboratory, Department of Materials Science and Engineering,
Henry Samueli School of Engineering and Applied Science, University of California,
Los Angeles, CA 90095, USA
e-mail: qpei@seas.ucla.edu

Y.S. Zhao (ed.), *Organic Nanophotonics*, Nano-Optics and Nanophotonics,
DOI 10.1007/978-3-662-45082-6_4

Inorganic LEDs are usually fabricated on single crystalline III–V epitaxial substrates using metal–organic chemical vapor precursors. The high cost and size limitation of the growth substrates, as well as the toxicity and low utilization of precursors, primarily result in the high cost of such devices. In addition, there are a few drawbacks in inorganic LEDs, for examples, the spatial distribution of the emitted light in inorganic LEDs highly depends on the crystal orientation and encapsulation, usually not Lambertian distribution; additional setups are required to make the emitted light diffusive for lighting applications. Meanwhile, inorganic LEDs prevail in single-color elements; it has been challenging to assemble LEDs into high-resolution full color displays.

In contrast, organic LEDs (OLEDs) based on conjugated small molecules or polymer can be processed into large areas through vacuum evaporation or solution process, respectively. OLEDs can also be made deformable in contrary to the rigid nature of inorganic electronic devices: Flexible or fully bendable devices have been achieved on both small molecular and polymer OLEDs by building the active structures on top of flexible polyethylene terephthalate substrates [1–3]. Noticeably, polymer materials can be dissolved in various organic solvents; high-quality thin films can be made through solution processes. Thus, there have been a lot of interests to fabricate polymer OLEDs with cost-effective methods, such as roll-to-roll and various printing techniques. However, certain technical challenges do exist due to the multilayered device architecture and ultra-thin (sub-100 nm) thickness for each layer in typical polymer OLED devices.

Polymer light-emitting electrochemical cells (PLECs) were introduced [4] employing a single electroluminescent layer sandwiched between two opposite electrodes. The electroluminescent layer in PLECs consists of a dissolved salt and an ionic conductor admixed in the electroluminescent conjugated polymer. The operation mechanism of PLECs is based on the in situ electrochemical doping of the emissive conjugated polymer to form a p-i-n junction within the thick polymer layer. The junction formation effectively removes the charge injection barriers and facilitates the injection of electrons and holes from the electrodes into the emissive polymer layer. Since the initial invention, PLECs have been widely investigated for electroluminescence as a low cost alternative to PLEDs. Significant advancements have been made in this field. Thus far, the response time, efficiency, and lifetime of PLECs can be on par with polymer LEDs. PLECs emitting different colors including red, green, blue, and white can be readily fabricated. PLECs are attractive for their extremely simple device architecture and fabrication process, which are very beneficial for fully printed polymer light-emitting devices [5] thus for truly realizing high-performance OLEDs at very low cost.

Many of the great achievements have been described in a number of review papers on PLECs [6–9]. Here, we only briefly introduce the basic mechanism and material selection in PLECs. The paper will focus on recent developments in this field, especially the work on stabilizing the dynamic junction in PLECs for fast response, high efficiency, and long lifetime. The paper will also describe the novel device applications enabled by the unique device structure of PLECs including whole solution-processed PLECs and stretchable PLECs.

4.2 Mechanisms and General Features

The operation mechanism of PLECs is based on two of the important semiconducting properties of conjugated polymers: electrochemical doping and electroluminescence. When a sufficient voltage is applied, electrochemical reactions occur in PLECs: The conjugated polymer is oxidized and thus become *p* doped on the anode; *n*-doped conjugated polymer is formed simultaneously on the cathode. The dopants for the *n*-doped or *p*-doped polymer come from the cations and anions of the salt, respectively, both of which are transported by the ionic conductor.

The doped polymer is conductive and thus allows the steady propagation of the doped regions; eventually, a p-i-n junction evolves in a region of undoped (intrinsic) polymer between the two doped conductive regions as shown in Fig. 4.1. The doped and highly conductive polymer provides good electrical contact with the electrodes, and the undoped part of the active layer remains highly luminescent, where efficient light emission can be electrically generated. The formation of the p-i-n junction removes the energy barriers between the polymer and the electrodes. Efficient and balanced injection of electron and hole is automatically achieved without using the low work function cathode or high work function anode. The formation of the p-i-n junction also shrinks the effective thickness of the emissive (undoped) polymer layer. In this way, thick polymer layer can also be allowed in PLECs. The p-i-n junction mechanism was proved in some of the early observations using a method of optical beam induced current [10] and direct imaging of the junction under optical microscope [4, 11].

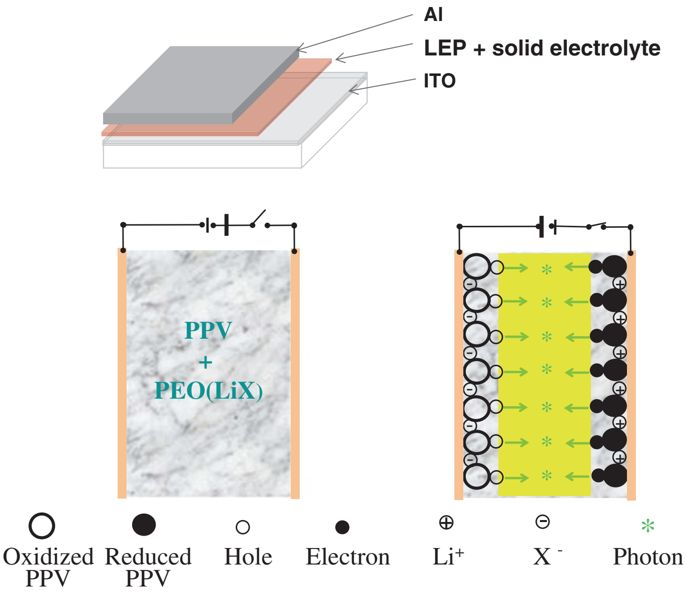

Fig. 4.1 Formation of a p-i-n junction in PLEC. The emissive layer comprises of a blend of luminescent conjugated polymer (e.g., PPV), salt (LiX), and ionic conductor (PEO)

Recently, Edman et al. [12] also found the same mechanism of p-i-n junction formation in PLECs. In their experiments, scanning Kelvin probe microscopy was used to measure the electrostatic potential within a PLEC device. Planar PLECs were fabricated with inter-electrode spacing of 120 μm. MEH-PPV, an orange light-emitting polymer, was used as the emissive polymer admixed with lithium trifluoromethane sulfonate (LiTf) (salt) and polyethylene oxide (PEO) (ionic conductor). Potential scanning was carried out on a PLEC device under steady state with observable light emission. The potential profile agreed very well with the prediction of a p-i-n junction mechanism: The majority of the potential drop occurred within around 20 μm spatial range inside the bulk of the emissive layer, corresponding nicely to the size and location of the light emission zone. The emission zone was found closer to the cathode side, and potential gradient was somewhat steeper on the cathode side than the anode side. This non-symmetry could be caused by the difference of redox for emissive polymer and conductivity between the p-doped and n-doped polymer or partial degradation of the n-doped polymer by trace amount of moisture or oxygen that raised the resistance of the n-doped region.

The ultimate external quantum efficiency (EQE) of the PLECs is limited to 5 % due to the use of fluorescent emissive material in PLECs, which can only harvest singlet excitons. Recently, LECs employing ionic transition metal complexes (iTMCs) have attracted significant attention [13]. Most of iTMCs are efficient phosphorescent emitters that can harvest both singlet and triplet excitons and achieve a theoretical 100 % internal quantum efficiency (IQE). The iTMC-based LECs could potentially exhibit higher EQE than the fluorescent PLECs while retaining the structural simplicity of the PLECs [14–17].

The iTMCs-based LECs share certain similarities with the conjugated polymer-based PLECs in both device architecture and operational features such as slow response due to sluggish ion transport in solid state. However, the fundamental driving mechanism may differ given the fact that the electrochemical doping behavior of the iTMCs has not been fully investigated. It is not known to the authors whether oxidized or reduced iTMCs are highly conductive like doped conjugated polymers. Without the oxidized or reduced iTMCs being conductive, either a p-i-n junction is not formed, or the oxidation and reduction are only limited to the iTMCs on the interfaces. Without the formation of a p-i-n junction, the LECs with iTMC would lack one important feature of the PLECs: The semiconductor layer cannot be thick such that the device fabrication could tolerate certain non-uniformity and defects in the organic layer.

4.3 PLEC Materials: Polymers, Salts, Ionic Conductors, and Solvents

The electroluminescent layer in PLECs is a tertiary mixture of a light-emitting material, an ionic source (salt) and an ionic conductor. Meanwhile, a suitable processing solvent has also to be used to form a relatively uniform film without large-scale phase aggregation. In the active layer of PLECs, nonpolar conjugated polymers and strongly polar solid electrolyte form a phase-separated interpenetrating polymer network. While the electrolyte network provides the channels for ionic transport, the conjugated polymer network provides the pathways for transport of electronic charge carriers. Therefore, the morphology of the phase-separated blend plays a key role in the operation of PLECs. New conjugated polymers and electrolytes have been used or developed for controlling the blend morphology and improving the PLEC performance.

Because of the polar character of electrolyte, the electrolyte complex is not soluble in nonpolar organic solvents that are typically used for processing EL polymer. Thus, many conjugated polymers with high PL efficiencies may not be used as the emissive material for PLECs. Crown ethers are known to form stable complexes with alkali metal cations [18, 19]. As shown in Fig. 4.2, these complexes are soluble in nonpolar solvents such as toluene and xylene, the solvents that could dissolve the EL polymers.

Ionic liquids are also useful as electrolyte in PLECs fabrication. The advantages of ionic liquids over inorganic salts are as follows: (i) They are soluble in common organic solvents and insoluble in water; (ii) the cations and anions are quite dissociated from each other and are chemically and electrochemically stable; and (iii) ionic liquids are nonvolatile. Stephan et al. [20–22] achieved high-performance PLECs using a highly lipophilic ionic liquid, tetrahexylammonium-bis-trifluoro-methyl-sulfonyl imide as the electrolyte (Fig. 4.3). Li et al. [23] demonstrated PLECs with similar ionic liquids except that the anions are based on imidazolium.

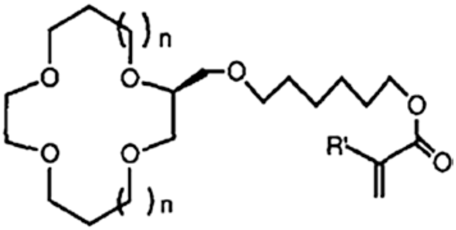

Fig. 4.2 Crown ether derivatives used for PLECs, wherein n is 0 or 1; R′ is methyl

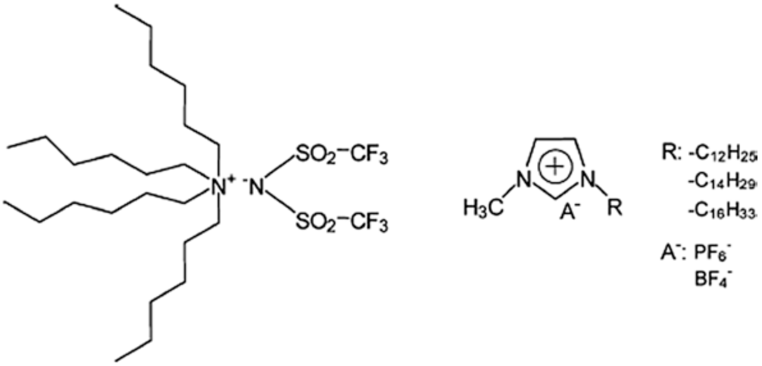

Fig. 4.3 Chemical structures of two kinds of ionic liquids: (*left*) tetrahexylammonium-bis-trifluoro-methyl-sulfonyl imide and (*right*) imidazolium salts with long alkyl substituents

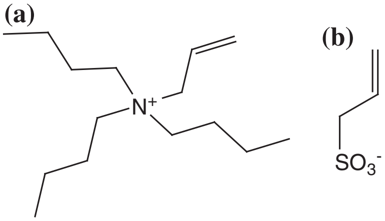

Fig. 4.4 Chemical structure of (**a**) a polymerizable organic cation and (**b**) a polymerizable anion

Polymerizable ionic species shown in Fig. 4.4 have been explored to suppress ionic mobility after junction formation and polymerization of the ionic species which have become electrochemical dopants in the p and n regions of the p-i-n junction. The polymerized ions are less mobile than the monomeric ions, and the resulting p-i-n junction can no longer relax even when applied bias is removed. The junction exhibits certain stability, though the efficiency and brightness of the PLECs appear rather low [24–26]. This is further discussed below.

4.4 Fixed Junction PLECs (Junction PLEDs)

The junction in LECs is formed in situ; however, it relaxes once the bias voltage is removed as a result of internal discharging and ionic redistribution. PLECs typically have slow response due to the finite time for the formation of the junction. In order to achieve instantaneous light emission, efforts have been made to preserve the p-i-n junction, for example, by restricting the mobility of the dopants either through temperature cooling [27] or polymerization of the ionic dopants [24, 25].

In our approach, we have focused on the use of curable ionic conductors such as methacrylate or acrylate oligomers as schematically illustrated in Fig. 4.5 [28, 29]. Each of such molecules contains multiple methacrylate (or acrylate) functional groups that polymerize and cross-link readily when heated, exposed to UV or charged species (ionic chain growth polymerization). Such molecules can also dissolve certain amount of the salt in the emissive thin film of the PLEC devices due to the polar nature of the methacrylate or acrylate groups in the ionic conductors, thus forming the ionic conduction channels in the composite film to support the movements of the cations (n-dopants) and anions (p-dopants) for the formation of the p-i-n junction. Those ionic conduction channels will then be cut off due to the crosslinking of the acrylate and methacrylate functional groups as initiated by heat from device operation particularly at high current density and/or by the ionic radicals from the electrochemically doped polymers. A drastic decrease in ionic conductivity of a cured glassy polymer matrix preserves the p-i-n junction even after withdrawing the external bias.

In contrast to previous work [27], all the procedures used in this process are carried out at room temperature; no cooling or heating–cooling cycle is used

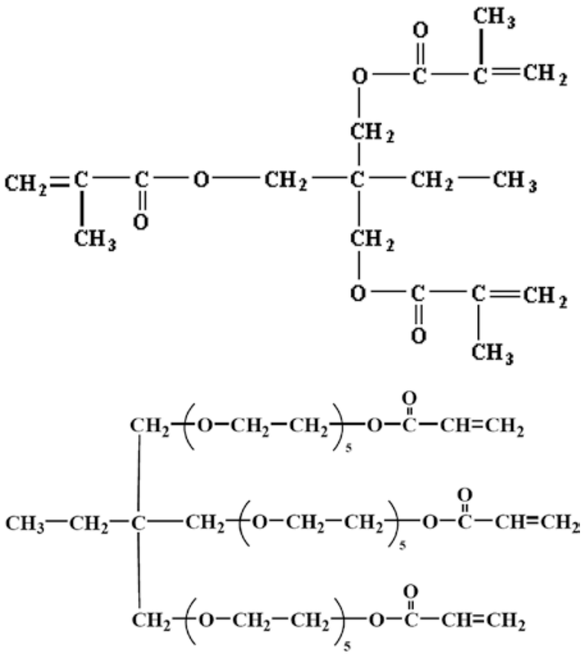

Fig. 4.5 Two ionic conductors employed for the formation of a fixed p-i-n junction in PLECs

which is believed to be beneficial for easy fabrication. On the other hand, a variety of methacrylate or acrylate oligomers containing different number of acrylic curing groups are commercially available, providing sufficient opportunities to tune their ionic conductivity, polymerization reactivity, and mixing capability within the active layer.

As the first proof of concept, trimethylolpropane trimethacrylate (TMPTMA) was used with its chemical structure drawn in Fig. 4.5 (left structure). TMPTMA has a relatively low vapor pressure at room temperature even in an ultrahigh vacuum (~10^{-6} Torr) that is usually used for the physical vapor deposition of metal thin films. As confirmed by FTIR measurements on films comprised of a conjugated polymer that emits yellow light, a lithium triflate salt and TMPTMA, a majority (~80 %) of the TMPTMA small molecules still remained as indicated by the strong carbonyl absorption after the films having gone through a high-vacuum environment used for the deposition of aluminum electrode. It is worthwhile to note that the samples should avoid overheating during top electrode deposition. Such heating could be quite significant and leading to a major loss of such small molecules, which might have occurred in the work by Edman et al. [30].

Figure 4.6 shows the PLEC devices fabricated with a simple sandwich structure of ITO/Polymer/Al. The polymer thin film contains a luminescent polymer, an alkoxyphenyl substituted poly(1,4-phenylene vinylene) that emits yellow light (SY-PPV, Covion Super-Yellow) [31], TMPTMA, and LiTf. The weight ratio of SY-PPV:TMPTMA:LiTf in the spin-cast film is 20:10:1. The devices were first biased

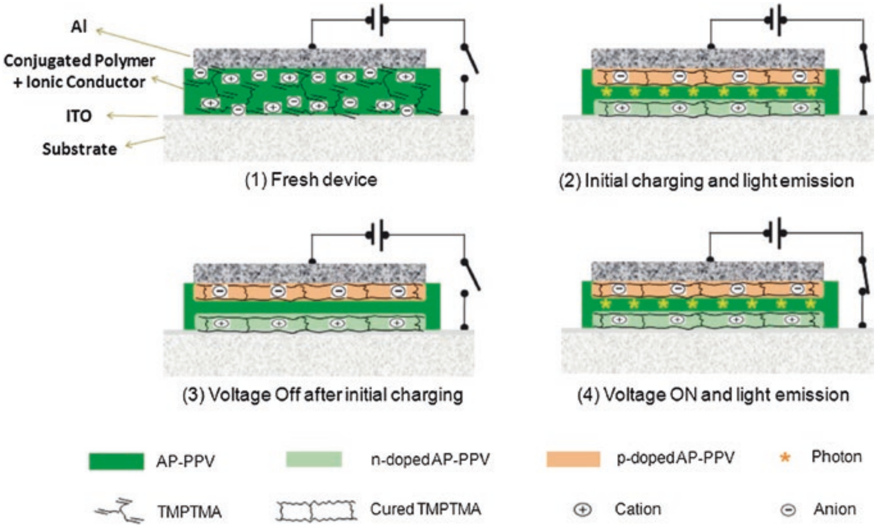

Fig. 4.6 Formation of a fixed p-i-n junction in a PLEC comprising a curable ionic conductor. Reprinted with the permission from [28]. Copyright 2009 American Chemical Society

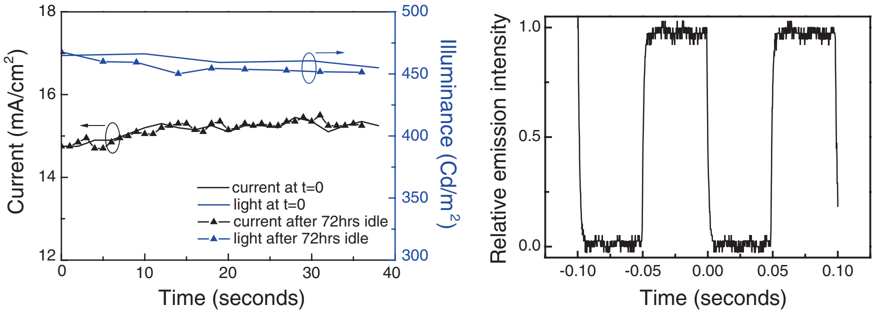

Fig. 4.7 Transient responses of current density and emission intensity of a PLEC containing a fixed p-i-n junction during constant voltage biasing (*Left*) and pulsed voltage biasing with 50 % duty cycle (*Right*)

at 12 V for junction formation, during which both device current and emission intensity exponentially increased with time. Lower bias of 10 V was then applied to measure the characteristics of the p-i-n junction in the SY-PPV:TMPTMA:LiTf device. Figure 4.7 shows the transient current and light intensity at 10 V immediately after the initial charging and after some specified idle time without bias voltage. In all instances, the current and light emissions turn on immediately and remain nearly constant afterward. Even idling for 72 h without biasing does not significantly modify the diode properties or emission intensity. The light emission turn on speed from the p-i-n junction in the ITO/SY-PPV:TMPTMA:LiTf (20:10:1)/Al devices after the initial charging is also examined under a 0–10 V pulse train with 50 % duty cycle at 10 Hz. The device shows an abrupt change between the on and off states within <5 mS, which is close to the RC time constant of the device. This instant light emission is in contrast to a conventional PLEC device where the junction relaxes during idling time and subsequent biasing involves slow turn on.

The stability of the junction was also confirmed by photovoltaic and impedance measurements. A freshly prepared device without initial biasing produces an open circuit voltage (V_{oc}) of around 0.8 V and short circuit current (I_{sc}) of around 2 μA/cm^2 under AM1.5 one sun illumination. Right after the device was initially charged at 12 V, the V_{oc} increased to about 1.5 V and I_{sc} to 6 μA/cm^2. The enhancement on the photovoltaic performance is consistent with the formation of a p-i-n junction in the devices. After the initial charging and photovoltaic measurements, the polymer device was left idle for 16 h without bias before it was subjected to solar illumination again. The current–voltage response shows similar characteristic as before idling: Both V_{oc} and I_{sc} remain practically unchanged. For comparison, a control device was also prepared containing SY-PPV, PEO, and LiTf at the weight ratio of 20:10:1. Photovoltaic measurements were performed in the same way as described ahead. V_{oc} and I_{sc} of the freshly prepared device are 0.6 V and 0.3 μA/cm^2, respectively. The values increased to 1.6 V and 2.4 μA/cm^2, respectively, immediately after voltage bias at 12 V that created a dynamic p-i-n junction with concurrent light emission. However, its photovoltaic behavior regains the characteristics of the fresh device after the charged device is allowed to idle for 15 min without bias. This result is consistent with the dynamic nature of the p-i-n junction in a PLEC that rapidly relaxes when no external bias is applied.

Impedance spectroscopy was also measured to extract the contact resistance between the polymer and the electrodes. The contact resistance was found to decrease by more than one order of magnitude after the initial charging at 12 V for both devices with TMPTMA or PEO as the ionic conductors, consistent with the formation of a p-i-n junction and consequently the alleviation of the charge injection barriers at the electrode/polymer interfaces in those devices. The contact resistance in the SY-PPV:PEO:LiTf (20:10:1) device recovered back to the original high value after as short as about 15 min of idling without bias, manifesting a fully dynamic junction characteristic in conventional PLECs. The reduced contact resistance in the SY-PPV:TMPTMA:LiTf (20:10:1) device remains unchanged after 72 h of idling without bias, a strong indication of junction stability when no external bias is applied in the device with TMPTMA as the ionic conductor.

TMPTMA shows its potential for fixed junction PLECs; nonetheless, the maximum efficiency was about 3 cd/A, which is about 4 times lower than the highest reported PLED efficiency based on the same light-emitting polymer. This lower performance was probably caused by a low ionic solubility and conductivity of TMPTMA. Moving forward, we improved the ionic solubility and conductivity by incorporating ionic conducting ethylene oxide blocks next to each curable

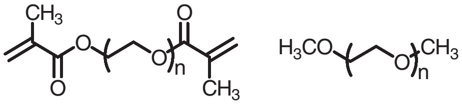

Fig. 4.8 A crosslinkable ionic conductor (PEO-DMA) and a non-crosslinkable ionic conductor (PEO-DME)

methacrylate functional group. For this purpose, a low molecular weight PEO with methacrylate termination on both ends was employed [29]. The chemical structure of one of such compounds is shown in Fig. 4.8 (PEO-DMA). The number averaged molecular weight is about 1,000 (with an n value of about 20). A high molecular weight PEO and a PEO oligomer terminated with a methyl group on each end (PEO-DME) were also used for comparison.

PLECs were fabricated having a structure of ITO/polymer/Al in which the polymer layer contained SY-PPV admixed with an ionic conductor (PEO-DMA, PEO-DME, or PEO) and LiTf at a weight ratio of 1:0.1:0.05. In a typical device characterization, the freshly prepared device was initially operated at 3 mA constant current and 10 V compliance for 6 h to allow the formation of the p-i-n junction. An incremental voltage scan (typically at 0.1 V/s) from 0 V upward was subsequently applied. All devices were found to have low turn-on voltages, very close to the measured optical band gap of SY-PPV ($E_g \approx 2.1$ eV). The observed turn-on voltage was 2.4 V with PEO, 2.3 V with PEO-DME, and 2.2 V with PEO-DMA.

When PEO is used, the maximum efficiency achieved is 4.4 cd/A (at 100 cd/m^2), on par with the results recently reported for SY-PPV admixed with PEO and potassium trifluoromethane sulfonate salt [32]. The PLECs with PEO-DME have maximum current efficiency of 5.4 cd/A (at 165 cd/m^2). In devices with PEO-DMA as the ionic conductor, the maximum current efficiency is 11.9 cd/A (at 160 cd/m^2). The luminous efficiencies of these PLECs are shown in Fig. 4.9 (left). The peak power efficiency is 15.3 lm/W (at 16 cd/m^2) for the PEO-DMA device; the efficiency remains 13.0 lm/W at 100 cd/m^2, 9.8 lm/W at 500 cd/m^2, and 8.0 lm/W at 1,000 cd/m^2. This performance represents a more than 200 % enhancement over those of the conventional PLECs having a dynamic p-i-n junction.

The lifetime of the PLECs was tested at 3 mA constant current in a nitrogen filled dry box without additional encapsulation. The temporal response of the light intensity is shown in Fig. 4.9 (right). The conventional PLECs based on PEO and PEO-DME both exhibited the characteristic rapid degradation after a short duration of relatively stable operation. This accelerated degradation is not observed in the PEO-DMA devices: After 102 h of continuous operation, the luminance decreased to 75 % of its 2,200 cd/m^2 peak brightness. The $T_{75\%}$ lifetime for the PEO-DMA PLECs from 100 cd/m^2 peak brightness was calculated to be 27,000 h. This long lifetime is comparable with the most stable polymer OLEDs optimized for commercial applications. In comparison, the $T_{75\%}$ for the PEO and PEO-DME devices is estimated to be 2,700 h and 1,000 h, respectively. A great enhancement in both device efficiency and operation lifetime has been achieved in use of curable ionic conductors.

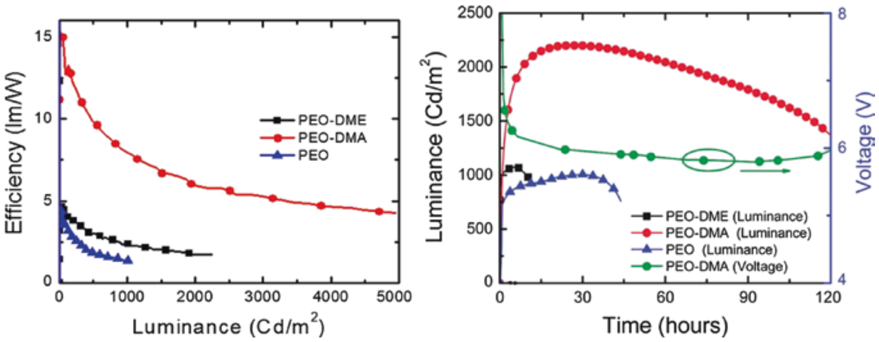

Fig. 4.9 (*Left*) Efficacy of representative PLECs as a function of emission intensity. (*Right*) Evolution of emission intensity of PLECs during stress test at 3 mA constant current. Reprinted with the permission from [29]. Copyright 2011 American Chemical Society

The device performance improvement of the fixed junction PLECs is further demonstrated in planar PLECs with 3 mm inter-electrode spacing. The evolution of the doping profiles and the junction formation in a conventional PLEC and a fixed junction PLEC is shown in the optical micrographs in Fig. 4.10. The devices were under UV irradiation, and a bias was applied between the aluminum anode (+) and cathode (–). In light of the dopant-induced photoluminescence quenching of conjugated polymers, the contrast within the active polymer film under UV irradiation reveals doping profiles and the junction formation. During operation at 1,000 V, the doping frontiers in the planar PLEC using PEO-DME as the ionic conductor (upper row in Fig. 4.10) start with relatively straight patterns but

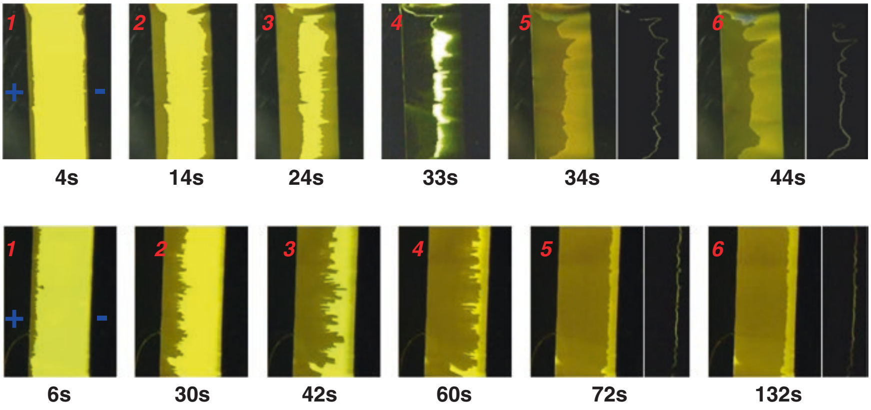

Fig. 4.10 Optical micrographs of planar PLECs based on PEO-DME (*upper row*) and PEO-DMA (*lower row*) at specified elapsed time of operation at a constant voltage. The photographs were taken under UV exposure except for the *right* photographs in 5 and 6 which were taken in *dark* field to show the *light* emission from the junction. Reprinted with the permission from Ref. [29]. Copyright 2011 American Chemical Society

grow into more irregular ones during propagation. Light emission was observed where the *p*- and *n*-doping frontiers meet with each other. It appears that the *p*- and *n*-doping frontiers in the PEO-DME device continue to advance after they meet each other, causing the device to eventually become electrically shorted. Micrograph 5 (left) shows the fully formed junction under UV exposure, and 5 (right) was taken in dark field to show the light emission pattern replicating the junction profile. After 10 s of further biasing, the light emission pattern and the junction profile were found noticeably reshaped, accompanying with an obvious decrease in emission intensity particularly at the shorted region near the top portion of the junction.

In the planar PLEC using PEO-DMA as the ionic conductor, the *n*-doped frontier grows remarkably more uniformly, which remains a fairly straight line till the completion of the junction formation (lower row in Fig. 4.10). Another major difference from the PEO-DME device was observed when the *p*-doping frontier meets with the *n*-doping frontier. The *p*-doping frontier appeared to cease propagation after it met with the *n*-doping frontier. As such, the area that had a slower *p*-doping propagation rate caught up, eventually leading to a relatively uniform junction.

The equalization of the doping profiles or the smoothening of the p-i-n junction is considered to be caused by the curing of PEO-DMA at the junction where excessive current flow and excitons could initiate the vinyl polymerization in the proximity of the p-i-n junction. The polymerization of PEO-DMA diminishes the local ionic conductivity, retards the further propagation of doping frontier, and prevents or slows down the crossover of the *p*- and *n*-doped regions. In the meantime, the slower propagating frontier has time to catch up. A uniform and static doping profile could therefore be obtained.

The curing of the methacrylate groups in PEO-DMA is also supported by the I–V characteristics of the LECs after 6 h of operation at 25 mA/cm^2. In the voltage scan from -4 V to 6 V a, characteristic diode behavior was observed, with current rectification ratio of 6×10^4 at ± 4 V. This I–V characteristic is not dependent on the scan rate of the applied voltage. The high rectification ratio was mostly maintained after the device had been idled, without voltage bias, for 1 h. The highest rectification ratio obtained in the PEO-DME device was 1,000 right after the 6 h continuous biasing at 25 mA/cm^2, and the value decreased to 10 after 10 min idle.

The results from the planar PLECs are consistent with the higher efficiency and stability obtained with the fixed junction PLECs than PLECs with a dynamic junction. The curing reaction of the methacrylate groups in the ionic conductor during junction formation lowers the ionic conductivity of the emissive polymer layer. The ionic species and dopants can no longer move, and thus, the junction is fixed or “frozen”. Since the operating voltage of the PLECs is rather high compared to the electrochemical stability window of the species present in the polymer, the diminished ionic conductivity help suppress electrochemical over-reactions and thus the degradation of the p-i-n junction. Note that fixed p-i-n junction formed in stacked organic layers deposited by successive deposition of the p-doped, intrinsic, and n-doped layers has recently been shown an effective approach to high-efficiency and stability OLEDs and solar cells [33, 34].

For years, the energy barrier at the metal/organic interface has been a critical issue affecting the performance of many organic semiconductor devices including OLEDs and solar cells wherein thin layers of a conjugated polymer or small molecules are in contact with two opposite electrodes. A low work function cathode, high work function anode, and charge transporting layers are often used in tandem to facilitate and/or balance the injection/collection of charges. Alternatively, inserting doped layers at the interfaces to form a p-i-n junction structure is also effective for improving the device performance, such as in the multilayer stacked OLEDs reported by Leo et al. [33, 34]. Similar junction diodes in polymers have also been fabricated using *p*-doped PEDOT:PSS, a light-emitting polymer (LEP), and an alkali metal n-doped LEP [35]. These p-i-n junction diodes have shown promising efficiency for electroluminescent and photovoltaic applications. However, the fabrication processes are rather complicated, and the devices may lose one of the most appealing features of organic semiconductor devices: low cost. With the use of a polymerizable ionic conductor, a stable p-i-n junction can be formed in situ in a single polymer layer in a relatively cost-effective way and in a process that is compatible to ambient environment and solution printing fabrication.

4.5 LEC-Enabled Novel Devices: All-Solution-Processed LECs

In the past decade, the R&D on OLEDs has focused on developing flat-panel displays with higher contrast ratio and efficiency than liquid crystal displays. While the efficiency of OLEDs can surpass that of fluorescent tubes, some of the originally perceived major advantages of the OLEDs, such as solution-based roll-to-roll, printing or laminating process for low cost and flexible form factors, have not been fully realized in commercial products. Cao et al. developed printable electron injection layers using water or alcohol-soluble conjugated polymers [36, 37]. They also fabricated PLEDs by printing three different polymer layers and a silver paste cathode [38]. Lee et al. [39] reported soft contact lamination using elastomeric polymers to laminate PLEDs in a less intrusive manner. However, several key challenges have yet to be overcome for all-solution processing:

(1) The conventional transparent electrode, indium-doped tin oxide (ITO), is brittle. ITO cracks under small tensile strain; as such, OLEDs fabricated on ITO-coated flexible substrates have limited flexibility.
(2) High-efficiency OLEDs require a multilayered device architecture to balance the injections of electrons and holes. The delicate control of the thickness of each layer leads to high fabrication cost.
(3) Reactive metals or metal salts are commonly used as the electron injection materials in OLEDs. These materials are sensitive to oxygen or moisture, and they are not very compatible with a solution-based process. Hermetic encapsulation is generally required for the OLEDs due to the reactivity of these materials.

(4) To obtain a low driving voltage and high power efficiency, the emissive polymer layer is limited to 100 nm or thinner. Direct printing of consecutive layers tends to impair the emission layer: The solvents contained in the inks may swell and contaminate the emissive polymer during printing. Lamination of 100 nm or thinner layers at elevated pressure and temperature may induce stress concentrations and thickness non-uniformities.

Due to these challenges, thermal evaporation in high vacuum has been the preferred method to deposit the cathode for OLEDs. The PLECs have been investigated to potentially address these challenges [29, 40–42]. The developments have paved the way toward all-solution processing of LECs.

Solution-processable transparent conductive electrode (TCE) has become the major challenge for realizing the all-solution processing of LEC devices. ITO has been the ubiquitous TCE material. However, high-quality ITO coating can only be obtained via high-temperature annealing. ITO coating formed on flexible substrates such as polyethylene terephthalate (PET) has higher sheet resistance than ITO formed on glass, and its flexibility is limited due to the brittleness of the ceramic coating [43]. Thus, ITO severely limits the application of common industrial solution-based processes including roll-to-roll for the LECs. Several alternative materials, including carbon nanotubes (CNTs), graphene, conducting polymers, and metallic nanowires, have been investigated to replace ITO in all-solution processing or printing of LECs.

4.5.1 LEC Fabricated on Printed Carbon Nanotube Electrodes

Single-walled carbon nanotube (SWNT) thin-film electrodes deposited onto various substrates via solution processes have been developed with conductivity and transmittance approaching those of ITO electrodes [44–46]. We have shown that ultrathin SWNT electrodes exhibit superior stretchability: The electrodes remain conductive even after more than 700 % elongation [47]. These electrodes have been used to drive dielectric elastomers to electrically actuated strains up to 300 % in area expansion [48]. The high compliancy of the SWNT electrodes arises from network formation of the high-aspect-ratio nanotubes. The electrodes consist of randomly oriented and highly interwoven carbon nanotubes. SWNT coatings have been studied as the electrodes for various electronic devices including inorganic LEDs [49], small molecule OLEDs [50, 51], PLEDs [52], organic solar cells [53, 54], and super capacitors [55].

The LEC devices were made by spin-coating an electroluminescent polymer layer onto a sheet of SWNT/PET and then laminating it with a second sheet of SWNT/PET at 120 °C using an office roll lamination equipment [3]. The polymer layer in the LECs contained a luminescent conjugated polymer, a curable ionic conductor, and LiTf. Three polyfluorene-based luminescent polymers were used for blue, yellow, and red light emission, respectively.

The ultrathin SWNT electrodes are porous and have a high surface roughness of above 100 nm [56]. This roughness is detrimental to the performance of conventional PLEDs. Planarization techniques are required to planarize the SWNT surface for high-efficiency PLEDs. In our experiments, high pressure and high temperature were both applied during roll lamination to form good electrical contact between the polymer and SWNT electrodes. A large polymer thickness was found to be important to eliminate the potential electrical shorts caused by the poking of protruding tubes. At a polymer layer thickness of around 1,200 nm, the lamination had a 100 % yield. The in situ formation of a p-i-n junction in the LECs when a bias voltage was applied reduced the driving voltage to be comparable with that of a conventional PLED with a 10–20 X thinner polymer layer.

The laminated polymer light-emitting devices with SWNT as both cathode and anode are quite transparent as shown by the photographs in Fig. 4.11. All the devices were placed on top of a sheet with color printed "UCLA" patterns to illustrate the transparency of the PLECs. The SWNT/PET bilayer together has a total transmission of 73 % averaged from 400 to 1,100 nm. The light-emitting devices all exhibit above 70 % transmission in the wavelength range outside the absorption spectrum of the conjugated polymers. The high flexibility of the devices was demonstrated also in Fig. 4.11 where in the devices were deformed to conform onto a 2.5 mm-radius glass tube. No significant damage was seen after the bending and the curved devices still emit bright and uniform light.

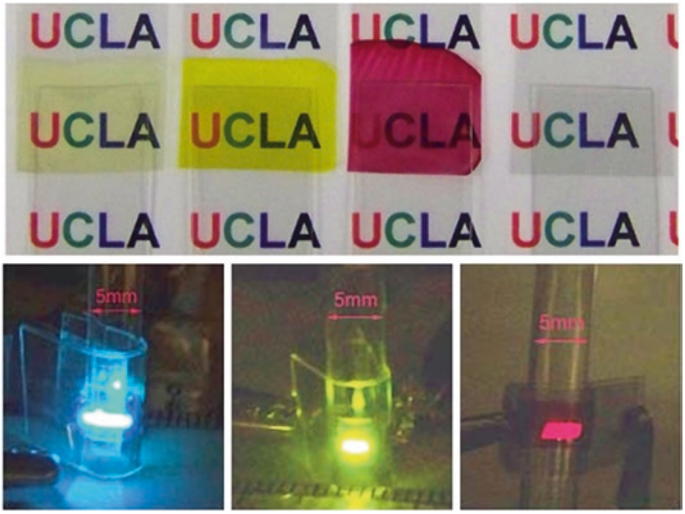

Fig. 4.11 Photographs of all-solution-processed devices fabricated by lamination. Reprinted with the permission from [56]. Copyright 2011 Society of Photo Optical Instrumentation Engineers (SPIE)

4.5.2 LEC Fabricated on Solution-Processable Graphene Electrodes

Graphene has recently emerged as an important solution-processable material with high conductivity and transparency [57, 58]. When oxidized and exfoliated from graphite, graphene oxide can be suspended in water, coated onto a surface, and then chemically reduced [59]. Upon thermal annealing, the chemically derived graphene (CDG) can form a conductive, transparent film suitable for use as the TCE in OLEDs and LECs.

Based on the graphene and TCE, Matyba et al. fabricated an LEC made entirely of organic materials (i.e., without any metal electrode), and all the components (cathode, anode, and active material) are solution-processed [60]. They used CDG as the cathode and a commercially available PEDOT-PSS "ink" (designed for screen printing) as the anode. The active layer contained a blend of a SY-PPY and an electrolyte in the form of the salt KCF_3SO_3 dissolved in PEO, as schemed in Fig. 4.12. The *p*- and *n*-doped regions extend from the anode and cathode, respectively, growing until a light-emitting p-i-n junction is formed. Thanks to the junction formation, the LEC devices presented in this work all have active layers between 1 and 2 um thick.

This graphene/{SY-PPY + PEO + KCF_3SO_3}/PEDOT-PSS device begins to emit light at 2.8 V, close to the band gap potential of SY (2.4–2.5 V). However, the current efficiency of the LEC device at its maximum brightness 1,200 cd/m^2 is about 2 cd/A. The light emitted from each side is measured similar in

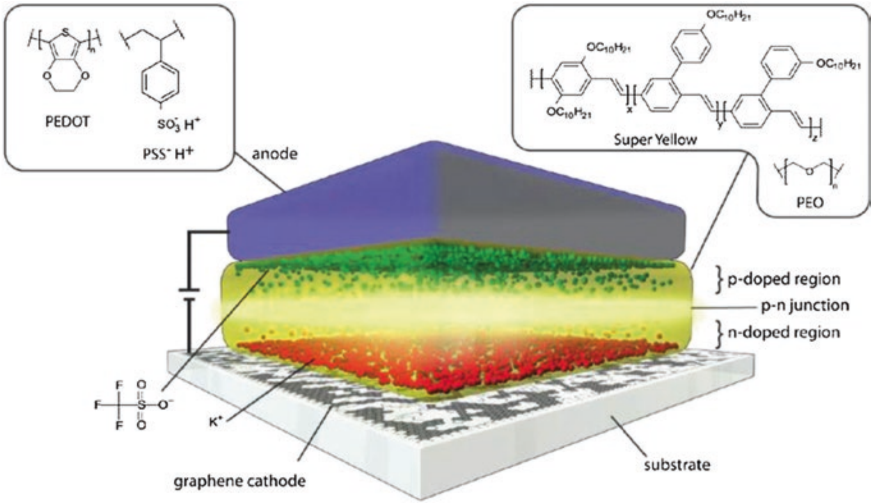

Fig. 4.12 Schematic illustration of the structure and operation of the device. During operation, light is emitted both upward, through the PEDOT-PSS electrode, and downward, through the graphene electrode. Reprinted with the permission from [60]. Copyright 2010 American Chemical Society

intensity. Thus, considering the light emitted from both sides of the device, it was estimated that the quantum efficiency and the luminous efficacy are to be 9 cd/A and 5 lm/W, respectively. A key limiting factor in the efficiency is the modest conductivity of the solution-processed graphene cathode (sheet resistivity ~5 k ohm/sq).

4.5.3 LEC Fabricated on Silver Nanowire/Polymer Composite Electrodes

Although carbon-based conducting materials, including SWNTs and graphene, and conducting polymer have been extensively investigated for the solution-processed transparent electrode, PLEC based on these TCE electrodes still exhibited limited device performance due to the high sheet resistance. Metallic nanowires, such as AgNW and copper nanowires, can form conductive coatings with figure of merit conductivity–transmittance performance comparable to ITO [61, 62] and could be a suitable choice for the fabrication of all-solution-processed PLECs. Solution-processed AgNW–polymer composite electrodes appear particularly attractive thanks to the simple process and low surface roughness [63–65]. However, one shortcoming of using AgNWs is the low surface coverage of AgNWs: The nanowires exposed on the surface to form electrical contact with light-emitting polymer coated on top of the electrode cover only a small fraction of the surface area. This low surface coverage could cause non-uniform charge injection across the electrode area and leave certain areas of the devices non-active. Thus, a dense conducting layer is required to cover on the surface of AgNW electrodes to increase the conductive surface coverage and thus enhance charge injection.

Liang et al. thus fabricated a solution-processable SWNT/AgNW bilayer–polymer composite TCE as anode for LEC application [66]. The fabrication started with successively coating on glass release substrate a dense layer of SWNT and a highly conductive layer of AgNW. A polymer precursor solution containing acrylate resin and photo initiator was cast on top of the bilayer coating and cured under UV light. The resulting composite electrodes were peeled off the release substrate. The SWNT/AgNW bilayer which was in contact with the glass surface was exposed on the conductive surface of the composite electrodes.

The SWNT/AgNW bilayer–polymer composite electrode has a conductive surface covered by the dense SWNT network. The surface microstructure of a composite electrode imaged by SEM is shown in Fig. 4.13a which reveals a dense, highly entangled network of SWNTs. The underlying AgNW percolation network is also clearly seen due to the much higher conductivity of AgNW than that of SWNT. Compared to the sparse network of AgNW on the surface of AgNW–polymer composite electrode [63–65], the surface of the bilayer composite electrode is covered with a dense SWNT network which should facilitate uniform charge distribution across the entire electrode surface. The SWNT/AgNW bilayer–polymer composite electrodes with 10, 15 ohm/sq and 30 ohm/sq sheet resistance have

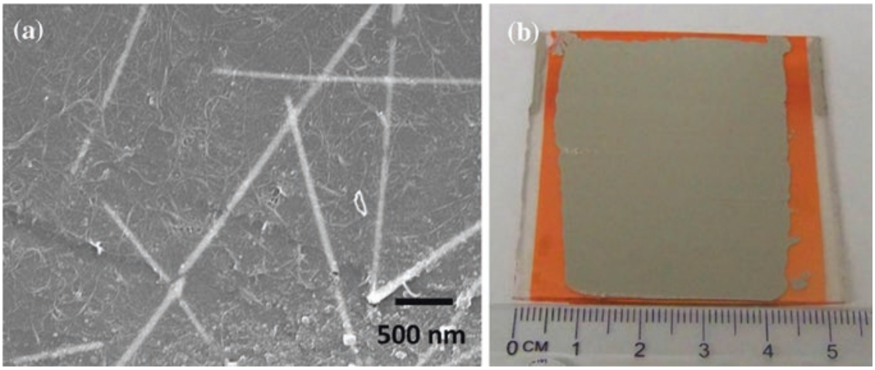

Fig. 4.13 **a** SEM micrographs of a SWCNT/AgNW bilayer–polymer composite electrode with 30 ohm/sq sheet resistance. **b** A finished all-solution-processed LEC device (active area ~4 × 4 cm^2) with printing Ag paste cathode deposited by blade coating

a transmittance of 78, 81, and 83 % at 550 nm, respectively. In comparison, a 10 ohm/sq ITO/glass electrode has a transmittance of 86 % at 550 nm. Moreover, unlike ITO/glass, the bilayer composite electrodes are highly flexible. The sheet resistance did not significantly change after repeatedly bending to concave and convex with 1.0 cm radius for 2,000 bending cycles (from 15 to 16 ohm/sq).

To fabricate fully solution-processed PLEC devices, a luminescent polymer layer comprising a red light-emitting conjugated polymer poly[2-methoxy-5-(3,7-dimethyloctyloxy)-p-phenylenevinylene] (OC1C10), a cross-linkable ionic conductor and lithium trifluoromethane sulfonate ionic source, was coated onto the conductive surface of the composite electrode by doctor-blade coating. The wet coating was then spinned on a spin coater to remove the residual THF solvent. The thickness of the electroluminescent layer, ~200 nm, was controlled via the gap between the doctor blade and the substrate surface as well as the spin-coating rate. Finally, a layer of commercial printing silver paste was coated by doctor-blade coating to complete the all-solution fabrication of a PLEC device (Fig. 4.13b). It is notable that the entire fabrication processes of the PLEC, including the formation of the electrodes, emissive polymer layer, and substrate, are all carried out by solution processing under ambient air.

The all-solution-processed red PLEC device has a turn-on voltage of 3.0 V and exhibits a maximum current efficiency of 3.02 cd/A at maximum brightness of 2,080 cd/m^2. The efficiency represents a 53 % improvement over the control device with conventional ITO/glass anode and evaporated alumina cathode (Fig. 4.14). The inset in Fig. 4.14d displays an optical photograph of an all-solution-processed device at 8 V bias, showing fairly uniform and bright light emission over the entire active area (~0.18 cm^2). This all-solution-processed red PLEC shows high flexibility due to the composite electrode anode. The devices were bent to concave and convex curvatures with 5.0 mm radius for 10 cycles. Compared to the freshly prepared device, the device after 10 cycles of bending still showed

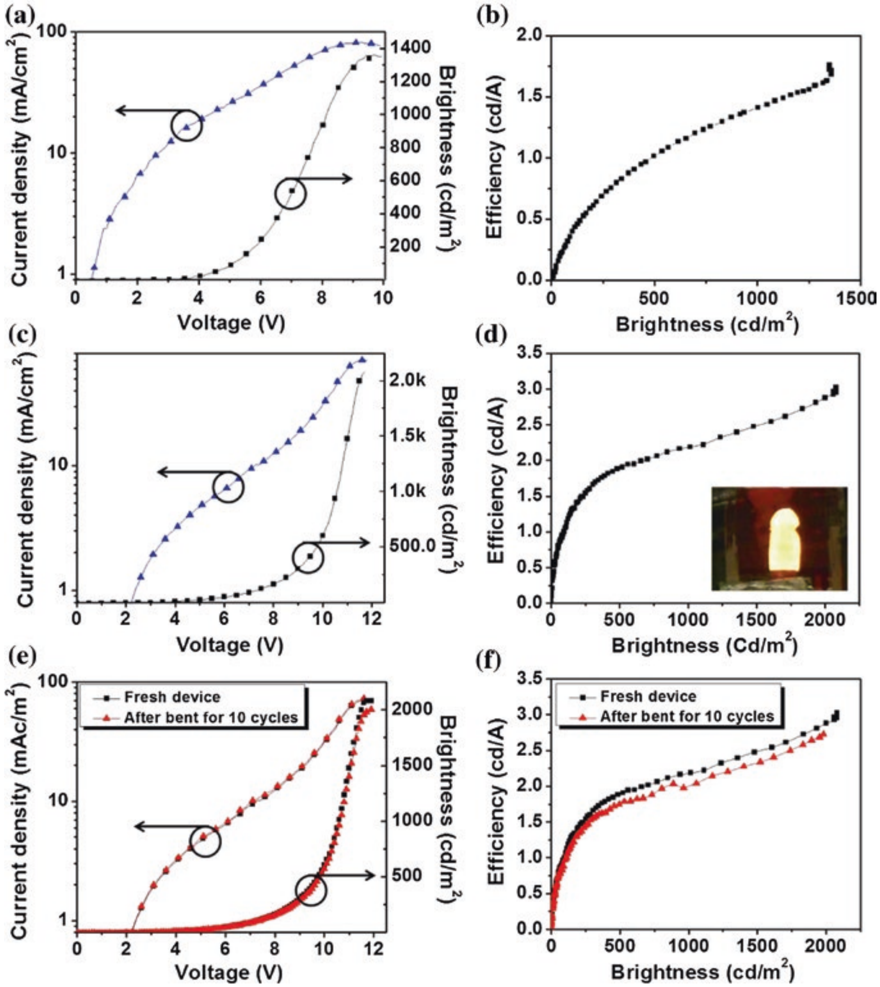

Fig. 4.14 **a** Current density–luminance–driving voltage characteristics and **b** current efficiency–brightness characteristics of a *red* PLEC device using ITO/glass as anode and Ag paste as cathode. Current density–luminance–driving voltage characteristics **c** and current efficiency–brightness characteristics **d** of an all-solution-processed *red* PLEC device, *inset* in **d** shows a photograph of a *red* PLEC driven at 8 V; lighting area ~0.18 cm^2. Current density–luminance–driving voltage characteristics **e** and current efficiency–brightness characteristics **f** of the all-solution-processed *red* PLEC before and after 10 cycles of bending recovery. Reprinted with the permission from [66]. Copyright 2013 American Chemical Society

the same turn-on voltage at 3.0 V. A slight degradation of current efficiency was observed: The maximum current efficiency decreased to 2.73 cd/A as a result of slight increase in current density and reduction in light intensity.

While investigation is still underway to optimize the all-solution processing technique and further improve device performance, the approach presented here may open up a new avenue toward the manufacturing of low-cost scalable polymer light-emitting devices and displays.

4.6 LEC-Enabled Novel Devices: Intrinsically Stretchable PLEC

Ultra-flexible or even stretchable electronics and optoelectronics have emerged as alternative technologies for the next generation of electronic applications [67–70]. In practice, stretchability is much more challenging to obtain than flexibility. While flexible displays normally need to withstand strains of no more than 1 %, skin-like stretchable displays must be able to endure strains greater than 10 %. The realization of stretchable displays would not only permit significantly more durable and even unbreakable devices to be achieved. To fabricate stretchable electronics, it is important to make the devices mechanically compliant and capable of stretching without undergoing physical damage [71]. Combining elastic interconnects with discrete rigid inorganic LEDs or OLEDs has been used in the manufacture of stretchable displays [72–76]. The rigid and brittle LEDs are embedded in or bonded onto the surface of soft rubbery polymers. The resulting displays and lighting systems show high stretchability and efficiency. However, these types of devices may encounter problems such as choppy device surface, large stress concentration at the rigid–soft interfaces that could cause crack formation or even fracture during repeated deformation and limited elongation.

An alternative approach to achieving stretchable displays is based on a different kind of mechanics, whereby intrinsically stretchable light-emitting devices are fabricated in which all the constituent materials are elastic. An external deformation of the light-emitting device causes more or less the same amount of strain in all constituent materials, including the electrodes, light-emitting semiconductor, and substrate. One of the major obstacles to fabricating stretchable light-emitting devices and displays had been the lack of an elastic transparent electrode that combines high visual transparency, good surface electrical conductivity, high stretchability, and high surface smoothness. These are all essential features for the fabrication of stretchable optoelectronics. Several alternative materials, including carbon nanotube, graphene, and conducting polymer, have been investigated to make stretchable transparent electrodes, with varied success [77–79].

By embedding a layer of SWNT into the surface layer an shape memory polymer substrate, Yu et al. developed an intrinsically stretchable PLEC device where all components in the PLEC, including the substrate, the electrodes, and the emissive polymer film, were intrinsically stretchable [80] (Fig. 4.15) by sandwiching an electroluminescent polymer blend layer between two composite electrodes. The device was shown stretchable by up to 45 % linear strain with uniform light emission at 70 °C, which is the transition glass temperature of the shape memory polymer substrate (Fig. 4.16). However, the limited stretchability and conductivity of SWNT/polymer composite electrodes, low electroluminescent performance, or

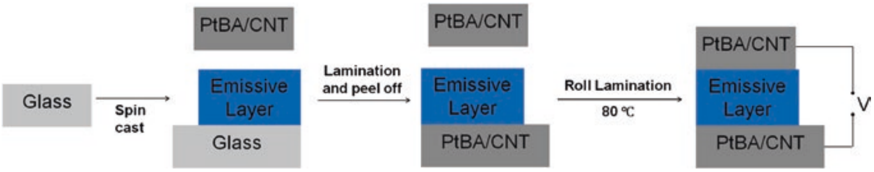

Fig. 4.15 Schematic illustration of fabricating a fully stretchable PLEC

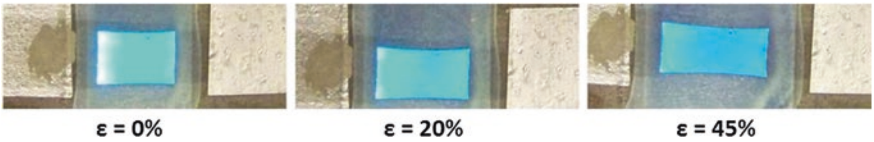

Fig. 4.16 Photographs of a PLEC being operated at 8 V and stretched uniaxially. Reproduced from [80] by permission of John Wiley and Sons Ltd

complicated processing methods still constitute significant obstacles to the fabrication of a stretchable display based on this light-emitting device architecture.

Through inlaying a thin percolation network of AgNW in the surface layer of a rubbery polyurethane matrix, AgNW/rubber composite electrodes have been developed to meet all the requirements for the fabrication of high-performance and stretchable light-emitting devices [81–85]. Silver nanowires with a length-to-diameter aspect ratio of approximately 500 were used to form a conductive silver nanowire network percolation network with high electrical conductivity and mechanical compliancy. According to a model for a one-dimensional random network [86], the surface nanowire percolation density is inversely proportional to the length of the AgNWs. The COMSOL numerical simulation also shows that a percolation network made from longer nanowires has better compliancy than one made from shorter nanowires [87].

This AgNW/rubber composite electrode with 15 ohm/sq resistance exhibits a transmittance higher than 81 % in the range of 500–1,000 nm, which is comparable to those of ITO/glass and better than commercial ITO/PET electrodes. Embedding the AgNW networks in the elastomeric matrix can limit the degree of junction disjointing and nanowire sliding under large strain and thus can increase the stretchability of the AgNW network [82–85]. The 15 ohm/sq composite electrodes can be stretched to as much as 100 % strain, while sheet resistance remains below 1 kohm/sq. Moreover, since the elastomeric composite electrodes have a conductive surface that replicates the surface of the release glass substrates, the surface roughness of the composite electrodes was found to be less than 5 nm. No cracks, voids, or buckling patterns were observable on the surface. Stretching–releasing cycles to 30 % strain did not significantly increase the roughness [85]. Thus, this AgNW/rubber composite electrode has high visual transparency, good surface electrical conductivity, high stretchability, and high surface smoothness, all features essential to the fabrication of the stretchable LEC device.

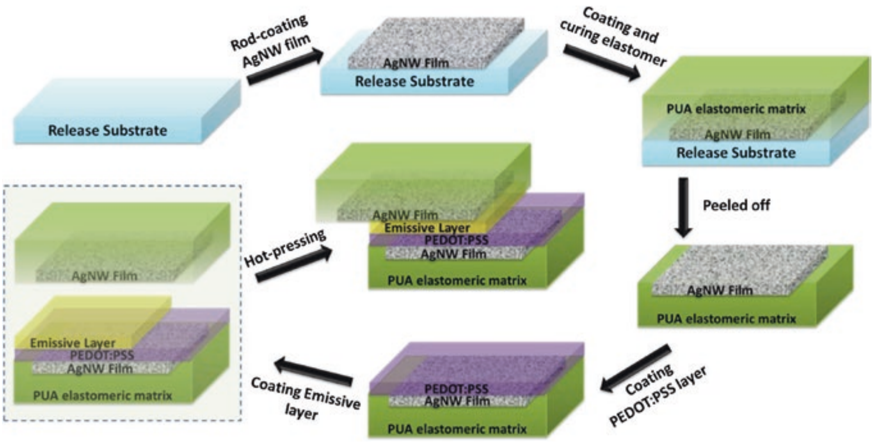

Fig. 4.17 Schematic illustration of the fabrication process of an elastic transparent AgNW–PUA composite electrode and a stretchable PLEC device based on AgNW–PUA composite electrode. The processes are all-solution based. Reprinted by permission from Macmillan Publishers Ltd: [84], Copyright 2013

The process of fabricating elastomeric PLEC, as illustrated in Fig. 4.17, started with spin-coating a thin layer of poly(3,4-ethylenedioxythiophene):poly(styrenesulfonate) (PEDOT:PSS) on a AgNW/polyurethane acrylate (PUA) composite electrode as an anode. The thin PEDOT layer helped protect the PUA matrix from solvent attack in the subsequent coating of the electroluminescent polymer layer. The electroluminescent polymer layer consisted of a blend of a SY-PPV ethoxylated trimethylolpropanetriacrylate (ETPTA), PEO, and LiTf. SY-PPY was selected for its very high molecular weight, which is suitable for large-strain stretchability. ETPTA was chosen for its capability to conduct ions and to polymerize to form a highly cross-linked polymer network that ceases to conduct ions. This property is important for the formation of a stable p-i-n junction. PEO, an ionic conductor widely used in PLECs, was added to enhance the stretchability of the cross-linked ETPTA network. A second AgNW–PUA composite electrode (as cathode) was stacked onto the emissive polymer layer, face down and hot-pressed and laminated to complete the device fabrication.

The PLEC was initially driven at a constant current to establish a p-i-n junction in the emissive polymer layer. Light emission in this device turns on at 6.8 V and reaches a peak brightness of 2,200 cd/m^2 at 21 V. The current efficiency reaches 5.7 cd/A at the maximum brightness. Both charge injection electrodes of the PLEC are transparent, and the emissive layer is semitransparent. The PLEC is thus semitransparent, as can be seen from the inset of Fig. 4.18b. Light produced in the electroluminescent polymer layer escapes from both surfaces of the device with nearly identical brightness and efficiency. The actual maximum external current efficiency of the stretchable PLEC at the maximum brightness thus should account for emissions from both surfaces and adds up to 11.4 cd/A. The calculated external

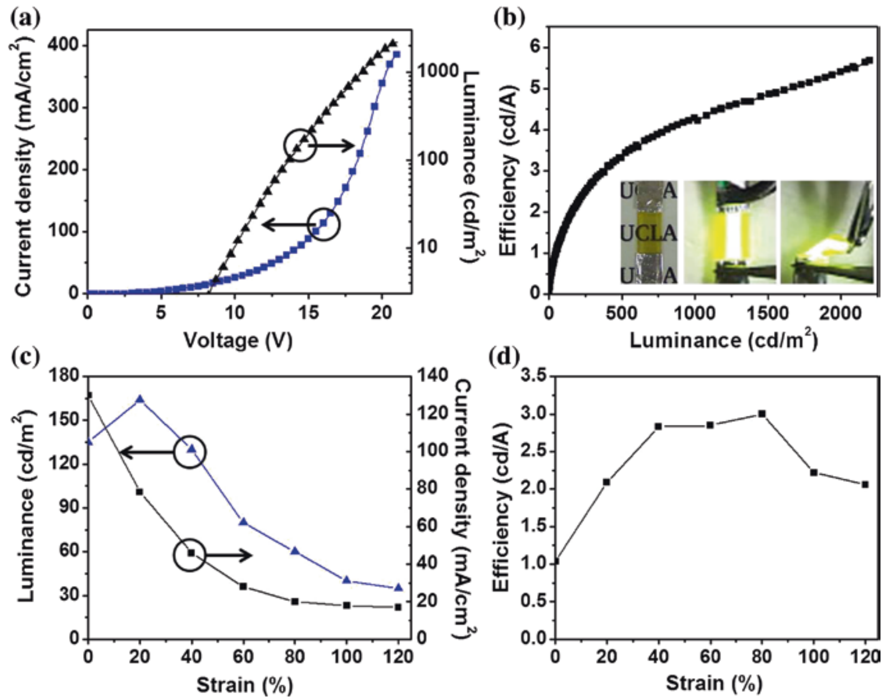

Fig. 4.18 **a** Current density–luminance–driving voltage characteristics of an elastomeric PLEC device. **b** Current efficiency–luminance characteristics of the device. Insets: photographs of the PLEC (original emission area, 3.0 × 7.0 mm^2) unbiased, biased at 12 V, and deformed to show light emission from both surfaces. **c** Current density and luminance characteristics of a PLEC device at 12 V with increasing strain. **d** Current efficiency characteristics of the device with strain. Reprinted by permission from Macmillan Publishers Ltd: [84], Copyright 2013

quantum efficiency is 4.0 %. This performance is comparable to state-of-the-art PLEC based on SY-PPY and fabricated on ITO/glass substrate as anode and evaporated aluminum as cathode.

Moreover, the stretchable LEC device is bendable and can be folded around a cardboard (thickness ~400 μm) without causing any damage to its mechanical integrity or electrical properties. The PLEC device can be uniaxially stretched up to 120 % strain with uniform bright emission across the entire luminous area at strains up to 120 % (Fig. 4.19). When biased at 12 V, the PLEC shows an initial increase of brightness from 0 to 20 % strain and then decreases as the strain is further increased. Interestingly, the current efficiency shows a 200 % increase, from 1.0 cd/A before stretching to 3.0 cd/A at 40 % strain. It levels off up to 80 % strain and then begins to decrease, but still remains at a fairly high value of 2.1 cd/A at 120 % strain, which is still 100 % higher than its original value. An investigation of charge injections indicates that the increasing current efficiency with strain probably results from a more balanced injection of electrons and holes when the

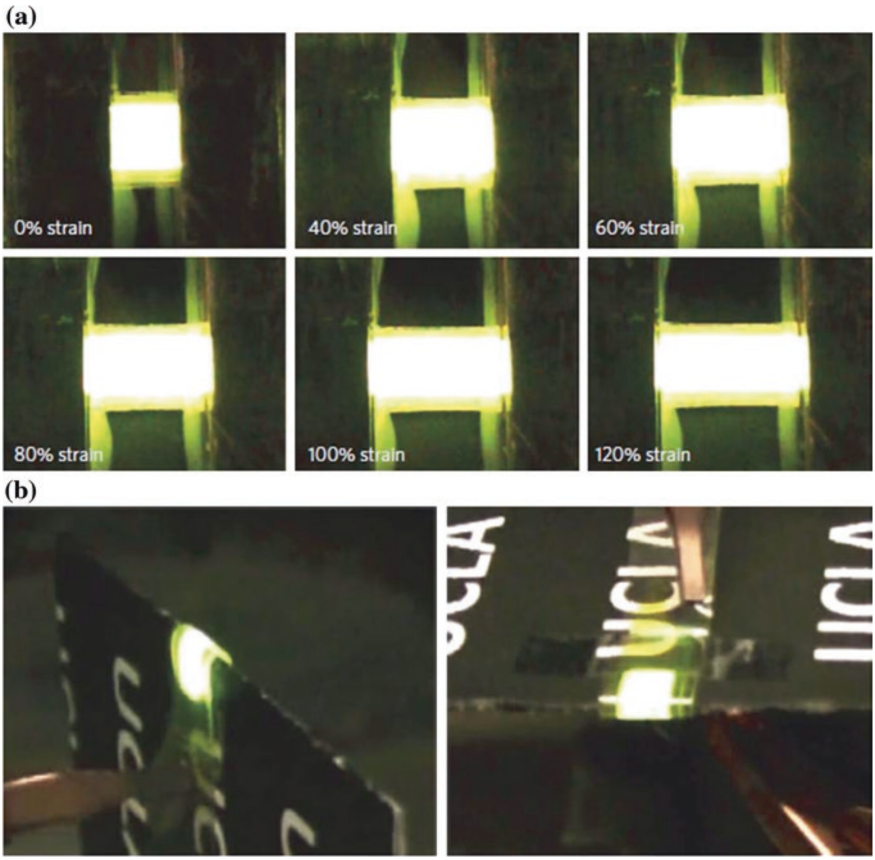

Fig. 4.19 **a** Photographs of a PLEC (original emission area, 5.0 × 4.5 mm^2) biased at 14 V at specified strains. **b** Images of a PLEC (original emission area of 3.0 × 7.0 mm^2, biased at 12 V) wrapped around the edge of 400-mm-thick cardboard. All measurements were carried out at room temperature. Reprinted by permission from Macmillan Publishers Ltd: [84], Copyright 2013

device was under strain. The charge carrier transport characteristics of the emissive material are displayed in Fig. 4.20. Figure 4.20a is for a hole-dominated device. The device structure is AgNW–PUA composite electrode/PEDOT:PSS/Emissive material/AgNW–PUA composite electrode. The LUMO energy level of the emissive materials is around 2.7 eV, and the work function of AgNW is around 4.2 eV. The electron-injection barrier is 1.5 eV. The current density is dominated by hole injection. Apparently, the hole injection current decreases with strain from 0 to 100 % strain. The device structure for Fig. 4.20b is AgNW–PUA composite electrode/Emissive material/PEI/AgNW–PUA composite electrode. Herein, electron injection is assisted by polyethylenimine (PEI) [88]. The HOMO energy level of the emissive material is 5.2 eV. The hole injection barrier is 1 eV. Therefore, the current density of the device is dominated by or significantly dependent on

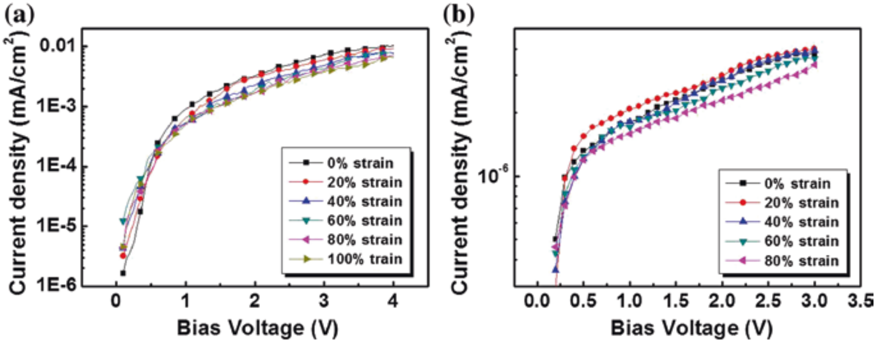

Fig. 4.20 **a** Current density versus bias voltage responses of a hole-dominated stretchable device under various strains. **b** Current density versus bias voltage responses of an electron-dominated stretchable device under various strains

electron injection. With the strain increasing, the electron injection is enhanced from 0 to 20 % strain and then turns to decrease at higher strains.

The PLEC can be repeatedly stretched between 0 and 30 % strain for 1,000 continuous cycles (Fig. 4.21a). Both the brightness and current efficiency of the device decreased steeply in the following 50 cycles and remained fairly stable in the subsequent 950 cycles. SEM imaging was used to study the microstructural changes of the emissive layer after the PLECs had been subjected to 0, 1, 10, 100, and 200 strain cycles between 0 and 30 %. The top view of SEM images in Fig. 4.22 shows that the emissive layer has a fairly smooth surface texture before and after 1 strain cycle. After 10 strain cycles, pinholes are observed at a density of about 30 pinholes/μm^2 and increased to 70 and 100 pinholes/μm^2 after 100 and 200 strain cycles, respectively. The size of the pinholes also increases with strain cycles. The formation of pinholes, as well as the gradual increase of the sheet resistance of the composite electrodes, are considered being responsible for

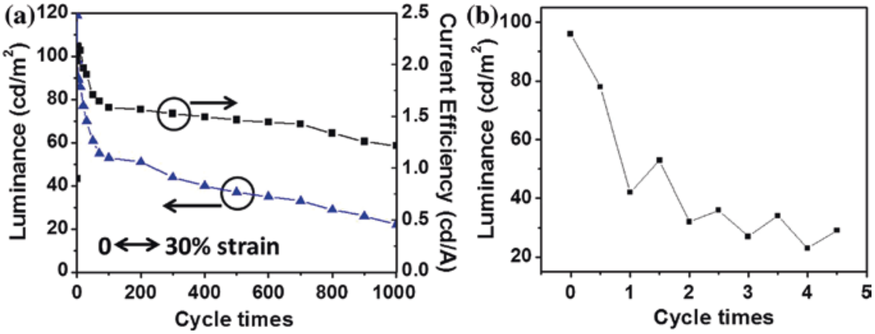

Fig. 4.21 **a** Plots of the luminance and current efficiency at 0 % strain during 1,000 continuous cycles of stretching–relaxing between 0 and 30 % strains. The bias voltage is 12 V. **b** Luminance characteristics of a PLEC device during 5 stretch–relaxation cycles between 0 and 40 % strains, driven at constant 12 V

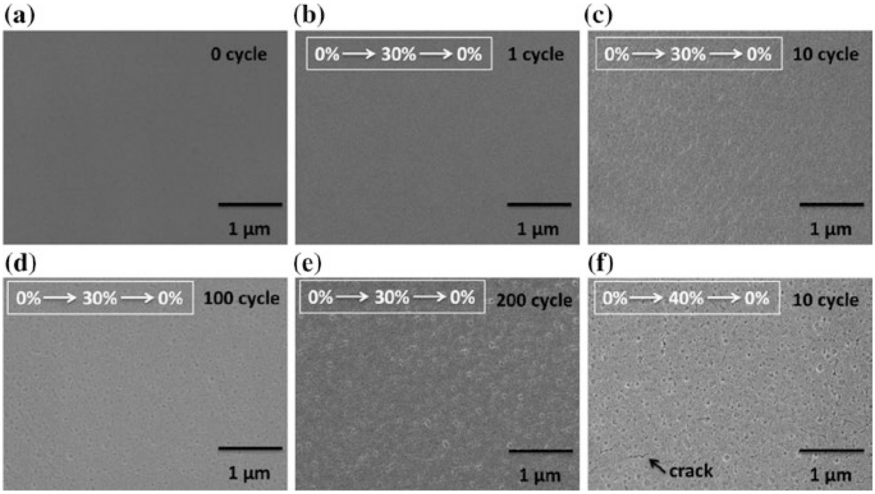

Fig. 4.22 SEM images of (**a**) the top view of unstretched emissive layer of an composite electrode and the top view of emissive layer on composite electrode after (**b**) 1 strain cycles, (**c**) 10 strain cycles, (**d**) 100 strain cycles, and (**e**) 200 strain cycles between 0 and 30 %. (**e**) SEM images of the top view of emissive layer on composite electrode after 10 strain cycles between 0 and 40 %. The samples were prepared by carefully peeling off the top AgNW–PUA composite electrode (cathode) from the PLEC device after continuous stretching–relaxation operation. The emissive layer sticks to the PEDOT layer on the composite electrode anode

the performance degradation of the PLECs over continuous strain cycles. When the strain is 40 % or larger, the EL performance of the devices rapidly deteriorated (Fig. 4.21b). SEM top view image of the emissive layer after 10 strain cycles between 0 and 40 % displayed in Fig. 4.22f shows the formation of pinholes and cracks after 10 stretching cycles. These results put an upper limit of ~30 % strain for the PLECs in cyclic deformation.

High-performance elastomeric PLECs can be fabricated through a relatively simple, all-solution-based process. A key development is the elastomeric transparent composite electrodes that combine high optical transmittance, surface electrical conductivity, surface smoothness, and rubbery elasticity, all essential for the fabrication of organic thin-film electronic devices. The ability to form a light-emitting p-i-n junction in situ in the emissive polymer layer simplifies the device architecture. There are plenty of opportunities to further increase the efficiency and stretchability.

4.7 Concluding Remarks

The polymer light-emitting electrochemical cell provides a different access to light emission assisted by mixed electronic and ionic conductivities in the active polymer layer. The PLEC is operated via an in situ electrochemical doping process and the formation of a p-i-n junction. This unique operation mechanism enables devices with a planar structure which facilitates the direct observation and investigation of the junction formation. The junction formation allows the use of air-stable electrodes for efficient charge injections, particularly the injection of electrons into the LUMO of the conjugated polymers. The emissive polymer layer can be made fairly thick, thus opening the door for low-cost fabrication using conventional printing and other industrial processes. However, the dynamic nature of the junction leads to slow turn-on and poor stability.

The performance of an LEC such as brightness and efficiency can be significantly improved by controlling the morphology of the active layer or freezing the ionic mobility after the p-i-n junction formation. Morphological control can be obtained by employing electrolytes or ionic conductors that are compatible with the conjugated polymers. Conjugated polymers containing covalently bonded ionic species or polar side groups are also useful to administer the compatibility among the mixed conductors in PLECs. Stabilization of p-i-n junction can be achieved by temperature controls or by employing polymerizable salts or ionic conductors. The use of ionic conductors containing methacrylate or acrylate functional groups turns out to be the most effective to stabilize the p-i-n junction and enhance the overall performance of the PLECs. PLECs with a fixed junction retained the simple device architecture of PLECs while exhibit the high efficiency and long lifetime at high brightness characteristic of state-of-the-art PLEDs.

The freedom in electrode selection for PLECs allows the fabrication of OLEDs without the use of high vacuum. Solution-processable conducting materials, such as silver paste, PEDOT:PSS, could be printed on as the cathode. Solution-processable SWNT, graphene, and metallic nanowire coating can also be used as the cathode, as well as the anode. These make it possible to fabricate flexible LEC using solution-based processes such as blade coating, printing, and roll-to-roll coating.

PLECs fabricated by sandwiching the emissive layer between a pair of stretchable transparent composite electrode exhibit both high EL performance and mechanical stretchability. These are the first ever intrinsically stretchable light-emitting devices.

Going forward, the PLECs could be further improved through new materials development. We are confident that these devices will find their niche applications where low cost or stretchability is paramount.

Acknowledgments The authors acknowledge the financial supports by the Air Force Office of Scientific Research (FA9550-12-1-0074) and National Science Foundation (ECCS-1028412).

References

1. G. Gu, Z.L. Shen, P.E. Burrows, S.R. Forrest, Transparent flexible organic light-emitting devices. Adv. Mater. **9**, 725–728 (1997)
2. G. Gustafsson, Y. Cao, G.M. Treacy, F. Klavetter, N. Colaneri, A.J. Heeger, Flexible light-emitting-diodes made from soluble conducting polymers. Nature **357**, 477–479 (1992)

3. Z. Yu, L. Hu, Z. Liu, M. Sun, M. Wang, G. Gruner, Q. Pei, Fully bendable polymer light emitting devices with carbon nanotubes as cathode and anode. Appl. Phys. Lett. **95**, 203–304 (2009)
4. Q. Pei, G. Yu, C. Zhang, Y. Yang, A.J. Heeger, Polymer light-emitting electrochemical-cells. Science **269**, 1086–1088 (1995)
5. http://www.add-vision.com/
6. Q. Sun, Y. Li, Q. Pei, Polymer light-emitting electrochemical cells for high-efficiency low-voltage electroluminescent devices. J Display Tech **3**, 211–224 (2007)
7. Q. Pei, A.J. Hegger, Operating mechanism of light-emitting electrochemical cells. Nat. Mater. **7**, 167–167 (2008)
8. Q. Pei, Y. Yang, G. Yu, C. Zhang, A.J. Heeger, Polymer light-emitting electrochemical cells: in situ formation of a light-emitting p-n junction. J. Am. Chem. Soc. **118**, 3922–3929 (1996)
9. Q. Pei, Y. Yang, G. Yu, Y. Cao, A.J. Heeger, Solid state polymer light-emitting electrochemical cells: recent developments. Synth. Met. **85**, 1229–1232 (1997)
10. D.J. Dick, A.J. Heeger, Y. Yang, Q. Pei, Imaging the structure of the p-n junction in polymer light-emitting electrochemical cells. Adv. Mater. **8**, 985–987 (1996)
11. J. Gao, J. Dane, Imaging the doping and electroluminescence in extremely large planar polymer light-emitting electrochemical cells. J. Appl. Phys. **98**, 063513 (2005)
12. P. Matyba, K. Maturova, M. Kemerink, N.D. Robinson, L. Edman, The dynamic organic p-n junction. Nat. Mater. **8**, 672–676 (2009)
13. N.E. Tokel, A.J. Bard, Electrogenerated Chemiluminescence. IX. Electrochemistry and emission from systems containing Tris(2,2'-bipyridine)ruthenium(II) dichloride. J. Am. Chem. Soc. **94**, 2862–2863 (1972)
14. T. Hu, L. He, L. Duan, Y. Qiu, Solid-state light-emitting electrochemical cells based on ionic iridium(III) complexes. J. Mater. Chem. **22**, 4206–4215 (2012)
15. J. Slinker, D. Bernards, P.L. Houston, H.D. Abruna, S. Bernhard, G.G. Malliaras, Solid-state electroluminescent devices based on transition metal complexes. Chem. Commun. **19**, 2392–2399 (2003)
16. S. Bernhard, X. Gao, G.G. Malliaras, H.D. Abruna, Efficient electroluminescent devices based on a chelated osmium(II) complex. Adv. Mater. **14**, 433–436 (2002)
17. Q. Zhang, Q. Zhou, Y. Cheng, L. Wang, D. Ma, X. Jing, F. Wang, Highly efficient electroluminescence from green-light-emitting electrochemical cells based on Cu-I complexes. Adv. Funct. Mater. **16**, 1203–1208 (2006)
18. Y. Cao, Q. Pei, M.R. Andersson, G. Yu, A.J. Heeger, Light-emitting electrochemical cells with crown ether as solid electrolyte. J. Electrochem. Soc. **144**, L317–L320 (1997)
19. L. Collie, D. Parker, C. Tachon, H.V.S. Hubbard, G.R. Davies, I.M. Ward, S.C. Wellings, Synthesis and lithium transport in ionically conducting crown-ether polymers. Polymer **34**, 1541–1543 (1993)
20. S. Panozzo, M. Armand, O. Stephan, Light-emitting electrochemical cells using a molten delocalized salt. Appl. Phys. Lett. **80**, 679–681 (2002)
21. T. Ouisse, T.M. Armand, Y. Kervella, O. Stephan, Fully transparent, organic light-emitting electrochemical cells. Appl. Phys. Lett. **81**, 3131–3133 (2002)
22. T. Ouisse, O. Stephan, M. Armand, J.C. Lepretre, Double-layer formation in organic light-emitting electrochemical cells. J. Appl. Phys. **92**, 2795–2802 (2002)
23. C. Yang, Q. Sun, J. Qiao, Y. Li, Ionic liquid doped polymer light-emitting electrochemical cells. J Phys Chem B **107**, 12981–12988 (2003)
24. J.M. Leger, D.B. Rodovsky, G.P. Bartholomew, Self-assembled, chemically fixed homojunctions in semiconducting polymers. Adv. Mater. **18**, 3130–3134 (2006)
25. J.M. Leger, D.G. Patel, D.B. Rodovsky, G.P. Bartholomew, Polymer photovoltaic devices employing a chemically fixed p-i-n junction. Adv. Funct. Mater. **18**, 1212–1219 (2008)
26. I. Kosilkin, M. Martens, M. Murphy, J. Leger, Polymerizable ionic liquids for fixed-junction polymer light-emitting electrochemical cells. Chem. Mater. **22**, 4838–4840 (2010)
27. G. Yu, Y. Cao, M. Andersson, J. Gao, A.J. Heeger, Polymer light-emitting electrochemical cells with frozen p-i-n junction at room temperature. Adv. Mater. **10**, 385–388 (1998)

28. Z. Yu, M. Sun, Q. Pei, Electrochemical formation of stable p-i-n junction in conjugated polymer thin films. J Phys Chem B **113**, 8481–8486 (2009)
29. Z. Yu, M. Wang, G. Lei, J. Liu, L. Li, Q. Pei, Stabilizing the dynamic p-i-n junction in polymer light emitting electrochemical cells. J Phys Chem Lett **2**, 367–372 (2011)
30. S. Tang, K. Irgum, L. Edman, Chemical stabilization of doping in conjugated polymers. Org. Electron. **11**, 1079–1087 (2010)
31. H. Spreitzer, H. Becker, E. Kluge, W. Kreuder, H. Schenk, R. Demandt, H. Schoo, Soluble phenyl-substituted PPVs—New materials for highly efficient polymer LEDs. Adv. Mater. **10**, 1340–1343 (1998)
32. A. Sandström, P. Matyba, L. Edman, Yellow-green light-emitting electrochemical cells with long lifetime and high efficiency. Appl. Phys. Lett. **96**, 053303 (2010)
33. K. Walzer, B. Maennig, M. Pfeiffer, K. Leo, Highly efficient organic devices based on electrically doped transport layers. Chem. Rev. **107**, 1233–1271 (2007)
34. S. Reineke, F. Lindner, G. Schwartz, N. Seidler, K. Walzer, B. Lussem, K. Leo, White organic light-emitting diodes with fluorescent tube efficiency. Nature **459**, 234–238 (2009)
35. J. Liu, L.N. Lewis, T.J. Faircloth, A.R. Duggal, High performance organic light-emitting diodes fabricated via a vacuum-free lamination process. Appl. Phys. Lett. **88**, 223509 (2006)
36. F. Huang, H. Wu, D. Wang, W. Yang, Y. Cao, Novel electroluminescent conjugated polyelectrolytes based on polyfluorene. Chem. Mater. **16**, 708–716 (2004)
37. H. Wu, F. Huang, Y. Mo, W. Yang, D. Wang, J. Peng, Y. Cao, Efficient electron injection from a bilayer cathode consisting of aluminum and alcohol-/water-soluble conjugated polymers. Adv. Mater. **16**, 1826–1930 (2004)
38. W. Zeng, H. Wu, C. Zhang, F. Huang, J. Peng, W. Yang, Y. Cao, Polymer light-emitting diodes with cathodes printed from conducting Ag paste. Adv. Mater. **19**, 810–814 (2007)
39. T. Lee, J. Zaumseil, Z. Bao, J. Hsu, J.A. Rogers, Organic light-emitting diodes formed by soft contact lamination. PNAS **101**, 429–433 (2004)
40. J. Fang, P. Matyba, L. Edman, The design and realization of flexible, long-lived light-emitting electrochemical cells. Adv. Funct. Mater. **19**, 2671–2676 (2009)
41. S. Graber, K. Doyle, M. Neuburger, C.E. Housecroft, E.C. Constable, R.D. Costa, E. Orti, D. Repetto, H.J. Bolink, A supramolecularly-caged ionic iridium (III) complex yielding bright and very stable solid-state light-emitting electrochemical cells. J. Am. Chem. Soc. **130**, 14944–14945 (2008)
42. Y. Shao, G.C. Bazan, A.J. Heeger, Long-lifetime polymer light-emitting electrochemical cells. Adv. Mater. **19**, 365–370 (2007)
43. D.R. Cairns, R.P. Witte, D.K. Sparacin, S.M. Sachsman, D.C. Paine, G.P. Crawford, R.R. Newton, Strain-dependent electrical resistance of tin-doped indium oxide on polymer substrates. Appl. Phys. Lett. **76**, 1425–1427 (2000)
44. V.C. Moore, M.S. Strano, E.H. Haroz, R.H. Hauge, R.E. Smalley, J. Schmidt, Y. Talmon, Individually suspended single-walled carbon nanotubes in various surfactants. Nano Lett. **3**, 1379–1382 (2003)
45. Z.C. Wu, Z.H. Chen, X. Du, J.M. Logan, J. Sippel, M. Nikolou, K. Kamaras, J.R. Reynolds, D.B. Tanner, A.F. Hebard, A.G. Rinzler, Transparent, conductive carbon nanotube films. Science **305**, 1273–1276 (2004)
46. M. Kaempgen, G.S. Duesberg, S. Roth, Transparent carbon nanotube coatings. Appl. Surf. Sci. **252**, 425–429 (2005)
47. L. Hu, W. Yuan, P. Brochu, G. Gruner, Q. Pei, Highly stretchable, conductive, and transparent nanotube thin films. Appl. Phys. Lett. **94**, 161108 (2009)
48. W. Yuan, L. Hu, Z. Yu, T. Lam, J. Biggs, S. Ha, D. Xi, B. Chen, M.K. Senesky, G. Gruner, Q. Pei, Fault-tolerant dielectric elastomer actuators using single-walled carbon nanotube electrodes. Adv. Mater. **20**, 621–625 (2008)
49. K. Lee, Z. Wu, Z. Chen, F. Ren, S.J. Pearton, A.G. Rinzler, Single wall carbon nanotubes for p-type ohmic contacts to GaN light-emitting diodes. Nano Lett. **4**, 911–914 (2004)
50. C.M. Aguirre, S. Auvray, S. Pigeon, R. Izquierdo, P. Desjardins, R. Martel, Carbon nanotube sheets as electrodes in organic light-emitting diodes. Appl. Phys. Lett. **88**, 183104 (2006)

51. D. Zhang, K. Ryu, X. Liu, E. Polikarpov, J. Ly, M.E. Tompson, C.W. Zhou, Transparent, conductive, and flexible carbon nanotube films and their application in organic light-emitting diodes. Nano Lett. **6**, 1880–1886 (2006)
52. J. Li, L. Hu, L. Wang, Y. Zhou, G. Gruner, T.J. Marks, Organic light-emitting diodes having carbon nanotube anodes. Nano Lett. **6**, 2472–2477 (2006)
53. A.D. Pasquier, H.E. Unalan, A. Kanwal, S. Miller, M. Chhowalla, Conducting and transparent single-wall carbon nanotube electrodes for polymer-fullerene solar cells. Appl. Phys. Lett. **87**, 203511 (2005)
54. M.W. Rowell, M.A. Topinka, M.D. McGehee, H.J. Prall, G. Dennler, N.S. Sariciftci, L. Hu, G. Gruner, Organic solar cells with carbon nanotube network electrodes. Appl. Phys. Lett. **88**, 233506 (2006)
55. C. Yu, C. Masarapu, J. Rong, B. Wei, H. Jiang, Stretchable supercapacitors based on buckled single-walled carbon nanotube macrofilms. Adv. Mater. **21**, 4793–4797 (2009)
56. Z. Yu, Z. Liu, M. Wang, M. Sun, G. Lei, Q. Pei, Highly flexible polymer light-emitting devices using carbon nanotubes as both anodes and cathodes. J Photon Energy **1**, 011003 (2011)
57. K.S. Novoselov, A.K. Geim, S.V. Morozov, D. Jiang, Y. Zhang, S.V. Dubonos, I.V. Grigorieva, A.A. Firsov, Electric field effect in atomically thin carbon films. Science **306**, 666–669 (2004)
58. A.K. Geim, Graphene: status and prospects. Science **324**, 1530–1534 (2009)
59. S. Stankovich, D.A. Dikin, R.D. Piner, K.M. Kohlhaas, A. Kleinhammes, Y. Jia et al., Synthesis of graphene-based nanosheets via chemical reduction of exfoliated graphite oxide. Carbon **45**(7), 1558–1565 (2007)
60. P. Matyba, H. Yamaguchi, G. Eda, M. Chhowalla, L. Edman, N.D. Robinson, Graphene and Mobile Ions: the key to all-plastic solution-processed light-emitting devices. ACS Nano **4**, 637–642 (2010)
61. S. De, T.M. Higgins, P.E. Lyons, E.M. Doherty, P.N. Nirmalraj, W.J. Blau, J.J. Boland, J.N. Coleman, Silver nanowire networks as flexible, transparent, conducting films: extremely high DC to optical conductivity ratios. ACS Nano **3**, 1767–1774 (2009)
62. H. Wu, L. Hu, M.W. Rowell, D. Kong, J.J. Cha, J.R. McDonough, J. Zhu, Y. Yang, M.D. McGehee, Y. Cui, Electrospun metal nanofiber webs as high-performance transparent electrode. Nano Lett. **10**, 4242–4248 (2010)
63. Z. Yu, L. Li, Q. Zhang, W. Hu, Q. Pei, Silver nanowire-polymer composite electrodes for efficient polymer solar cells. Adv. Mater. **23**, 4453–4457 (2011)
64. Z. Yu, Q. Zhang, L. Li, Q. Chen, X. Niu, J. Liu, Q. Pei, Highly flexible silver nanowire electrodes for shape-memory polymer light-emitting diodes. Adv. Mater. **23**, 664–668 (2011)
65. L. Li, Z. Yu, W. Hu, C.-H. Chang, Q. Chen, Q. Pei, Efficient flexible phosphorescent polymer light-emitting diodes based on silver nanowire-polymer composite electrode. Adv. Mater. **23**, 5563–5567 (2011)
66. J. Liang, L. Li, X. Niu, Z. Yu, Q. Pei, Fully solution-based fabrication of flexible light-emitting device at ambient conditions. J. Phys. Chem. C **117**, 16632–16639 (2013)
67. H.L. Filiatrault, G.C. Porteous, R.S. Carmichael, G.J.E. Davidson, T.B. Carmichael, Stretchable light-emitting electrochemical cells using an elastomeric emissive material. Adv. Mater. **24**, 2673–2678 (2012)
68. T. Someya, Flexible electronics: tiny lamps to illuminate the body. Nature Mater. **9**, 879–880 (2010)
69. R. Sprengard et al., OLED devices for signage applications: a review of recent advances and remaining challenges. Proc. SPIE **5519**, 173–183 (2004)
70. J. Viventi et al. A conformal, bio-interfaced class of silicon electronics for mapping cardiac electrophysiology. Sci. Transl. Med. **2**, 24ra22 (2010)
71. M. Vosgueritchian, J.B.H. Tok, Z. Bao, Stretchable LEDs: light-emitting electronic skin. Nat. Photonics **7**, 769 (2013)
72. R.H. Kim et al., Stretchable, transparent graphene interconnects for arrays of microscale inorganic light emitting diodes on rubber substrates. Nano Lett. **11**, 3881–3886 (2011)

73. R.H. Kim et al., Waterproof AlInGaP optoelectronics on stretchable substrates with applications in biomedicine and robotics. Nature Mater. **9**, 929–937 (2010)
74. S.I. Park et al., Printed assemblies of inorganic light-emitting diodes for deformable and semitransparent displays. Science **325**, 977–981 (2009)
75. T. Sekitani et al., Stretchable active-matrix organic light-emitting diode display using printable elastic conductors. Nature Mater. **8**, 494–499 (2009)
76. G.S. Jeong et al., Solderable and electroplatable flexible electronic circuit on a porous stretchable elastomer. Nat. Commun. **3**, 997 (2012)
77. K. Liu, Y. Sun, P. Liu, X. Lin, S. Fan, K. Jiang, Cross-stacked superaligned carbon nanotube films for transparent and stretchable conductors. Adv. Funct. Mater. **21**, 2721–2728 (2011)
78. T. Sekitani, Y. Noguchi, K. Hata, T. Fukushima, T. Aida, T. Someya, A rubberlike stretchable active matrix using elastic conductors. Science **321**, 1468–1472 (2008)
79. M.K. Shin, J. Oh, M. Lima, M.E. Kozlov, S.J. Kim, R.H. Baughman, Elastomeric conductive composites based on carbon nanotube forests. Adv. Mater. **22**, 2663–2667 (2010)
80. Z. Yu, X. Niu, Z. Liu, Q. Pei, Intrinsically stretchable polymer light emitting devices using carbon nanotube-polymer composite electrodes. Adv. Mater. **23**, 3989–3994 (2011)
81. J. Liang, L. Li, K. Tong, Z. Ren, W. Hu, X. Niu, Y. Chen, Q. Pei, Silver nanowire percolation network soldered with graphene oxide at room temperature and its application for fully stretchable polymer light-emitting diodes. ACS Nano **8**(2), 1590–1600 (2014)
82. W. Hu, X. Niu, R. Zhao, Q. Pei, Elastomeric transparent capacitive sensors based on an interpenetrating composite of silver nanowires and polyurethane. Appl. Phys. Lett. **102**, 083303 (2013)
83. W. Hu, X. Niu, L. Li, S. Yun, Z. Yu, Q. Pei, Intrinsically stretchable transparent electrodes based on silver-nanowire–crosslinked-polyacrylate composites. Nanotechnology **23**, 344002 (2012)
84. S. Yun, X. Niu, Z. Yu, W. Hu, P. Brochu, Q. Pei, Compliant silver nanowire-polymer composite electrodes for bistable large strain actuation. Adv. Mater. **24**, 1321–1327 (2012)
85. J. Liang, L. Li, X. Niu, Z. Yu, Q. Pei, Elastomeric polymer light-emitting devices and displays. Nat. Photonics **7**, 817–824 (2013)
86. G.E. Pike, C.H. Seager, Percolation and conductivity: a computer study. I. Phys. Rev. B **10**, 1421–1434 (1974)
87. P. Lee et al., Highly stretchable and highly conductive metal electrode by very long metal nanowire percolation network. Adv. Mater. **24**, 3326–3332 (2012)
88. T. Xiong, F.X. Wang, X.F. Qiao, D.G. Ma, A soluble nonionic surfactant as electron injection material for high-efficiency inverted bottom-emission organic light emitting diodes. Appl. Phys. Lett. **93**, 123310 (2008)

Chapter 5
Miniaturized Photonic Circuit Components Constructed from Organic Dye Nanofiber Waveguides

K. Takazawa, J. Inoue and K. Mitsuishi

Abstract Self-assembled nanofibers of organic dye thiacyanine (TC) with lengths of up to $\sim 250\,\mu\text{m}$ function as efficient active waveguides that propagate fluorescence (FL) over their entire lengths along the fiber axis. A spectroscopic investigation of the active waveguiding properties revealed that the FL strongly couples with molecular excitons and propagates in the form of exciton-polaritons. Such long-range propagation of exciton-polaritons at room temperature is rarely observed in inorganic materials. The high stability of the exciton-polaritons in the organic dye nanofibers is attributed to the large longitudinal transverse exciton splitting energy and exciton binding energy with respect to thermal energy. Unlike light propagating in conventional waveguides, exciton-polaritons can pass through bends in nanofibers with micron-scale radii of curvature. Utilizing this property, we fabricated miniaturized photonic circuit components using nanofiber building blocks. The fabricated components, including Mach–Zehnder interferometers and microring resonators, exhibit considerably high performance for their micron-scale dimensions. In addition to such photonic device applications, the organic dye nanofibers are ideal systems for studying the physics underlying strong light–matter interactions. In particular, the highly stable nature of the exciton-polaritons at relatively high temperature offers the possibility of a representative novel quantum phenomenon in their Bose–Einstein condensation (BEC). A theoretical analysis of this exciton-polariton BEC in the nanofiber system is presented in this chapter.

K. Takazawa (✉) · J. Inoue · K. Mitsuishi
National Institute for Materials Science (NIMS), Tsukuba, Japan
e-mail: takazawa.ken@nims.go.jp

J. Inoue
e-mail: inoue.junichi@nims.go.jp

K. Mitsuishi
e-mail: mitsuishi.kazutaka@nims.go.jp

Y.S. Zhao (ed.), *Organic Nanophotonics*, Nano-Optics and Nanophotonics,
DOI 10.1007/978-3-662-45082-6_5

5.1 Introduction

Photonic circuits possess advantages over electronic circuits in terms of bandwidth, resistance to electromagnetic wave interference, and energy consumption. For these reasons, miniaturized photonic circuits are suitable for a number of important device applications in fields such as telecommunication, computing, and sensing [1]. The photonic counterpart of an electric wire is a waveguide, which confines light and transmits it between optical components. Hence, waveguides that can guide and bend light in a microscopic area are essential building blocks in miniaturized photonic circuits. Conventional dielectric waveguides confine light through total internal reflection at the interface between the waveguide and the surrounding media. However, when a waveguide is bent with a radius of curvature smaller than a critical value, which is determined by the difference in refractive index between the waveguide and the surrounding media, a large leakage of guided light, i.e., bending loss, occurs. The bending loss prevents waveguide-based photonic circuits from being miniaturized to the degree of electronic circuits. Thus, waveguide technologies based on different light confinement mechanisms, such as plasmon waveguides [2] and photonic crystal waveguides [3], have been developed extensively to overcome the miniaturization limit.

In this chapter, we present a new approach for guiding and bending light on a subwavelength scale, which will potentially enable photonic circuits to be miniaturized considerably. We use single-crystal organic dye nanofibers that propagate their FL along the nanofiber axis. In conventional waveguides, a waveguide material is required to be as transparent as possible so that the propagation loss due to absorption is minimized. In contrast, organic dye crystals have large oscillator strengths of the exciton transition, seemingly leading to large propagation loss. However, the large oscillator strength leads to a light propagation mechanism that does not occur in transparent waveguides. Namely, the light strongly couples with excitons in the crystals and propagates in the form of exciton-polaritons [4]. We show that this exciton-polariton propagation indeed occurs in single-crystal nanofibers of organic dye thiacyanine (TC) and offers a remarkable advantage for light manipulation in microscopic areas.

First, we describe how TC nanofibers act as exciton-polariton waveguides with low loss at micron-scale bends. Then, we demonstrate that miniaturized photonic circuit components can be fabricated using TC nanofiber building blocks. These photonic circuit components, including Mach–Zehnder interferometers and microring resonators, exhibit considerably high performance for their micron-scale dimensions. Finally, we discuss the future application of organic dye nanofibers to a novel model system to study the physics underlying the strong light–matter interaction. The highly stable nature of the exciton-polaritons in the organic dye nanofibers offers the possibility of a representative novel quantum phenomenon, namely their BEC at relatively high temperature. The exciton-polariton BEC in the nanofiber system is theoretically investigated and the findings are presented.

5.2 Exciton-Polariton Waveguides

5.2.1 Nanofiber Active Waveguides

Waveguides that propagate light coupled from an external light source are referred to as passive waveguides, of which the commonly used silica-based waveguides are typical examples. On the other hand, waveguides that propagate their FL or photoluminescence (PL) are referred to as active waveguides [5]. TC nanofibers are classified as active waveguides because they propagate FL. Here, preceding studies on nanofiber/nanowire active waveguides are briefly introduced. The active waveguiding behavior of self-assembled nanofibers/nanowires was initially observed for inorganic semiconductors such as ZnO [6, 7]. Photonic and optoelectronic device applications of these active waveguides are now being developed. To the best of our knowledge, organic active waveguides were first reported by Yanagi et al. [8] for p-sexiphenyl (6P) nanofibers, which were epitaxially grown on a KCl (001) surface. They observed that on exciting the 6P nanofibers with ultraviolet light, the nanofibers propagate blue PL (λ = 400–600 nm), which can be outcoupled at the end of the nanofiber. Balzer et al. [9, 10] demonstrated that highly aligned 6P nanofibers can be grown epitaxially on mica substrates. They investigated the active waveguiding properties of 6P nanofibers both experimentally and theoretically.

Following these works, our group demonstrated for the first time that organic nanofibers synthesized by a solution-phase process can function as active waveguides. Nanofibers of TC (Fig. 5.1a) self-assembled in solution with submillimeter-scale lengths exhibited efficient active waveguiding behavior, and FL (λ = 480 –600 nm) was propagated along their entire lengths (Fig. 5.1b) [11]. The solution-phase self-assembly has advantages over the epitaxial method in terms of the ease of fabrication and applicability to a wide variety of molecules. In the last decade, organic nanofiber active waveguides have been synthesized from various molecules

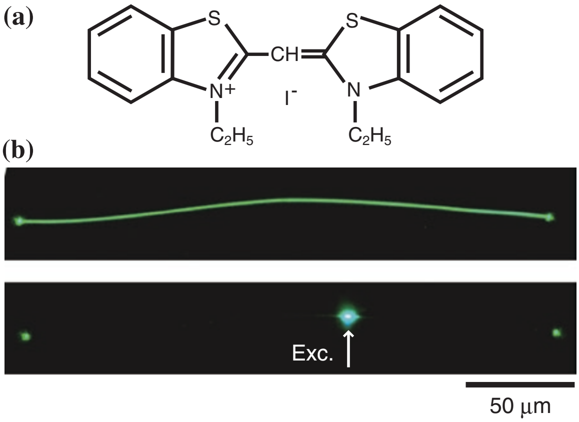

Fig. 5.1 **a** Chemical formula of thiacyanine (TC), **b** FL microscopy image of a TC nanofiber on a glass substrate (*upper panel*), and FL microscopy image of the nanofiber recorded by exciting the point labeled “Exc.” with a laser spot (λ = 405 nm) (*lower panel*)

through both epitaxial and solution-phase processes, and important applications have been reported, such as the lasing of the nanofibers [12, 13] and tuning the wavelength of the guided light by synthesizing nanofibers from multiple compound molecules [14].

5.2.2 Exciton-Polariton Waveguiding in TC Nanofibers

Hereafter, we focus on TC nanofibers and the mechanism of their active waveguiding behavior. TC nanofibers were self-assembled in water [11, 15]. The water solution containing the nanofibers shows an exciton absorption band peaking at ~395 nm, which is blue-shifted from the monomer absorption band (Fig. 5.2a). The blue-shifted absorption band suggests that the nanofiber has an H-aggregate-like internal molecular arrangement. Atomic force microscopy of the nanofibers transferred on a solid support showed that they have rectangular cross sections and typical heights and widths of 100–200 and 100–1,000 nm, respectively [11]. Scanning electron microscopy (SEM) images revealed that the nanofibers have very smooth surfaces (Fig. 5.2b) [16].

Figure 5.3a shows a FL microscopy image of a nanofiber with a length of 92 μm transferred on a glass substrate. Self-assembled organic nanostructures are highly flexible because constituent molecules are held together by non-covalent bonds, such as hydrogen bonds and van der Waals interactions. Due to this high flexibility, nanofibers can easily assume tightly bent shapes. The nanofiber in Fig. 5.3a has three main bends: a 220° bend with $r = 2.0$ μm (A), a 70° bend with $r = 9.0$ μm (B), and a 45° bend with $r = 9.5$ μm (C), where r is the radius of curvature. Figure 5.3b shows a FL microscopy image obtained by exciting a point near the right tip of the nanofiber with a diffraction-limited laser spot ($\lambda = 450$ nm). Interestingly, a bright FL spot was observed at the left tip, indicating that the FL

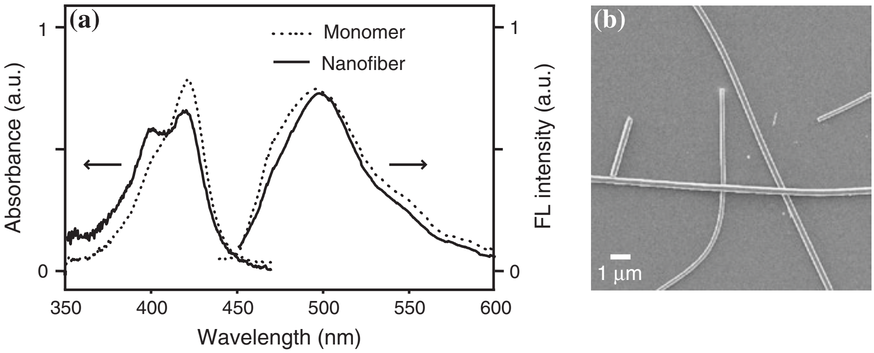

Fig. 5.2 **a** Absorption and FL spectra for a TC nanofiber in solution (*solid curves*) and a TC monomer (*dashed curve*), **b** SEM image of TC nanofibers on a substrate

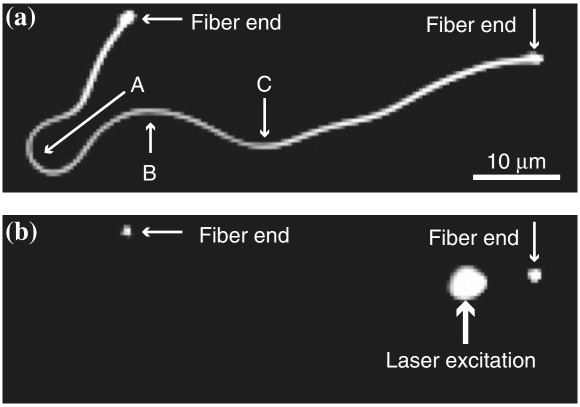

Fig. 5.3 **a** FL microscopy image of a bent nanofiber, **b** FL microscopy image of the nanofiber obtained by exciting the point labeled "laser excitation." Reprinted from [17], Copyright 2008, with permission from Elsevier

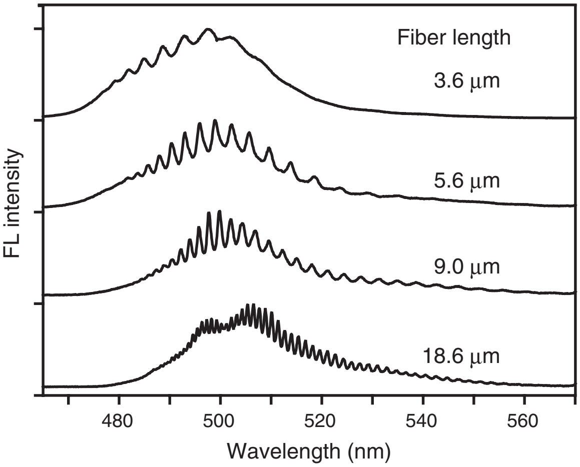

Fig. 5.4 Spectra of the outcoupled light measured for nanofibers of various lengths

passed through these bends with micrometer-scale radii. The refractive indices of organic materials are generally $n \approx 1.5$. If the nanofiber is a simple dielectric waveguide with $n \approx 1.5$, large bending loss should be observed. However, a quantitative investigation showed that no apparent losses associated with these bends occurred [17]. This suggests that the nanofibers are not simple waveguides, and a mechanism specific to this system plays a role.

The active waveguiding mechanism was investigated by measuring the spectra of the light outcoupled from the fiber tips produced by the laser spot excitation. Figure 5.4 shows the spectra of the outcoupled light for nearly straight nanofibers with lengths ranging from 3.6 to 18.6 µm. A series of peaks was observed across the whole broad spectra and the spacing between these peaks decreased with nanofiber length. These peaks are attributed to the Fabry–Perot modes caused by the reflection of guided light at the end faces of the nanofibers.

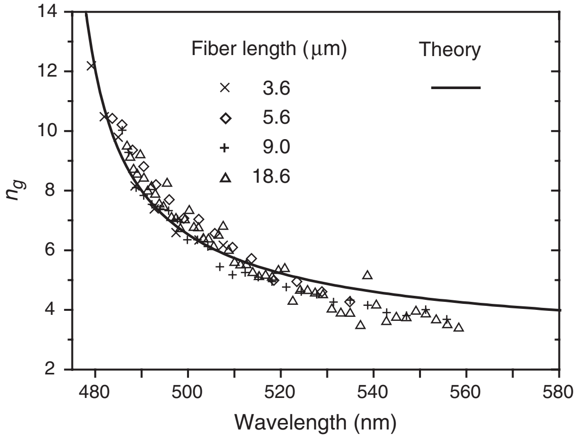

Fig. 5.5 Plot of n_g evaluated from the Fabry–Perot modes for nanofibers of different lengths (*symbols*). The *solid line* was obtained using polariton theory (for details see [18])

The spacing between the Fabry–Perot modes is given by

$$\Delta\lambda = \frac{\lambda^2}{2n_gL}, \tag{5.1}$$

where n_g is the group index and L is the cavity length. From the observed $\Delta\lambda$, n_g was evaluated for each nanofiber using (5.1) (Fig. 5.5). The n_g values obtained from the nanofibers of different lengths form a single curve that divergently increases with decreasing λ (or as approaching the exciton absorption band). n_g exceeds 10 in the short-wavelength region, which is an anomalously large value for simple dielectric waveguides. This is a characteristic feature of n_g for (lower branch) exciton-polaritons [4, 18].

The propagation of exciton-polaritons for a few hundred micrometers through a crystal at room temperature is a rare phenomenon to observe. Although millimeter-scale propagation has been observed in waveguide structures made from inorganic semiconductors, it is only possible at low temperatures due to exciton-polariton instability [19]. Hence, our observation demonstrates that exciton-polaritons in TC nanofibers exhibit remarkable thermal stability. The stability of exciton-polaritons is determined by the magnitude of the longitudinal transverse exciton splitting energy $\Delta E_{L-T} = E_L - E_T$ and the exciton binding energy E_{ex} with respect to the thermal energy k_BT, where k_B is the Boltzmann constant and T is the temperature. ΔE_{L-T} is the energy gap between two anticrossed exciton-polariton dispersion curves, i.e., the upper and lower branches (Fig. 5.6) and is proportional to the oscillator strength of the exciton transition. The exciton-polaritons are stable when both ΔE_{L-T} and E_{ex} are greater than k_BT. Because of the large oscillator strength of organic dyes, the exciton-polaritons in the nanofibers have a significantly large ΔE_{L-T} of a few hundred meV to 1 eV [18, 20].

Moreover, Frenkel excitons formed in organic dye crystals have an E_{ex} in the order of eV. Owing to the fact that ΔE_{L-T} and E_{ex} are much larger than k_BT at

Fig. 5.6 Schematic representation of the dispersion curves of an exciton-polariton

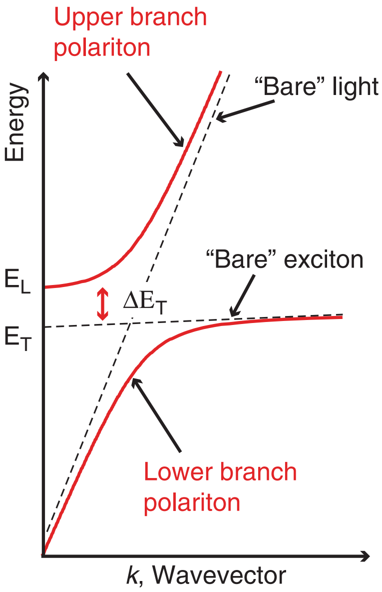

room temperature (~30 meV), the exciton-polaritons in the nanofibers are sufficiently stable to propagate over submillimeter-scale distances. The exciton-polariton formation results in a substantially high refractive index of the nanofiber, which leads to the remarkably low bending loss.

5.3 Miniaturized Photonic Circuit Components Constructed from TC Nanofibers

5.3.1 Asymmetric Mach–Zehnder Interferometers

The low bending loss property of TC nanofibers, which is attributed to exciton-polariton formation, makes them favorable for light manipulation in microscopic areas. In addition, the nanofibers have subwavelength-scale dimensions and high mechanical flexibility. All of these properties make TC nanofibers promising building blocks for miniaturized photonic circuits. To demonstrate this suitability, we fabricated miniaturized photonic circuit components through the micromanipulation of nanofibers on a substrate, performed using a glass probe tip attached to a piezo-micromanipulator under microscope observation [21, 22].

The first photonic circuit component presented is a micron-scale asymmetric Mach–Zehnder interferometer (AMZI). AMZIs are widely used as channel drop filters, modulators, and switching devices [23, 24]. In an AMZI, the input light is split into two beams that are recombined after traveling along paths with different

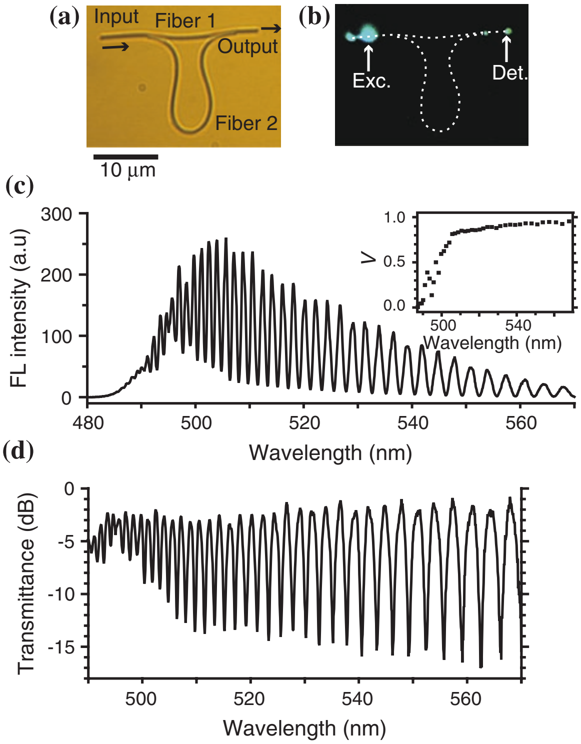

Fig. 5.7 **a** Optical micrograph of the AMZI, **b** FL microscopy image of the AMZI obtained by exciting the point labeled "Exc." with a laser spot, **c** FL spectrum measured at "Det." in a *inset* Plot of the visibility, **d** Transmittance spectrum. Reproduced from [21] by permission of John Wiley & Sons Ltd

lengths. Due to the resulting phase difference between the two beams, they interfere with each other and produce interference fringes in the output signal. To construct a miniaturized AMZI, the waveguides must be bent with small r to create the path length difference. Therefore, TC nanofibers are suitable building blocks because of their low bending loss and high flexibility.

Figure 5.7a shows an optical micrograph of an AMZI fabricated through the micromanipulation of two nanofibers: Fiber 1 (length: 24.1 µm) and Fiber 2 (length: 39.3 µm). The widths of both nanofibers are $d = 210$ nm. Fiber 2 was sharply bent to contact both its ends with Fiber 1. In this device, exciton-polaritons created near the left tip of Fiber 1 are split into two at the first junction through evanescent coupling. After propagating the two different length paths, they are recombined at the second junction. Then, the light is outcoupled from the right tip of Fiber 1 and observed. The path length difference (ΔL) of this device was 26.4 µm and r of the 180° bend in Fiber 2 was ~2.5 µm. Owing to the sharp bend, the footprint of this device is only ~20 µm × 20 µm.

In order to obtain the highest visibility in an AMZI, the input light must be divided equally at the first junction (3-dB coupler). In our nanofiber AMZI, the splitting ratio of the exciton-polaritons at the junction can be tuned by adjusting the contact length between the two nanofibers. We adjusted the contact length of both junctions to ~1 µm.

A point near the left tip of Fiber 1 was excited to produce the exciton-polaritons as shown in Fig. 5.7b. The spectrum, plotted in Fig. 5.7c, was measured at the right tip of Fiber 1 and shows sharp interference fringes over the entire measured range, proving that this device functioned as an AMZI. The visibility of the interference fringes is defined as

$$V = \frac{I_{\max} - I_{\min}}{I_{\max} + I_{\min}}, \tag{5.2}$$

where $I_{\max}$ and $I_{\min}$ are the intensity maxima and minima of the fringe, respectively. The visibility is plotted in the inset of Fig. 5.7c. V was 0.8–1.0 for 510 nm $< \lambda <$ 570 nm, indicating that almost perfect interference occurred in this wavelength region.

The transmittance of the AMZI was determined to evaluate its performance as a channel drop filter by normalizing the output spectrum (Fig. 5.7c) with respect to that of Fiber 1 before Fiber 2 was attached. The result is plotted in dB in Fig. 5.7d. The extinction ratio, defined as $r_e = T_{\max} - T_{\min} (= 10\log I_{\max}/I_{\min})$, was 13–15 dB for 510 nm $< \lambda <$ 570 nm, where $T_{\max}$ and $T_{\min}$ are the transmittance maxima and minima, respectively. These values demonstrate the remarkable performance of this AMZI. The linewidths (3-dB widths) of the drop channels were 1.6 and 0.8 nm at $\lambda = 560$ and 510 nm, respectively.

To confirm that these fringes can be attributed to the interference of the exciton-polaritons, n_g of the nanofibers was evaluated from the observed fringe pattern. The value of n_g is related to the spacing between fringes (free spectral range, FSR) through the following equation:

$$n_g = \frac{\lambda^2}{\mathrm{FSR} \times \Delta L}. \tag{5.3}$$

FSR evaluated from the spectrum was FSR = 3.3 nm at $\lambda = 560$ and decreased to FSR = 1.3 nm at $\lambda = 500$ nm. The value of n_g was calculated using (5.3) and

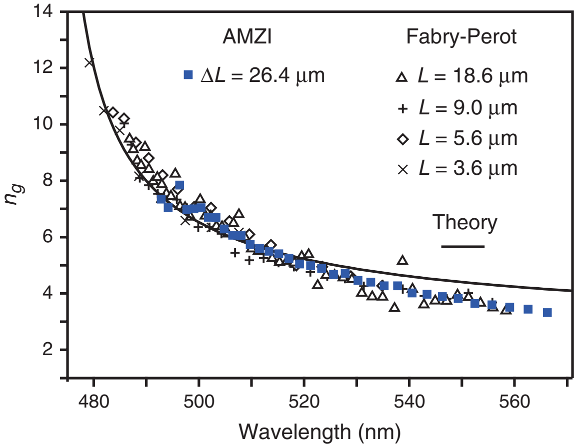

Fig. 5.8 Plot of n_g for the AMZI (blue squares). The symbols show n_g evaluated from the Fabry–Perot modes of nanofibers with different lengths. Reproduced from [21] by permission of John Wiley & Sons Ltd

plotted in Fig. 5.8 together with that obtained from the Fabry–Perot modes of the straight nanofibers, shown in Fig. 5.5. They agree well with each other and show a divergent increase with decreasing λ, confirming that the observed fringes are due to the interference of the exciton-polaritons. The interference order of an AMZI is given by $N = n_g \Delta L/\lambda$. Using the n_g values, N of this device was calculated to be $N \approx 170$ and 370 at $\lambda = 560$ and 500 nm, respectively.

The fabricated AMZI with $\Delta L = 26.4\,\mu\text{m}$ occupied an area of only $\sim 20\,\mu\text{m} \times 20\,\mu\text{m}$. Despite its compact size, the AMZI exhibited a visibility of nearly unity and functioned as channel drop filters with considerably high extinction ratios of up to ~15 dB in the wavelength range of $\lambda = 490{-}570$ nm. Such ultra-compact, high-performance AMZI channel drop filters operating in the visible wavelength region have rarely been developed with other waveguide technologies.

5.3.2 *Ring Resonators*

In this section, we present microring resonators as the second example of TC nanofiber-based photonic circuit components. Microring resonators are ideal for demonstrating the flexibility and low bending loss properties of TC nanofibers because the flexibility determines the minimum ring size and the bending loss affects the resonator performance. Moreover, the ring resonators that confine the exciton-polaritons provide a means to explore fundamental physics, namely strong light–matter interactions, as discussed in Sect. 5.4.

When two TC nanofibers are in contact with a certain contact length, exciton-polaritons transfer from one nanofiber to the other through evanescent coupling, as described in Sect. 5.3.1. This implies that a ring structure constructed by jointing both ends of a nanofiber can function as a ring resonator, which confines exciton-polaritons within the ring. The performance of a ring resonator, i.e., the finesse and Q-factor, is governed by the losses in the resonator. The losses can be divided into two components: the intrinsic propagation loss and the extrinsic losses. The extrinsic losses include the bending loss and the transmission loss in the contact region of the nanofiber ends. Thus, if we fabricate rings of different radii and constant transmission loss, we can extract information on the propagation and bending losses by comparing the finesses and Q-factors of the rings.

The insets of Fig. 5.9a–d show optical micrographs and FL microscopy images of fabricated rings of various sizes. r_{ave} is the average radius of a ring evaluated from $r_{\text{ave}} = L_c/2$, where L_c is the circumference and $r_{\min}$ is the radius of the most tightly bent part of the ring. The connections between the ends of the nanofibers are rather robust, probably due to the intermolecular forces. Throughout the fabrication process, particular attention was given to the contact length at both ends, because the contact length influences the transmission loss. For constant transmission loss, we made all contacts with a contact length of 4–6 μm.

The rings were excited by a laser spot, and the spectra of the FL spots at the fiber tip positions were measured (Fig. 5.9a–d). All of the spectra showed clear

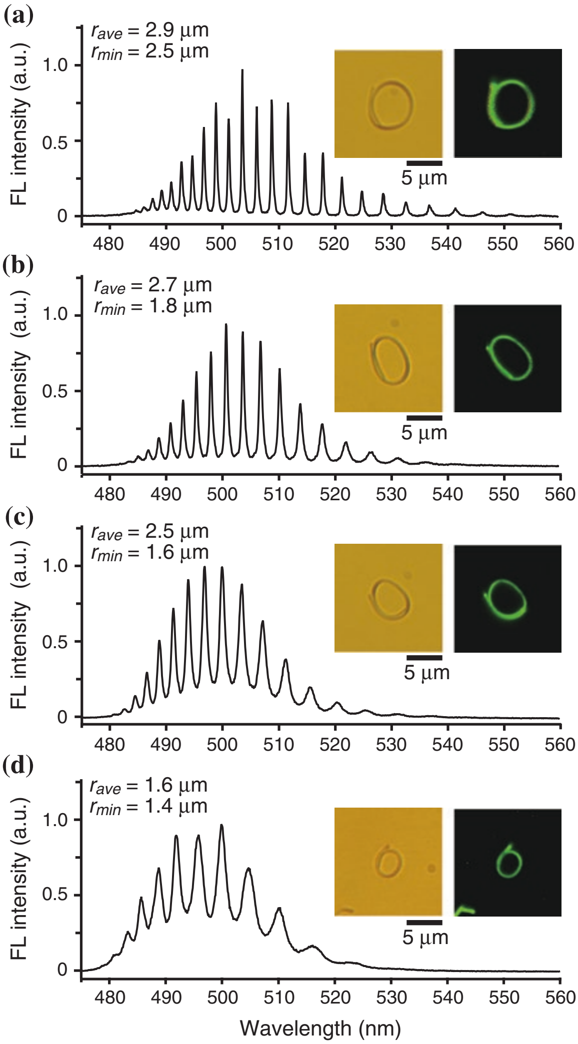

Fig. 5.9 FL spectra for different-sized rings, the *insets* show optical micrographs and FL microscopy images of the rings. Reprinted with the permission from [22], Copyright 2013 American Chemical Society

resonance peaks with spacing that increases as ring size decreases, proving that the rings functioned as ring resonators. Note that even the smallest ring with $r_{\text{ave}} = 1.6$ μm ($r_{\text{min}} = 1.4$ μm) functioned as a ring resonator. Such small ring resonators operating in the visible wavelength region have rarely been achieved using other waveguide technologies. It should also be noted that although the smallest ring that we were able to fabricate had $r_{\text{ave}} = 1.6$ μm, TC nanofibers are flexible enough to form even smaller rings. The minimum r_{ave} was merely limited by the resolution of our micromanipulation system, which is determined by the diffraction limit of light.

These spectra clearly show the effect of bending loss on the resonator performance. Bending loss causes weakening and broadening of the resonance peaks in the long-wavelength region of each spectrum. For example, the ring with $r_{\mathrm{ave}} = 2.9\ \mu\mathrm{m}$ exhibits its maximum intensity peak at $\lambda \approx 504$ nm, and the peaks become weaker and broader with increasing λ (Fig. 5.9a). As r_{ave} decreases, the most intense peak shifts toward shorter wavelengths, indicating that bending loss reduces resonator performance in the long-wavelength region. On the other hand, the effect of propagation loss can be seen in the short-wavelength region. For the ring with $r_{\mathrm{ave}} = 2.9\ \mu\mathrm{m}$, the resonance peaks were observed at $\lambda \gtrsim 485$ nm (Fig. 5.9a). With decreasing ring size, they are shifted to the shorter wavelength region; for the smallest ring, they were observed at $\lambda \gtrsim 480$ nm (Fig. 5.9d). This extension of the resonance peak region toward shorter wavelengths can be attributed to the propagation loss in the short-wavelength region, because this loss limits the polaritons to completing a full lap of the ring, which is what yields the resonance peaks. Hence, using a smaller ring allows for resonance at shorter wavelengths. Therefore, as the ring size decreases, the visibility of the resonance peaks in the shorter wavelength region increases.

To evaluate the performance of these ring resonators, the finesse (F) and Q-factor (Q) were evaluated using the relationships $F = \mathrm{FSR}/\Delta\lambda$ and $Q \approx \lambda_0\Delta\lambda$, where λ_0 is the peak wavelength. In Fig. 5.10a and b, F and Q of the rings are plotted as functions of λ. These curves clearly demonstrate the λ and r_{ave} dependences of the resonator performance, which were qualitatively discussed in the previous paragraph. The F and Q values of the rings form convex curves with a well-defined peak that shifts toward shorter wavelengths as r_{ave} decreases. This is because of the reduction in the resonator performances due to the bending loss in the long-wavelength region. On the other hand, in the short-wavelength region ($\lambda \lesssim 490$ nm), the F values of all rings almost overlap each other, indicating that the propagation loss alone determines the F values and the bending loss is negligible in this wavelength region. From the peak values of the $Q(F)$ curves, we found the highest $Q(F)$ values to be $Q(F) \approx 1500$ (8), 800 (6), 600 (3), 300 (2) for the rings with $r_{\mathrm{ave}} = 2.9$, 2.7, 2.5, and 1.6 μm, respectively.

5.3.3 *Microring Resonator Channel Drop/Add Filters*

We demonstrated that microrings constructed from TC nanofibers with average radii as small as 1.6 μm functioned as ring resonators. Here, we describe the application of such microring resonators to miniaturized photonic circuit devices. Microring resonators with one or two closely located I/O bus channel waveguides, which input (output) optical signals to (from) the ring, are commonly used in photonic circuits as channel drop/add filters [25]. Thus, the fabrication of such devices at a miniaturized scale using TC nanofibers is particularly interesting. We fabricated a channel drop filter that consists of a microring and a single I/O bus channel nanofiber. When the I/O bus channel nanofiber and the microring are placed close enough to allow evanescent coupling, the exciton-polaritons propagating along

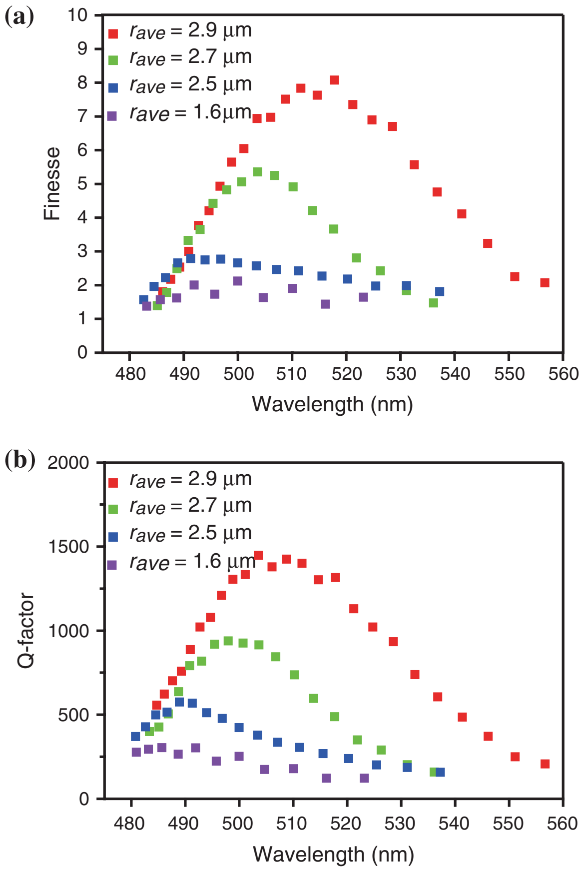

Fig. 5.10 **a** Plot of the finesses, **b** Plot of the Q-factors. Reprinted with the permission from [22], Copyright 2013 American Chemical Society

the bus fiber can be transferred to the ring. In this situation, the exciton-polaritons that resonate in the ring destructively interfere with those in the bus fiber passing through the coupling region. Consequently, the exciton-polaritons that are transmitted through the coupling region should exhibit drops in intensity at the wavelengths of the ring resonator modes (the drop channels).

Figures 5.11a and b show the optical micrograph and FL microscopy images, respectively, of a microring resonator that consists of a microring with $r_{\mathrm{ave}} = 3.9\ \mu\mathrm{m}$ ($r_{\mathrm{min}} = 2.2\ \mu\mathrm{m}$) and an I/O bus channel nanofiber with a length of 26.5 µm. We excited a point near the left tip of the I/O bus channel nanofiber with a laser spot and measured the spectrum of the FL outcoupled from the right tip (the inset in Fig. 5.11c). For a ring resonator channel drop filter, the optimum structure that provides the highest extinction ratio in the drop channels has been studied in detail [26, 27]. To obtain the highest extinction ratio, the power splitting ratio between the light (exciton-polaritons) being loaded into the ring and that passing through the coupling region must be optimized with respect to the finesse

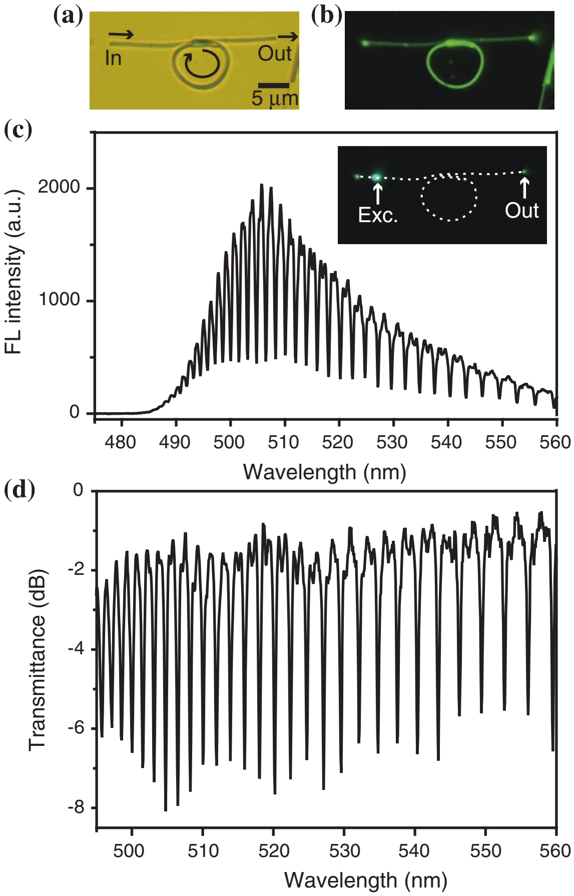

Fig. 5.11 **a** Optical micrograph of the channel drop filter, **b** FL microscopy image of the channel drop filter, **c** FL spectrum obtained by exciting the point labeled "Exc." and measuring FL at "Out" (see the *inset*), **d** Transmittance spectrum of the device. Reprinted with the permission from [22], Copyright 2013 American Chemical Society

of the ring resonator [27]. In our device, the power splitting ratio can be tuned by varying the contact length between the ring and the I/O bus fiber to yield the highest extinction ratio. It was observed that the channel widths as well as the extinction ratio were highly sensitive to changes in the contact length. High extinction ratios and narrow channel widths were obtained for a contact length of 6.0 µm, the spectrum for which is shown in Fig. 5.11c. To obtain the transmittance spectrum, we normalized this spectrum with respect to that measured prior to ring contact. The normalized spectrum converted to dB is displayed in Fig. 5.11d. From the transmittance spectrum, we find the extinction ratios in the drop channels to be 4–6 dB. The channel widths evaluated by best-fitting the spectrum to Lorentz functions are <0.4 nm over a wide spectral range of 490–560 nm. These performances are considerably high for a compact device of micrometer-scale dimensions.

5.4 Future Applications: Bose–Einstein Condensation of Exciton-Polaritons in Organic Dye Nanofibers

5.4.1 A Unique Workplace for Fundamental Science

Thus far, the nanofibers' potential for use in high-performance devices has been discussed, and several example applications were presented in the previous sections. The final aim of the present chapter is to draw attention to a further remarkable aspect of the nanofibers, which is that they offer an ideal playground to explore basic and fundamental physics. This omnipotent character nowadays can be seen in a wide range of research fields, e.g., in cold atom physics [28], and in this sense, the nanofiber system certainly follows the modern trend.

In this work, we focused specifically on the BEC of an exciton-polariton. BEC is a quantum phenomenon that is described as the occupation of the lowest energy level by a macroscopic number of Bose particles. In spite of the vast quantity of research on this subject since it was theoretically predicted, unambiguous experimental realization was not achieved until 1995 when the BEC of gaseous Rb^{87} [29] was realized. The temperature at which atomic BEC occurs is in the order of hundreds of nanokelvin.

As seems to be true throughout the history of physics, the manifestation of macroscopic quantum effects such as BEC and superconductivity is more widely appreciated when they are observed at higher temperatures. According to the elementary theory of BEC, the transition temperature is inversely proportional to the mass of the Bose particle [30]. Thus, lighter elements are advantageous for realizing BEC, and the photon in particular is a good candidate since it is a massless boson. Although this leads to another difficulty for achieving BEC [31], it can be overcome by coupling photons with different (quasi) Bose particles with finite mass. In this way, BEC was achieved at comparatively high temperatures for exciton-polaritons in GaAs quantum wells [32, 33]. Curiously, in this case, the transition temperature was limited by the exciton binding energy. The exciton in this material is unstable at higher temperatures because the binding energy of an electron and a hole is rather small. Consequently, for higher temperature realization, we need a more stable exciton.

An organic system would be advantageous in this respect, since the dielectric constant of these systems is generally larger than that of inorganic ones, leading to a larger exciton binding energy. Indeed, the room-temperature BEC of exciton-polaritons in an organic system was achieved [34] soon after the related phenomenon, room-temperature lasing in organic systems [35], was made possible. The structure of these systems used for the observation can be likened to semiconductor quantum wells, and in this sense, the BEC here is a strict counterpart of the exciton-polariton BEC achieved in the GaAs quantum wells. The natural direction of the progress in this field will be to explore the BEC of exciton-polaritons, not in quantum well structures, but in other nanostructured systems. Doing so will undoubtedly further our understanding of polariton BEC physics. The nanofibers featured in this chapter have the potential to make such work possible.

5.4.2 Exciton-Polariton BEC in the Nanofibers: Mean Field Study on a Phenomenological Model

In theoretically examining exciton-polariton BEC in nanofibers, a practical strategy is to assume a phenomenological model that adequately describes the physics while being as basic as possible. The relevant degrees of freedom in the present case are the Frenkel excitons and photons, both of which tightly couple within the nanostructure. The nanofiber should be constructed from bundles of aggregates, each of which is considered to be a chain of N monomers with equal separation of $a(=1)$. Hereafter, we set $\hbar = 1$ for simplicity.

First, we model the Frenkel exciton as an electric dipole excitation from HOMO to LUMO in an individual monomer, whose energy separation is denoted by Ω. The two-level system is equivalent to a (quasi-) spin 1/2 and is known to be mathematically encoded by the usual Pauli matrices σ^x, σ^y and σ^z (in the following, conventional symbols $\sigma^{\pm} \equiv \sigma^x \pm i\sigma^y$ are used). The exciton can migrate and thus has finite kinetic energy. This migration is dominantly driven by a dipole–dipole interaction, whose range is short, so that the kinetic energy of the exciton corresponds to the hopping integral J between the nearest neighbor sites. Taking all of this into consideration, the Hamiltonian for the Frenkel exciton is assumed to be

$$H_{-} = \frac{\Omega}{2}\sum_{i=1}^{N}\sigma_i^z - J\sum_{i=1}^{N}(\sigma_i^+\sigma_{i+1}^- + \sigma_{i+1}^+\sigma_i^-), \tag{5.4}$$

where a site index i is used. Note that $J > 0$ when the exciton migration reduces the kinetic energy, corresponding to the J-aggregate.

Due to the cavity-like character of the nanofiber, the Frenkel exciton tightly couples to photons that reside nearby. For the present purpose, it is sufficient to consider a single mode (energy ω_0) of cavity photons and represent it using a Bose creation (annihilation) operator $b^\dagger$ (b). The Hamiltonian for the photon field is

$$H_{\mathrm{ph}} = \omega_0 b^\dagger b. \tag{5.5}$$

Finally, the Frenkel exciton and the cavity photon are assumed to couple via electric dipole interaction, which is classically described by an inner product of the electric polarization and electric field, $\sim\mathbf{P}\cdot\mathbf{E}$. In the present usage, an essential part of the former is represented as $\mathbf{P} \sim \sigma_i^+ + \sigma_i^-$, while the latter is $\mathbf{E} \sim (1/\sqrt{N})(b^\dagger + b)$. Then, the Hamiltonian for the coupling becomes

$$H_{\mathrm{c}} = \frac{g_1}{\sqrt{N}}\sum_i[b\sigma_i^+ + b^\dagger\sigma_i^-] + \frac{g_2}{\sqrt{N}}\sum_i[b^\dagger\sigma_i^+ + b\sigma_i^-], \tag{5.6}$$

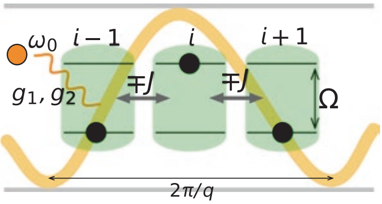

Fig. 5.12 Schematic view of an aggregate that consists of N monomers. The Frenkel exciton is created within an individual monomer, which can migrate to neighboring sites with magnitude J. The exciton also tightly couples to a single-mode photon via dipole interaction. A given parameter q characterizes the intensity pattern of the photon field

where g_1 and g_2 are introduced as parameters for the coupling strength. Consequently, our model Hamiltonian is constructed as the sum of these three terms: $H = H_- + H_{\mathrm{ph}} + H_{\mathrm{c}}$ (see, Fig. 5.12).

Having constructed the model Hamiltonian, we perform a mean field analysis to describe the phase transition toward the BEC of the exciton-polariton. Among several well-established techniques for the analysis, we rely on a functional integral method. The advantage of this method is that one can straightforwardly derive an effective action that describes low-energy properties of the system. From this perspective, the state that minimizes the action is the most probable state to be realized. Thus, we concentrate our focus on this state or mean field.

The outline of the calculation is as follows (for the technical details see [36, 37]). The effective action is obtained through evaluation of a partition function $Z = \mathrm{tr}(e^{-H/k_BT})$. In the functional integral method, the trace operation corresponds to the integral of variables included in the Hamiltonian in question. Since the present system is not integrable, all we can do is to evaluate the integral with respect to a limited number of variables. After this integration, we finally reach an effective action in the long-wavelength limit that governs the low-energy physics of our system:

$$S_-^{\mathrm{eff}} = \omega_0\phi_0^2 + \frac{1}{2}\overline{\Delta}_0^2 + \frac{1}{2}\Delta_0^2 - \frac{1}{\Omega}\tanh\frac{\beta\Omega}{2}\Big[(g_1+g_2)^2\phi_0^2 + 2\sqrt{J}(g_1+g_2)\phi_0(\Delta_0+\overline{\Delta}_0) + J(2\overline{\Delta}_0\Delta_0 + \Delta_0^2 + \overline{\Delta}_0^2)\Big], \tag{5.7}$$

where $\beta = 1/k_BT$ is the inverse temperature. The quantities ϕ_0 and $\Delta_0(\overline{\Delta}_0)$ correspond to order parameters that characterize BEC, defined as $\phi_0 = \langle b\rangle$, $\Delta_0 = \langle\sigma^+\rangle$, and $\overline{\Delta}_0 = \langle\sigma^-\rangle$. When the minimum of the action is provided by order parameters with nonzero values, it is a hallmark of BEC.

To validate these nonzero solutions, we first consider the high-temperature limit $T \to \infty$, or $\beta = 0$, in the effective action. Obviously, the minimum of the action is realized when all of these order parameters take null values, and thus, no condensation occurs. On the contrary, in the low temperature case, we can expect that the minimum of the effective action appears when the order parameters take certain finite values, since the two kinds of order parameters, Δ_0, $\overline{\Delta}_0$ and ϕ_0, link.

The boundary between the high- and low-temperature phases can be determined through stationary phase analysis. In order to perform this procedure, rewriting the effective action into the form of a 3 × 3 matrix is required: The phase boundary is fixed from the condition that the matrix has a null determinant. From this scheme, we arrive at an equation to fix the temperature below which the non-trivial order parameters appear:

$$\tanh\frac{\beta\Omega}{2} = \frac{\omega_0\Omega}{(g_1+g_2)^2+4J\omega_0}. \tag{5.8}$$

Since the nonzero order parameters that minimize the effective action are a linear combination of $\Delta_0, \overline{\Delta}_0$ and ϕ_0, it is the exciton-polaritons that condense. It can be observed that the expected transition temperature given by the mean field equation is higher for larger J. This is consistent with conventional BEC theory, since the hopping amplitude J is inversely proportional to the mass of the exciton.

In the above discussion, the photon field that strongly couples with the exciton is assumed to be uniformly distributed. Here, we generalize it and introduce a non-uniform electric field. The electric field is represented as $E(r) \sim b^\dagger e^{-iqr} + be^{iqr}$, with a given parameter q. The extra phase factors that the photon operators carry lie only in the coupling Hamiltonian. Using this generalized Hamiltonian, the mean field equation becomes

$$\tanh\frac{\beta\Omega}{2} = \frac{\Omega\omega_0}{g_1^2+g_2^2+2g_1g_2\delta_{q0}+4J\omega_0\cos q}. \tag{5.9}$$

This equation yields a phase diagram spanned by the wavenumber q and phase transition temperature.

For completeness, we also perform a parallel analysis for the H-aggregate. As before, we need to construct an effective Hamiltonian. In contrast to the J-aggregate, the absorption spectrum associated with the H-aggregate peaks at a higher energy than that of a monomer. This can be accounted for in the phenomenological Hamiltonian by simply replacing $-J$ with $+J$ in H. Consequently, the corresponding mean field equation is identical in form to (5.9), excluding the sign of J. However, we would like to emphasize that the calculation procedure to derive the result for the H-aggregate is totally different from that for the J-aggregate. The difficulties originate from the fact that the procedure for the J-aggregate breaks the positive definiteness which is necessary for the convergence of the integral when the sign change is performed [36, 37].

On the basis of the mean field equations, we draw a phase diagram in the $q - T$ plane for nanofibers consisting of the J- and H-aggregates. The result is shown in Fig. 5.13, where exciton-polariton BEC can be expected in the shaded regions for the J- and H-aggregates, respectively. The diagram is symmetrical with respect to $q = \pi/2$. This can be understood by considering the momentum conservation and the Frenkel exciton bands. The latter, $E = \mp 2J\cos k$, are symmetric with respect to $k = \pi/2$. The highest transition temperature for exciton-polariton BEC is expected at $q = 0(\pi)$ for J- (H-) aggregates. This requires neighboring monomers to

Fig. 5.13 Mean field phase diagram that shows the possible BEC of Frenkel exciton-polaritons for the J- and H-aggregates

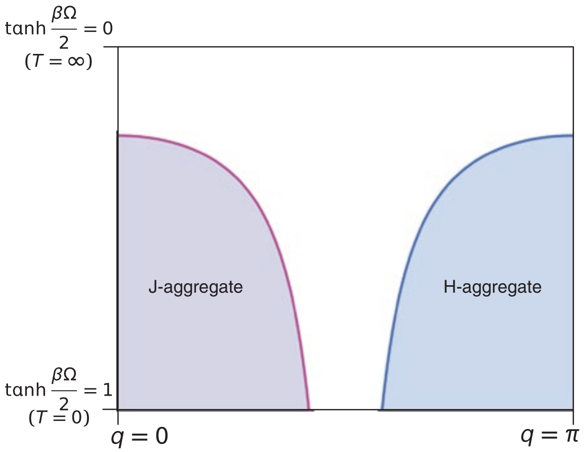

experience an in (out-of) phase electric field for J- (H-) aggregates. Thus, depending on the HOMO-LUMO gap, a cavity mode that meets this condition must be selected.

Because this analysis has been carried out within the mean field, some noteworthy subtleties are present. The nanofiber consists of a large number of aggregates, so inter-aggregate interactions (not explicitly considered in the present model) play an important role. Thus, the system exhibits a mean field nature to a certain degree. We rely on this feature in using the mean field analysis. Furthermore, we do not employ mathematical tools that are specific to low-dimensional systems; thus, we can expect that the essential qualitative aspects are reasonably well captured. That said, further theoretical studies beyond mean field approximations are needed to obtain quantitative results and further our knowledge of this field.

Another subtlety is the assumption of thermal equilibrium, which is not the case in real experiments. In an analysis of the exciton-polariton BEC in GaAs quantum wells, the application of non-equilibrium theory was emphasized [38], although it was not employed from the outset. In this sense, the present work may act as a reference for future, more advanced studies. Related to this, a curious connection between the non-equilibrium condition and a phase transition was proposed theoretically: In a non-equilibrium state, a true phase transition at finite temperature is allowed even in low-dimensional systems [39]. Theoretical developments along these lines should also be possible for this organic nanofiber system.

5.4.3 *Further Examples*

Finally, we briefly discuss some other areas that are theoretically compatible with the nanofiber system.

(1) The model introduced in this work is very similar to that used for examining BCS superconductivity. Although not explicitly shown here, the kinetic energy

term for excitons corresponds to an electron interaction in BCS theory, which is attractive or repulsive depending on the sign of J. Using this fact, the similarity of the present BEC with superconductivity and the crossover between the two macroscopic quantum phenomena can be addressed in the present framework.

(2) The present Hamiltonian corresponds to a newly introduced derivative model of a spin-boson model, which is applicable to a range of areas including super-radiance [40], the Kondo effect [41], and spin relaxation [41]. The novelty of our approach is the introduction of the interaction between spins, making the model highly non-trivial. The influences of the spin–spin interaction on the phenomena listed above are important subjects in both physics and material science.

Acknowledgments We thank Drs. T. Takamasu and T. Kuroda for helpful discussions. This work was supported by the grant-in-aid for Scientific Research (24540332), Japan Society for the Promotion of Science.

References

1. R.G. Hunsperger, *Integrated Optics: Theory and Technology*, 5th edn. (Springer, Berlin, 2002)
2. S.I. Bozhevolnyi, V.S. Volkov, E. Devaux, J.Y. Laluet, T.W. Ebbesen, Channel plasmon subwavelength waveguide components including interferometers and ring resonators. Nature **440**, 508–511 (2006)
3. S. Noda, K. Tomoda, N. Yamamoto, A. Chutinan, Full three-dimensional photonic band-gap crystals at near-infrared wavelengths. Science **289**, 604–606 (2000)
4. J.J. Hopfield, Theory of the contribution of excitons to the complex dielectric constant of crystals. Phys. Rev. **112**, 1555–1567 (1958)
5. C.J. Barrelet, A.B. Greytak, C.M. Lieber, Nanowire photonic circuit elements. Nano Lett. **4**, 1981–1985 (2004)
6. J.C. Johnson, H.Q. Yan, P.D. Yang, R.J. Saykally, Optical cavity effects in ZnO nanowire lasers and waveguides. J. Phys. Chem. B **107**, 8816–8828 (2003)
7. M. Law, D.J. Sirbuly, J.C. Johnson, J. Goldberger, R.J. Saykally, P.D. Yang, Nanoribbon waveguides for subwavelength photonics integration. Science **305**, 1269–1273 (2004)
8. H. Yanagi, T. Morikawa, Self-waveguided blue light emission in p-sexiphenyl crystals epitaxially grown by mask-shadowing vapor deposition. Appl. Phys. Lett. **75**, 187–189 (1999)
9. F. Balzer, V.G. Bordo, A.C. Simonsen, H.G. Rubahn, Isolated hexaphenyl nanofibers as optical waveguides. Appl. Phys. Lett. **82**, 10–12 (2003)
10. F. Balzer, V.G. Bordo, A.C. Simonsen, H.G. Rubahn, Optical waveguiding in individual nanometer-scale organic fibers. Phys. Rev. B **67**, 115408 (2003)
11. K. Takazawa, Y. Kitahama, Y. Kimura, G. Kido, Optical waveguide self-assembled from organic dye molecules in solution. Nano Lett. **5**, 1293–1296 (2005)
12. F. Quochi, F. Cordella, A. Mura, G. Bongiovanni, F. Balzer, H.G. Rubahn, Gain amplification and lasing properties of individual organic nanofibers. Appl. Phys. Lett. **88**, 041106 (2006)
13. Y.S. Zhao, A. Peng, H.B. Fu, Y. Ma, J.N. Yao, Nanowire waveguides and ultraviolet lasers based on small organic molecules. Adv. Mater. **20**, 1661–1665 (2008)
14. Y.S. Zhao, H.B. Fu, F.Q. Hu, A.D. Peng, W.S. Yang, J.N. Yao, Tunable emission from binary organic one-dimensional nanomaterials: an alternative approach to white-light emission. Adv. Mater. **20**, 79–83 (2008)

15. K. Takazawa, Waveguiding properties of fiber-shaped aggregates self-assembled from thiacyanine dye molecules. J. Phys. Chem. C **111**, 8671–8676 (2007)
16. K. Takazawa, J. Inoue, K. Mitsuishi, T. Takamasu, Micron-scale photonic circuit components based on propagation of exciton polaritons in organic dye nanofibers. Adv. Mater. **23**, 3659–3663 (2011)
17. K. Takazawa, Flexibility and bending loss of waveguiding molecular fibers self-assembled from thiacyanine dye. Chem. Phys. Lett. **452**, 168–172 (2008)
18. K. Takazawa, J. Inoue, K. Mitsuishi, T. Takamasu, Fraction of a millimeter propagation of exciton polaritons in photoexcited nanofibers of organic dye. Phys. Rev. Lett. **105**, 067401 (2010)
19. K. Ogawa, T. Katsuyama, H. Nakamura, Polarization dependence of excitonic-polariton propagation in a GaAs quantum-well waveguide. Phys. Rev. Lett. **64**, 796–799 (1990)
20. H. Takeda, K. Sakoda, Exciton-polariton mediated light propagation in anisotropic waveguides. Phys. Rev. B **86**, 205319 (2012)
21. K. Takazawa, J. Inoue, K. Mitsuishi, T. Kuroda, Ultracompact asymmetric mach-zehnder interferometers with high visibility constructed from exciton polariton waveguides of organic dye nanofibers. Adv. Funct. Mater. **23**, 839–845 (2013)
22. K. Takazawa, J. Inoue, K. Mitsuishi, Optical microring resonators constructed from organic dye nanofibers and their application to miniaturized channel drop/add filters. ACS Appl. Mater. Interfaces **5**, 6182–6188 (2013)
23. W.E. Martin, Appl. Phys. Lett. **26**, 562–564 (1975)
24. R.A. Becker, Appl. Phys. Lett. **43**, 131–133 (1983)
25. B.E. Little, S.T. Chu, H.A. Haus, J. Foresi, J.P. Laine, J. Lightwave Technol. **15**, 998–1005 (1997)
26. A. Yariv, Electron. Lett. **36**, 321–322 (2000)
27. A. Yariv, IEEE. Photon. Technol. Lett. **14**, 483–485 (2002)
28. M. Lewenstein, A. Sanpera, V. Ahufinger, *Ultracold Atoms in Optical Lattices: Simulating Quantum Many-Body Systems* (Oxford University Press, Oxford, 2012)
29. M.H. Anderson, J.R. Ensher, M.R. Matthews, C.E. Wieman, E.A. Cornell, Observation of Bose–Einstein condensation in a dilute atomic vapor. Science **269**, 198–201 (1995)
30. K. Huang, *Statistical Mechanics*, 2nd edn. (Wiley, New York, 1987)
31. C. Kittel, *Thermal Physics* (Wiley, New York, 1969)
32. J. Kasprzak, M. Richard, S. Kundermann, A. Baas, P. Jeambrun, J.M.J. Keeling, F.M. Marchetti, M.H. Szymanska, R. Andre, J.L. Staehli, V. Savona, P.B. Littlewood, B. Deveaud, L.S. Dang, Bose–Einstein condensation of exciton polaritons. Nature **443**, 409–414 (2006)
33. H. Deng, H. Haug, Y. Yamamoto, Exciton-polariton Bose–Einstein condensation. Rev. Mod. Phys. **82**, 1489–1537 (2010)
34. J.D. Plumhof, T. Stoferle, L. Mai, U. Scherf, R.F. Mahrt, Room-temperature Bose–Einstein condensation of cavity exciton-polaritons in a polymer. Nat. Mater. **13**, 247–252 (2013)
35. S. Kena-Cohen, S.R. Forrest, Room-temperature polariton lasing in an organic single-crystal microcavity. Nat. Publishing Group **4**, 371–375 (2010)
36. J.-I. Inoue, Functional integral approach to a full Dicke model with nearest-neighbour interaction. J. Phys. A: Math. Theor. **45**, 305003/1–30503/11 (2012)
37. J.-I. Inoue, Possible condensation of Frenkel exciton polaritons in an organic nanofiber. Eur. Phys. J. B **86**, 70/1–70/5 (2013)
38. M. Yamaguchi, K. Kamide, R. Nii, T. Ogawa, Y. Yamamoto, Second thresholds in BEC-BCS-laser crossover of exciton-polariton systems. Phys. Rev. Lett. **111**, 026404 (2013)
39. A. Imamoglu, R.J. Ram, S. Pau, Y. Yamamoto, Nonequilibrium condensates and lasers without inversion: exciton-polariton lasers. Phys. Rev. A **53**, 4250–4253 (1996)
40. Y.K. Wang, F.T. Hioe, Phase transition in the Dicke model of superradiance. Phys. Rev. A **7**, 831–836 (1973)
41. A.J. Leggett, Fisher, S. Chakravarty, A.T. Dorsey, M.P.A. Fisher, A. Garg, W. Zwerger, Dynamics of the dissipative two-state system. Rev. Mod. Phys. **59**, 1–85 (1987)

Chapter 6
Nonlinear Optical Polymer Photonic Crystals and Their Applications

Shin-ichiro Inoue

Abstract Photonics has evolved toward device miniaturization with the ultimate objective of integrating many optical components onto a single compact chip to produce photonic integrated circuits with multiple functionalities. In conventional optics, miniaturization of structures in photonic active manipulations is restricted by very weak matter–radiation interaction. In this chapter, starting with a brief description of photonic crystals, we show experimental evidence that the performance of nonlinear optical applications such as all-optical switching, two-photon excited fluorescence, and electro-optic modulation devices are dramatically improved by controlling the matter–radiation nonlinear interaction in the nonlinear optical polymer photonic crystals fabricated by organic nanofabrication technology. The results will open up possibilities in unprecedented applications such as highly efficient and ultrafast optical data processing systems in organic nanophotonic architectures.

6.1 Photonic Crystals

The growth and overlap of research in the fields of photonic crystals and organic nonlinear optical polymer materials should lead to new exciting, active functions and high-efficiency nonlinear optical applications because nonlinear optical effects in photonic crystals may allow for significant advances in various optical processes by using resonantly stored light and anomalous band dispersions, in combination with nonlinear optical polymer materials.

Photonic crystals are materials composed of dielectric structures with periodicity in one, two, or three directions on the optical wavelength scale [1–5]. The ability of

---

S. Inoue (✉)
Advanced ICT Research Institute, National Institute of Information and Communications Technology (NICT), Kobe 651-2492, Japan
e-mail: s_inoue@nict.go.jp

Y.S. Zhao (ed.), *Organic Nanophotonics*, Nano-Optics and Nanophotonics,
DOI 10.1007/978-3-662-45082-6_6

a photonic crystal to control the light dispersion relation (i.e., photonic band structure) with a high degree of freedom is an issue of scientific and practical importance. Tailoring of the band dispersion in photonic crystal systems can give rise to anomalous dispersion characteristics including photonic band gap and extremely slow group velocities (a phenomenon known as “slow light”) that cannot be achieved in homogeneous materials and conventional waveguides. These characteristics have opened up unprecedented and exciting possibilities in a wide range of photonics with multiple applications in photonic information and communication, laser technologies, optoelectronics, integrated, and nonlinear optics.

Since a crystal for photons is a periodic arrangement of potential distribution (refractive index contrast of dielectric arrays), this lattice introduces the *photonic band structure* of the crystal due to Bragg-like diffraction of electromagnetic wave. From general symmetry principles, the electromagnetic modes of a photonic crystal with periodicity can be written as Bloch states in Maxwell’s equations. Here, the functions of the mode profiles are determined by the eigenvalue problem restricted to a single unit cell of the photonic crystal because of the boundary condition. These Bloch boundary conditions over a unit cell of a photonic crystal give the k vector dependence of the eigen mode, and the spectral information can be obtained by a Fourier transform of the fields. The information contained in these functions is called the photonic band structure of the photonic crystal. If the lattice potential is strong enough, the photonic band gap is produced into the photonic band structure. In this photonic band gap frequency region, the propagation of electromagnetic wave is forbidden in certain or all directions.

6.2 Experimental Photonic Band Structure

In order to design high-efficiency photonic applications and to achieve a proper understanding of the unique optical phenomena in nonlinear optical polymer photonic crystals, it is essential to engineer the optical dispersion relation and to study the experimental photonic band structure and the key fundamental characteristics such as the group velocity dispersion characteristics.

The experimental photonic band structure of the photonic crystal waveguide can be determined from the incident angle dependence of the wavelength positions of sharp resonance dips in the polarized angular-dependent reflectance spectra [4–8]. The sharp dips in the reflectivity spectra originate from surface coupling between external free photons and in-plane photonic band modes in the waveguide at resonance energies and in-plane wave vectors [7]. Therefore, these dips provide information about the photonic band dispersion, but not about the photonic band gap and its angular dependence on the Bragg peak [9].

However, the photonic bands that can be probed with this technique are limited to those above the light cone. The light line in a vacuum ($\omega = ck$) separates the observable region ($\omega > ck$), in which the modes are oscillatory in air, from the region in which modes are evanescent in air and cannot couple with external free photons ($\omega < ck$). However, engineering applications of two-dimensional (2D) photonic crystal waveguides require the use of modes below the light line due to their vertical confinement and long lifetimes. The dispersion characteristics of waveguiding modes below the light line have been studied indirectly by interference measurements of transmission in a 2D photonic crystal slab [10]. This method can deduce the group index (n_g) dispersion, but it cannot accurately determine the shape of the band dispersion due to the uncertainty in the origin position of the k-axis. Although determining the photonic band dispersion relation of the waveguiding modes below the light line is indispensable for understanding the unique properties of photonic crystal waveguides, experimental information on the specific shape of these band dispersions has scarcely been obtained directly.

In this subsection, we demonstrate the direct determination of the experimental photonic band structure below the light line in a two-dimensional photonic crystal waveguide using angle-resolved attenuated total reflection spectroscopy of a prism coupling arrangement over a wide frequency range. By this technique, we can observe sharp dips in the reflectance spectra originating from resonance coupling between the external evanescent wave from total reflection off the prism and the waveguiding modes in the photonic crystal waveguide. This provides clear information on individual band components by resolving the angle (i.e., wave vector k) and photon energy.

Because waveguiding modes in 2D photonic crystals with $k > \omega/c$ cannot be matched to propagating modes incident from free space, they cannot be detected by external plane wave excitation. To examine the experimental photonic band structure of these modes, the incident radiation is coupled to waveguiding modes using a coupling prism in the Otto configuration [11]. The experimental geometry is shown in Fig. 6.1. A beam of radiation is incident from air through one face of

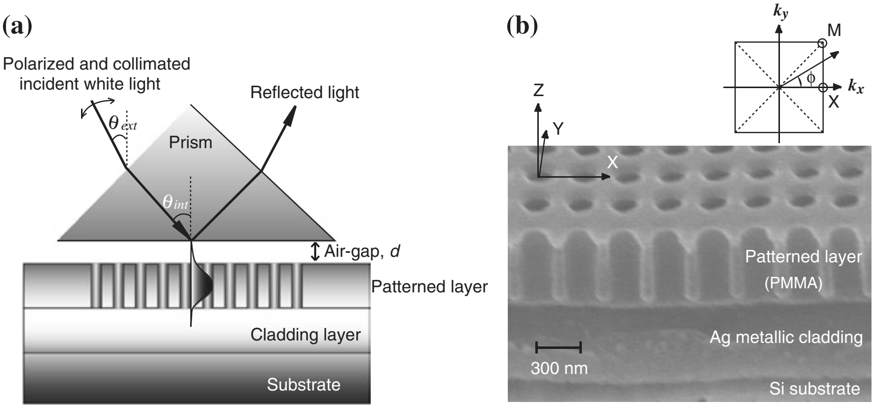

Fig. 6.1 **a** Schematic showing the experimental geometry of angle-resolved attenuated total reflection spectroscopy. The coupling prism in the Otto configuration is used to couple incident radiation to waveguiding modes. **b** Example of the 2D photonic crystal waveguide used in the experiments. The *inset* shows the corresponding 2D first Brillouin zone and the high-symmetry lattice points. Reprinted with permission from [12], Copyright 2008 Optical Society of America

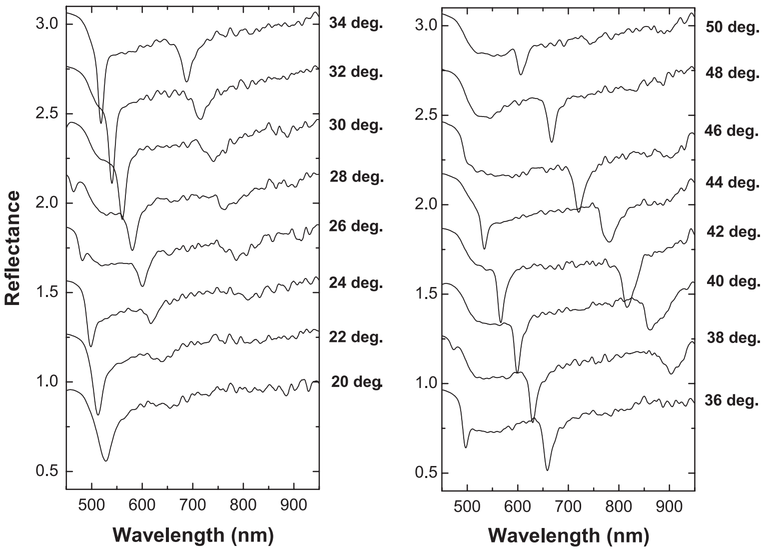

Fig. 6.2 Typical measured reflectance spectra for various angles of incidence with TE polarization along the Γ–X direction. For clarity, the spectra are shifted along the vertical axis by 0.3 with respect to each other. Reprinted with permission from [12], Copyright 2008 Optical Society of America

a high-refractive index prism. The beam passes through the prism and is incident on a second interface at an angle. For angles greater than a critical angle, the beam undergoes total internal reflection at the second interface and exits the prism at the third interface. At the surface of the reflection interface, a decaying evanescent wave exists on the air side of the prism, for which the parallel component of the wave vector satisfies $k_{//} > \omega/c$. When the surface of the 2D photonic crystal waveguide is brought close to (but not touching) the prism, this evanescent wave can couple to the guiding mode. A sharp dip originating from resonance between the evanescent wave and the waveguiding mode can be detected in the reflectance spectrum.

As an example, Fig. 6.2 shows typical angle-dependent attenuated total reflection spectra of the 2D photonic crystal slab waveguide along the Γ–X lattice direction, taken with TE polarization. Several sharp dips are clearly observable, demonstrating that the evanescent field above the prism resonantly couples to in-plane photonic band modes in the 2D photonic crystal. The observed resonance wavelengths clearly depend on the incident angle, which determines the in-plane wave vectors, $k_{//} = (2\pi/\lambda)\ n_p \sin\theta_{\mathrm{int}}$, where λ is the wavelength of the incident light and $\theta_{\mathrm{int}} = 0°$ is normal incidence. The resonance dip at each resonance angle in the reflectivity is thus directly connected to the experimental dispersion curves, i.e., the experimental photonic band structure.

Figure 6.3 shows an example of experimental photonic band structure of the photonic crystal along the Γ–X line obtained from the angle-dependent attenuated

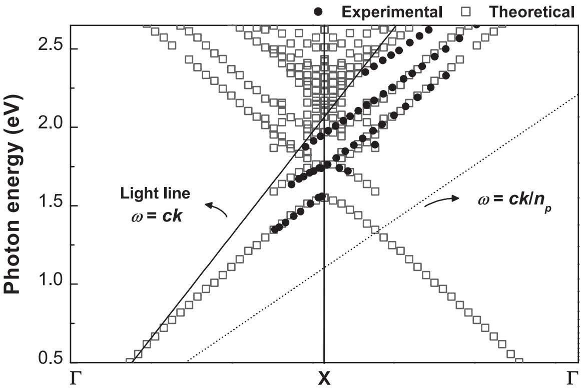

Fig. 6.3 Experimental photonic band structure under the light line of the 2D photonic crystal waveguide along the Γ–X line obtained by polarized angular-dependent reflection spectroscopy (*closed circles*) and the theoretical band structure calculated by the 3D FDTD method (*open squares*). No empirical adjustments were made in the calculations. Adapted with permission from [12], Copyright 2008 Optical Society of America

total reflection spectra, compared with the theoretical band structure calculated by the 3D-FDTD method for a model structure identical to the experimental sample structure. The straight solid line corresponds to the light line in a vacuum ($\omega = ck$) and separates the region in which the modes are oscillatory in air ($\omega > ck$) from the region in which modes are evanescent in air ($\omega < ck$). In a standard angular-dependent reflectivity measurement without a coupling prism, the experimental bands that can be probed are limited to those above the light cone. In angle-resolved attenuated total reflection spectroscopy, the in-plane wave vectors $k_{//}$ of the incident plane wave are increased in proportion to the prism index n_p, and hence, many of the photonic band dispersions under the straight dashed line correspond to the boundary of the enlarged light cone in the prism ($\omega > ck/n_p$). The features of the experimental band structure are in reasonably good agreement with the theoretical curves. This agreement demonstrates that it is realistically possible to design advanced fundamental research and technological applications of photonic crystal slabs using this technology, since many optical properties of the waveguiding modes are closely related to the shape of the band structure under the light line in air.

It has been also proved that the fluctuation in the photon energy domain between the band modes of the photonic crystal with the prism and the isolated photonic crystal are barely significant ($\Delta h\nu / h\nu < 0.6\ \%$) even at the well-coupled separation distance d of 300 nm between the photonic crystal and prism [12]. These results clearly demonstrate that except in the case of over coupling ($d < 100$ nm), the angle-resolved attenuated total reflection spectroscopy technique is accurate and suitable for directly determining the experimental photonic band structure below the light line in 2D photonic crystal waveguides.

6.3 Enhancement of Nonlinear Optical Processes in Photonic Crystals

Photonic crystals are very attractive materials for use in the propagation of electromagnetic radiation and for their ability to control the band dispersion characteristics. These characteristics have opened up unprecedented and exciting possibilities in a wide range of photonic information technologies, including photonic circuit devices [13–15], controlling spontaneous emission [16–18], microcavity works [19–21], negative refraction [22–25], and diverse applications [26–30]. For example, in line-defect photonic crystal waveguides, a waveguiding mode located in a photonic band gap can produce a wavelength-scale sharp bend in the light propagation [13, 15]. Also, specific features of the band dispersion relation and conservation of the tangential component of the wave vector at the boundary in photonic crystals enable the realization of superprism, focusing, and negative refraction effects [22–25, 31, 32]. Furthermore, photonic band structure features and large group velocity dispersion characteristics in photonic crystals are expected to find use in new active and novel high-efficiency nonlinear optical applications such as high-efficiency optical switching [33–36], frequency conversion devices [37–41], and others [42–44], in combination with nonlinear optical host materials. These applications are possible with photonic crystals because an extremely slow group velocity, originating from anomalous band dispersions at the band edge and/or a very flat band, produces a strong enhancement in the electromagnetic field of the excitation wave. In this section, we show the exciting possibilities of a nonlinear optical polymer photonic crystal in nonlinear optics.

6.3.1 Nonlinear Optical Switching

Interest has grown rapidly in photonic crystals exhibiting nonlinear optical switching effects as such materials are strong candidates for practical all-optical signal processing devices [33–36]. The optical nonlinearities of conventional nonlinear materials are usually very weak. However, tailoring of the band dispersions in photonic crystal systems can produce large nonlinearities and minimize the power requirements for switching processes. This arises from the anomalous dispersion characteristics of photonic crystals, which enhance the electromagnetic field due to their extremely slow group velocities as compared with conventional uniform materials. In this regard, a two-dimensional photonic crystal waveguide represents one of the most promising photonic crystal structures for efficient nonlinear applications. Unique band dispersions can be designed through control of the 2D photonic crystal configuration, and a high optical intensity can be maintained over a long interaction distance.

Clarifying the relation between the nonlinear optical response and the nature of the band dispersion at the resonance state, and engineering the matter–radiation nonlinear interaction by controlling the band dispersion are essential for the realization of desirable nonlinear applications, such as practical all-optical switching and processing devices with very low operational power and ultrasmall dimensions, which are greatly demanded by photonic information technology. In this subsection, we experimentally identify nonlinear optical changes arising from modification of the photonic band structure in a nonlinear optical polymer 2D photonic crystal waveguide with a Kerr nonlinearity.

To examine the nonlinear optical changes arising from modifications of the photonic bands driven by an external laser field resonantly coupled to the photonic bands, linear and nonlinear angle-resolved reflectivity measurements are performed. The examples of the linear and nonlinear angle-dependent reflectivities of the 2D photonic crystal waveguide composed of the nonlinear optical polymer DR1/PMMA are shown in Fig. 6.4. These measurements provide a sharp distinction between the different photonic bands by separating the linear components in the angle (or wave vector, k) domain and also convey information on the nonlinear optical responses by monitoring the distinct dynamics of each photonic band in the 2D photonic crystal system. Furthermore, because this technique can separate photonic bands of the same energy, we can investigate the nonlinear optical changes of the different photonic bands without having to consider the energy dispersions of the linear and nonlinear susceptibilities.

Figure 6.4b shows the angle-dependent reflectivities for different incident peak powers at a wavelength of 800 nm in two different angle ranges in the vicinity of the resonance angles α and β. Clearly, the resonance dip positions in the reflectivities are shifted with increasing incident peak power for both resonance dips. The angular shifts at resonances α and β have different sign. These shifts are accompanied by large nonlinear changes in the reflectivities at the resonance angles. These novel and unusual nonlinear phenomena, exhibiting differences in sign and quantity of the nonlinear angular shifts at the resonances, indicate that the nonlinear changes are strongly influenced by the photonic band dispersion properties.

To find the underlying physical mechanism of these results, Fig. 6.5a shows the experimental photonic band structure along the Γ–X line of the sample examined by angle-dependent optical reflectivity measurements compared with the theoretical band structure calculated by the 3D-FDTD method for a model structure identical to the experimental sample structure (see scheme in Sect. 6.2). The features of the observed band dispersion are in reasonably good agreement with the theoretical curves. The experimental and theoretical band structures provide a very clear picture of the relation between the observed nonlinear responses and the photonic band dispersion. In Fig. 6.5a, the horizontal solid line shows the photon energy corresponding to the energy of the incident laser used in the nonlinear experiments. The positions of the in-plane wave vectors k of the incident light at the angles of resonances α and β at this photon energy are indexed as points I and II, respectively. The group velocities v_g of these corresponding bands, estimated by the slope of the dispersion curve ($v_g = \partial\omega/\partial\boldsymbol{k}$), are $v_g = 0.46c$ and $v_g = -0.19c$ at points I and II, respectively.

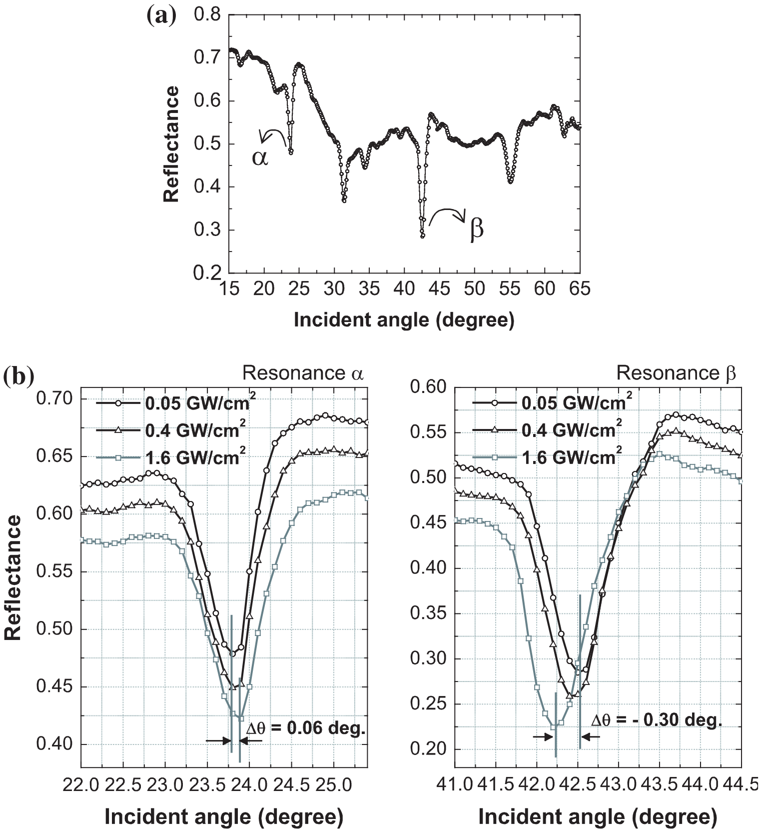

Fig. 6.4 Examples of linear and nonlinear angle-dependent reflectivities of a 2D photonic crystal waveguide with Kerr nonlinearity. **a** Linear angle-dependent reflectivity at a wavelength of 800 nm, measured with TE polarization along the Γ–X lattice direction. **b** Nonlinear angle-dependent reflectivities for three different incident peak powers at two different angle ranges in the vicinity of the resonances α (*left*) and β (*right*), measured at a fixed wavelength of 800 nm along the Γ–X direction. For clarity, the reflectivities are shifted by −0.03 along the *vertical axis* with respect to each other. Here, the *vertically* unshifted reflectivity used as a base is for a peak power of 0.05 GW/cm^2 (*black circles*). Adapted with permission from [35], Copyright (2005) by The American Physical Society

We now directly compare the observed nonlinear optical responses with the photonic band structure features in the vicinity of the resonances. The k shift values obtained from the observed resonance angle shifts in Fig. 6.4b are $\Delta ka/2\pi = +9.5 \times 10^{-4}$ for resonance α and $\Delta ka/2\pi = -3.9 \times 10^{-3}$ for resonance β, where a is the lattice constant. The refractive index change Δn of the nonlinear optical polymer layer can be estimated by equating the observed Δk amplitude with the value of the refractive index change in the 3D-FDTD band calculations, giving $\Delta n = +\ 1.7 \times 10^{-3}$ and $\Delta n = +3.7 \times 10^{-3}$ at α and β, respectively. The detailed linear band structure and nonlinear band shifts in the vicinity of I and II are shown in Fig. 6.5b. The shifts in the photon energy domain are toward the low photon energy side for both bands because of the positive susceptibility of the nonlinear optical polymer at the energy of the incident laser. On the other hand, the bands are shifted in opposite directions in the k domain, with a positive shift at α and a negative shift at β, which results from the positive and negative slopes of the band dispersion curves at these resonances. The agreement between the band structure features and the resonance angle shifts demonstrates the essential role of the band dispersion character in the nonlinear dynamics.

A direct comparison between the observed nonlinear responses and the dispersion characteristics for the two different band components provides information on the group velocity of the nonlinear optical properties and clarifies the enhancement effect of the nonlinear processes in photonic crystal systems. In the work, we found basic agreement between the ratio of the inverse group velocities of the photonic bands at I and II, $|v_{g\ \mathrm{I}}|^{-1}{:}|v_{g\ \mathrm{II}}|^{-1} = 1.0{:}2.4$, and the ratio of the refractive index changes at α and β, $\Delta n_\alpha{:}\Delta n_\beta = 1.0{:}2.2$, as well as between the ratio of the squared inverse group velocities at I and II, $|v_{g\ \mathrm{I}}|^{-2}{:}|v_{g\ \mathrm{II}}|^{-2} = 1.0{:}5.8$, and the ratio of the observed nonlinear resonance angle shifts at α and β, $|\Delta\theta_\alpha|{:}|\Delta\theta_\beta| = 1.0{:}5.0$. These results clearly demonstrate that the observed nonlinear changes are dominated by the band group velocities at the resonance conditions. The refractive index change in these processes is considered to be enhanced in proportion to v_g^{-1} because the electric field intensity of the resonance band mode is enhanced in proportion to v_g^{-1} based on conservation of energy in the first approximation. The resonance angle shift is enhanced in proportion to v_g^{-2} because the wave vector shift Δk, which depends on the resonance angle shift, is affected by the combination of the larger refractive index change ($\propto v_g^{-1}$), and the larger k vector shift ($\propto v_g^{-1}$) arising from the slower group velocity, as shown in Fig. 6.5b.

These data give direct evidence that the nonlinear optical changes arising from modifications of the photonic bands by an external laser field resonantly coupled to the photonic band (i.e., by purely optical means) in a 2D photonic crystal waveguide with a Kerr nonlinearity are dominated by the dispersion nature and the group velocity of the photonic bands. Thus, with current technology, active manipulation of these nonlinear optical processes is a realistic possibility through engineering of the band dispersion and band group velocity characteristics.

6.3.2 Two-Photon-Excited Fluorescence

Two-photon excitation (TPE) processes have attracted considerable interest because of their potential to be applied to diverse fields, including three-dimensional fluorescence imaging [45, 46], high-density optical data storage [47], lithographic microfabrication [48], and photodynamic cancer therapy [49]. From the viewpoint of such applications, a third-order nonlinear TPE process has two important advantages over a single-photon excitation process: the ability to generate excited states using photons with half the linear excitation energy and a

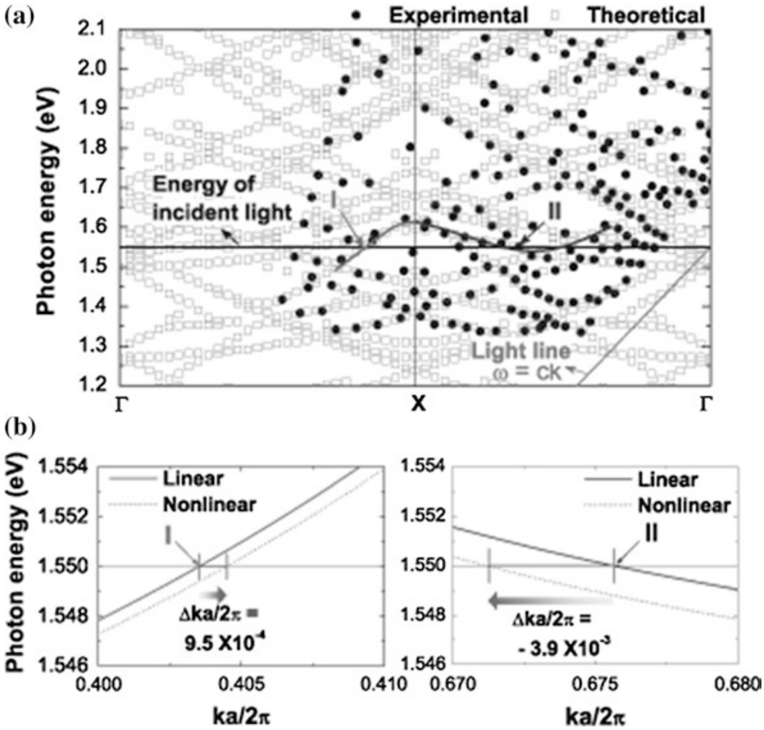

Fig. 6.5 **a** Experimental photonic band structure of the 2D photonic crystal waveguide along the Γ–X line obtained by polarized angular-dependent reflectivity measurements (*closed circles*), and theoretical band structure calculated by the 3D FDTD method (*open squares*). No empirical adjustments of any kind were made in the calculations. Points I and II are the positions of the wave vectors k and photon energies at the resonances α and β (see Fig. 6.4). The photonic bands contributing to the nonlinear reflectivity changes in the vicinity of α and β are indicated by solid lines. **b** Detailed theoretical linear band structure (*solid lines*) in the vicinity of points I (*left*) and II (*right*) and the nonlinear band shifts (*dashed lines*) obtained from an analysis of the observed resonance angle shifts in Fig. 6.4. Adapted with permission from [35], Copyright (2005) by The American Physical Society

quadratic dependence on laser intensity. These advantages can increase the light penetration depth in absorbing media and provide a high three-dimensional spatial resolution under tight-focusing conditions, without being restrained by the diffraction limit. Unfortunately, the majority of known organic molecules (and most inorganic materials) have very small nonlinear absorption cross sections (σ), typically $\sigma \sim 1$ GM ($=10^{-50}$ cm^4 s photon^{-1} molecule^{-1}). Consequently, very high laser powers are required, making the widespread use of two-photon excited fluorescence (TPEF) impractical.

However, the combination of a photonic crystal structure and highly nonlinear materials can produce large nonlinearities, thus reducing the power requirements for TPE processes. The ability to control the light dispersion relation (i.e., the photonic band structure) including extremely slow group velocities v_g in photonic

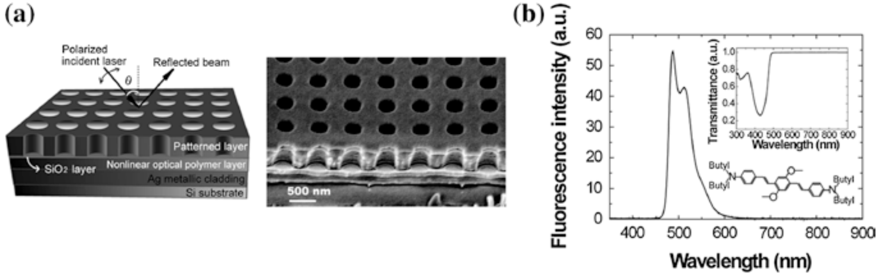

Fig. 6.6 **a** Schematic showing experimental geometry and SEM image showing cross section of fabricated nonlinear optical polymer 2D photonic crystal waveguide. The patterned layer is a square lattice of 360-nm-diameter circular airholes with a lattice constant of 650 nm. **b** Linear fluorescence spectrum for the two-photon absorbing molecule used in the core of the 2D photonic crystal structure. *The inset* shows transmittance spectrum of the molecule and its molecular structure. Reprinted with permission from [51]. Copyright (2008), AIP Publishing LLC

crystal systems enables nonlinear light–matter interactions to be enhanced due to the enhancement of the electromagnetic field of the excitation wave. In conventional waveguides, c/v_g is limited to the order of unity, whereas slower v_g in 2D photonic crystal waveguides can be achieved with many more degrees of freedom.

An example of a fabricated 2D photonic crystal slab waveguides produced from a highly nonlinear host polymer doped with molecules possessing a large two-photon absorption cross section is shown in Fig. 6.6a. A nonlinear optical molecule is the derivative of bis(styryl)benzene that exhibits a very large TPE cross section σ (as high as 900 GM) [50] due to a large delocalized π-electron system, and has very high fluorescence quantum yields. Figure 6.6b shows the fluorescence and transmittance spectra of the core of the 2D photonic crystal structure; the molecular structure of the bis(styryl)benzene derivative is shown in the inset. For the specular TPEF measurements, a mode-locked Ti:sapphire laser operating at a wavelength of 800 nm is used as the excitation light source. To eliminate the pump wavelength beams, an interference filter that transmits only the TPEF beams is placed behind the sample. Further detailed techniques can be found in [51].

Figure 6.7a shows the incident-angle dependence of the TPEF intensity at 486 nm for the highly nonlinear optical polymer 2D photonic crystal slab waveguide. The average pulse energy of the laser beam was 5 nJ. A strong peak was observed in the TPEF spectrum at an incidence angle of 47.5°. A large TPEF enhancement of approximately two orders of magnitude was achieved relative to that for an unpatterned nonlinear optical polymer waveguide. In the low-incident-angle region, a weak peak was observed at 32.5° in the TPEF spectrum. These enhancements in the specular TPEF stem from resonant coupling between the fundamental external laser fields and the corresponding photonic band modes.

To directly clarify the enhancement phenomena in the specular TPEF processes, linear-polarized angular-resolved reflectivity measurements were performed for the same sample. Figure 6.7b shows the reflectivity spectrum along the Γ–X direction for TE polarization at a wavelength of 800 nm. Two sharp dips (depressions) are clearly observed in the reflectivity. The observed angles of the dips are in good agreement with the TPEF enhancement angles at 32.5° and 47.5°. These dips originate from resonant phenomena associated with surface coupling to in-plane photonic bands at resonance energies and in-plane wave vectors. The observed resonance angles have associated in-plane wave vectors, $k = (2\pi/\lambda)\sin\theta$, where λ is the incident light wavelength and $\theta = 0°$ for normal incidence. The resonance dip at each resonance angle in the reflectivity is thus directly related to the in-plane photonic band mode. Accordingly, it was directly verified that the observed enhancements in the TPEF intensity originate from resonant couplings between the external pump laser field and the corresponding photonic band mode for the resonant energy and the in-plane wave vector.

Figure 6.8 shows the theoretical photonic band structure of the highly nonlinear optical polymer photonic crystal slab waveguide along the Γ–X line calculated by the 3D-FDTD method for a model structure identical to the experimental sample structure. No empirical adjustments of any kind were made in the calculations. The black line corresponds to light in a vacuum ($\omega = ck$). The dashed line represents the photon energy corresponding to the energy of the incident laser used in the experiments. The experimentally probed positions of the resonance band modes in the polarized angular-resolved reflectivity are indicated by points *A* and *B*, and they agree well with the theoretical band structure. The experimental and theoretical band structures provide a useful picture of the relationship between the nonlinear optical responses and photonic band dispersions. The band dispersion branches denoted by points *A* and *B* correspond to the resonance band branches that contribute to the observed TPEF responses at incidence angles of 32.5° and 47.5° in Fig. 6.7a, respectively. Resonances *A* and *B* were found to be bands symmetric about the X point. The group velocities v_g of these bands were estimated to be $v_g = \pm 0.18c$ using the slope of the dispersion curve ($v_g = \partial\omega/\partial\boldsymbol{k}$). This result demonstrates the enhancement of the TPEF resulting from the slower group

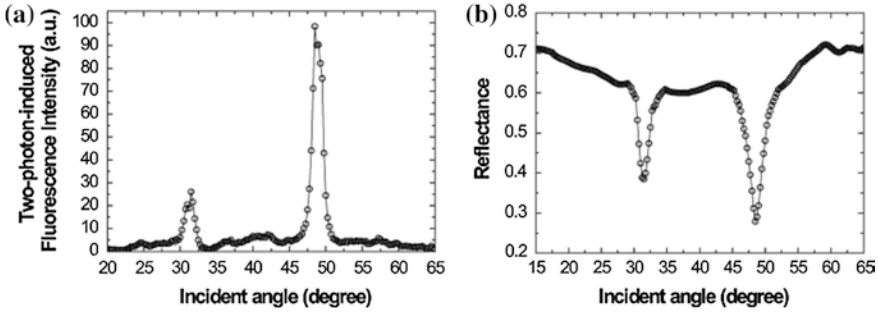

Fig. 6.7 **a** Incidence angle dependence of TPEF intensity at 486 nm for the nonlinear optical polymer 2D photonic slab waveguide. **b** Angular dependence of the linear reflectivity of the same sample at a fixed wavelength of 800 nm along the Γ–X direction. Reprinted with permission from [51]. Copyright (2008), AIP Publishing LLC

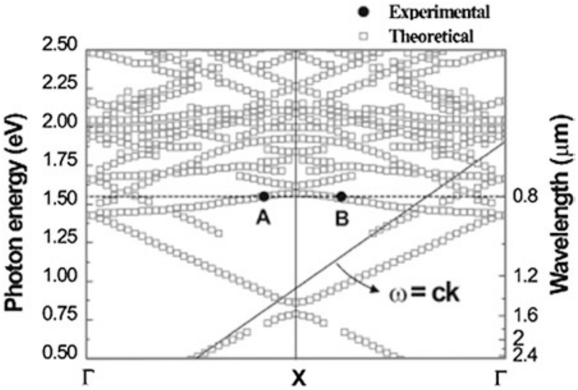

Fig. 6.8 Photonic band structure of the nonlinear optical polymer photonic crystal slab waveguide along the Γ–X line calculated by the 3D-FDTD method (*open squares*). The experimentally probed positions (*closed circles*) of the resonance band modes in the polarized angular-resolved reflectivity are indexed as points *A* and *B*. Reprinted with permission from [51]. Copyright (2008), AIP Publishing LLC

velocity. By comparing the specular TPEF intensities of resonances *A* and *B*, it is reasonable to consider that these enhancements depend strongly on the resonance in-plane ***k*** vectors, that is, the surface coupling efficiency of the incident light fields.

A large TPEF enhancement of approximately two orders of magnitude was observed, originating from resonance between the external pump laser field and a photonic band mode. The results for TPEF enhancement are in good agreement with experimental and theoretical photonic band structure. Future work in this direction should lead to dramatic improvements in the performance of TPE applications.

6.3.3 Electro-Optic Modulation

Silicon-based optical modulators fabricated using CMOS-compatible nanofabrication technology are critical components to enable high-speed optical transceivers and optical interconnects for intra- and inter-chip networks [52–54]. Most of these silicon devices rely on free carrier dispersion effects in the *p*–*n* structures, because no $\chi^{(2)}$ nonlinearity is present in pure silicon because of its centrosymmetry. Therefore, the bandwidths of these modulators are usually limited by the free carrier dynamics. To achieve higher modulation speeds and to minimize the drive voltage, the combination of silicon with another high-nonlinearity material is required. Interest has grown particularly rapidly in silicon–organic hybrid photonics [55–57], which has great potential for diverse applications ranging from ultrafast electro-optic (EO) modulation [56, 58] to all-optical signal processing [59].

Organic EO polymers can provide extremely high modulation speeds in excess of 150 GHz [60, 61], and very high in-device EO coefficients (e.g., $r_{33} = 138$ pm/V at 1,550 nm) [62] that are much higher than those of inorganic materials, such as lithium niobate (~30 pm/V).

We designed a Mach–Zehnder interferometer (MZI) modulator based on a slow-light one-dimensional (1D) photonic crystal waveguide. A schematic of the device is shown in Fig. 6.9a–c. The device consists of an asymmetric MZI with a silicon input/output strip waveguide, which is coupled to a slow-light phase shifter. Figure 6.9c gives a close-up view of the device. The slow-light phase shifter is a 1D photonic crystal laid on SiO_2, composed of a simple periodic array of silicon blocks in a rectangular parallelepiped shape that is filled with and surrounded by an organic EO polymer. An external electric field is applied to the EO polymer cladding through the metal electrodes. Further details can be found in [63].

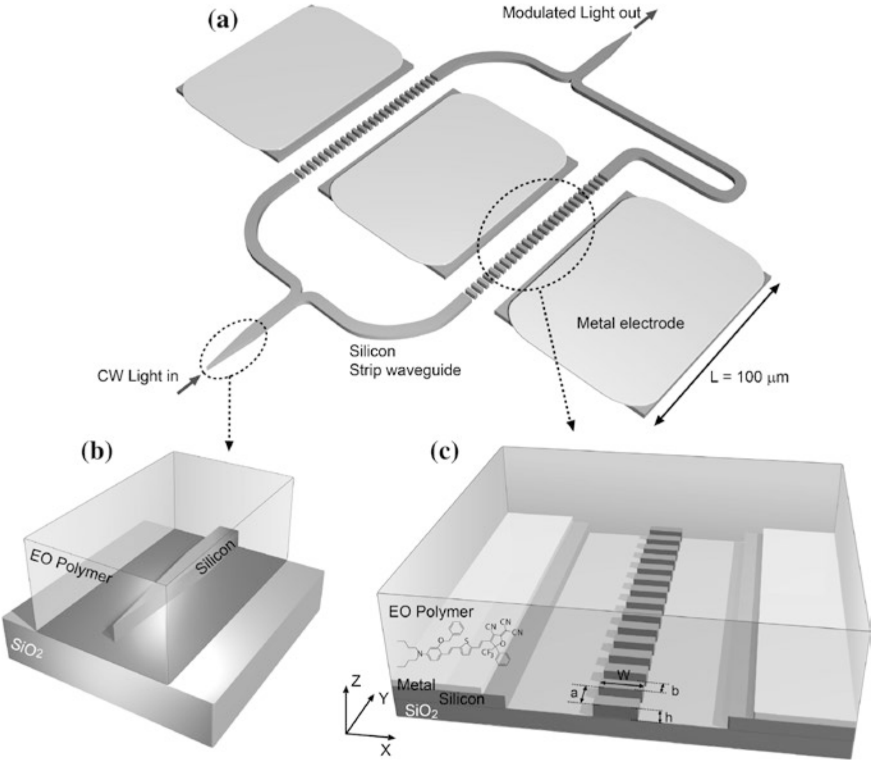

Fig. 6.9 **a** Schematic showing modulator based on an asymmetric MZI. **b** Schematic of the spot size converter optimized for EO polymer/silicon hybrid photonic circuit. **c** Close-up view of slow-light phase shifter consisting of EO polymer/silicon hybrid 1D photonic crystal waveguide. The *inset* shows the molecular structure of the second-order nonlinear chromophore. Reprinted with permission from [63]. Copyright (2013), AIP Publishing LLC

Fig. 6.10 Output spectra of MZI modulator with 100-μm-long phase shifters when bias fields varying from 0 to 15 V/μm are applied to one of the arms. Reprinted with permission from [63]. Copyright (2013), AIP Publishing LLC

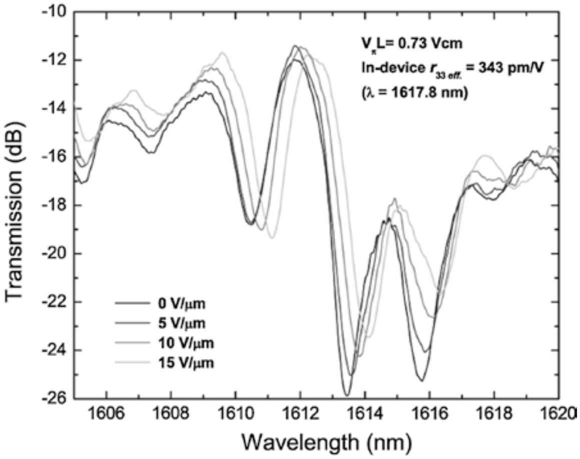

Figure 6.10 shows the output spectra under varying DC bias electric fields. The asymmetric MZI arm means that each output spectrum shows the oscillations as a function of wavelength. The MZI output spectrum shows a redshift with increasing applied bias field. The bias-induced phase shift ($\Delta\varphi$) can then be estimated from the bias-induced wavelength shift ($\Delta\lambda$) in the MZI output spectrum using the relationship $\Delta\varphi = 2\pi\Delta\lambda/FSR$, where FSR denotes the free spectral range of the asymmetric MZI. Typical EO modulation efficiencies ($V_\pi L$) as low as 2.42, 1.43, and 0.73 Vcm have been estimated at wavelengths of 1,607.3, 1,613.5, and 1,617.8 nm, respectively, where V_π is the "half-wave" voltage required to produce the phase shift $\Delta\varphi = \pi$ between the light beams in the two interference arms. Interestingly, the observed modulation efficiency is clearly more efficient at longer wavelengths. Figure 6.11 shows the dependence of the experimental in-device effective EO coefficient $r_{33\text{ eff.}}$ values on the wavelength when compared with the theoretical group index n_g for a 3D model structure that is identical to

Fig. 6.11 Experimental in-device effective EO coefficient $r_{33\text{ eff.}}$ values and the corresponding theoretical group index as a function of wavelength. Reprinted with permission from [63]. Copyright (2013), AIP Publishing LLC

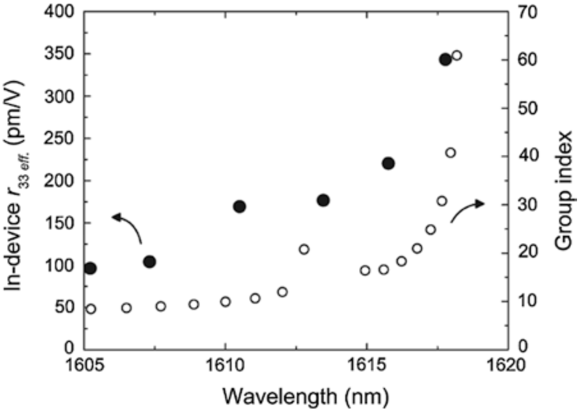

the sample structure. We can clearly see that the in-device effective EO coefficients increase with increasing group index. The maximum in-device effective $r_{33\ \mathrm{eff.}}$ value is 343 pm/V at a wavelength of 1,617.8 nm. These results provide direct evidence that the in-device effective EO coefficients and modulation efficiencies are enhanced by the slower group velocities in the EO polymer/silicon hybrid 1D photonic crystal phase shifter structure. The observed in-device effective EO coefficient ($r_{33\ \mathrm{eff.}} = 343$ pm/V) is about 10 times larger than that of lithium niobate. Good agreement was obtained between the enhanced modulation efficiency and the group index of the photonic band structure, indicating that EO polymer/silicon hybrid photonic crystal platform effectively enables EO modulation using a simple geometry and an extremely small device footprint at potentially ultrafast modulation speeds.

The enhancement of the nonlinear optical processes resulting from the slower group velocity, as demonstrated in this section, should lead to dramatic improvements in the performance of nonlinear optical devices, and will open up new possibilities in nonlinear active applications. Furthermore, the agreement between the observed nonlinear responses and the band dispersion characteristics means we can begin to engineer the nonlinear optical properties of organic nonlinear optical polymer materials by controlling the photonic crystal configuration, which is essential for the realization of desirable photonic applications, such as practical nonlinear optical devices with very low operational power and ultrasmall dimensions.

References

1. E. Yablonovitch, Phys. Rev. Lett. **58**, 2059 (1987)
2. S. John, Phys. Rev. Lett. **58**, 2486 (1987)
3. J.D. Joannopoulos, R.B. Meade, J.N. Winn, *Photonic Crystals: Molding the Flow of Light* (Princeton University Press, Princeton, 1995)
4. K. Sakoda, *Optical Properties of Photonic Crystals* (Springer, Berlin, 2004)
5. S. Inoue, Photonic crystals: manipulating light with periodic structures, Chap. 2, in *Optical Properties of Advanced Materials* (Springer, Heidelberg, 2013)
6. V.N. Astratov, D.M. Whittaker, I.S. Culshaw, R.M. Stevenson, M.S. Skolnick, T.F. Krauss, R.M. De La Rue, Phys. Rev. B **60**, R16255 (1999)
7. D.M. Whittaker, I.S. Culshaw, Phys. Rev. B **60**, 2610 (1999)
8. S. Inoue, Y. Aoyagi, Phys. Rev. B **69**, 205109 (2004)
9. M.S. Thijssen, R. Sprik, J.E.G.J. Wijnhoven, M. Megens, T. Narayanan, Phys. Rev. Lett. **83**, 2730 (1999)
10. M. Notomi, K. Yamada, A. Shinya, J. Takahashi, C. Takahashi, I. Yokohama, Phys. Rev. Lett. **87**, 253902 (2001)
11. A. Otto, Z. Phys. **216**, 398–410 (1968)
12. S. Inoue, S. Yokoyama, Y. Aoyagi, Opt. Express **16**, 2461 (2008)
13. S.Y. Lin, E. Chow, V. Hietala, P.R. Villeneuve, J.D. Joannopoulos, Science **282**, 274 (1998)
14. S.J. McNab, N. Moll, Y.A. Vlasov, Opt. Express **11**, 2927 (2003)
15. P.I. Borel, A. Harpøth, L.H. Frandsen, M. Kristensen, P. Shi, J.S. Jensen, O. Sigmund, Opt. Express **12**, 1996 (2004)

16. P. Lodahl, A. Floris van Driel, I.S. Nikolaev, A. Irman, K. Overgaag, D. Vanmaekelbergh, W.L. Vos, Nature **430**, 654 (2004)
17. D. Englund, D. Fattal, E. Waks, G. Solomon, B. Zhang, T. Nakaoka, Y. Arakawa, Y. Yamamoto, J. Vuckovic, Phys. Rev. Lett. **96**, 013904 (2005)
18. S. Noda, M. Fujita, T. Asano, Nat. Photonics **1**, 449 (2007)
19. Y. Akahane, T. Asano, B. Song, S. Noda, Nature **425**, 944 (2003)
20. T. Yoshie, A. Scherer, J. Hendrickson, G. Khitrova, H.M. Gibbs, G. Rupper, C. Ell, O.B. Shchekin, D.G. Deppe, Nature **432**, 200 (2004)
21. S.L. Portalupi, M. Galli, C. Reardon, T.F. Krauss, L. O'Faolain, L.C. Andreani, D. Gerace, Opt. Express **15**, 16064 (2010)
22. E. Cubukcu, K. Aydin, E. Ozbay, S. Foteinopoulou, C.M. Soukoulis, Nature **423**, 604 (2003)
23. S. Foteinopoulou, C.M. Soukoulis, Phys. Rev. B **67**, 235107 (2003)
24. A. Berrier, M. Mulot, M. Swillo, M. Qiu, L. Thylen, A. Talneau, S. Anand, Phys. Rev. Lett. **93**, 073902 (2004)
25. S. Kocaman, R. Chatterjee, N.C. Panoiu, J.F. McMillan, M.B. Yu, R.M. Osgood, D.L. Kwong, C.W. Wong, Phys. Rev. Lett. **102**, 203905 (2009)
26. P. Russell, Science **299**, 358 (2003)
27. J.C. Knight, Nature **424**, 847 (2003)
28. T. Baba, Nat. Photonics **2**, 465 (2008)
29. J.J. Wierer, A. David, M.M. Megens, Nat. Photonics **3**, 163 (2009)
30. Y. Chassagneux, R. Colombelli, W. Maineult, S. Barbieri, H.E. Beere, D.A. Ritchie, S.P. Khanna, E.H. Linfield, A.G. Davies, Nature **457**, 174 (2009)
31. H. Kosaka, T. Kawashima, A. Tomita, M. Notomi, T. Tamamura, T. Sato, S. Kawakami, Phys. Rev. B **58**, R10096 (1998)
32. K. Guven, K. Aydin, K.B. Alici, C.M. Soukoulis, E. Ozbay, Phys. Rev. B **58**, 205125 (2004)
33. M. Scalora, J.P. Dowling, C.M. Bowden, M.J. Bloemer, Phys. Rev. Lett. **73**, 1368 (1994)
34. M. Soljacis, J.D. Joannopoulos, Nat. Mater. **3**, 211 (2004)
35. S. Inoue, Y. Aoyagi, Phys. Rev. Lett. **94**, 103904 (2005)
36. X. Hu, P. Jiang, C. Ding, H. Yang, Q. Gong, Nat. Photonics **2**, 185 (2008)
37. K. Sakoda, K. Ohtaka, Phys. Rev. B **54**, 5742 (1996)
38. A.R. Cowan, J.F. Young, Phys. Rev. B **65**, 5751 (2002)
39. S. Inoue, Y. Aoyagi, Jpn. J. Appl. Phys. **45**, 6103 (2006)
40. S. Inoue, S. Yokoyama, Thin Solid Films **518**, 470 (2009)
41. K. Rivoire, S. Buckley, J. Vuckovi, Opt. Express **19**, 22198 (2011)
42. C. Monat, B. Corcoran, M. Ebnali-Heidari, C. Grillet, B.J. Eggleton, T.P. White, L. O'Faolain, T.F. Krauss, Opt. Express **17**, 2944 (2009)
43. J.M. Dudley, J.R. Taylor, Nat. Photonics **3**, 85 (2009)
44. R.E. Slusher, B.J. Eggleton, *Nonlinear Photonic Crystals* (Springer, Berlin, 2003)
45. W. Denk, J.H. Strickler, W.W. Webb, Science **248**, 73 (1990)
46. R.H. Kohler, J. Cao, W.R. Zipfe, W.W. Webb, M.R. Hansen, Science **276**, 2039 (1997)
47. D.A. Parthenopoulos, P.M. Rentzepis, Science **245**, 843 (1989)
48. B.H. Cumpston, S.P. Ananthavel, S. Barlow, D.L. Dyer, J.E. Ehrlich, L.L. Erskine, A.A. Heikal, S.M. Kuebler, I.-Y.S. Lee, D. McCord-Maughon, J. Qin, H. Röckel, M. Rumi, X.-L. Wu, S.R. Marder, J.W. Perry, Nature **398**, 51 (1999)
49. J.D. Bhawalkar, G.S. He, P.N. Prasad, Rep. Prog. Phys. **59**, 1041 (1996)
50. M. Kuebler, I.-Y.S. Lee, D. McCord-Maughon, J. Qin, H. Rockel, M. Rumi, X.-L. Wu, S.R. Marder, J.W. Perry, Nature **398**, 51 (1999)
51. S. Inoue, S. Yokoyama, Appl. Phys. Lett. **93**, 111110 (2008)
52. G.T. Reed, G. Mashanovich, F.Y. Gardes, D.J. Thomson, Nat. Photonics **4**, 518 (2010)
53. A. Liu, R. Jones, L. Liao, D. Samara-Rubio, D. Rubin, O. Cohen, R. Nicolaescu, M. Paniccia, Nature **427**, 615 (2004)
54. L. Liao, A. Liu, D. Rubin, J. Basak, Y. Chetrit, H. Nguyen, R. Cohen, N. Izhaky, M. Paniccia, Electron. Lett. **43**, 1196 (2007)

55. J. Leuthold, C. Koos, W. Freude, Nat. Photonics **4**, 535 (2010)
56. J.-M. Brosi, C. Koos, L.C. Andreani, M. Waldow, J. Leuthold, W. Freude, Opt. Express **17**, 4177 (2008)
57. T. Baehr-Jones, M. Hochberg, G. Wang, R. Lawson, Y Liao, P.A. Sullivan, L. Dalton, A.K.-Y. Jen, A. Scherer, Opt. Express **13**, 5216 (2005)
58. R. Ding, T. Baehr-Jones, Y. Liu, R. Bojko, J. Witzens, S. Huang, J. Luo, S. Benight, P. Sulliwan, J-M Fedeli, M. Fournier, L. Dalton, A. Jen, M. Hochberg, Opt. Express **15**, 15618 (2010)
59. C. Koos, P. Vorreau, T. Vallaitis, P. Dumon, W. Bogaerts, R. Baets, B. Esembeson, I. Biaggio, T. Michinobu, F. Diederich, W. Freude, J. Leuthold, Nat. Photonics **3**, 216 (2009)
60. M. Lee, H.E. Katz, C. Erben, D.M. Gill, P. Gopalan, J.D. Heber, D.J. McGee, Science **298**, 1401 (2002)
61. B. Bortnik, Y.-C. Hung, H. Tazawa, B.-J. Seo, J. Luo, A.K.-Y. Jen, W.H. Steier, H.R. Fetterman, IEEE J. Sel. Top. Quantum Electron. **13**, 104 (2007)
62. Y. Enami, C.T. Derose, D. Mathine, C. Loychik, C. Greenlee, R.A. Norwood, T.D. Kim, J. Luo, Y. Tian, A.K.-Y. Jen, N. Peyghambarian, Nat. Photonics **1**, 180 (2007)
63. S. Inoue, A. Otomo, Appl. Phys. Lett. **103**, 171101 (2013)

Chapter 7
Mastering Nano-objects with Photoswitchable Molecules for Nanotechnology Applications

R. Barillé, E. Ortyl, S. Zielinska and J.M. Nunzi

Abstract Advance in the fabrication of nano-objects becomes more important for the development of new nanodevices with local properties leading to new functional devices. In this direction, the assembly of nanometer-scaled building objects into device configurations and functionalization is a promising investigated research field in nanotechnology. Optical recording and photofabrication techniques that exploit changes in material properties have gained importance, and there is a requirement for a decrease of the dimensions of the recording and processing surfaces. Photochromic materials leading to submicron structures responding to stimuli and in particular light are the best materials that exhibit multifunctional behaviors. Photomechanical properties of azopolymers show the perfect performance in photoinduced nanopatterning and reshaping by tailored light fields. Azopolymer nanostructures are then recognized as an excellent choice for a broad range of fundamental and applied research in modern nanotechnology. This chapter shows how polymer nanofilms, nanotubes, nanospheres, or nanowires containing azobenzene can be controlled by light for new photonics applications. Spatially confined excitation of unidirectional motions could make possible the local control of mechanical properties of the material and its structuration. The unprecedented flexibility of the reported photofluidization lithography with this material allows producing well-defined structures as lines, ellipsoids, rectangles, and circles at azopolymer surface with several tenth nanometers structural features.

R. Barillé (✉)
Moltech Anjou, CNRS UMR 6200, PRES UNAM, University of Angers, 2, bd Lavoisier,
49045 Angers, France
e-mail: regis.barille@univ-angers.fr

E. Ortyl · S. Zielinska
Department of Polymer Engineering and Technology, Wrocław University of Technology,
50-370 Wrocław, Poland

J.M. Nunzi
Department of Chemistry, Queen's University, 90 Bader Lane, K7L 3N6 Kingston ON, Canada

Y.S. Zhao (ed.), *Organic Nanophotonics*, Nano-Optics and Nanophotonics,
DOI 10.1007/978-3-662-45082-6_7

7.1 Introduction

A first look on the scientific material journals reveals that the past decade has indeed seen transformative challenges in the scientific landscape due to nanoscience and nanotechnology advances. Optical recording and photofabrication techniques that exploit changes in material properties have gained importance, and there is a requirement for a decrease of the dimensions of the recording and processing surfaces. Advance in the fabrication of nano-objects becomes more important for the development of new nanodevices with local properties leading to new functional devices [1]. Many directions can be taken for their realizations. One is the reduction of the way information can be stored and how tightly irradiating light or stimuli can be focused. The other direction exploits the fabrication of nano-objects reaching the nanometer-scale dimensions for configuring these nano-objects in order to contain information. The techniques used to generate nanoscale structures can commonly be categorized as top-down and bottom-up approaches.

For this reason, photochromic materials have attracted the focus of researchers as promising media for different applications as data recording, storage, and readout in both nonlinear optics and holography [2]. Among these materials, aromatic azo compound holds a prominent place. Photochromic transformations in azo compounds are related to the photoinduced *trans–cis* isomerization of their molecules. Photoinduced isomerism of azobenzene proceeds with large structural change as reflected in the dipole moment and change in geometry. During their photoinduced excitation, *trans* monomers are transformed into the *cis* form. The isomerization process can have a deep effect on the physical and optical properties of materials which contain the azobenzene chromophore as a parent molecule or as a dopant. Azo labels can be selectively attached to the side chains, main chains, cross-links, or chain ends of the polymer. One of the most interesting phenomena associated with the photoisomerization process is massive macroscopic motions of the polymer chains leading to physical deformation of the material well below the glass transition temperature. With this molecule, polymer materials are changed from structural materials to functional materials and the current trend is to employ the azobenzene moiety as a trigger to induce morphological changes which can be light driven [3, 4].

Azopolymer nanostructures are recognized as an excellent choice for a broad range of fundamental and applied research in modern nanotechnology. Owing to unique photomechanical properties of azopolymers, these nanostructures show the perfect performance in photoinduced nanopatterning and reshaping by light fields. Unprecedented flexibility of recently reported photofluidization lithography allows producing well-defined lines, ellipsoids, rectangles, and circles at azopolymer surface with several tenth nanometer structural features [5].

We present in this review how the structure properties of polymer nanofilms, nanotubes, nanospheres, or nanowires containing azobenzene can be controlled by light for new photonics applications. Spatially confined excitation of unidirectional motions could make possible the local control of mechanical properties of the material and its structuration.

In this goal, the production of uniform-sized nano-objects is important. We show the possibilities given by these nanosize objects in view of future applications in photonics and biology. We will split the different parts of the chapter as a function of the topology of the material. The first part will deal with 2D materials (nanofilms). The second part will be devoted to nanotubes corresponding to 1D materials. Finally, if we reduce by an order the topology dimension of the nano-objects, we end up to 0D materials with nanospheres. In the different parts, we will give technological applications of these nano-objects.

7.2 Nanofilms

Polymeric ultra-thin films or nanofilms show noteworthy properties making them potentially useful for several applications in photonics and metrology [6, 7]. They are usually characterized by a thickness lower than one micron meter. Azopolymer nanofilms are good candidates for top or bottom techniques used to generate nanoscale structures. Irradiation of a flat isotropic azopolymer film surface with an intensity distribution of a plane polarized light results in a transfer of an optical pattern to the film surface known as a surface relief grating (SRG). The pitch of the pattern can be controlled by the angle producing the interferences. Typically, two interfering beams are used to create a pattern. The obtained photoinduced surface patterns can be used either directly as functional optical elements or indirectly to microstructures or nanostructures as other optical materials. Once the azopolymer films have been patterned, they can be used as templates to create patterns in other materials [8]. However, the bottom–up approach has the advantage of cheaper setup, operating costs, and the ease of use, but cannot offer the accuracy in producing the shape and location of nanostructures that demonstrate the top–down techniques. Different alternatives to the conventional method with interference pattern are presented using a single laser beam only or with an additional white light. The process uses the molecular self-organization of the photoinduced material.

7.2.1 SRG with a Single Beam

The use of a single beam to induce a pattern on the surface is a challenge because it requires anticipating molecular reactions and controlling the nanoscale pattern. Most of the experiments with one single beam are done with a light illuminating a mask [9]. A photolithographic technique involving the exposure of azopolymer as a photosensitive material through soft conformable phase mask was done [10]. The conformable phase mask was made of transparent flexible materials such as

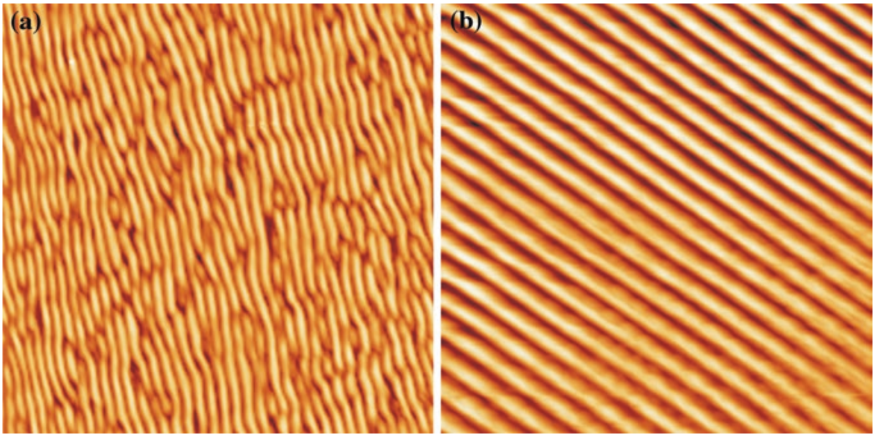

Fig. 7.1 Comparison of surface relief gratings produced by illuminating an azopolymer thin film with **a** one beam by molecular self-organization and **b** by two beam interference

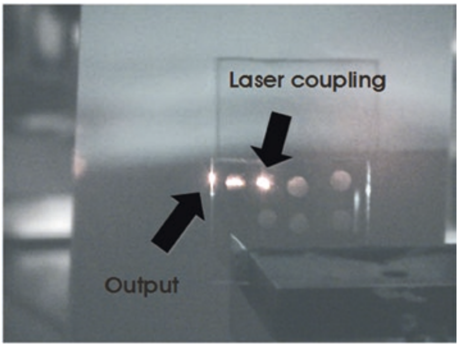

Fig. 7.2 Light coupling of a laser beam in a polymer thin film with a SRG

polydimethylsiloxane (PDMS). Passage of light through the phase mask generates a complex 3D intensity distribution of light in the azopolymer material and nanoscale patterns. Very recently, a multistate storage of a single beam polarization was achieved and read out in a polymer material. This original technique uses only one beam with a controlled polarization to photoinduce a SRG whose wave vector direction depends on the light polarization [11]. Different polarizations of the input laser beam, for example 0°, 30°, 60°, and 90°, can be stored on the surface of azopolymers. Figure 7.1 compares the topography of the surface for the two techniques. In both techniques, the amplitude of the grating is similar with a depth of 50 ± 5 nm. The surface pattern obtained with a single beam is slightly irregular but allows its use in different applications. Figure 7.2 gives one example showing the coupling of light in the thin film with a grating obtained by surface molecular self-organization.

7.2.2 SRG with Incoherent Light

In the goal to find low cost methods to photoinduce SRGs on the surface of thin films, no real solutions were proposed because the general opinion about SRGs is that patterning of photoactive systems needs coherent light.

In the standard setup of SRG inscription on azo dye-based photoactive polymers, the photoactive molecules are excited by an illumination pattern. It was recently showed that a well-defined SRG can be induced in an azopolymer film by the combination of a low-power coherent laser beam with another high-power incoherent and unpolarized beam [12]. It appears that the low-power beam carries information about pitch and orientation of the diffraction grating that is transferred to the surface illuminated by the incoherent light (Fig. 7.3). In this way, a simple system allowing figuring out the minimal requirements to organize disordered materials by an incoherent light into well-organized structures was found. This result showed experimentally that random motions plus information exchanges lead to molecular self-organization. Information is then exchanged locally by the nanorelief of the polymer surface.

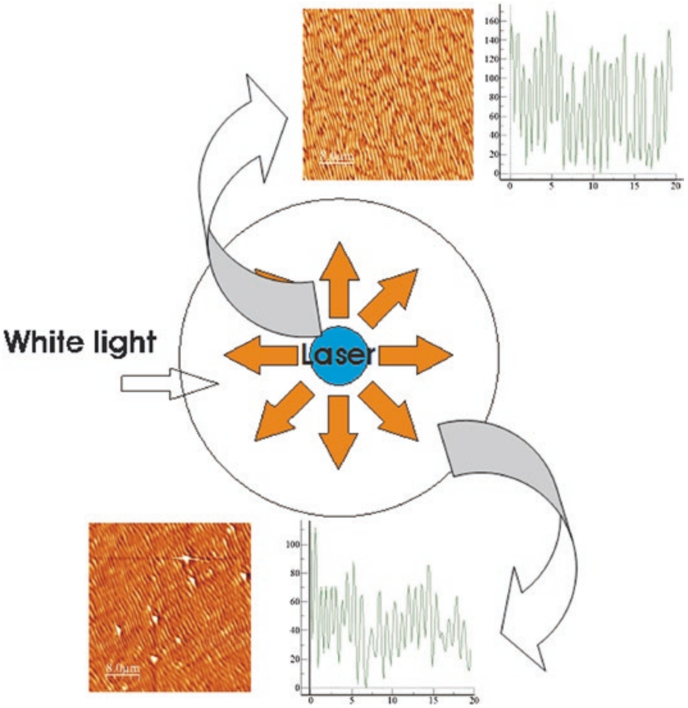

Fig. 7.3 SRG produced on the whole surface illuminated by the superposition of a low-power laser beam with a high-power incoherent light

7.2.3 *Applications*

SRG can find large applications in photonics as waveguide coupling [13] or sensor [14]. The fabrication of a hologram with a single beam can be advantageous in the special case of optical metrology and atmospheric turbulence. Outdoor environment has a significant impact on the quality of a laser beam propagating through the atmosphere over long distances. A method was proposed to measure the effect of turbulence influencing a laser beam with basically this idea: The spatial deformation of a laser propagating in atmospheric turbulence cannot be suppressed but can be used to discriminate the laser parameters influenced by the turbulence. A photochromic material able to self-organize the molecular thin-film surface in relief gratings was used. The contribution of the turbulence when a laser beam passes through a turbid medium with a non-uniform refractive index was measured [15]. The modification of the laser beam parameters modifies the regular written structuration of the thin film. This modification was analyzed by observing the diffraction pattern obtained when the laser beam is diffracted on the surface pattern. This new measurement was simple, was easily implemented, and gave absolute values of atmospheric turbulence (C_n^2) with a previous calibration [16].

In biology, a simple and easy technique to produce erasable and directly in vitro submicron-scale SRGs for the guidance of neurons with a new biocompatible photoswitching material and a single-step laser irradiation was demonstrated [17]. The material uses a photoresponsive polymer with azo chromophores. The glass surface for deposition of chromophoric polymers was modified to be able to form diffraction gratings and resistant to defoliation in aqueous solutions. Methacrylate terpolymers containing 2-hydroxyethyl group in side polymer chain was used to change the glass surface [18]. The results showed that cells sense ultrafine substrate topographies. Nanogrooves acted as scaffolds providing directional cues that guided PC12 cell alignment and orientation similar to microscale grooves.

7.3 Nanotubes

Nanotubes or tubular nanostructures have attracted a great deal of interest during the past decade because of their potential applications in ultrafiltration, catalysis, medicine, or sensors [19]. Tubular nanostructures can be prepared by various synthesis methods. The template synthesis method is regarded as a simple and very effective way for preparing various materials, including polymers, and metals [20]. Porous alumina template synthesis is one of the most commonly used methods because of the walls exhibiting a high surface energy. Researchers have used various kinds of membranes such as polycarbonates and anodized alumina membranes as templates for the fabrication of nanotubes and nanorods. The polymer nanotubes can be obtained by wetting the porous templates with polymer melts or solutions. Such novel nanostructures are expected to provide new functions in optoelectronic and biological applications that cannot be attained with conventional spherical nanoparticles. The synthesis of azopolymer can lead to promising applications due to the surface or geometric modifications by molecular mass transport.

7.3.1 Fabrications

Nanostructures with extraordinarily small diameters were prepared with the method of wetting of porous anodic alumina membrane templates whose porosity consisted of an array of parallel and straight channels, as such low diameters are impossible to be obtained using lithographic methods. This template method has previously been shown to be capable of efficiently forming nanotubes for a variety of organic materials [21].

The alumina membrane filters (Anodisc) had a diameter of 13 mm and thickness of 60 μm. The cylindrical pores had uniform diameters, and each of these pores is viewed as a baker, in which an object of the desired material is shaped. The pores in the membrane had monodispersed diameters of 100 nm. An azopolymer nanocylinder was obtained in each pore. Figure 7.4a shows a scanning electronic microscope image of dispersed nanotubes. The average monodispersed diameter of the nanotubes was found to be 100 nm.

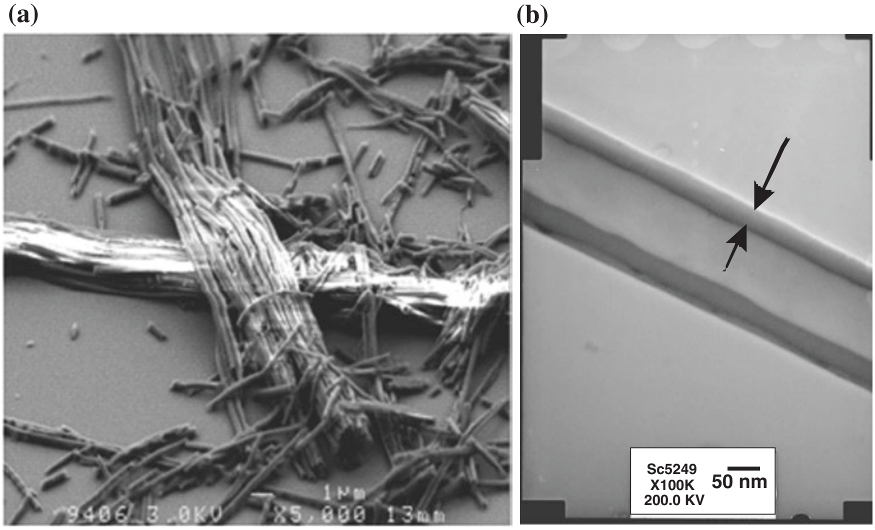

Fig. 7.4 **a** SEM of azopolymer nanotubes prepared with a 200 nm pore diameter Anodisc membrane, **b** TEM image of one nanotube. The nanotube wall thickness indicated by *arrows* is about 15 nm

The length depends on the different chosen areas on the sample but an average length of 10–15 μm was measured. Figure 7.4b shows cross sections of nanotubes dispersed on a grid and observed with TEM. A typical inner wall of 15 nm is measured. The TEM observations confirm the hollow core structure of the nanotubes with a constant cross section along axis.

7.3.2 Nanostructuration of Nanotubes

Periodic structures in the submicrometer scale are in high demand for many applications ranging from electronics to photonics, and large results have been obtained but less on nano-objects [22]. Up to now, patterning of structures was possible on the surface of thin films. We recently demonstrate the possibility to inscribe a nanostructure on the surface of azopolymer nanotube with laser illumination [23, 24]. In this view, assembly of nanometer-scale building blocks into device configurations with different individual patterns could be promising for tag of information and data storage. Building patterns on the surface of nanometer objects permits optical processing for nanoscale engineering and for biotechnologies. At this scale, only instruments with enough resolution as near-field optical microscope are able to fit the pattern dimension required.

7.3.3 Nonlinear Effects with Nanotubes

Beyond all nonlinear phenomena, the second harmonic generation (SHG) is particularly interesting because it can be generated through surface interactions, local imperfections, and deformations resulting from the assembly of the nano-objects on the surface. The use of polymer nanotubes dispersed on the surface as randomly oriented mess can give rise to interesting nonlinear phenomena which are influenced by the structure of the nano-objects.

For the needs of the SHG investigation, the sample has been placed on X, Y, Z, θ stage and in the focal point of a x50 objective microscope (Olympus SLMPLN50X, numerical aperture = 0.45) with a diffraction-limited spot diameter of about 1.8 μm. The angle θ, defined between the normal to the surface of the sample and the optical axis, is chosen to maximize the SHG signal. The X, Y, Z motorized displacement stages were controlled in order to keep the focal point in the plane of the sample. The exciting beam was provided by a Tsunami Ti/saphire tuneable laser (670–1,100 nm) with 120-fs pulse duration and 80 MHz repetition rate. The polarization and the power of the incident beam on the sample have been adjusted with a half-wave plate and a Glan-Taylor polarizer. The light exiting the sample has been collected by a second microscope objective and then directed to the input slit of a spectrometer. The spectrum was then recorded by a fast liquid nitrogen-cooled CCD camera (Princeton research) at the exit plane of the monochromator. A Schott BG 39 filter eliminated the fundamental laser wavelength.

Fig. 7.5 Log–log plot of the SHG intensity of dispersed nanotube on glass substrate versus pumping intensity ($\lambda = 750$ nm)

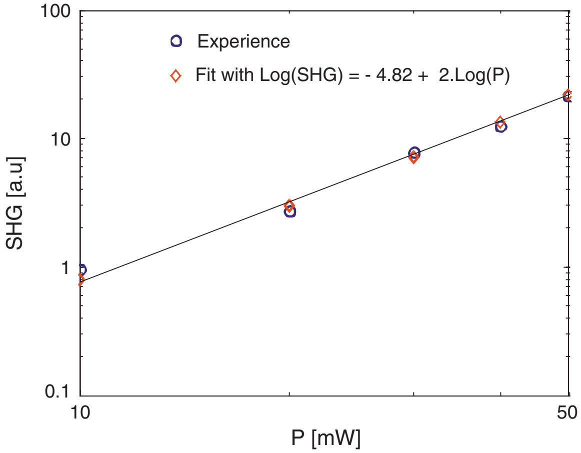

At a wavelength of 750 nm, employing a 10 mW laser power (corresponding to 125 pJ per pulse and 400 W peak power), nearly uniform SHG signal over the surface of the sample has been obtained.

To ensure that the acquired signals were entirely related to second-order nonlinear processes, several precautions were taken. Firstly, the dependence of the SHG response upon the incident laser power has been checked by performing SHG measurements, with few nanotubes dispersed on the glass substrate. An area has been chosen, where nanotubes with equal length were well dispersed, and less than 10 nanotubes were within the laser-beam-spot-irradiated area. The average power of the laser has been varied, without changing any other experimental parameters, while recording the SHG signal coming from the same area on the sample surface. An upper threshold of 50 mW has been used to avoid damaging of the sample. In Fig. 7.5, the SHG efficiency as a function of the incident laser power is plotted in logarithmic scales. As it can be seen in the same figure, the slope of the fitted line is equal to 2 confirming the quadratic dependence of the signal with the input power, verifying the second-order nonlinear origin of the signal and that no saturation of the response was taking place. Similar results have been obtained in other areas on the sample, while the contribution of the glass has been found to be negligible under the same experimental conditions and even higher laser powers.

Based on these SHG findings, further measurements have been carried out in order to investigate the possibility to detect signal coming from only one nanotube. During this investigation, the power of the fundamental beam was fixed to 10 mW with vertical (s) polarization. In Fig. 7.6, typical SHG spectrum (blue line) of a nanotube is obtained using 3-min integration time. We use a spline fitting curve (red line) for a better estimation of the intensity peak of the spectrum. The signal to noise ratio is 2.5. Long exposure time has been chosen in order to increase the signal to noise ratio without increasing the laser power, which could possibly result in

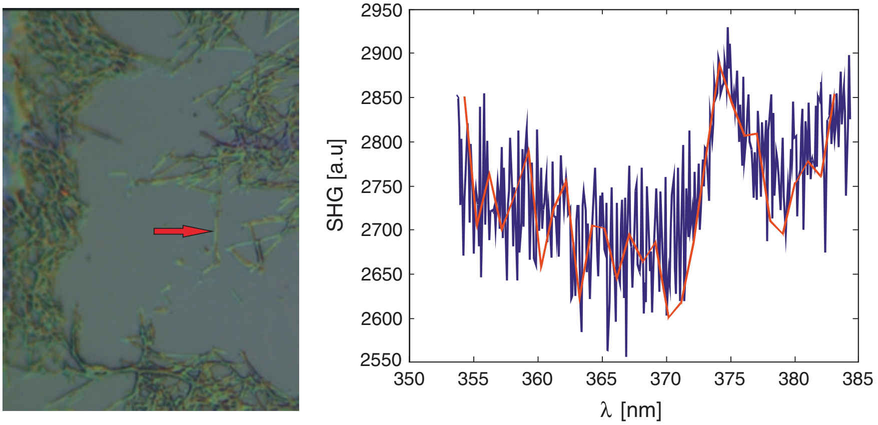

Fig. 7.6 High magnification optical image of azopolymer nanotubes dispersed on a glass substrate (*left*) with the SHG intensity measured on a single nanotube (*right*). The *arrow* indicates where the SHG measurement has been done

the damage of the sample. This long exposure time could be reduced by choosing a laser with a laser fundamental wavelength out of the range of our current laser wavelengths in order to limit the SHG absorption by the sample in the light path.

The investigated area, which includes only one nanotube, is shown in the upper part of the same figure and has been checked after the measurements to verify that no damage of the sample during the irradiation has been done. The peak at a wavelength of 375 nm confirms the existing second harmonic signal generated from one nanotube. This result of high SHG intensity with a nanotube correlates collagen fiber SHG results [25]. Moreover, the SHG efficiency has been mapped over an area on the film providing 2D SHG mapping of the sample surface (Fig. 7.7). The area has a size of 100 μm by 80 μm and has been scanned with two different polarizations of the laser beam (s and p). It is interesting to note the big contrast between the two polarizations. For a vertical (s) polarization, an intense SHG has been observed, while in the case of horizontal (p) polarization, almost no signal has been obtained, under the same experimental conditions.

All the nanotubes were randomly laid down on the surface scanned by the laser, so the negligible signal in the case of horizontal polarization cannot be attributed to the geometric configuration of the nanotubes. We make the assumption that the axially transverse alignment of the molecules during the fabrication of the nanotubes gives this anisotropy concerning the SHG efficiency.

A polar diagram in Fig. 7.8 gives the integrated SHG intensity of the whole sample containing nanotubes dispersed on the surface as a function of the linear laser beam polarization. During this measurement, the laser beam has been focused by means of a microscope objective with a low magnification (×10, NA = 0.25) and the signal was collected with a photomultiplier. The maximum response of the sample is obtained for a laser beam polarization of 90°, in agreement with our previous findings.

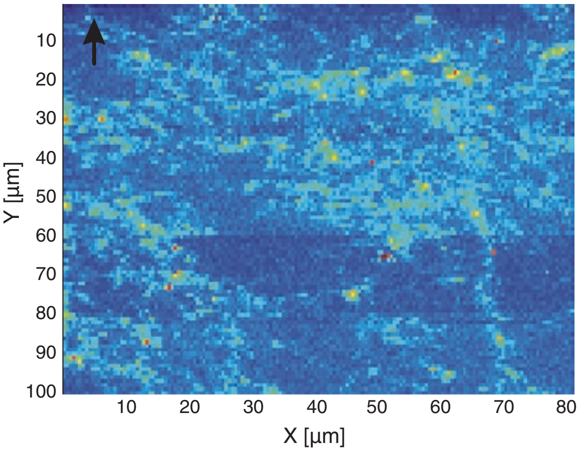

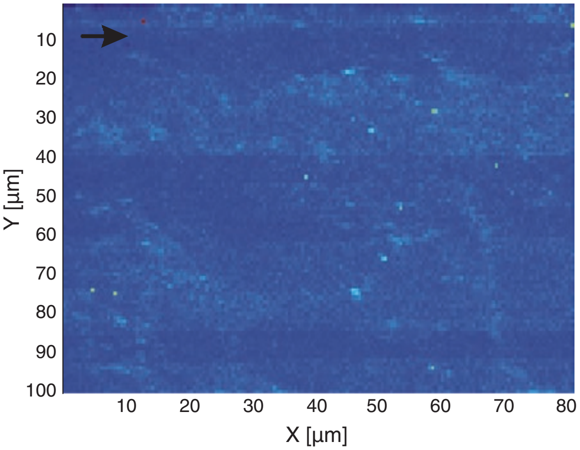

Fig. 7.7 SHG mapping of the surface of dispersed azopolymer nanotubes for the vertical polarization (*above*) and the horizontal polarization (*below*) of the laser beam. In both images, the laser beam intensity is the same

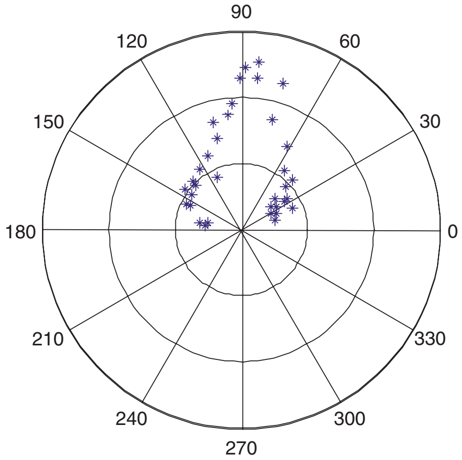

Fig. 7.8 Polar diagram for SHG measurements of the dispersed azopolymer nanotubes on the surface of a glass substrate

In order to shed light into the fact that different laser polarizations result in different SHG intensities, complementary measurements with a confocal Raman microscope have been carried out. These studies were expected to reveal information related to the conformation and molecular order of the azopolymer nano-objects. We show that there is a strong dependency between the intensity of certain Raman bands and the orientation of the nanotube with respect to the incident laser light.

Raman spectra were taken with a confocal Raman microscope (Renishaw in-Via) with a laser wavelength at $\lambda = 647$ nm and 600 lines/mm grating. The laser wavelength is chosen far from the absorption band of the material. The CW laser power was set to 1.0 mW to avoid denaturation of the sample. The laser has a polarization ratio of 100:1. The laser beam polarization direction is referred as perpendicular or parallel to the substrate. However, the measurements can be considered as unpolarized because no analyzer was used. The integration time is fixed to 10 s. The microscope objective used for focusing the incident laser beam and collecting the Raman signal has a high magnification ($\times 100$, NA $= 0.75$). We have checked that the sample's substrate did not contribute to the measured Raman signal.

The anisotropy of Raman bands has its origin in the preferential orientation of vibrating molecular fragments with respect to the nano-object axis and incident polarization orientation [26]. We consider how alignment of nanotubes along the two axes x and y will influence the observed anisotropy and how we can use Raman anisotropy measurements to probe the molecular alignment. To account on this possibility, we choose two individual isolated nanotubes on the sample in the vertical and horizontal position with two different linear laser beam polarizations as it is described in Fig. 7.6. The Raman spectra shown were obtained on nanotubes with long axes aligned in parallel and perpendicular with respect to the polarization of the incident laser beam in Fig. 7.9.

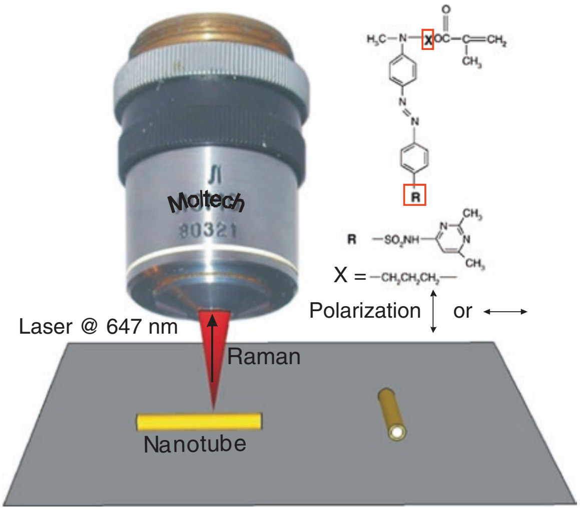

Fig. 7.9 Scheme of the confocal Raman measurements on a single nanotube. The chemical structure of the azopolymer sample is inserted in the figure

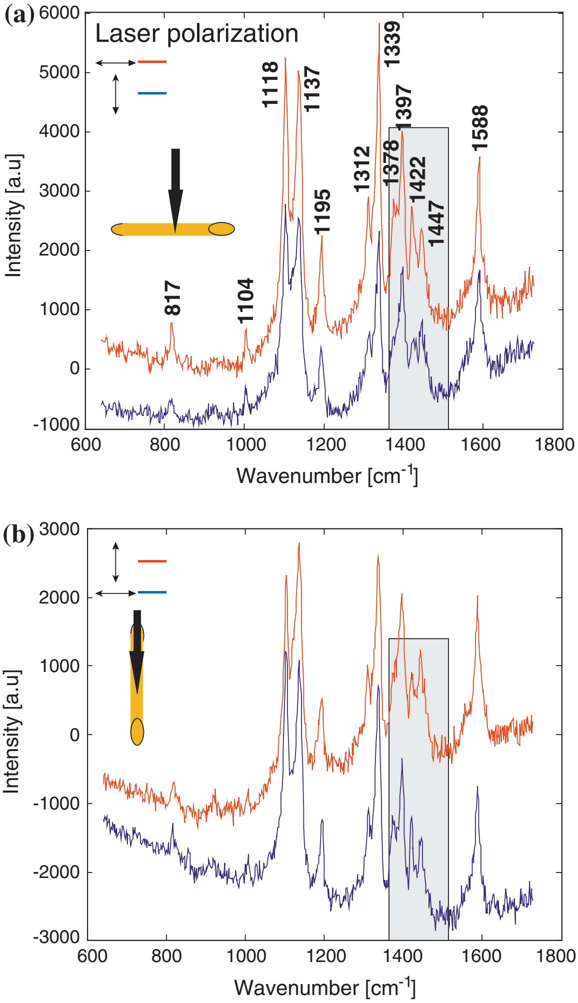

Fig. 7.10 Raman spectra obtained with the confocal Raman microscope and taken on a single azopolymer nanotube for two incident laser beam polarizations. The orientation of the nanotube is inserted. The *gray squares* indicate the selected bands that show the strongest anisotropic Raman scattering

The experimental Raman spectra have first been processed to eliminate the signal background offset with a first-order polynomial. The final flattened Raman spectra are shown in Fig. 7.10. They display a difference in intensity offset between the vertical and horizontal polarization which does not affect the analysis based on the spectrum's peaks. The spectra present eight main bands representing the different vibrations of the molecule shown in the inset of Fig. 7.10. They feature the characteristic of azopolymer bands.

Very fine details of the spectrum in the window from 1,000 to 1,600 cm^{-1} are present with double peaks not measured in previous studies on azobenzene materials [27]. The band assignments for the Raman spectra of nanotubes were made by referring to Raman spectra of various azobenzene derivatives for which vibrational assignments have been well established [28]. We have four double peaks with intense signals at 1,104 cm^{-1} ($\nu(\Phi\text{-N})$, 18a), 1,137 and 1,195 cm^{-1} (δ(CH) ring 9a and 9b), 1,339 cm^{-1} ($\nu(\text{NO}_2)$), 1,397 cm^{-1} ($\nu(\text{N} = \text{N})$), 1,422 and 1,447 cm^{-1} (δ(CH) ring 19a and 19b). The assignment of the main bands of azobenzene at 1,137 cm^{-1}, 1,447 cm^{-1}, and 1,588 cm^{-1} as the C–N, N=N, and phenyl C=C stretches, respectively, is consistent with the available literature [14]. The Raman frequencies in the spectrum present a cluster of three bands of almost equal intensities at 1,312–1,339 cm^{-1}, 1,378–1,397 cm^{-1}, and 1,422–1,447 cm^{-1}. These bands in the spectra feature the characteristic of the *trans–cis* isomerization and are assigned to the –N=N– stretching mode with a contribution from the phenyl ring mode (ν_{19}). The frequency of the –N=N– stretching band of azobenzene derivatives is very sensitive to the conformation around the –N=N– group. Moreover, the $\nu(\text{NO}_2)$ mode at 1,339 cm^{-1} is oriented along the long molecular axis of the *trans*-shape azobenzene chromophore and is a good probe to estimate the orientation of the rod-shape azobenzene chromophore. We focus our analysis on the peak at 1,339 cm^{-1}, and the peaks in the frequency range from 1,330 to 1,430 cm^{-1} corresponding to the gray square in Fig. 7.10.

The peak at 1,339 cm^{-1} and its intensity ratio compared to the peak at 1,312 cm^{-1} do not show a significative variation when the polarization is changed. This mode is sensitive to reorientation mechanisms in the light-induced isomerization meaning that no molecular movement took place in the nanotube. No laser light with a wavelength matching the absorption spectrum of the azopolymer nanotubes has been sent to the sample. Then, no photoinduced translation diffusion motion of the azo dyes during isomerization has been involved before our measurements.

Two double peaks are present: one for $\nu_1 = 1{,}378$ cm^{-1} and $\nu_2 = 1{,}397$ cm^{-1} and the second one for the frequencies $\nu_3 = 1{,}422$ cm^{-1} and $\nu_4 = 1{,}447$ cm^{-1}. The first peak at $\nu_1 = 1{,}378$ cm^{-1} exhibits an orientation-dependent intensity. This intensity vanishes when rotating the polarization by 90°, whereas the peak at 1,378 cm^{-1} stays with nearly the same intensity.

Such behavior is also observed for the band at 1,422 and 1,447 cm^{-1}. We find again this variation of intensity when the nanotube is rotated by 90°. Raman spectra with the nanotube long axis aligned in the vertical direction confirm the polarization orientation-dependent intensity.

It is clear that the bands at 1,378 and 1,422 cm^{-1} are less intense when the polarization is perpendicular or when the nanotube is oriented in the vertical direction. They show an enhanced Raman intensity in the parallel direction of the polarization. The variation of the Raman bands shows that all the molecular bonds at 1,312, 1,378, and 1,422 cm^{-1} are oriented parallel to the nanotube axis. The 1,339 cm^{-1} of the phenyl ring mode possesses a similar orientation. The anisotropic scattering for these bands indicates that the most probable orientation of the molecules is in the direction of the nanotube long axis [29]. The intensity of the spectra is sensitive to the average molecular orientation of the molecules and gives a maximum for one polarization.

Raman scattering measurements on the whole surface of the nanotubes are presented in Fig. 7.11. They do not present polarization orientation-dependent intensities as we have found in the case of the Raman measurements on individual nanotubes.

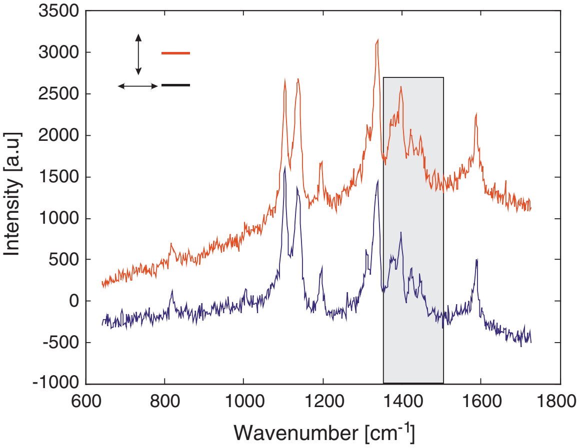

Fig. 7.11 Raman spectra obtained with the confocal Raman microscope with a low magnification of the microscope objective on large number of randomly dispersed nanotubes

We attribute this result to the fact that the signal emanates from a mixing of randomly oriented nanotubes. The small difference in the peak intensities is then difficult to be observed with the intensity resolution of the utilized instrument. Previous experiments on collagen allowed the observation of different spectra with far-field Raman measurements, when the sample is aligned in parallel or perpendicular with respect to the polarization of the incident laser [30] but the sample presented highly collagen structures with well-defined uniaxial parallel-aligned collagen fibrils contrary to our ample where the nanotubes are dispersed on the surface.

Confocal Raman measurements and polarized scanning near-field experiments on structured thin film electrically poled with a wire poling scheme have revealed a strong polar ordering of the azobenzene chromophores [31]. Moreover, concerning the SHG study, s polarization SHG measurements in this study resulted in a higher SHG response compared with those carried out with the p-polarized laser beam. After calculations, the authors showed that molecular orientational distribution calculations had a polar asymmetry along the reference direction normal to the film plane. Raman and SHG are two complementary measurements where the optical contrast relative to polar orientations is exclusively observed in SHG [32]. Nanotubes are hollow cylinders with extreme thin wall thickness. The high confinement of material in surface during the template fabrication leads to a molecular radial self-assembly and organized along the nanotube long axis. Then, inside the nanotubes with no light previously sent to photoisomerize the molecules and no electric field applied, azo molecules present a natural polar distribution along the Z reference revealing a quite efficient poling in the nanotube. Assuming the molecular backbone lies perpendicular to the circular geometry of the nanotube, considering molecular vibrations with a highly uniaxial Raman tensor and the principal axis is coincident with the polymer chain axis, the mechanism of SHG in the case of p-polarized laser beam, whatever the random distribution of the nanotubes on the glass surface, can be then well explained. However, a small component of the angular orientation of the molecules in the horizontal direction explains the nonzero variation of the polarizability and the polarization orientation-dependent Raman spectra, if the electric field is applied parallel or perpendicular to the molecular axis. Precise angular distribution of molecules inside the nanotubes requires further, complete calculations, which are not necessary in the context of further developments of azopolymer nanotubes for photonic or biological applications.

7.4 Nanospheres

Current interest in the properties of polymers (mechanical, electrical, …) confined into nanometer scale is very intense, both from the fundamental and practical perspectives. Polymers are widely used in nanofabrication processes such as wires of nanometer-scale diameters, nano-imprinting, and nanoscale polymeric particles. Confined polymers are central to a broad range of advanced materials and emerging nanotechnologies, with applications including biomaterials, micro- and optoelectronics, and energy capture/storage, among others [33]. Nanometer-sized functional particles are attractive for optical, electrical, magnetic, and biological applications. Besides cutting-edge fabrication strategies, control over the changes in properties induced by nanoscale confinement is a central issue to be taken into account. Moreover, in addition to size, the shape of a nanoparticle was reported to be crucial, for example, how it interacts with light.

For several years, modification of the physical properties due to size effects when approaching nanometer lengths in glass forming systems in general, and in polymers in particular, has been strongly debated. Among the different properties, variations of the glass transition of confined polymers as in thin nanometer-thickness films have motivated a good number of experimental works [34]. Confinement experiments in polymer systems in general have been considered as a very elegant way of probing the existence of a correlation length (ξ) of cooperative motions that produces molecules under light [35]. For azobenzene molecules, the thermal relaxation from the *cis* state to the *trans* state completes an optomechanical cycle that could leave the azobenzene group in a new orientation leading a mass transport and a surface modification when the molecule is grafted to the polymer chain of the polymer matrice. It is potentially interesting to study the molecular mass transport in geometric system with a restricted freedom of movements.

Although there are tremendous potential advantages of using anisotropic nanoparticles like nanorice instead of conventional spherical nanoparticles, the development of controlling such shape on the nanoscale is in its early stages. Even though polymer nanospheres have commonly been produced, the terminal shape modification of a large number of polymer nanoparticles or individual ones into nanorice or nanospears has remained a challenging task. If functional polymer nanoparticles can be shaped in the desired forms on the nanoscale, they can easily be functionalized to have much enhanced multifunctional properties using them as nanotemplates or substrates.

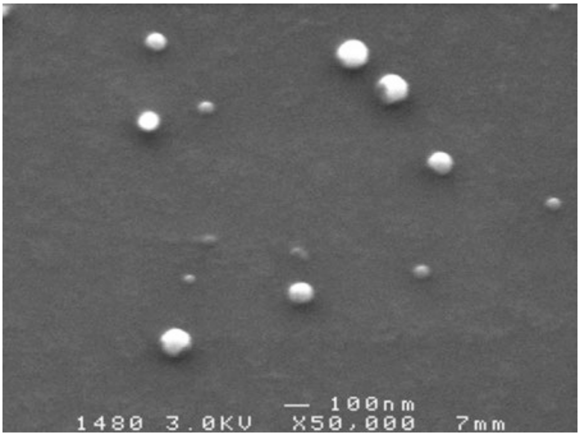

Fig. 7.12 SEM image of azopolymer nanospheres

7.4.1 Fabrication of Azopolymer Nanospheres

The azopolymer was dissolved at 50 mg/ml in tetrahydofurane (THF). The nanospheres were prepared following the method used for aggregate formation from polystyrenepoly (acrylic acid) block copolymers micelles [36]. Deionized water was added dropwise into the THF solution. When micellization occurs, the nanospheres are dropped on a glass substrate. Density of the nanospheres on the surface is about 9 μm^{-2}. Figure 7.12 presents a scanning electron microscope (SEM) image of the nanospheres dispersed on the surface of a microscope glass slide. We can estimate their external diameter by statistical analysis of the image around 84 ± 10 nm.

7.4.2 Photomechanical Effect on Azopolymer Nanospheres

The shape modification of azopolymer nanoparticles used a white light with enough power to avoid melting of the nanospheres onto the sample. Figure 7.13 shows an AFM image of two nanospheres before and after irradiation of the sample surface with the incoherent white light. After irradiation, the nanosphere width has expanded. A cross section in the horizontal and vertical directions of nanosphere surface topographic profiles before and after irradiation have shown that the sphere has been expanded almost uniformly in the film plane, with a recorded increase of 20 % for the horizontal cross section and 35 % for the vertical cross section in the substrate plane. The photoelastic force exerted by light was estimated around 1 μN corresponding to an order of magnitude larger than typical forces needed for the deformation of hollow polyelectrolyte microcapsules using an atomic force microscope [37]. In the case of the nanosphere, the photoinduced deformation effect restricted to a very small surface produces a different behavior

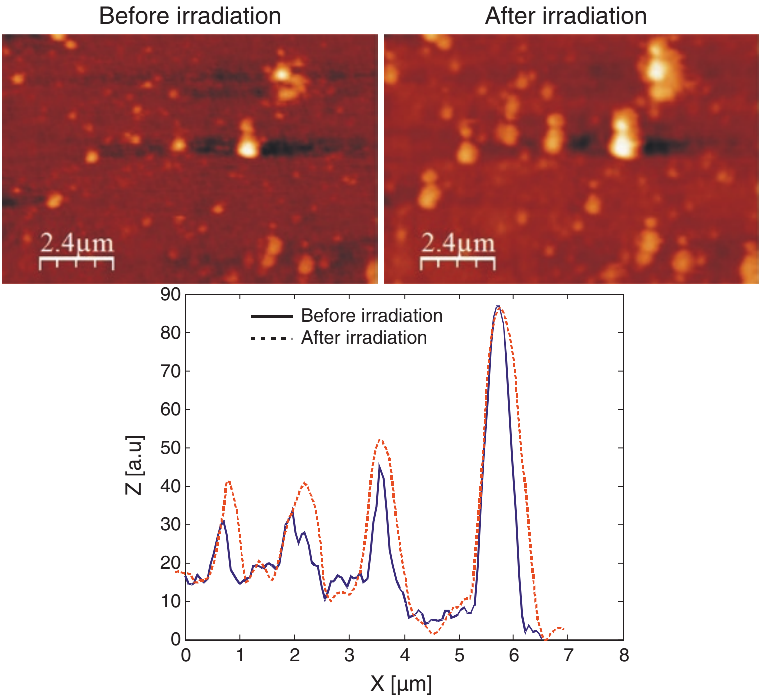

Fig. 7.13 AFM profiles in the X direction of nanospheres before and after irradiation with an incoherent along the substrate plane

than in thin films. A white light incoherent beam can be used for uniform mass motion. The conclusion of this experiment shows that the use of incoherent light is a promising technique in the case of formation or patterning of nano-objects with dimensions in the order of the coherence property of light.

7.4.3 Other Nano-Objects

A simple bottom-up approach has been experimentally demonstrated to form donut-shaped nanostructures at the tailored surface of an azopolymer film by an incoherent unpolarized light illumination. The key difference in this approach is the use of an incoherent light for growing nanostructures rather than for optical erasing and simultaneously directing the final shape of a nanostructure by the initial seed of tiny nanoscale holes. The surface of the film was covered with randomly placed nanoholes with a monodispersed diameter but with different depths. The method chosen is solvent-induced dewetting of thin azopolymer films on glass substrates. Contact of a thin polymer film to its solvent droplet reduces the glass transition

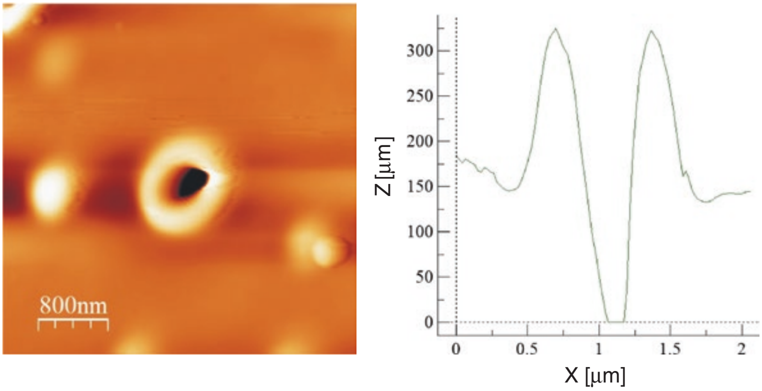

Fig. 7.14 A typical close-up topographical image of azopolymer nanodoughnut obtained by AFM and corresponding height cross section

temperature as the solvent molecules penetrate into the film matrix. The length scale period between the nanohole structures is a function of the film thickness as well as the surface and interfacial tensions of the film and the substrate material.

In the experiment, incoherent white light from xenon halogen lamp was used to initiate photoinduced mass transport in the film. To prove the ability of photoinduced nanostructuring, a detailed AFM image of the film after the illumination was made (Fig. 7.14). Nanodonuts represent a structure which consists of a central hole and a surrounding ring. According to the photoinduced material used in the experiment, the geometry of the nanostructures can be modified by light.

7.5 Conclusion

In conclusion, azopolymer is a photoinduced material giving a large number of possibilities to manage the fabrication and modification of nano-objects. A large number of geometric shapes and topologies of nano-objects can be fabricated. Moreover, this material opens the way to the emerging field of polymer nanostructuration with the ability to generate a variety of different morphologies with structural definition on the nanometric scale. Properties and behaviors of this material used for nanometric structures depend on both the nature of its molecular constituents and their precise spatial self-positioning. We have shown that these unique features are mainly obtained by molecular mass transport due to a *trans–cis* isomerization. Nanostructured materials can led to the development of new miniatures devices. For example, nanotube or tubular nanodevices can be functionalized with organic/inorganic materials to combine fluorescent multi-properties [38]. With the progress in synthesis routes, it is possible to reproduce and easily fabricate and study nanostructured polymer systems, such as thin films, nanowires, nanotubes, and nanoparticles.

References

1. S.F.Y. Li, S.S. Mark, L.J. Kricka, Polymeric nanotubes and nanorods for biomedical applications. Cur. Nanosci. **5**, 182–188 (2014)
2. A. Priimagi, A. Shevchenko, Azopolymer-based micro—and nanopatterning for photonic applications. J. Polym. Sci. Part B: Polym. Phys. **52**(3), 163–182 (2014)
3. H. Zollinger, *Azo and diazo chemistry: aliphatic and aromatic compounds* (Interscience Publishers, New York, 1961)
4. N.K. Viswanathan, D.Y. Kim, S. Bian, J. Williams, W. Liu, L. Li, L. Samuelson, J. Kumar, S.K. Tripathy, Surface relief structures on azo polymer films. J. Mater. Chem. **9**, 1941–1955 (1999)
5. X. Wang, J. Yin, X. Wang, Self-structured surface patterns on epoxy-based azo polymer filmsinduced by laser light irradiation. Macromolecules **44**, 6856–6867 (2011)
6. R.J. Moerland, J.E. Koskela, A. Kravchenko, M. Simberg, S. van der Vegte, M. Kaivola, A. Priimagi, R.H.A. Ras, Large-area arrays of three-dimensional plasmonic subwavelength-sized structures from azopolymer surface-relief gratings. Mater. Horiz. **1**, 74–80 (2014)
7. G. Ye, C. Yang, X. Wang, Sensing diffraction gratings of antigen-responsive hydrogel for human immunoglobulin-g detection. Macromol. Rapid Commun. **31**, 1332–1336 (2010)
8. H. PilHo, Y. Fadong, L. Lian, K. Myunghwan, R. Mosurkal, A.L. Samuelson, J. Kumar, Simple fabrication of zinc oxide nanostructures. J. Mater. Chem. **18**, 637–639 (2008)
9. Z. Sekkat, S. Kawata, Laser nanofabrication in photoresists and azopolymers. Laser Photonics Rev. **8**(1), 1–26 (2014)
10. R.H. Lambeth, J. Park, H. Liao, D.J. Shir, S. Jeon, J.A. Rogers, J.S. Moore, Proximity field nanopatterning of azopolymer thin films. Nanotechnology **21**, 165301 (2010)
11. S. Ahmadi Kanjani, R. Barille, B.S. Dabos-Seignon, J.-M. Nunzi, E. Ortyl, S. Kucharski, Multistate polarization addressing using one single beam in an azopolymer film. Opt. Lett. **30**(15), 1986–1988 (2005)
12. S. Ahmadi Kanjani, R. Barille, B.S. Dabos-Seignon, J.-M. Nunzi, E. Ortyl, S. Kucharski, Incoherent light induced self-organisation of molecules. Opt. Lett. **30**(23), 3177–3179 (2005)
13. E. Heydari, E. Mohajerani, A. Shams, All optical switching in azo-polymer planar waveguide. Opt. Comm. **284**(5), 1208–1212 (2011)
14. Y. Luo, J. Zhou, Q. Yan, W. Su, Z. Li, Q. Zhang, J. Huang, K. Wang, Optical manipulable polymer optical fiber Bragg gratings with azopolymer as core material. Appl. Phys. Lett. **91**, 071110 (2007)
15. R. Barille, Y. Morille, D.G. Perez, S. Kucharski, S. Zielinska, E. Ortyl, Simple turbulence measurements with Azopolymer thin films. Opt. Lett. **38**(7), 1128–1130 (2013)
16. A. Consortini, Y.Y. Sun, G. Conforti, A mixed method for measuring the inner scale of atmospheric turbulence. J. Mod. Opt. **37**(10), 1555–1560 (1990)
17. R. Barille, R. Janik, S. Kucharski, J. Eyer, F. Letournel, Photo-responsive polymer with erasable and reconfigurable micro- and nano-patterns: An in vitro study for neuron guidance. Colloids Surf. B. **88**(1), 63–71 (2011)
18. R. Janik, S. Kucharski, A. Sobolewska, R. Barille, Chemical modification of glass surface with a monolayer of nonchromophoric and chromophoric methacrylate terpolyme*r*. Appl. Surf. Sci. **257**(3), 861–866 (2010)
19. D.T. Bong, T.D. Clark, J.R. Granja, M.R. Ghadiri, Self-assembling organic nanotubes. Angew. Chem. Int. Ed. **40**, 988 (2001)
20. J. Martín, J. Maiz, J. Sacristan, C. Mijangos, Tailored polymer-based nanorods and nanotubes by “template synthesis”: from preparation to applications. Polymer **53**, 1149–1166 (2012)
21. M. Steinhart, J.H. Wendorff, A. Greiner, R.B. Wehrspohn, K. Nielsch, J. Schilling, J. Choi, U. Gösele, Polymer nanotubes by wetting of ordered porous templates. Science **296**(5575), 1997 (2002)
22. Banu S, Birtwell S, Chen Y, Galitonov G, Morgan H, Zheludev N (2006) High capacity nano-optical diffraction barcode tagging for biological and chemical applications, NSTI-Nanotech, 1

23. R. Barillé, P. Tajalli, J.M. Nunzi, S. Zielińskaa, S. Kucharski, E. Ortyl, surface relief grating on azopolymer nanosurface. Appl. Phys. Lett. **95**, 053102 (2009)
24. I. Freund, M. Deutsch, A. Sprecher, Connective tissue polarity. Optical second-harmonic microscopy, crossed-beam summation, and small-angle scattering in rat-tail tendon. Biophys. J. **50**, 693–712 (1986)
25. H.M. Liem, P. Etchegoin, K.S. Whitehead, D.C. Bradley, Raman anisotropy measurements: An effective probe of molecular orientation in conjugated polymer thin films. Adv. Funct. Mater. **3**(1), 66–72 (2003)
26. M.I. Klima, A.V. Kotov, L.A. Gribov, Analysis of the vibrational spectrum of azobenzene. J. Struct. Chem. **13**(6), 987–990 (1973)
27. C.M. Stuart, R.R. Frontiera, R.A. Mathis, Excited-state structure and dynamics of cis- and trans-azobenzene from resonance Raman intensity analysis. J. Phys. Chem. A **111**, 12072–12080 (2007)
28. S. Frisk, R.M. Ikeda, D.B. Chase, J.F. Rabolt, Determination of the molecular orientation of Poly(propylene terephthalate) fibers using polarized Raman spectroscopy: a comparison of methods. Appl. Spect. **58**(3), 279–286 (2004)
29. M. Janko, P. Davydovskaya, M. Bauer, A. Zink, R.W. Stark, Anisotropic Raman scattering in collagen bundles. Opt. Lett. **35**(16), 2765–2767 (2010)
30. R.D. Schaller, R.J. Saykally, Y.R. Shen, F. Lagugné-Labarthet, Poled polymer thin-film gratings studied with far-field optical diffraction and second-harmonic near-field microscopy. Opt. Lett. **28**(15), 1296–1298 (2003)
31. F. Eisert, O. Dannenberger, M. Buck, Molecular orientation determined by second-harmonic generation: Self-assembled monolayers. Phys. Rev. B **58**(16), 10860–10870 (1998)
32. J. Prasad Raoa, K.E. Geckeler, 'Polymer nanoparticles preparation techniques and size-control parameters'. Prog. Polym. Sci. **36**, 887–913 (2011)
33. M. Alcoutlabi, G.B. McKenna, Effects of confinement on material behaviour at the nanometer size scale. J. Phys.: Condens. Matter **17**(15), R461 (2005)
34. C. Zhang, Y. Guo, R.D. Priestley, Glass transition temperature of polymer nanoparticles under soft and hard confinement. Macromolecules **44**(10), 4001–4006 (2011)
35. C. Zhang, Y. Guo, R.D. Priestley, Characteristic length of the glass transition in isochorically confined polymer glasses. ACS Macro Lett. **3**, 501–505 (2014)
36. L. Zhang, A. Eisenberg, Multiple morphologies of "crew-cut" aggregates of polystyrene-*b*-poly(acrylic acid) block copolymers. Science **268**, 1728 (1995)
37. V.V. Lulevich, I.L. Radtchenko, G.B. Sukhorukov, O.I. Vinogradova, Deformation properties of nonadhesive polyelectrolyte microcapsules studied with the atomic force microscope. J. Phys. Chem. B **107**, 2735 (2003)
38. A. Garreau, F. Massuyeau, S. Cordier, Y. Molard, E. Gautron, P. Bertoncini, E. Faulques, J. Wery, B. Humbert, A. Bulou, J.L. Duvail, Color control in coaxial two-luminophore nanowires. ACS Nano. **7**(4), 2977–2987 (2013)

Chapter 8
Design, Fabrication, and Optoelectronic Performance of Organic Building Blocks for Integrated Nanophotonic Devices

Yongli Yan and Yong Sheng Zhao

Abstract One-dimensional (1D) nanostructures have been used extensively to fabricate photonic elements for optical information processing due to the huge advantages over traditional silicon-based electronic ones in bandwidth, heat dissipation, and resistance to electromagnetic wave interference. Organic materials are a promising candidate to support these optical-related applications as they combine the properties of plastics with broad spectral tunability, high performance, easy fabrication, as well as low cost. Their outstanding compatibility allows for organic composite structures which consist of two or more kinds of materials, showing great superiorities to single-component materials due to the introduced interactions among multiple constituents. The easy processability of organic 1D crystalline heterostructures enables a fine topological control of both composition and morphology, which offsets the intrinsic deficiencies of individual material. In the mean time, the strong exciton–photon coupling and exciton–exciton interaction impart the excellent confinement of photons in organic microstructures; thus, light can be manipulated according to our intention to realize various functions. These collective properties indicate a potential utility of organic heterogeneous material for photonic integrated circuitry. Herein, we focus on the 1D organic crystalline composite structures, with special emphasis on the novel design, controllable construction, diverse properties, as well as wide applications as isolated photonic elements.

Y. Yan · Y.S. Zhao (✉)
Beijing National Laboratory for Molecular Science(BNLMS),
CAS Key Laboratory of Photochemistry, Institute of Chemistry,
Chinese Academy of Sciences, 100190 Beijing, China
e-mail: yszhao@iccas.ac.cn

Y.S. Zhao (ed.), *Organic Nanophotonics*, Nano-Optics and Nanophotonics,
DOI 10.1007/978-3-662-45082-6_8

8.1 Introduction

The development of information technology is a key issue in modern world. People are actively pursuing smaller and faster integrated chips because of their essential role in both the technical frontier and our daily life. The Moore's law, which has been a great success in the past years, points out that the number of transistors on an integrated circuit doubles approximately every eighteen months. According to this trend, there will be less than one electron on a single transistor by the year of 2020, which would be a fundamental limit to the rapid development of information technology. Therefore, scientists devote themselves to find out a new way to advanced computing systems beyond traditional electronics. There have been many attempts to achieve this goal, including using spin [1, 2], genes [3], or other quantum states [4]. Photonics that deals with optical signals has been recently considered to be a promising approach to completing the mission [5, 6]. Unlike Femi particles (electrons), photons can exist as highly coherent states due to the bosonic characteristics which do not need to obey Pauli exclusion principle. Thereby, light beams have superiorities on parallel transmission in transparent materials without the need of applying an external voltage and immunization to the cross talk effect from adjacent wires. In addition, the information capacity of photons is relatively high since the multiple properties, including intensity, wavelength, polarization, and phase, can all be modulated to load signals. Also, photonics may benefit from the ongoing trend of merging both photonics and electronics down to nanoscale in a single material system, as photons and electrons are destined to interact closely within the same material systems or devices [6].

To realize all-optical information processing, a simple yet efficient way is to construct photonic elements as corresponding analogies of current electronics and then integrate on a chip. For example, light sources could be compared to electric power supplies, while optical waveguides could be compared to conducting wires. Nevertheless, there are still many differences between photonic analogies and electronic devices, since the nature of photons implies that the light flow follows the time-reversal symmetry. Photons can rarely interact with each other or external field, bringing big challenges to the development of all-optical signal processing. Fortunately, photons can be indirectly manipulated via light–matter interactions in various photoresponsive materials. Thus, the exploration of high-performance optical materials, including both inorganic and organic systems, becomes the key issue in fabricating photonic integrated circuits.

Owing to the rapid development of nanoscience and nanotechnology, various kinds of solid-state optical materials have been designed and synthesized at an ever diminishing size in the past decades. Low-dimensional structures, especially nanowires, have been proved to be efficient optical waveguides [7]. In these structures, photons are confined and transported, with tunable parameters of intensity, polarization, phase, etc. Therefore, such tiny structures could be regarded as optical resonators, which enable photon absorption, light amplification, exciton–photon coupling [8–10], and many other optical properties. Although modern state-of-the-art lithography techniques are capable of fabricating nanostructured features, nanowires grown chemically still possess some unique advantages of being single-crystalline, relative defect-free, atomic-level smooth surfaces and ability of accommodating large lattice mismatches. Self-assembled crystalline micro-/nanostructures from organic dyes are highly expected to play an important role in the next generation of miniaturized optoelectronics due to the excellent performance in both photonics and electronics [11]. Moreover, organic molecules, as a kind of active optical materials, show great potentials for manipulating light signals because they can benefit from chemical versatility, structural processability, and excellent tunability in their optical properties. More importantly, the strong coupling between Frenkel-type excitons and photons would form a new kind of quasiparticle, named exciton polaritons (EPs), which may bring surprising opportunities to the improvement of the optical performances.

Among the organic crystals with various morphologies, 1D nanostructures have been highly valued as building blocks for miniaturized optoelectronic devices [7, 12]. Several kinds of functional optoelectronic devices, such as lasers [13], waveguides [14], field-effect transistors [15], and solar cells [16], have been successfully fabricated with organic 1D crystalline materials. These single-component systems provide ideal theoretical models to investigate the light–matter interactions and cavity effect, while the construction of organic structures with more than one component is essential to achieve practical functions in photonic nanodevices. Such complex systems could not only maintain the advantages of each constituent, but also exhibit novel performance from physical and chemical processes, including energy/charge transfers, photon–plasmon coupling, and exciton conversion. Utilizing these, we can realize the overall control of multiple photon parameters, such as intensity, wavelength, polarization, and phase, in optical systems toward the processing of light signals.

In this chapter, we would like to introduce recent advances focused on the ingenious design, contrivable fabrication as well as optoelectronic property optimization of organic composite material as distinct photonic devices. The 1D feature of these functional elements would greatly facilitate the integration in the practical application. Here, special emphasis is laid on the function-oriented material design, including the structural control of composition and morphology, the interactions among each component, and the relationships between material property and the device performance.

8.2 Functional Photonic Elements Based on 1D Heterostructures

Various photonic devices have to be assembled together to fulfill a practical function. Optical fibers are essential for the integration process due to the ability of transferring signals within the whole optical network. Benefit from the huge capacitance as well as low loss, optical fibers have been widely used in modern fiber optics communication. A typical optical fiber used commercially contains two distinct layers: The inter core is commonly made up of SiO_2 or other transparent media, while the outside cladding layer is usually made up of glasses with a higher refractive index than that of the core. This core/sheath structure allows the signal transmission over tens of kilometers away because of the total internal reflection at the interface between the core and cladding. Today, fabricating optical waveguides at an ever diminishing size is growing vigorously since signal transmission is indispensable in constructing a photonic integrated circuit. In the past years, various solid-state materials, including inorganic semiconductors [5], polymers [17], organic aggregates [18, 19], and metals [20], have been used as tiny optical waveguides. Unlike traditional optical fibers, most of these nanowaveguides are serving as "active optical waveguides," which show corresponding response to external excitation. Thus, one could manipulate light signals at the same time of transmission in an active optical waveguides, because the light guided in these active waveguides is not the original incident beam, but the emissions from the active media under the excitation.

Almost all photonic functionalities, including light generation, signal split, modulation, processing, combination, and detection, could be achieved in such active optical systems by utilizing appropriate photochemical or photophysical processes. The optically active organic molecular micro-/nano-aggregates are reasonably expected to play a significant role in the construction of functional optoelectronic devices, along with their inorganic and polymer counterparts. Till now, the preparation methods and optical performances in organic nanocomposites are still less developed in comparison with those in inorganic semiconductors and conjugated polymers. Benefit from the vast number of small organic molecules and tunable optical properties from the proper doping, the chemically synthesized organic 1D hybrid nanostructures show several unique features that make them good candidates for functional devices, such as easy and facile size control, great surface quality, as well as a variety of optical properties arose from hybridization. In addition, the excellent optical confinement of 1D nanostructures via light–material interaction facilitates the assembling of different elements, which is vital for the realization of highly integrated photonic circuitry, as shown in Fig. 8.1. A fully functional photonic circuit may contain several types of on-chip components over light sources, optical routers, modulators, multiplexers, photonic diodes/transistors, logical gates, directional couplers, and signal transducers [21], which are interconnected with optical waveguides. Most of these elements are optical analogies of corresponding electronic devices, but also exhibit important photonic advantages such as ultrafast response, high-speed transmission, and parallel processing. The organic hybrid systems provide the strong light–matter interactions among different constituents, which are useful to access simultaneous manipulation of optical signals during the propagation.

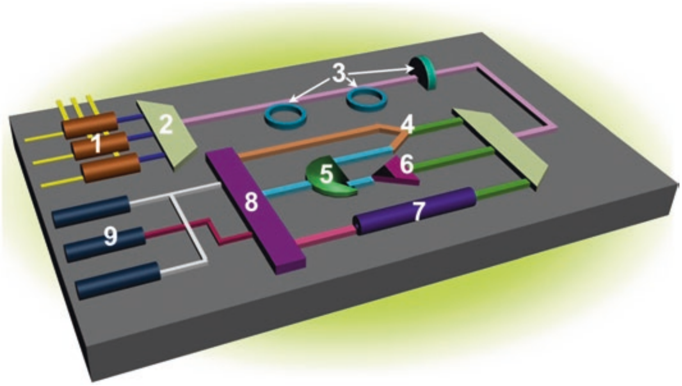

Fig. 8.1 Schematics of future nanophotonic circuit for information processing. The required primary elements include laser diodes/LEDs as light source (*1*), wavelength division multiplexer (WDM, *2*), modulator (*3*), routers (*4*), logic operator (*5*), transistor (*6*), chemical transducer (*7*), directional coupler (*8*), photoelectric converter (*9*), and so on. Reproduced with permission from [21]. Copyright 2013 Wiley

8.2.1 Uniformly Doped Organic Hybrid Nanowire as White Light Source

Organic nanoscale light sources that generate tiny light spots down to the diffraction limit are supposed to drive integrated photonic chips with ultralow power consumption [22–25]. One-dimensional structures synthesized through liquid-phase assembly or vapor-phase epitaxial growth have been a research hot spot in recent years. One of their most attractive applications is the realization of nanolasers, because the smooth end facets of nanowires can reflect guided light forth and back to form an optical resonator [13]. Once the amplification exceeds the loss in a single cycle, lasing begins in such a miniature optical resonator. These nanolasers offer an efficient way to microscopic emitters of single color [23, 24, 26] or bicolor [27, 28] with highly localized spot sizes and low pump thresholds. However, for some complicated circumstance, light sources with color-tunable outputs, and stable white light emission, are widely needed since it provides more possibilities in novel optical control of multi-level computing.

Doping technique has been widely used to tune the emission color of composite materials, especially in organic light-emitting diodes (OLEDs) [29]. A traditional way to acquire white light is the color mixing of two or more components at a given doping ratio. Utilizing energy transfer from one component (donor) to another (acceptor) has been demonstrated to be an effective alternative to multicolor emission in composite systems [27], which is supersensitive to slight changes in the donor/acceptor ratio. The simplest energy transfer process is often referred as radiative energy transfer, involving emission from the donor and subsequent re-absorption of the emitted light by the acceptor. The re-absorption process is of low efficiency due to the limitations of distance and chromophore density in organic materials. Instead, two non-radiative mechanisms may be more predominant for the energy transfer between donor and acceptor in organic nanocomposites. One is facilitated by a dipole–dipole interaction between the excited donor and the adjacent ground-state acceptor, which is known as Förster resonant energy transfer (FRET) [30]. The other involves an electron-exchange mechanism between the donor and the acceptor, which is often referred to Dexter-type energy transfer [31].

In solid-state organic materials, non-radiative energy transfers are quite efficient [32], but very sensitive to environmental changes, including heating, oxidation, or light irradiation [33, 34]. Yao group reported that white light emission could be realized in organic donor–acceptor pairs via Förster energy transfer through finely controlling the doping ratio in binary nanowires [34, 35]. However, it is not a constructive solution to white light emission from such organic waveguides since a slight variation of acceptor content caused by external stimuli may influence the output significantly [35]. Therefore, developing an intelligent mechanism that can adjust the output automatically, regardless of doping ratio and environmental conditions, is necessary. Previously, organic nanostructures involving triplet–triplet energy transfer (TTET) [31] and triplet–triplet annihilation (TTA) [36] have been demonstrated to achieve optical up-conversion with a high quantum yield [37]. The stable up-converted emission has been reported in organic core–shell nanospheres, where a metal-to-ligand charge transfer (MLCT) sensitizer was selected as the triplet energy donor. These photonic up-conversion systems are capable of converting long-wavelength excitation to short-wavelength radiation, which have wide applications in fluorescence imaging.

The combination of FRET down-conversion and TTET up-conversion in a single system is then supposed to be a novel strategy to achieve intelligent white light generation at nanoscale. The small amount of acceptor molecules can be uniformly doped into the matrix of energy donor material [38], and the research on composite waveguide materials involving bidirectional energy transfer between singlet and triplet excitons has been performed recently [39]. Such a kind of optical devices has been realized with organic nanowire waveguides of 9,10-diphenylanthracene (DPA) and iridium$_{(\mathrm{III})}$ bis(2-phenylbenzothiozolato-N,C$^{2'}$) acetylacetonate ($(BT)_2Ir(acac)$) pair, which can convert different input colors into the identical white light output, as displayed in Fig. 8.2a–b. The DPA molecule was selected as host material to fabricate nanowires because of the planar molecular structure, which endows the excellent assembly performance due to the strong intermolecular π interaction. It plays a dual role in modulating the output of nanowires: energy donor in FRET with a high S1 energy state, and annihilator in TTET with a lower T1 energy state. To ensure the simultaneous occurrence of FRET and TTET processes in the nanowire waveguide, the guest compound should be a phosphorescent triplet sensitizer, whose S1 energy level is lower and T1 energy level is higher than those of DPA. Here, $(BT)_2Ir(acac)$ molecule with proper energy structures was chosen as guest material.

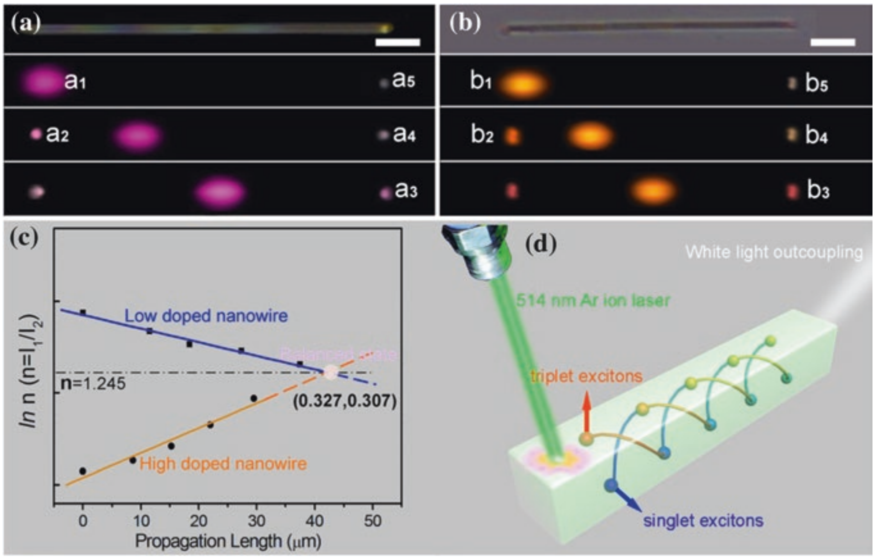

Fig. 8.2 Stable white light output from bidirectional energy transfer in a single nanowire. **a**, **b** Bright field and PL microscopy images of two identical nanowires with low and high doping ratio, respectively. Scale bars are 5 μm. **c** The exponential relationship between the contribution ratio of blue to orange emission and the propagation length in the nanowires with low and high doping ratios. It reaches an identical point after a certain distance transmission. **d** Schematic illustration of the EP propagation and energy transfers in the nanowire waveguides. The DPA and $(BT)_2Ir(acac)$ excitons can adjust their ratios intelligently through bidirectional energy transfers and self-modulated white light outcoupling can be achieved. Reproduced with permission from[39]. Copyright 2011 Wiley

The well-defined composite nanowires were fabricated in a surfactant-assisted assembly method, and the doping content was finely tuned with the relative host/guest ratio of injected mixed solution. In this binary system, singlet energy transfer from DPA to $(BT)_2Ir(acac)$ and reverse triplet energy transfer from $(BT)_2Ir(acac)$ to DPA coexist, resulting in the fluctuations of the singlet and triplet excitons during the light propagation. The excitons can fluctuate between the blue emission of DPA and the orange emission of $(BT)_2Ir(acac)$ and form the final color-tunable output. The color ratios of two outcoupling colors from either low- or high-doped nanowires can reach the same value after the light transmission over a certain distance (Fig. 8.2c), demonstrating a self-modulated white light outcoupling at wire ends. The mechanism of white light generation is the equilibrium between two kinds of excitons via commutative energy transfer during the light guiding process; thus, the morphology effect is ignorable as long as these 1D structures are uniformly doped. Such an optical waveguide behaves like a regulator which can convert different input colors into an identical white light output, regardless of the doping ratio, as displayed in Fig. 8.2d. These results offer a comprehensive understanding of exciton conversion in active materials and effective strategies for developing novel multi-component waveguide building blocks.

8.2.2 Organic Multi-segmented Nanowire as Optical Wavelength Converter

In an integrated photonic circuit, a wavelength converter is necessary since the working wavelength may need changes occasionally as required. However, it is not easy to alter the wavelength in a single-component material. The energy transfer processes provide a powerful tool for wavelength converting in organic composite systems. In comparison with uniformly doped 1D structures, the selectively doped heterogeneous structures may offer more freedom for multiple photonic applications [33]. Thus, the programmable design and fabrication of heterostructures along the longitude direction are essential for optical signal processing in organic optical waveguides via the spatial control of energy transfer. Hard template method [40] and reactive ion etching technique [41, 42] have been used to obtain 1D axial heterostructure of metals, semiconductors, and polymers. As mentioned above, organic crystalline nanomaterials assembled from various molecules present a novel, cheap, and flexible way to multi-segmented structures employable in integrated photonic circuit at nanoscale.

Recently, Zhao et al. found that axial segments may appear in 1D host/guest systems if the intermolecular interactions of host and guest are rationally controlled along the growth direction [38, 43]. Figure 8.3a illustrates the assembly process of 2,4,5-triphenylimidazole (TPI) microtubes, which can be divided into nucleation, 1D growth, and termination stages [43]. A sphere-like organometallic complex $(BT)_2Ir(acac)$ and a planar π-conjugated compound 9,10-bis(phenylethynyl) anthracene (BPEA) were selected as guest molecules to modulate the axial composition via different intermolecular interactions. At beginning, TPI molecules quickly nucleate into short rod-like hollow structures. With the evaporation of the good solvent, these nucleus grows gradually in two directions, and the guest components start to aggregate into the TPI host matrix. Finally, barcode-like microtubes are obtained. The PL images in Fig. 8.3b and c indicate that the spatially banded colors are emitted along these as-prepared two kinds of microstructures under UV radiation, with the features of triblock and multi-block, respectively. It is the difference in the intermolecular interaction strengths (van der Waals force and π-stacking interaction) that led to the uneven doping of guest molecules in the TPI host. Therefore, more segments with various colors in a single wire should be expectable reasonably if there are more than one guest molecules with appropriate design of intermolecular interaction strength. The energy transfer process can only occur efficiently in the doped areas, so these photonic heterostructures exhibited spatially dependent multi-color emission of donors and acceptors.

These multi-segmented 1D microstructures could be used as wavelength converters that output multi-color signals for information processing in the nanophotonic circuit. As shown in Fig. 8.3d, the orange–blue–orange triblocks presented

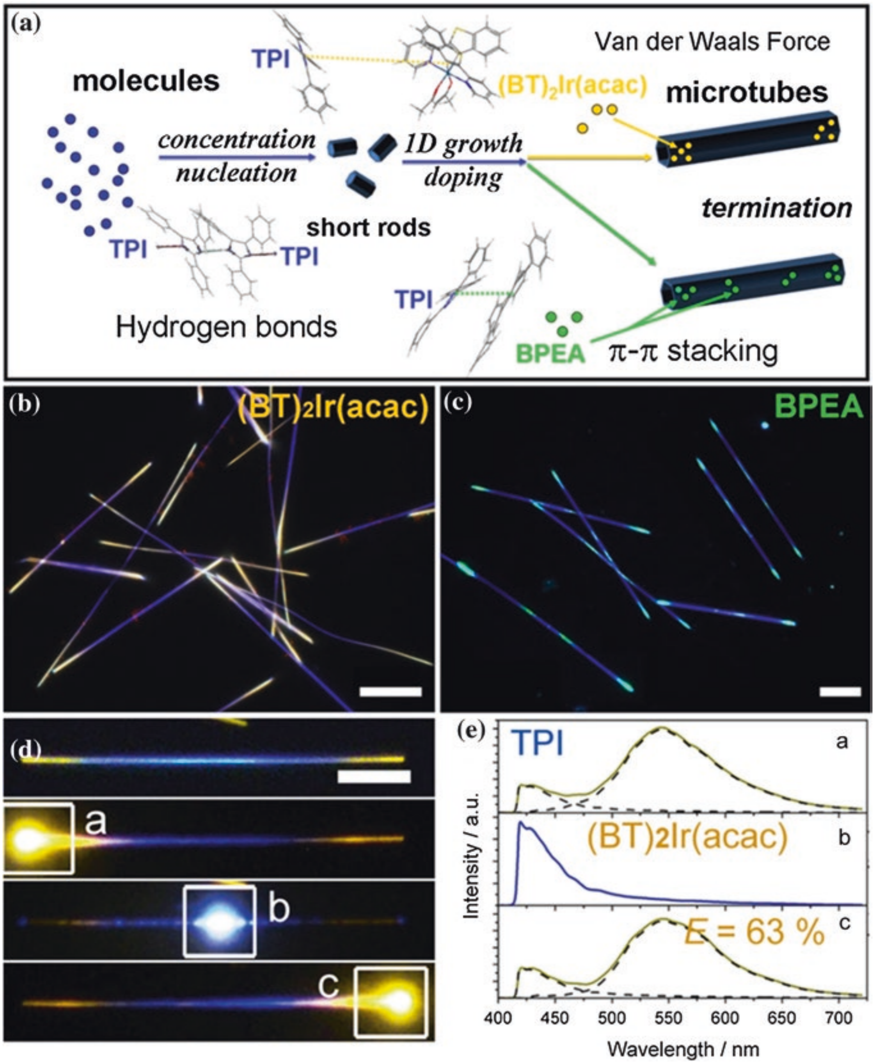

Fig. 8.3 Multi-color light source via axial componential modulation. **a** Schematic illustration of the typical formation of heterogeneous TPI microstructure. PL images of **b** triblock (BT)$_2$Ir(acac) and **c** multi-block BPEA doped TPI tubes under the illumination of UV band of a mercury lamp. Scale bars are 20 μm. **d** PL images of a single triblock microtube excited with unfocused UV light and a focused UV laser, respectively. The *white squares* (*a*–*c*) indicate the laser excited spots. Scale bar is 20 μm. **d** Corresponding PL spectra of the excited areas (*a*–*c*) at tube tips and body. A FRET efficiencies as high as 63 % is obtained through the fitting of local spectra in doped areas. Reproduced with permission from [43]. Copyright 2012 Wiley

continuously multi-color emissions during light propagation. The locally emitted PL and the propagation behavior could be modulated well within a large range by varying the irradiation position. As shown in Fig. 8.3e, the PL of both TPI and the guest molecules are generated at doped tips via FRET process, while only pure TPI PL were observed when locally excited at middle tube bodies. It indicates that TPI excitons could generate along the entire tubes and transfer energy to the dopants during light propagation. This is induced by the unidirectional FRET process that energy can only flow out of the donors with high energy and infuse into acceptors with low energy. The irreversible energy flow, which is similar to the behavior of electrons in a rectifier diode, provides key clues for the directional manipulation of photons for future photonic diodes and transistors.

8.2.3 Organic Dendritic Structure as Multiple Optical Channels

Tightly linked to optical signal sources, the multi-channel waveguides (i.e., optical splitters, routers, and multiplexers) are supposed to deliver the incident signals to individual functional elements in integrated nanophotonic networks [44]. One kind of structures that can simultaneously transfer multiple light signals to different destinations is a complex waveguide with some parallel branches. Thereby, each end of the multi-channel waveguide system can serve as a new nanoemitter for the further cascade of more units. An ingenious way to fabricate such branchy heterostructures is utilizing nanocrystals of one component to template the crystallization of the other, either by epitaxial growth or by heterogeneous nucleation [45]. Recently, a novel “shish-kebabs” nanostructure has been synthesized during solvent casting of blend solutions of Poly(3-hexylthiophene-2,5-diyl (P3HT) with perylene tetracarboxy diimide (PDI) species [45]. P3HT kinetically stabilizes the supersaturated solutions of PDI and modifies the growth of PDI crystals, leading to the formation of extended PDI shish nanowires that in turn serve as heterogeneous nucleation sites for P3HT kebabs, providing a simple route to acquire phase-separated donor/acceptor assemblies. However, these as-prepared structures can hardly be used for signal processing because of the poor flatness of surfaces and the loose connections between main waveguide and branches.

Previously, Huang and co-workers reported that the vaporized organic molecules tend to nucleate preferentially and grow more rapidly on sites with smaller curvature radii or higher surface energies, such as dusts, particles, and sharp tips [46, 47]. This facile method is very powerful in acquiring organic nanowire arrays, which may play an important role in future high-density integration. Inspired by this result, Zhao et al. obtained dendritic heterojunctions of donor/acceptor pair (aluminum tris(8-hydroxyquinoline, Alq_3 and 1,5-diaminoanthraquinone, DAAQ), which function as multi-channel waveguides [48]. Ultralong crystalline donor microwires were prepared using an antisolvent diffusion method combined with solvent evaporation-induced assembly. The donor microwires, with tunable morphologies through the growth time and evaporation rate of the antisolvent, serve as the site-selective nucleation centers for the epitaxial growth of branches. Also, the length and positioning density of acceptor branches could be modulated by varying the growth time as well as growth temperature. The good spectral overlapping

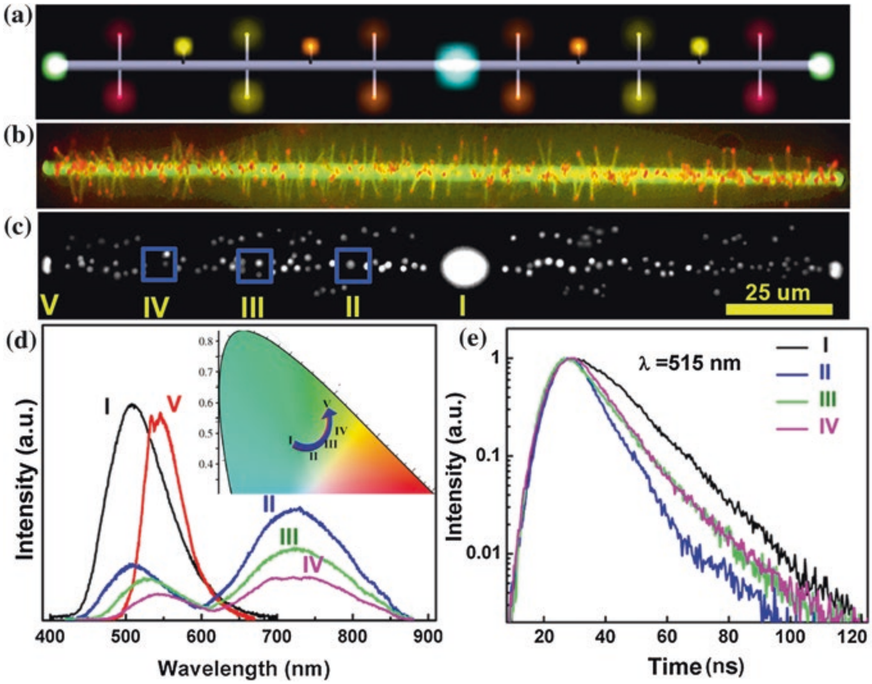

Fig. 8.4 Optical routing via organic dendritic nanostructure. **a** Schematic illustration of the Alq3-DAAQ nanowire heterojunction-based optical routers. **b** PL microscopy image of a single dendritic heterojunction under UV band excitation. **c** PL microscopy image of the nanowire heterojunction in B excited with a focused UV laser beam, which demonstrates the multiple optical channeling illustrated in **a**. Scale bar is 25 µm. **d** PL spectra of the excited spot (*I*) and the output signals from the DAAQ branches (*II–IV*) and the Alq3 tip (*V*) taken from the regions marked in C. The *inset* shows the variation of the CIE coordinates with propagation length. The gradual red shift is ascribed to the combination of energy transfer and re-absorption effects. **e** PL decay profiles of Alq3 emissions indicating the variation of the energy transfer efficiencies from Alq3 to DAAQ at different propagation lengths. Reprinted with permission from [48]. Copyright 2012 American Chemical Society

between the PL of Alq3 and the absorption of DAAQ ensures an efficient FRET process. Figure 8.4a illustrates the working mechanism of multiple optical channels from the unique dendritic heterostructures. There are two processes occurring when the green light emitted by the Alq3 trunk is coupled to the branches, the FRET process whereby the red PL of DAAQ generates at the interface of the junctions and the photon reabsorption process of the directly coupled Alq3 emission in the DAAQ nanowires. The combination of the two processes results in a gradual change in color.

As displayed in Fig. 8.4b, more than 100 DAAQ branches are supported by a single Alq3 wire, manifesting great potentials in loading capacity for parallel processing. Under the excitation of a focused laser beam (Fig. 8.4c), the guided light could be outputted simultaneously from both the tips of the trunk and each branch.

The outcoupled light from each branch end is a superposition of the green and red emissions from the two compositions (see Fig. 8.4d), and the ratio of green to red lights decreases with the increase of the light propagation length. This also induces the variation of energy transfer efficiency at the interfaces, as proved by the obvious decreases in fluorescence lifetimes with the increase of propagation length (Fig. 8.4e). Such a controllable multiple-channel optical nanostructure may hold a primary position of efficient splitter/router/multiplex to generate modulated signals as inputs for cascaded devices in future information technology.

8.2.4 Organic/Metal Heterojunction as Nanoscale Logic Gate

In a typical photonic integrated circuit, the light beam from a single source can be divided into hundreds of portions and delivered to parallel computing units through micro-sized multiple-channel devices. One of the most important steps before information processing is the signal loading through a modulator. Only in this way can the light transferred in the nanophotonic network be called optical signals. Thus, developing nanoscale optical modulators with high speed and low driving power are imperative for future miniaturized information technology [49]. Most of the present optical modulators are designed on the basis of linear or nonlinear optical effects, such as interference [50], refractive indices variation [51], and frequency mixing [52]. Therefore, the lateral dimensions of these devices are on the order of the working wavelength, restricting the implementation of photonic modules into nanoscale electronic chips. Surface plasmon-based photonics provides an effective solution to this size-compatibility problem, since surface plasmons could spatially confine light well below diffraction limit in metallic nanostructures [53]. Unfortunately, the large inherent metal loss makes it impractical to transfer optical signals across an entire chip solely with plasmonic waveguides [54]. Thus, it is increasingly important to be able to integrate plasmonic waveguides with dielectric interconnections which can launch SPPs efficiently and conveniently.

It was reported that SPPs can be launched with dielectric waveguides through direct photon–plasmon coupling, presenting a solution to this difficulty [54–56]. Most hybrid metallic structures constructed with micromanipulators suffers from the low SPP launching efficiency since the point contact is unfavorable to photon–plasmon coupling. In organic/metal composites, the strong coupling between Frenkel-type excitons and SPPs interacts at the interface, yielding new optical behavior associated with energy transfer and other physicochemical processes [57]. Zhao group synthesized a novel organic-silver nanowire heterojunctions via site-specific epitaxial growth method [58]. BPEA was chosen as the model compound because of its versatile properties of good stability, planar molecular structure for assembly, high emission efficiency, and, especially, the proper PL range.

The broad emission range of BPEA aggregates makes it easy to launch SPPs of silver nanowires due to the small momentum increment needed in the red region. In a typical synthesis, chemically synthesized silver nanowires were deposited on a coverslip, which serves as the substrate in subsequent epitaxial growth process of BPEA molecules. Since organic molecules tend to first nucleate on sites with large surface energy, the convex vertices of silver nanowires synthesized chemically give the silver wires an overwhelming superiority in attracting the BPEA vapor. Such a growth mechanism ensures a good reproducibility of heterogeneous structures. The enlarged adherent area in as-prepared hybrid junctions could substantially improve the coupling efficiency, and a SPP launching efficiency of as high as 20.5 % was confirmed.

This kind of heterojunction functions as an optical modulator due to the polarization-dependent absorption of closely packed molecules in organic crystal [59, 60]. The great contrast of the two wires in Fig. 8.5a, b indicates that the heterostructures are made of different materials. Figure 8.5c–f present the PL microscopy images of the exact heterojunction under the four different combinations of two simultaneous polarized excitations. According to the relationship between SPP launching efficiency and incident polarization, these four images can be regarded as different groups of input values: (1, 1), (1, 0), (0, 1), and (0, 0), respectively, which is in accordance with the standard Boolean logic inputs. Such a heterostructure acts as a nanoscale logic gate with two input ports (I1 and I2) and one output port (O), as shown in Fig. 8.5g. By setting an intensity threshold to separate ON and OFF states (T1 and T2 in Fig. 8.5h), we can realize either OR or AND logic operation, which was demonstrated by the total outputs with different thresholds summarized in Fig. 8.5i. These hybrid structures constituted with both plasmonic and dielectric nanowires could reduce the whole losses of the entire photonic circuit at micro-/nanoscale, indicating a way to the realization of dielectric/metal hybrid integration. This concept can be further generalized and expanded to more complex systems to play a key part in nanoscale devices well below diffraction limit, such as splitters, routers, and so on.

8.2.5 *Organic/Metal Heterostructure as Nanoscale Directional Coupler*

Logic operation is one of the most central sections in integrated photonic circuits. After that, the calculated results need to be transferred to the right terminals via a directional coupler, which separates signals based on the direction of signal propagation. Such devices are often used to split the signal flowing in the mainline and to fully pass the signal flowing in the opposite direction. As stated previously, implantation of plasmonic units into organic photonic systems is a way of tightly confining optical signals well below diffraction limit. The strong interactions between EPs and SPPs at the organic/metal junctions could bring novel

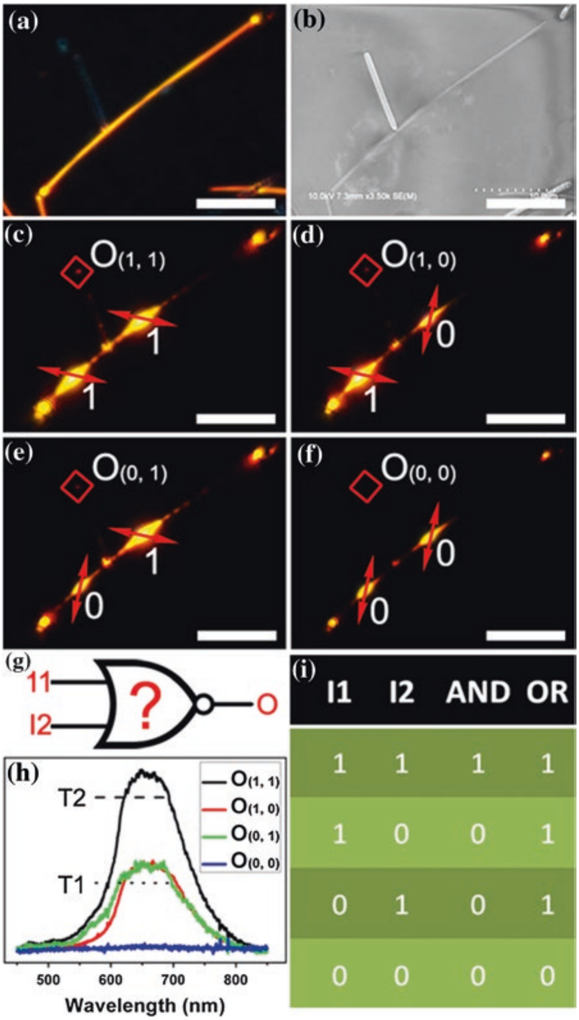

I1	I2	AND	OR
1	1	1	1
1	0	0	1
0	1	0	1
0	0	0	0

Fig. 8.5 Realization of basic Boolean operations in an organic/metal nanowire heterojunction. **a**, **b** SEM and PL microscopy images of a typical BPEA-silver nanowire heterojunction. **c**–**f** PL microscopy images of the heterojunction under the excitations of four different combinations of the two polarized inputs. Red arrows indicate the polarization directions of the two laser beams. Here, 1 and 0 were defined, respectively, according to the intensities of the launched SPPs. **g** The formed basic logic gate with two simultaneous inputs and one output signal. **h** The scattering spectra of SPPs ant the O terminal under the excitations shown in **c**–**f**. T1 and T2 represent the thresholds for OR and AND gates, respectively. **i** Summary of optical logic operations for OR and AND gates. Reproduced with permission from [58]. Copyright 2012 Wiley

optical properties for the actualization of nanophotonic devices [58]. Organic molecules, especially the aromatic ones, can aggregate into tiny crystals molecule by molecule in liquid phase [61], which makes it possible to embed several metal nanostructures in one organic waveguide to compose devices with multiple ports.

By adding prefabricated silver nanowires during the reprecipitation process, Zhao et al. obtained amount of dendritic organic/metal nanowire heterostructures successfully, demonstrating a facile but mass fabrication method of hybrid nanostructure [62]. Here, fac-tris(2-phenylpyridine) iridium ($Ir(ppy)_3$) was chosen as the host material for three major reasons. One is the phosphorescence range of $Ir(ppy)_3$ (500–600 nm), making it easy to launch the SPPs of Ag nanowires. Another is the emergence of irregular distal ends during assembling process, which can capture and stick multiple Ag nanowires suspended in solution. Last but not least, the aromatic ligands in this molecule could distort and reorient at the organic/metal interfaces to minimize defects along the interfaces. In addition, the organic molecules adsorbed on the Ag nanowires could also reduce the interfacial energy and stabilize the heterostructures. As shown in Fig. 8.6a, these structures consist of several Ag branches on each trunk, in which it is clearly seen in both the bright field and PL microscopy images taken under UV excitation. The bright PL points at the corresponding intersections, mainly originated from the scattering, reveal the possibility of interaction between EPs and SPPs. The TEM image and SAED patterns in Fig. 8.6b indicate that both the $Ir(ppy)_3$ trunk and Ag branches are crystalline with smooth surfaces and thus good waveguiding behaviors. The distribution of electric field intensity in Fig. 8.6c suggests that SPP modes can be launched through the light scattering at the junction area and transfer to wire tips. At the end of the silver nanowire, the intensity of the electric field $|E|$ with $\theta = 45°$ is much larger than that with $\theta = 135°$. Such a strongly angle-dependent SPP launch efficiency provides new ideas to construct directional couples in photonic integrated circuit.

The nanostructure consisting of one organic trunk and two branches was chosen to realize the concept of directional coupler, as illustrated in Fig. 8.6d. Three input regions (labeled as I1, I2, and I3) locate on the organic waveguide and the two distal ends of Ag branches act as output terminals (O1 and O2). In this structure, the signals inputted from different positions can be selectively delivered to the predetermined subwavelength output terminals. If the left silver nanowire leans toward right with an angle of 45° to the trunk, while the right one leans toward left with an angle of 135°, then the optical signals inputted from the left and right ends can only be transferred to the neighboring branches, respectively, whereas the signals inputted from the middle section can hardly be transferred to any Ag branch channels (see Fig. 8.6e bottom). If the relative positions of the two Ag branches were exchanged, as shown in Fig. 8.6f, the designed structure would offer a complementary function in comparison with the previous one. The functions can be further expanded by altering the cross angle of the branches in a similar way (Fig. 8.6g). By modifying the inserting angle of the two Ag wires, we can get directional couplers with different applications based on the angular dependence of photon–plasmon coupling. Though it is still challenging to control the inserting angles of Ag nanowires at present, it might be achieved by an external electric field [63], by a fluidic arrangement, or with a surfacing patterning during assembly process [64]. This concept suggests a novel strategy to fabricate complex nanostructures for manipulation of photons and can be generalized to construct other photonic components, such as multiplexer, WDM, and so on.

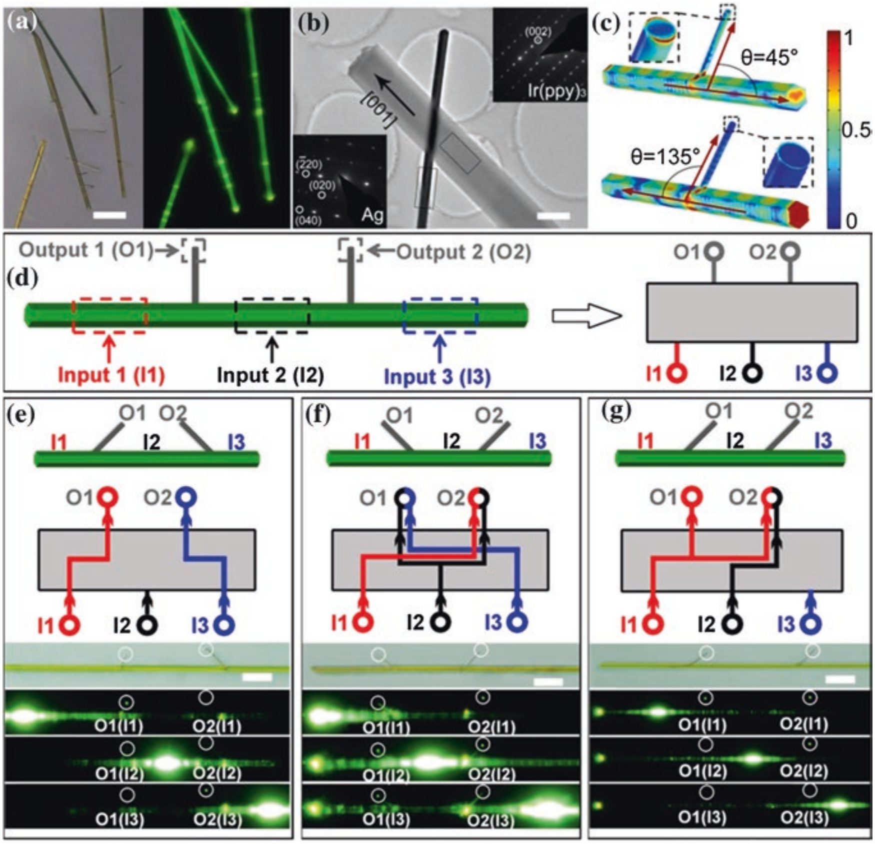

Fig. 8.6 Controllable light flows in organic/metal nanowire heterojunctions as directional couplers. **a** Bright field and PL microscopy images of the Ir(ppy)$_3$-silver nanowire heterostructures. Scale bar is 20 μm. **b** TEM image of the nanowire heterojunction. Scale bar is 1 μm. *Insets* SAED patterns of the Ir(ppy)$_3$ and Ag wires. **c** Local electric field $|E|$ distributions in a typical heterostructure with a insert angle of 45°. **d** Schematic illustration for the design of the photonic device, which has three input positions (*I1*, *I2,* and *I3*) located on the organic waveguide (marked with the red, black, and blue dotted line box, respectively) and two output terminals (*O1* and *O2*). **e**–**g** The structure and schematic sketch of the directional couplers with different relative angles of two Ag wires, where the optical signals inputted from *I1*, *I2,* and *I3* can be selectively transferred to *O1* and *O2*. The bottoms are demonstrations of each configuration, respectively. Reproduced with permission from [62]. Copyright 2013 Wiley

8.2.6 Organic Coaxial Heterojunction as Nanoscale Photoelectrical Transducer

Hybrid integration, where interactive communications among photonic chips are fulfilled via electronic signal, would be a notable landmark in the progress of information technology before the full implementation of all-optical computer.

In this sense, nanostructures with the ability to convert optical inputs into electronic signals efficiently are of great importance to the fabrication of a single chip. One-dimensional p–n junctions are the most attractive elements in modern electronics due to the unique optoelectronic properties toward diodes and transistors. During the past years, inorganic p–n nanostructures have been successfully employed in photonic devices, including light-emitting devices [65], light-controlled diodes [66], solar cells [16, 67], and detectors [68]. Since organic semiconductors exhibit advantages in the ease of molecular design [69] and chemical compositing [70] for property optimization, organic p–n junctions may provide a better choice toward future hybrid integration. Nevertheless, it remains a hard task to keep good connection between different compounds in each single junction, which is vital to thermal stability and charge carrier mobility. Thus, fabricating 1D partially core–shell coaxial heterostructures with proper complementary p- and n-type organic semiconductors may solve the problem, which is of great importance to the exploration of practical optoelectronic devices.

By using one-step vapor-phase epitaxial growth, Zhao et al. synthesized single-crystalline coaxial p–n junction nanowire arrays with two organic semiconductors, as shown in Fig. 8.7b [71]. The p-type material (copper phthalocyanine, CuPc) and n-type material (5,10,15,20-tetra(4-pyridyl)-porphyrin, H_2TPyP) were selected for synthesizing the p–n junctions due to their distinct photoelectric properties as well as high thermal stabilities. Both the two π-conjugated molecules were put into a tube furnace with two different quartz boats, so that the two compounds could be co-evaporated. The boat with H_2TPyP was placed at the center of the tube to ensure a high evaporation rate. During the heating process, vertically aligned H_2TPyP hollow structures formed in the first place, providing nucleation centers for the vaporized CuPc compound which was laid on the upstream. Finally, the two molecules were physically deposited onto the substrates to form the 1D p–n junction arrays. The relative distances of two boats, furnace temperature, and growth time are all key factors to the success in large-scale production of such p–n heterostructures.

Both H_2TPyP and CuPc are planar molecules; thus, the strong π–π interactions between the two compounds assure good connections at the junction area, which endow each coaxial nanowire heterojunction with great potentials in high-quality optoelectronic device. The asymmetrical (Au/Al) electrodes (Fig. 8.7b) were adopted to reduce the energy barrier between the electrodes and semiconductors and facilitate the charge collection. Such a device behaves as a good photoelectronic transducer, as depicted in Fig. 8.7c and d. A repeatable photocurrent is observed under the light illumination and remains almost unchanged within five cycles, indicating a reversible and stable response to external radiations. The large energy difference between the lowest unoccupied molecular orbital (LUMO) of H_2TPyP and the highest occupied molecular orbital (HOMO) of CuPc at the heterointerface offers a considerable room for the further improvement of device efficiency. The performance of these junction devices is positively related to the contact area. Commonly speaking, the larger the wire diameters are, the higher the device efficiency is. Owing to the special cable-type structure and the large

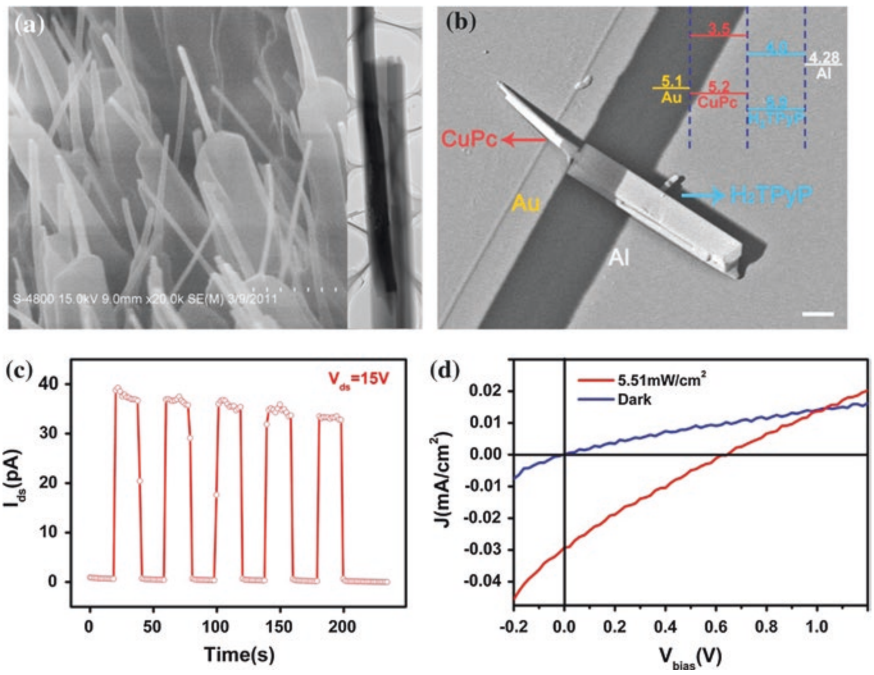

Fig. 8.7 An individual organic p–n junction as photoelectrical converter. **a** Tilted view SEM image of the CuPc-H_2TPyP heterojunction nanowire arrays. *Inset* TEM image of a single wire for the interface. **b** SEM image of a single heterojunction nanowire device as photoelectric converter. *Inset* the energy level diagram of a CuPc-H_2TPyP nanowire device. Scale bar is 1 μm. **c**, **d** Sensitive and stable response of the distinct CuPc-H_2TPyP nanowire heterojunction junction to optical radiation. Reproduced with permission from [71]. Copyright 2012 Wiley

interfacial gap, the single junction device exhibits better optoelectronic conversion performance than those of single-component nanowires as well as sandwiched film devices, showing great possibility to be applied as highly sensitive photoelectrical transducers toward photonic integration.

8.2.7 Organic Core/Sheath Heterostructure as Nanoscale Chemical Transducer

Besides dealing with optical signals, future photonic integrated circuits are supposed to be able to convert signals of different types into optics through various transducers. A transducer is a photonic device which has response to external stimuli, including humidity [72], chemical gas [73], and so on. As described above, organic axial p–n junctions can be regarded as nanoscale photoelectric transducers because of the good capacity of converting light irradiation to electric signals [71]. However, the acquirement of chemical gas responsive systems at micro-/nanoscale remains a major obstacle in the field of photonics. Previous methods either require bulky testing equipment and tedious sample preparation, or have poor selectivity and limits of detection. The 1D optical waveguide emerges as a promising strategy for the convenient and sensitive detection of environmental variation since nanowire working under single-mode leaves a large amount of guided field outside the wire [74, 75]. In addition, photonic devices based on 1D structures also simplify the integration greatly. Aim to improve the performance of efficiency, Zhao et al. designed a fast and ultrasensitive optical transducer with core/sheath structure, where a crystalline organic nanowire was chosen as the core and peroxalate ester as the shell [76].

The gas transducer was fabricated through decorating the crystalline BPEA nanowire with chemo-reactive bis(2,4,5-trichloro-6-carbopen-toxy-phenyl) oxalate (CPPO), which shows highly sensitive and selective response to chemical gas (H_2O_2) because of chemiluminescence effect. Such a strategy could not only retain the high chemical activity of CPPO, but also improve its mechanical and optical properties through the introduction of BPEA nanowires. The doping ratio of two materials could be tuned preciously to get the exact products according to the requirement. At low doping ratio, BPEA molecules exhibit great compatibility with CPPO in solution and there are no solid structures with regular shape. With the increase of the BPEA amount, the excess BPEA monomers began to aggregate into short rod-like structures inside the dye-doped CPPO. The further increase of BPEA content would induce the formation of cable-like structures, in which the BPEA nanowires are fully wrapped by the dye-doped CPPO shell.

The reaction between peroxalate ester groups in CPPO and H_2O_2 can generate a high-energy intermediate, which could excite the fluorescent dye and influence the beam transferred within the wire [77]. Therefore, monitoring the output light would reflect the gas variations during the waveguiding process. A single core/sheath nanostructure was employed for gas sensing based on a gas concentration-dependent evanescent power leakage effect, as shown in Fig. 8.8a. The nanowaveguide was put into a sealed transparent chamber with gas flow system. Once there are traces of H_2O_2 in the gas mixture, the output of the waveguide was drastically attenuated (ca. 50 %), while the input luminous flux was kept unchanged (Fig. 8.8b). The corresponding spectra of the input and output light as a function of exposing time are shown in Fig. 8.8c and Fig. 8.8d, respectively. The optical response time of the nanowires exposed to the gas vapors is determined to be only as short as 35 ms. This cable-like optical waveguide sensing system complements the present nanowire field-effect sensors with the ability to rapidly and specifically monitor the magnified optical variation, showing that a single nanocable is very promising for developing optical transducers to detect special response on chip. The use of a single nanowire for optical waveguiding not only bestows the transducer with small dimensions, fast response, and high sensitivity, but also enables easy integration into the nanophotonic networks.

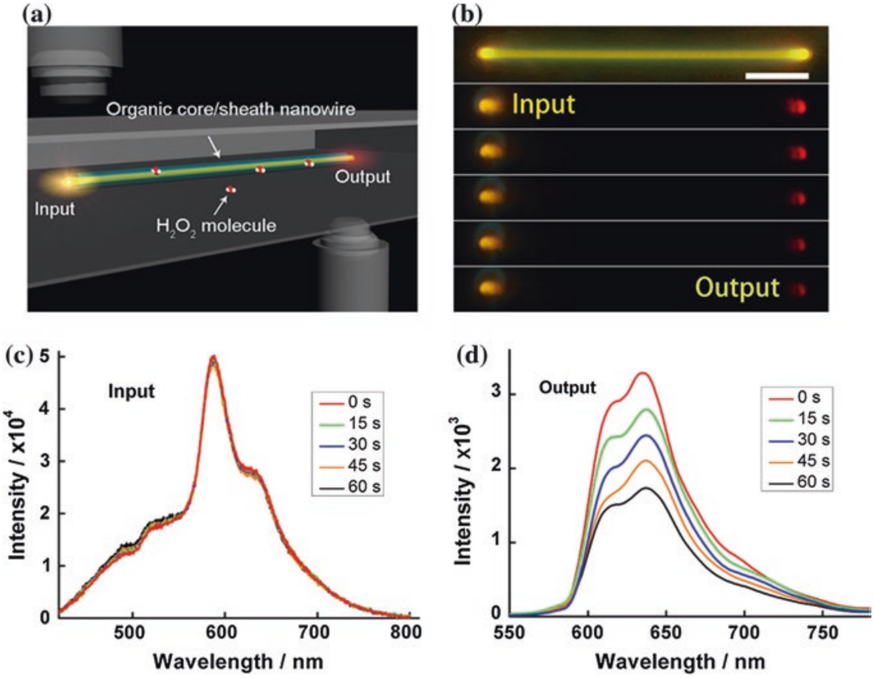

Fig. 8.8 Organic 1D core/sheath structure as chemical gas transducer. **a** Schematic illustration of the coaxially heterogeneous waveguide transducer. **b** PL images of a single heterostructure in the atmosphere chemical gas as time increases. Scale bar is 5 μm. **c**, **d** Time-dependent PL intensities of the input and output light on exposure to trace chemical gas. The output quenched dramatically with the increase of explosion time, while the input was keeping constant, demonstrating a highly sensitive device. Reproduced with permission from [76]. Copyright 2012 Wiley

8.3 Conclusions and Outlook

The ever-growing demand for integrated optical information processing has stimulated great progresses in disciplines including material design, structural synthesis, optical property modulation, and device fabrication. Organic 1D composite material provides intriguing opportunities for both theoretical investigations on the interactions among individual components and the practical applications. In the past couple of years, numerous efforts have been made in the fabrication and characterization of 1D crystalline hybrid nanostructures, including organic/organic, organic/inorganic, and organic/metal composite materials. Now, we reached a preliminary comprehension in both synthesizing organic composite nanomaterials and modulating their photonic properties based on multiple energy transfer routes and other effects, such as self-absorption, EP conversion, and exciton–SPPs coupling. Since the energy transfer process is much more efficient in assembled organic molecular aggregates than that in liquid solutions, both the luminescence efficiency and optical properties are greatly enhanced. In binary organic systems, the combination of the inter-molecular interactions and their own original optical properties could lead to some novel luminescent behaviors. Hybridization with SPPs makes organic units possible to confine light well below the diffraction limit, which is a great boon to miniaturized photonic circuitry. More importantly, the congregate effect in composite materials could not only overcome their own inherently deficiencies, but also bring a great deal of adjustabilities, which is beneficial to the design of tiny functional photonic elements.

As we move forward to the photonic age, the structures and materials used to manufacture individual devices will probably change a lot from current inorganic semiconductors that have supported the electronic technology revolution till now. The general requirement for any photonic signal processing devices is to be robust, low cost, high speed, and easy to integrate. Organics offer low-cost fabrication and convenience to integrate into existing networks made either purely from organics or a combination of organics with others. However, it is still a difficulty to attain high-speed operation through photoluminescence, which is generally related to the lifetimes of excited states (on the order of milliseconds). Fortunately, organics afford a way to overcome this problem as the nonlinear response time of organics is in the femtosecond range. Organic nanomaterials also exhibit great superiorities in broad color tunability, large active areas, and good mechanical flexibility, making them good candidates for photonic applications. In addition, these nanostructures from bottom-up process are single crystals with remarkable improvements in structural and thermal stabilities in comparison with amorphous structures due to the fixed molecular packing.

However, the inorganic technology is still unbeatable in photonic field at present as well as in the near future. The major reason is not the performance of organics, but certainly the price. Thus, continuous efforts should be paid on the rational design and convenient synthesis of molecules with excellent optical and optoelectronic properties through molecular engineering. Also, creation of multifunctional hybrid materials based on comprehensive understanding of synergistic effects among each constitute is essential. In addition, exploration of effective large-scale and high-throughput assembly technique with low cost is highly demanded to meet the requirements of commercial production. The vast choice of organic molecules, facile preparation method, large tunability in both structures and luminescent properties, and the great potential in device applications all of these factors make the organic nanocomposites an amazing field to be investigated on. We might see an increased number of fundamental discoveries and sciences soon.

Now, there is still a long way to impel the research and applications of these optical nanocomposites, because the fabrication and integration of functional devices are still in their infancy. There are tremendous challenges in the actual prototyping of photonic devices, not to mention the difficulties in how to assemble diverse components into a large robotic network for practical integrated circuits. We hope the bottom-up method will open many unique approaches for nanophotontics, since assembling organic small molecules into complex structures could merge multifarious materials with distinct composition, structure, size, and morphology together. In addition, the development of 3D multi-function hybrid systems may provide a new way to the future photonic information technology.

Acknowledgements This work was supported by the National Natural Science Foundation of China (Nos. 21125315, 21373241), the Strategic Priority Research Program of the Chinese Academy of Sciences, (Grant No. XDB01020300), the Ministry of Science and Technology of China (2012YQ120060 and National Basic Research 973 Program), and the Chinese Academy of Sciences.

References

1. I. Zutic, M. Fuhrer, Spintronics: A path to spin logic. Nature Phys. **1**(2), 85–86 (2005)
2. B. Behin-Aein, D. Datta, S. Salahuddin, S. Datta, Proposal for an all-spin logic device with built-in memory. Nature Nanotech. **5**(4), 266–270 (2010)
3. B. Wang, R.I. Kitney, N. Joly, M. Buck, Engineering modular and orthogonal genetic logic gates for robust digital-like synthetic biology. Nature Commun. **2**, 508 (2011)
4. Y. Zhang, Y. Chen, X. Chen, Polarization-based all-optical logic controlled-NOT, XOR, and XNOR gates employing electro-optic effect in periodically poled lithium niobate. Appl. Phys. Lett. **99**(16), 161113–161117 (2011)
5. P. Yang, R. Yan, M. Fardy, Semiconductor nanowire: What's next? Nano Lett. **10**(5), 1529–1536 (2010)
6. H.J. Caulfield, S. Dolev, Why future supercomputing requires optics. Nat. Photon **4**(5), 261–263 (2010)
7. R. Yan, D. Gargas, P. Yang, Nanowire photonics. Nat. Photon **3**(10), 569–576 (2009)
8. S. Kéna-Cohen, M. Davanço, S.R. Forrest, Strong exciton-photon coupling in an organic single crystal microcavity. Phys. Rev. Lett. **101**(11), 116401 (2008)
9. K. Takazawa, J. Inoue, K. Mitsuishi, T. Takamasu, Fraction of a millimeter propagation of exciton polaritons in photoexcited nanofibers of organic dye. Phys. Rev. Lett. **105**(6), 067401 (2010)
10. D. Pile, S. Forrest, Organic polariton laser. Nat. Photon **4**(6), 402 (2010)
11. R. Kirchain, L. Kimerling, A roadmap for nanophotonics. Nat. Photon **1**(6), 303 (2007)
12. Y. Li, F. Qian, J. Xiang, C.M. Lieber, Nanowire electronic and optoelectronic devices. Mater. Today **9**(10), 18–27 (2006)
13. Q.H. Cui, Y.S. Zhao, J. Yao, Photonic applications of one-dimensional organic single-crystalline nanostructures: optical waveguides and optically pumped lasers. J. Mater. Chem. **22**(10), 4136–4140 (2012)
14. C. Zhang, Y.S. Zhao, J. Yao, Optical waveguides at micro/nanoscale based on functional small organic molecules. Phys. Chem. Chem. Phys. **13**(20), 9060–9073 (2011)
15. J.E. Anthony, Functionalized acenes and heteroacenes for organic electronics. Chem. Rev. **106**(12), 5028–5048 (2006)
16. A.L. Briseno, T.W. Holcombe, A.I. Boukai, E.C. Garnett, S.W. Shelton, J.J.M. Fréchet, P. Yang, Oligo- and polythiophene/ZnO hybrid nanowire solar cells. Nano Lett. **10**(1), 334–340 (2009)
17. A. Gumennik, A.M. Stolyarov, B.R. Schell, C. Hou, G. Lestoquoy, F. Sorin, W. McDaniel, A. Rose, J.D. Joannopoulos, Y. Fink, All-in-fiber chemical sensing. Adv. Mater. **24**(45), 6005–6009 (2012)
18. Y.S. Zhao, J.J. Xu, A.D. Peng, H.B. Fu, Y. Ma, L. Jiang, J. Yao, Optical waveguide based on crystalline organic microtubes and microrods. Angew. Chem. Int. Ed. **47**(38), 7301–7305 (2008)

19. Y.S. Zhao, H.B. Fu, A.D. Peng, Y. Ma, Q. Liao, J.N. Yao, Construction and optoelectronic properties of organic one-dimensional nanostructures. Acc. Chem. Res. **43**(3), 409–418 (2010)
20. W.L. Barnes, A. Dereux, T.W. Ebbesen, Surface plasmon subwavelength optics. Nature **424**(6950), 824–830 (2003)
21. Y.L. Yan, C. Zhang, J.N. Yao, Y.S. Zhao, Recent advances in organic one-dimensional composite materials: Design, construction, and photonic elements for information processing. Adv. Mater. **25**(27), 3627–3638 (2013)
22. M.H. Huang, S. Mao, H. Feick, H. Yan, Y. Wu, H. Kind, E. Weber, R. Russo, P. Yang, Room-temperature ultraviolet nanowire nanolasers. Science **292**(5523), 1897–1899 (2001)
23. C. Zhang, C.-L. Zou, Y. Yan, R. Hao, F.-W. Sun, Z.-F. Han, Y.S. Zhao, J. Yao, Two-photon pumped lasing in single-crystal organic nanowire exciton polariton resonators. J. Am. Chem. Soc. **133**(19), 7276–7279 (2011)
24. Y.S. Zhao, A.D. Peng, H.B. Fu, Y. Ma, J.N. Yao, Nanowire waveguides and ultraviolet lasers based on small organic molecules. Adv. Mater. **20**(9), 1661–1665 (2008)
25. J. Li, C. Meng, Y. Liu, X. Wu, Y. Lu, Y. Ye, L. Dai, L. Tong, X. Liu, Q. Yang, Wavelength tunable CdSe nanowire lasers based on the absorption-emission-absorption process. Adv. Mater. **25**(6), 833–837 (2013)
26. S. Kena Cohen, S.R. Forrest, Room-temperature polariton lasing in an organic single-crystal microcavity. Nat. Photon **4**(6), 371–375 (2010)
27. L. Cerdan, E. Enciso, V. Martin, J. Banuelos, I. Lopez-Arbeloa, A. Costela, I. Garcia-Moreno, FRET-assisted laser emission in colloidal suspensions of dye-doped latex nanoparticles. Nat. Photon **6**(9), 621–626 (2012)
28. J. Xu, L. Ma, P. Guo, X. Zhuang, X. Zhu, W. Hu, X. Duan, A. Pan, Room-temperature dual-wavelength lasing from single-nanoribbon lateral heterostructures. J. Am. Chem. Soc. **134**(30), 12394–12397 (2012)
29. C.W. Tang, S.A. VanSlyke, C.H. Chen, Electroluminescence of doped organic thin films. J. Appl. Phys. **65**(9), 3610–3616 (1989)
30. T. Förster, Zwischenmolekulare energiewanderung und fluoreszenz. Ann. Phys. **437**(1–2), 55–75 (1948)
31. S. Reineke, F. Lindner, G. Schwartz, N. Seidler, K. Walzer, B. Lussem, K. Leo, White organic light-emitting diodes with fluorescent tube efficiency. Nature **459**(7244), 234–238 (2009)
32. Y.S. Zhao, H. Zhong, Q. Pei, Fluorescence resonance energy transfer in conjugated polymer composites for radiation detection. Phys. Chem. Chem. Phys. **10**(14), 1848–1851 (2008)
33. Y. Lei, Q. Liao, H. Fu, J. Yao, Orange−blue−orange triblock one-dimensional heterostructures of organic microrods for white-light emission. J. Am. Chem. Soc. **132**(6), 1742–1743 (2010)
34. Y.S. Zhao, H.B. Fu, F.Q. Hu, A.D. Peng, W.S. Yang, J. Yao, Tunable emission from binary organic one-dimensional nanomaterials: An alternative approach to white-light emission. Adv. Mater. **20**(1), 79–83 (2008)
35. J.Y. Zheng, C. Zhang, Y.S. Zhao, J. Yao, Detection of chemical vapors with tunable emission of binary organic nanobelts. Phys. Chem. Chem. Phys. **12**(40), 12935–12938 (2010)
36. R.R. Islangulov, J. Lott, C. Weder, F.N. Castellano, Noncoherent low-power upconversion in solid polymer films. J. Am. Chem. Soc. **129**(42), 12652–12653 (2007)
37. C. Zhang, J.Y. Zheng, Y.S. Zhao, J. Yao, Organic core-shell nanostructures: microemulsion synthesis and upconverted emission. Chem. Commun. **46**(27), 4959–4961 (2010)
38. Q. Liao, H. Fu, C. Wang, J. Yao, Cooperative assembly of binary molecular components into tubular structures for multiple photonic applications. Angew. Chem. Int. Ed. **50**(21), 4942–4946 (2011)
39. C. Zhang, J.Y. Zheng, Y.S. Zhao, J. Yao, Self-modulated white light outcoupling in doped organic nanowire waveguides via the fluctuations of singlet and triplet excitons during propagation. Adv. Mater. **23**(11), 1380–1384 (2011)

40. S.J. Hurst, E.K. Payne, L. Qin, C.A. Mirkin, Multisegmented one-dimensional nanorods prepared by hard-template synthetic methods. Angew. Chem. Int. Ed. **45**(17), 2672–2692 (2006)
41. X. Li, T. Wang, J. Zhang, D. Zhu, X. Zhang, Y. Ning, H. Zhang, B. Yang, Controlled fabrication of fluorescent barcode nanorods. ACS Nano **4**(8), 4350–4360 (2010)
42. H. Wang, M. Sun, K. Ding, M.T. Hill, C.-Z. Ning, A top-down approach to fabrication of high quality vertical heterostructure nanowire arrays. Nano Lett. **11**(4), 1646–1650 (2011)
43. C. Zhang, Y. Yan, Y.-Y. Jing, Q. Shi, Y.S. Zhao, J. Yao, One-dimensional organic photonic heterostructures: rational construction and spatial engineering of excitonic emission. Adv. Mater. **24**(13), 1703–1708 (2012)
44. R.S. Tucker, The role of optics in computing. Nature Photon **4**(7), 405–405 (2010)
45. L. Bu, E. Pentzer, F.A. Bokel, T. Emrick, R.C. Hayward, Growth of polythiophene/perylene tetracarboxydiimide donor/acceptor shish-kebab nanostructures by coupled crystal modification. ACS Nano **6**(12), 10924–10929 (2012)
46. Y.S. Zhao, J. Wu, J. Huang, Vertical organic nanowire arrays: controlled synthesis and chemical sensors. J. Am. Chem. Soc. **131**(9), 3158–3159 (2009)
47. Y.S. Zhao, P. Zhan, J. Kim, C. Sun, J. Huang, Patterned growth of vertically aligned organic nanowire waveguide arrays. ACS Nano **4**(3), 1630–1636 (2010)
48. J.Y. Zheng, Y. Yan, X. Wang, Y.S. Zhao, J. Huang, J. Yao, Wire-on-wire growth of fluorescent organic heterojunctions. J. Am. Chem. Soc. **134**(6), 2880–2883 (2012)
49. M. Haurylau, G. Chen, H. Chen, J. Zhang, N.A. Nelson, D.H. Albonesi, E.G. Friedman, P.M. Fauchet, On-chip optical interconnect roadmap: challenges and critical directions. IEEE J Sel Top Quant **12**(6), 1699–1705 (2006)
50. Y. Zhang, Y. Zhang, B. Li, Optical switches and logic gates based on self-collimated beams in two-dimensional photonic crystals. Opt. Express **15**(15), 9287–9292 (2007)
51. J. Chieh, C. Hong, S. Yang, H. Horng, H. Yang, Study on magnetic fluid optical fiber devices for optical logic operations by characteristics of superparamagnetic nanoparticles and magnetic fluids. J. Nanopart. Res. **12**(1), 293–300 (2010)
52. V.R. Almeida, C.A. Barrios, R.R. Panepucci, M. Lipson, All-optical control of light on a silicon chip. Nature **431**(7012), 1081–1084 (2004)
53. E. Ozbay, Plasmonics: Merging photonics and electronics at nanoscale dimensions. Science **311**(5758), 189–193 (2006)
54. R. Yan, P. Pausauskie, J. Huang, P. Yang, Direct photonic-plasmonic coupling and routing in single nanowires. Proc Nat Acad Sci USA **106**(50), 21045–21050 (2009)
55. X. Guo, M. Qiu, J. Bao, B.J. Wiley, Q. Yang, X. Zhang, Y. Ma, H. Yu, L. Tong, Direct coupling of plasmonic and photonic nanowires for hybrid nanophotonic components and circuits. Nano Lett. **9**(12), 4515–4519 (2009)
56. A.L. Pyayt, B. Wiley, Y. Xia, A. Chen, L. Dalton, Integration of photonic and silver nanowire plasmonic waveguides. Nature Nanotech **3**(11), 660–665 (2008)
57. Y. Yan, Y.S. Zhao, Exciton polaritons in 1D organic nanocrystals. Adv. Funct. Mater. **22**(7), 1330–1332 (2012)
58. Y. Yan, C. Zhang, J.Y. Zheng, J. Yao, Y.S. Zhao, Optical modulation based on direct photon-plasmon coupling in organic/metal nanowire heterojunctions. Adv. Mater. **24**(42), 5681–5686 (2012)
59. H. Najafov, B. Lee, Q. Zhou, L.C. Feldman, V. Podzorov, Observation of long-range exciton diffusion in highly ordered organic semiconductors. Nat. Mater **9**(11), 938–943 (2010)
60. Q. Bao, B.M. Goh, B. Yan, T. Yu, Z. Shen, K.P. Loh, Polarized emission and optical waveguide in crystalline perylene diimide microwires. Adv. Mater. **22**(33), 3661–3666 (2010)
61. M. Sindoro, Y. Feng, S. Xing, H. Li, J. Xu, H. Hu, C. Liu, Y. Wang, H. Zhang, Z. Shen, H. Chen, Triple-layer (Au@perylene)@polyaniline nanocomposite: unconventional growth of faceted organic nanocrystals on polycrystalline Au. Angew. Chem. Int. Ed. **50**(42), 9898–9902 (2011)
62. Y.J. Li, Y. Yan, C. Zhang, Y.S. Zhao, J. Yao, Embedded branch-like organic/metal nanowire heterostructures: liquid-phase synthesis, efficient photon-plasmon coupling, and optical signal manipulation. Adv. Mater. **25**(20), 2784–2788 (2013)

63. C. Yang, L. Wei, S. Jialin, H. Yaping, Z. Jianhong, L. Sheng, S. Hongsan, G. Jihua, A technique for controlling the alignment of silver nanowires with an electric field. Nanotechnology **17**(9), 2378 (2006)
64. Y. Huang, X. Duan, Q. Wei, C.M. Lieber, Directed assembly of one-dimensional nanostructures into functional networks. Science **291**(5504), 630–633 (2001)
65. X. Duan, Y. Huang, Y. Cui, J. Wang, C.M. Lieber, Indium phosphide nanowires as building blocks for nanoscale electronic and optoelectronic devices. Nature **409**(6816), 66–69 (2001)
66. Y. Guo, Q. Tang, H. Liu, Y. Zhang, Y. Li, W. Hu, S. Wang, D. Zhu, Light-controlled organic/inorganic P–N junction nanowires. J. Am. Chem. Soc. **130**(29), 9198–9199 (2008)
67. B. Tian, X. Zheng, T.J. Kempa, Y. Fang, N. Yu, G. Yu, J. Huang, C.M. Lieber, Coaxial silicon nanowires as solar cells and nanoelectronic power sources. Nature **449**(7164), 885–889 (2007)
68. X. Li, C. Gao, H. Duan, B. Lu, Y. Wang, L. Chen, Z. Zhang, X. Pan, E. Xie, High-performance photoelectrochemical-type self-powered UV photodetector using epitaxial TiO2/SnO2 branched heterojunction nanostructure. Small **9**(11), 2005–2011 (2013)
69. Y.S. Zhao, H.B. Fu, A.D. Peng, Y. Ma, D.B. Xiao, J.N. Yao, Low-dimensional nanomaterials based on small organic molecules: Preparation and optoelectronic properties. Adv. Mater. **20**(15), 2859–2876 (2008)
70. Y. Che, H. Huang, M. Xu, C. Zhang, B.R. Bunes, X. Yang, L. Zang, Interfacial engineering of organic nanofibril heterojunctions into highly photoconductive materials. J. Am. Chem. Soc. **133**(4), 1087–1091 (2010)
71. Q.H. Cui, L. Jiang, C. Zhang, Y.S. Zhao, W. Hu, J. Yao, Coaxial organic p-n heterojunction nanowire arrays: one-step synthesis and photoelectric properties. Adv. Mater. **24**(17), 2332–2336 (2012)
72. F. Gu, L. Zhang, X. Yin, L. Tong, Polymer single-nanowire optical sensors. Nano Lett. **8**(9), 2757–2761 (2008)
73. A. Berrier, R. Cools, C. Arnold, P. Offermans, M. Crego-Calama, S.H. Brongersma, J. Gómez-Rivas, Active control of the strong coupling regime between porphyrin excitons and surface plasmon polaritons. ACS Nano **5**(8), 6226–6232 (2011)
74. D.J. Sirbuly, S.E. Létant, T.V. Ratto, Hydrogen sensing with subwavelength optical waveguides via porous silsesquioxane-palladium nanocomposites. Adv. Mater. **20**(24), 4724–4727 (2008)
75. S. Lal, S. Link, N.J. Halas, Nano-optics from sensing to waveguiding. Nature Photon **1**(11), 641–648 (2007)
76. J.Y. Zheng, Y. Yan, X. Wang, W. Shi, H. Ma, Y.S. Zhao, J. Yao, Hydrogen peroxide vapor sensing with organic core/sheath nanowire optical waveguides. Adv. Mater. **24**(35), OP194–OP199 (2012)
77. M. Orlovic, R.L. Schowen, R.S. Givens, F. Alvarez, B. Matuszewski, N. Parekh, A simplified model for the dynamics of chemiluminescence in the oxalate-hydrogen peroxide system: toward a reaction mechanism. J. Org. Chem. **54**(15), 3606–3610 (1989)

Index

Y.S. Zhao (ed.), *Organic Nanophotonics*, Nano-Optics and Nanophotonics,
DOI 10.1007/978-3-662-45082-6